Sting Interference Effects as Determined by Measurements of Dynamic Stability Derivatives, Surface Pressure, and Base Pressure for Mach Numbers 2 through 8

B. L. Uselton and F. B. Cyran
ARO, Inc.

October 1980

Final Report for Period May 25, 1977 – March 2, 1978

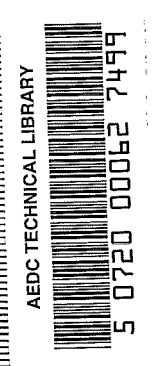

Approved for public release; distribution unlimited.

ARNOLD ENGINEERING DEVELOPMENT CENTER
ARNOLD AIR FORCE STATION, TENNESSEE
AIR FORCE SYSTEMS COMMAND
UNITED STATES AIR FORCE

NOTICES

When U. S. Government drawings, specifications, or other data are used for any purpose other than a definitely related Government procurement operation, the Government thereby incurs no responsibility nor any obligation whatsoever, and the fact that the Government may have formulated, furnished, or in any way supplied the said drawings, specifications, or other data, is not to be regarded by implication or otherwise, or in any manner licensing the holder or any other person or corporation, or conveying any rights or permission to manufacture, use, or sell any patented invention that may in any way be related thereto.

Qualified users may obtain copies of this report from the Defense Technical Information Center.

References to named commercial products in this report are not to be considered in any sense as an indorsement of the product by the United States Air Force or the Government.

This report has been reviewed by the Office of Public Affairs (PA) and is releasable to the National Technical Information Service (NTIS). At NTIS, it will be available to the general public, including foreign nations.

APPROVAL STATEMENT

This report has been reviewed and approved.

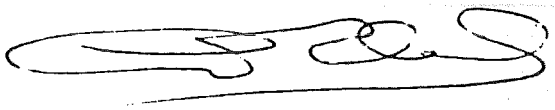

ALVIN R. OBAL, Captain, CF
Project Manager
Directorate of Technology

Approved for publication:

FOR THE COMMANDER

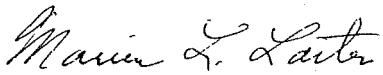

MARION L. LASTER
Director of Technology
Deputy for Operations

REPORT DOCUMENTATION PAGE		READ INSTRUCTIONS BEFORE COMPLETING FORM
1. REPORT NUMBER AEDC-TR-79-89	2. GOVT ACCESSION NO.	3. RECIPIENT'S CATALOG NUMBER
4. TITLE *(and Subtitle)* STING INTERFERENCE EFFECTS AS DETERMINED BY MEASUREMENTS OF DYNAMIC STABILITY DERIVATIVES, SURFACE PRESSURE, AND BASE PRESSURE FOR MACH NUMBERS 2 THROUGH 8		5. TYPE OF REPORT & PERIOD COVERED Final Report-May 25, 1977 to March 2, 1978 6. PERFORMING ORG. REPORT NUMBER
7. AUTHOR(s) Bob L. Uselton and Fred B. Cyran, ARO, Inc., a Sverdrup Corporation Company		8. CONTRACT OR GRANT NUMBER(s)
9. PERFORMING ORGANIZATION NAME AND ADDRESS Arnold Engineering Development Center/DOT Air Force Systems Command Arnold Air Force Station, Tennessee 37389		10. PROGRAM ELEMENT, PROJECT, TASK AREA & WORK UNIT NUMBERS Program Element 65807F
11. CONTROLLING OFFICE NAME AND ADDRESS Arnold Engineering Development Center/DOS Air Force Systems Command Arnold Air Force Station, Tennessee 37389		12. REPORT DATE October 1980 13. NUMBER OF PAGES 147
14. MONITORING AGENCY NAME & ADDRESS*(if different from Controlling Office)*		15. SECURITY CLASS. *(of this report)* UNCLASSIFIED 15a. DECLASSIFICATION/DOWNGRADING SCHEDULE N/A

16. DISTRIBUTION STATEMENT *(of this Report)*

Approved for public release; distribution unlimited.

17. DISTRIBUTION STATEMENT *(of the abstract entered in Block 20, if different from Report)*

18. SUPPLEMENTARY NOTES

Available in Defense Technical Information Center (DTIC)

19. KEY WORDS *(Continue on reverse side if necessary and identify by block number)*

wind tunnel tests	nose cones	oscillation
sting mounts	dynamic tests	angle of attack
interference	static stability	laminar boundary layer
hypersonic flow	pitch (motion)	turbulent boundary layer
supersonic flow	base pressure	

20. ABSTRACT *(Continue on reverse side if necessary and identify by block number)*

Wind tunnel tests were conducted to provide support interference information for planning and directing wind tunnel tests at supersonic and hypersonic Mach numbers. Sting-length and sting-diameter effects on base and surface pressures of a blunt 6-deg cone with a sliced base were investigated at Mach numbers 2, 3, 5, and 8 in the Arnold Engineering Development Center (AEDC) von Karman Gas Dynamics Facility (VKF). Dynamic stability tests on a blunt 7-deg cone were also conducted at AEDC-VKF at Mach numbers

DD FORM 1 JAN 73 1473 EDITION OF 1 NOV 65 IS OBSOLETE

20. ABSTRACT (Continued)
2, 5, and 8. The objectives of the 7-deg cone tests were to define critical sting lengths as determined by the measurement of dynamic stability derivatives, static pitching moment, and base pressure. Two frequencies of oscillation were investigated, and data were obtained for laminar, transitional, and turbulent boundary-layer conditions at the model base. The data from the 6- and 7-deg cone tests showed that the critical sting length depended on the interference indicator, Mach number, angle of attack, state of the model boundary layer, and frequency of oscillation. The critical sting length was generally less for models with turbulent boundary layers than for those with laminar boundary layers. A critical sting length of 2.5 model diameters was determined to be suitable for all test conditions that produced a turbulent boundary layer at or ahead of the model base.

AFSC
Arnold AFS Tenn

PREFACE

The research reported herein was conducted by the Arnold Engineering Development Center (AEDC), Air Force Systems Command (AFSC). The results were obtained by ARO, Inc., AEDC Group (a Sverdrup Corporation Company), operating contractor for the AEDC, AFSC, Arnold Air Force Station, Tennessee. The work was done under ARO Project Numbers V32F-09, V32A-A1A, V41A/B-N9A, V32A-R0A, and V41A/B-W4A. Alexander F. Money, Directorate of Technology, was the Air Force project manager. The manuscript was submitted for publication on October 9, 1979.

CONTENTS

Page

1.0 INTRODUCTION 7
2.0 UPDATING REFERENCES AND STING CRITERIA 8
3.0 APPARATUS
3.1 Test Facilities 8
3.2 Pressure Model and Sting Hardware 9
3.3 Pitch-Damping Model and Sting Hardware 9
3.4 Pitch/Yaw Damping Test Mechanism 10
3.5 Instrumentation 10
4.0 TEST DESCRIPTION
4.1 Test Conditions 12
4.2 Test Procedures 12
4.3 Data Reduction 13
4.4 Uncertainty of Measurements 14
5.0 RESULTS AND DISCUSSION
5.1 Steady-State, Heat-Transfer Data (Sliced-Base, 6-deg Cone Model) 16
5.2 Pressure Data (Sliced-Base, 6-deg Cone Model) 16
5.3 Pitch-Damping Data (7-deg Cone Model) 18
6.0 CONCLUDING REMARKS 20
REFERENCES 21

ILLUSTRATIONS

Figure

1. Wind Tunnels and Model Injection Systems 27
2. Details of Pressure Model 29
3. Pressure Model Instrumentation Locations 30
4. Pressure Tap and Gardon Gage Locations 34
5. Boundary-Layer Trip Details for Pressure-Heat-Transfer Tests 37
6. Sting Configurations for Pressure Model, $D_s/D = 0.19$ 38
7. Sting Configurations for Pressure Model, $D_s/D = 0.35$ 39
8. Sting Configurations for Pressure Model, $D_s/D = 0.50$ 40
9. Pressure Model Installation in Tunnel A Test Section Tank, $L_s/D = 1.0$, $D_s/D = 0.19$, 6-in. Flare 41
10. Pressure Model Installation in Tunnel A Test Section, $L_s/D = 3.9$, $D_s/D = 0.19$ 42

Figure Page

11. Pressure Model Installation in Tunnel B Test Section, $L_s/D = 3.9$, $D_s/D = 0.35$ . . . 43
12. Details of Pitch-Damping Model . . . 44
13. Boundary-Layer Trip Details for Pitch-Damping Tests . . . 45
14. Details of Pitch-Damping Model Support Configurations . . . 46
15. Plate Details . . . 49
16. 1-DOF Test Mechanism (VKF-1.C) Details . . . 50
17. 1-DOF Test Mechanism (VKF-1.C) . . . 50
18. Details of Thermopile Gardon Gage . . . 51
19. Presentation of Steady-State Heat-Transfer Results . . . 52
20. Typical Pressure Distributions . . . 55
21. Sting Effects as a Function of Angle of Attack, M = 3, Turbulent Boundary Layer . . . 57
22. Sting Effects on Base Pressure, M = 2 . . . 64
23. Sting Effects as a Function of Angle of Attack, M = 8, Turbulent Boundary Layer . . . 66
24. Sting Effects as a Function of Angle of Attack, M = 8, Laminar Boundary Layer . . . 73
25. Base and Surface Pressure as a Function of Effective Sting Length, Turbulent Boundary Layer, M = 2 . . . 80
26. Base and Surface Pressure as a Function of Effective Sting Length, Turbulent Boundary Layer, M = 3 . . . 82
27. Base and Surface Pressure as a Function of Effective Sting Length, Turbulent Boundary Layer, M = 5 . . . 84
28. Base and Surface Pressure as a Function of Effective Sting Length, Turbulent Boundary Layer, M = 8 . . . 86
29. Base and Surface Pressure as a Function of Effective Sting Length, Laminar Boundary Layer, M = 8 . . . 88
30. Critical Sting Length Defined by Base and Surface Pressure Measurements . . . 90
31. Base and Surface Pressure as a Function of Sting Diameter, Turbulent Boundary Layer, M = 3 . . . 91
32. Base and Surface Pressure as a Function of Sting Diameter, Turbulent Boundary Layer, M = 8 . . . 93
33. Base and Surface Pressure as a Function of Sting Diameter, Laminar Boundary Layer, M = 8 . . . 95
34. Boundary-Layer Trip Effects at M = 5 . . . 97

Figure | Page

35. Boundary-Layer Trip Effects at M = 8 98
36. Sting Effects as a Function of Angle of Attack, M = 2 99
37. Sting Effects as a Function of Angle of Attack, M = 3 Turbulent Boundary Layer 101
38. Sting Effects as a Function of Angle of Attack, M = 5 RFP = 0.0027 102
39. Sting Effects as a Function of Angle of Attack, M = 5, RFP = 0.0047 105
40. Sting Effects as a Function of Angle of Attack, M = 8, RFP = 0.0019 108
41. Sting Effects as a Function of Angle of Attack, M = 8, RFP = 0.0032 110
42. Damping and Static Stability Derivatives as a Function of Effective Sting Length, M = 2 112
43. Damping Derivatives as a Function of Effective Sting Length D_s/D = 0.22, M ≈ 3 (Reproduced from Ref. 1) 113
44. Damping Derivatives as a Function of Effective Sting Length for Two Reduced Frequencies, M = 5 114
45. Static Stability Derivatives as a Function of Effective Sting Length for Two Reduced Frequencies, M = 5 115
46. Damping Derivatives as a Function of Effective Sting Length for Two Reduced Frequencies, M = 8 116
47. Static Stability Derivatives as a Function of Effective Sting Length for Two Reduced Frequencies, M = 8 117
48. Base Pressure as a Function of Effective Sting Length, M = 2 118
49. Base Pressure as a Function of Effective Sting Length, M ≈3 (Reproduced from Ref. 1) 118
50. Base Pressure as a Function of Effective Sting Length, M = 5 119
51. Critical Sting Length Defined by Static and Dynamic Measurements, 7-Deg Cone 120
52. Splitter-Plate Effects on Damping Derivatives and Base Pressure Ratio, M = 5, L_s/D = 3.3 121
53. Splitter-Plate Effects on Damping Derivatives for Two Reduced Frequencies, Laminar Boundary Layer, M = 8, L_s/D = 1.0 122
54. Splitter-Plate Effects on Damping Derivatives for Two Reduced Frequencies, Turbulent Boundary Layer, M = 8, L_s/D = 1.0 123
55. Splitter-Plate Effects on Damping Derivatives for Two Reduced Frequencies, Laminar Boundary Layer, M = 8, L_s/D = 3.3 124

Figure Page

56. Splitter-Plate Effects on Damping Derivatives for Two Reduced Frequencies, Turbulent Boundary Layer, M = 8, L_s/D = 3.3 125

TABLES

1. Test Conditions (Pressure Tests) 126
2. Test Conditions (Pitch-Damping Tests) 126
3. Pressure Test Summary (Tunnel A) 127
4. Pressure Test Summary (Tunnel B) 128
5. Tunnel A Pitch-Damping Test Summary (RFP ≈ 0.003) 129
6. Tunnel A Pitch-Damping Test Summary (RFP ≈ 0.006) 130
7. Tunnel B Pitch-Damping Test Summary (RFP ≈ 0.002) 131
8. Tunnel B Pitch-Damping Test Summary (RFP ≈ 0.003) 132
9. Test Condition Uncertainties (Pressure Tests) 133
10. Test Condition Uncertainties (Pitch-Damping Tests) 133
11. Uncertainties of Pressure Measurements 133
12. Uncertainties of Pitch-Damping Measurements 134

APPENDIXES

A. SUMMARY OF AVAILABLE REFERENCES 135
B. SUGGESTED STING CRITERIA 141

NOMENCLATURE 144

1.0 INTRODUCTION

The aerodynamicist must rely on theoretical and experimental information from ground test facilities for prediction of full-scale flight behavior and, in the last few years, has become more concerned about the effects of wind-tunnel model support interference on test data. As the accuracy required of wind-tunnel data becomes more precise, the evaluation of model support interference effects becomes critical. To evaluate this interference, a research program was conducted at the Arnold Engineering Development Center (AEDC) von Kármán Gas Dynamics Facility (VKF) in 1976. The purpose of that program was to evaluate sting interference effects at Mach number 3; the results are documented in Ref. 1. The support interference technology program was continued, and this report documents the work completed in 1977 and 1978. The general objective of the three-year technology program was to provide support interference information for planning and directing wind-tunnel tests for supersonic through hypersonic Mach numbers. Technology was developed in these programs for evaluating support effects on base pressure, surface pressure, static pitching moment, and dynamic derivatives for models with laminar, transitional, and turbulent boundary layers near the model base.

The objective of the 1977 technology program was to investigate sting-length and sting-diameter effects on the base and surface pressures of a blunt, 6-deg cone with a sliced base. The tests supplied information pertinent to wind tunnel configurations with control surfaces in the model base region. Pressure data were obtained at Mach numbers (M) 2, 3, 5, and 8 over an angle-of-attack (α) range from 0 to 25 deg. Effective sting length was varied from 1 to 4 model diameters, and sting diameter was varied from 0.19 to 0.5 model diameters. Steady-state, heat-transfer measurements were also made at M = 3, 5, and 8 at α = 0 to determine the type of boundary layer existing over the sliced region. Heat-transfer measurements were compared with theoretical estimates for establishing the nature of the boundary layer. These tests were conducted May 25–26, 1977 [AEDC-VKF Supersonic Wind Tunnel (A)] and June 2–3, 1977 [AEDC-VKF Hypersonic Wind Tunnel (B)].

The 1978 support interference technology program extended the 1976 work to include Mach numbers 2, 5, and 8. The objectives of the 1978 program were to define critical sting lengths for two reduced frequencies as determined by the measurement of dynamic stability derivatives, static pitching-moment, and base pressure for different boundary-layer conditions. Results were obtained for laminar, transitional, and turbulent boundary layers at the model base. (When "boundary-layer condition" is herein associated in the dynamic stability data, the term refers to the boundary-layer condition at the model base). The effects on the dynamic derivatives of splitter plates located behind the model were also investigated. Previous investigators have shown that adding a

splitter plate to the support strut behind the sting significantly smoothed and reduced the base pressure. Tests were conducted in Tunnels A and B on a blunt, 7-deg half-angle cone for a reduced frequency range from 0.002 to 0.007. The effective sting length was varied from 1 to 3.3 model diameters. Angles of attack ranged from -8 to 8 deg. The small amplitude (±1 deg) forced-oscillation technique was used. The tests were conducted on February 22–23, 1978 (Tunnel B) and February 28–March 2, 1978 (Tunnel A).

2.0 UPDATING REFERENCES AND STING CRITERIA

The report on the 1976 program (Ref. 1) summarized the pertinent facts of available references (Refs. 2 through 35) on support interference. These references have been updated (Refs. 36 through 41) and are summarized in Appendix A.

Reference 1 also presents a chart suggesting critical sting lengths for various configurations for the subsonic to hypersonic range of Mach numbers. The chart is based on the survey data and is intended to be a guide for selecting support stings and for evaluating existing data for support effects. The chart readily notes the scarcity of sting criteria. An updated version of the chart is presented in Appendix B.

3.0 APPARATUS

3.1 TEST FACILITIES

Tunnels A and B (Fig. 1) are continuous-flow, closed-circuit, variable-density wind tunnels. Tunnel A has an automatically driven flexible-plate-type nozzle and a 40- by 40-in. test section. The tunnel can be operated at Mach numbers from 1.5 to 6 at maximum stagnation pressures from 29 to 200 psia, respectively, and at stagnation temperatures as great as 750°R at Mach number 6. Minimum operating pressures range from about one-tenth to one-twentieth of the maximum at each Mach number.

Tunnel B has a 50-in.-diam test section and two interchangeable axisymmetric contoured nozzles for providing Mach numbers of 6 and 8. The tunnel can be operated continuously over a range of pressure levels from 20 to 300 psia at Mach number 6, and from 50 to 900 psia at Mach number 8. Stagnation temperatures sufficient to avoid air liquefaction (up to 1,350°R) in the test section are obtained through the use of a natural-gas-fired combustion heater. The entire tunnel (throat, nozzle, test section, and diffuser) is cooled by integral, external water jackets. Each tunnel has a model injection system that allows removal of the model from the test section while the tunnel remains in operation. A description of the tunnels may be found in Ref. 42.

3.2 PRESSURE MODEL AND STING HARDWARE

The stainless-steel model (Fig. 2) consisted of a blunt, 6-deg cone with two flat surfaces (a double slice) in the base region. Two nose configurations (R_N/R_B = 0.0025 and 0.1) were tested. The nose portion was taken from a previous test model. The aft-nose portion of the model was designed and fabricated at AEDC-VKF and was instrumented with 22 surface pressure taps (Fig. 3a) in the sliced region and four base pressure taps (Fig. 3b) in the base plate. The model surface opposite the sliced region was instrumented with nine Gardon-type heat flux gages (Fig. 3c) for determining the type of boundary layer existing over the sliced region. The Stanton numbers determined from the heat gage outputs were compared with theoretical estimates for establishing the nature of the boundary layer. Photographs of the instrumentation are shown in Fig. 4. Trip rings (Fig. 5) were used to trip the boundary layer so that turbulent heating rates would exist over the sliced base region. Number 60 grit was used for M = 2 and 3 and number 36 grit for M = 5. Spheres 0.063 in. in diameter (K) were used at M = 8. Additional trips were used (see Fig. 5) during the heat-transfer tests.

The basic sting consisted of a long slender sting (Fig. 6a) that had an effective sting length ratio (L_s/D) of 3.9 and a sting-to-model-diameter ratio (D_s/D) of 0.19. Effective sting length was varied by sliding either a 4- or 6-in.-diam flare along the sting; sting diameter was increased by installing a sleeve over the basic sting. Effective sting length ratios of 1.0, 2.0, 2.5, 3.0, 3.9, and 4.2 and sting-to-model-diameter ratios of 0.19, 0.35, and 0.50 were tested. Photographs of these sting configurations are presented in Figs. 6, 7, and 8. Installation photographs are shown in Figs. 9, 10, and 11. Although the model was tested at ϕ = 180 deg, the data and model sketches are presented for ϕ = 0.

3.3 PITCH-DAMPING MODEL AND STING HARDWARE

The stainless-steel model for the pitch-damping tests (Fig. 12) was a flat-base, 7-deg half-angle cone with a 15-percent bluntness ratio nose (R_N/R_B = 0.15). The moment reference point (also pivot axis location) was located at 60.9 percent of the model length aft of the nose. The model was balanced so that the center of gravity was located on the balance pivot axis. Trip rings (Fig. 13) were used to obtain transitional and turbulent boundary layers at the model base.

The cross-flexure balance of the forced-oscillation mechanism (VKF-1.C) is supported by a long slender sting; this allows obtaining large effective sting lengths (L_s) and small effective sting diameters (D_s) to minimize sting interference effects. When mounted to the VKF-1.C test mechanism, the model had an effective sting length of 3.5 model diameters and an effective sting-to-model-diameter ratio of 0.22. This sting configuration was used for the present test and also for the Ref. 1 tests. For the present

interference study, the effective sting length was shortened by positioning a conical flare (Fig. 14) at 3.3, 2.5, 2.0, and 1.0 model diameters from the rear of the model base. The flare was mounted to the motor housing in such a manner that it did not touch the sting forward of the motor housing. This eliminated the chance that the flare would change the sting frequency characteristics or model tare damping. The splitter plates were attached to the flare (Figs. 14c, d, and e) and did not touch the sting. Plate details are shown in Fig. 15.

3.4 PITCH/YAW DAMPING TEST MECHANISM

The pitch/yaw damping test mechanism (VKF-1.C) (Figs. 16 and 17) utilizes a cross-flexure pivot, an electric shaker motor, and a one-component moment beam that is instrumented with strain gages to measure the forcing moment of the shaker motor. The motor is coupled to the moment beam by means of a connecting rod and flexural linkage which converts the translational force to a moment to oscillate the model at amplitudes of up to ±3 deg (depending on flexure balance) and at frequencies from 2 to 20 Hz. The cross flexures, which are instrumented to measure the pitch/yaw displacement, support the model loads and provide the restoring moment to cancel the inertia moment when the system is operating at its natural frequency. At present, there are five cross-flexure balances, each of which is composed of three beams. The beam thicknesses of the five balances are 0.08, 0.10, 0.15, 0.17, and 0.20 in. and the restoring moments produced are 16.2, 29.9, 97.6, 138.0, and 224.6 in.-lb/deg, respectively.

Since the moment beam used to measure the forcing moment is not subject to the static loads, it can be made as sensitive as necessary for the dynamic measurements. Moment beams are available in AEDC-VKF to measure forcing moments up to ±4, ±8, ±12, and ±20 in.-lb.

A pneumatic and spring-operated locking device is provided to hold the model during injection into or retraction from the tunnel or during tunnel startup. The cross-flexure balance is supported by a 1.76-in.-diam, water-cooled sting. The 29.9- and 97.6-in.-lb/deg cross-flexure balances and the ±4- and ±8-in.-lb moment beams were used in the present tests.

3.5 INSTRUMENTATION

3.5.1 Test Conditions

Stilling chamber pressure is measured with a 15-, 60-, 150-, or 300-psid transducer in Tunnel A and with either a 200- or 1,000-psid transducer in Tunnel B. Both transducers are referenced to a near vacuum. Stilling chamber temperature is measured with copper-constantan thermocouples in Tunnel A and with Chromel®-Alumel® thermocouples in Tunnel B.

3.5.2 Model Pressures

The Tunnel A pressure system uses 15-psid transducers referenced either to a vacuum or to a variable reference pressure, with full-scale calibrated ranges of 1, 5, and 15 psia. The Tunnel B pressure system is equipped with 1- and 15-psid transducers referenced to a near vacuum. The system automatically selects the transducers and the calibrated ranges for best precision for each pressure measurement.

3.5.3 Thermopile Gardon Gages

Steady-state heat-transfer-rate measurements were made with the nine thermopile Gardon gages (Refs. 42 and 43) shown in Fig. 18. These gages were designed, fabricated, and calibrated at AEDC-VKF. The Gardon gages are 0.125 in. in diameter. They have a constantan sensing foil nominally 2 mils thick mounted on a cylindrical copper heat sink. The thermopile rosette on the sensing foil was formed with use of a vacuum-depositing technique. The rosette consisted of alternating legs of antimony and bismuth. In this study, the output of the thermopile Gardon gage was nominally 1.0 mv/(Btu/ft^2-sec) with a nominal operating temperature range from 60 to 300°F. (At higher temperatures the gage elements begin to separate or fail.) The thermocouple rosette is used to sense the temperature difference across the gage sensing foil; this temperature difference is essentially proportional to the heat flux imposed on the constantan foil. Gardon gage wall temperature measurements were made with iron-constantan thermocouples.

3.5.4 Pitch-Damping

The forced-oscillation instrumentation (Ref. 44) utilizes an electronic analog system with precision electronics. The instrumentation to control, monitor, and acquire data is contained in a portable console that interfaces easily with the instrumentation of the various tunnels.

The control instrumentation provides a system to vary the oscillation amplitude of the model within the flexure limits. The amplitude is controlled by an electronic feedback loop that permits testing of both dynamically stable and unstable configurations.

Data are normally obtained at or near the natural frequency of the model flexure system; however, the electronic resolvers permit data to be obtained off resonance. All gages are excited by d-c voltages, and outputs are increased to optimum values by d-c amplifiers. Typical balance outputs from an oscillating model are composed of oscillatory components (OC) superimposed on static components (SC). These components are separated in the data system by bandpass and low-pass filters. The SC outputs are sent

directly to the tunnel scanner and computer, which calculate the static moment coefficients and sting deflections. The OC outputs are input to the resolver instrumentation and precise frequency-measuring instrumentation. The resolvers use very accurate analog electronic devices to process the OC signals and then to output the d-c voltages. The output d-c voltages are proportional to the amplitude squared and to the in-phase and quadrature sting components. The resolver and frequency outputs are read by the tunnel scanner and sent to the computer. The frequency instrument controls the length of the data interval in increments of from approximately 2 to 60 sec, during which time the scanner reads each input approximately 10 times per second. The average values of the reading are calculated by the computer, which then uses these average values to calculate the dynamic derivatives. The method used to reduce the data is described in Refs. 44 and 45.

4.0 TEST DESCRIPTION

4.1 TEST CONDITIONS

Nominal tunnel conditions at which the tests were conducted are shown in Tables 1 and 2. The test summaries are presented in Tables 3 through 8.

4.2 TEST PROCEDURES

4.2.1 General

In Tunnels A and B, the model is mounted on a sting support mechanism in an installation tank directly underneath the tunnel test section. The tank is separated from the tunnel by a pair of fairing doors and a safety door. When closed, the fairing doors, except for a slot for the pitch sector, cover the opening to the tank, and the safety door seals the tunnel from the tank area. After the model is prepared for a data run, the personnel access door to the installation tank is closed, the tank is vented to the tunnel flow, the safety and fairing doors are opened, and the model is injected into the airstream. After data acquisition is completed, the model is retracted into the tank and the sequence is reversed; the tank is vented to atmosphere to allow access to the model in preparation for the next run.

4.2.2 Steady-State, Heat-Transfer Data

The steady-state, heat-transfer data were recorded only at $\alpha = 0$. Once the tunnel conditions were established, the model was injected into the airstream, the fairing doors were closed, and the data were recorded about every 2 sec for a period of generally 20 to 30 sec.

4.2.3 Pressure Data

Model attitude positioning was accomplished using the AEDC-VKF Model Attitude Control System (MACS). Model pitch requirements were entered into the controlling computer before the test. Once the tunnel conditions were established, the model was injected into the airstream and the fairing doors were closed. The pressures were allowed to stabilize; then the data acquisition switch was energized. After the pressures were read once, the MACS moved the model to the next condition in the α-matrix. When the next condition was reached, the pressures were again allowed to stabilize, and the data-taking sequence was repeated. This procedure was repeated until the α-matrix was completed. In Tunnel B, the 26 pressure gages were read in groups of 13 using a Scanivalve®. Pressure stabilization was required before each group was read. Stabilization times in Tunnel A lasted from 3 to 5 min, depending on the test conditions. In Tunnel B, the initial stabilization time was about 8 min. A delay of 70 sec between the two groups was built into the MACS. After the α-matrix was completed, the model was returned to $\alpha = 0$ by the MACS and retracted for a model change.

4.2.4 Pitch-Damping Data

Once the tunnel conditions were established, the model was injected into the airstream and the fairing doors were closed. Model attitude positioning was accomplished with the MACS. The forced-oscillation control system was used to oscillate the model at a constant amplitude of ±1 deg. With model conditions set, the data acquisition switch was activated and data were recorded for 10 to 30 sec. This sequence was repeated for each desired attitude; then the model was retracted into the tank. Oscillation frequency was varied by changing either balance stiffness or model inertia. The reduced frequency parameter ranged from 0.0019 to 0.0068 radians.

4.3 DATA REDUCTION

4.3.1 Steady-State, Heat-Transfer Data

Conventional methods (Ref. 43) were used to calculate heat flux rates from the data. This information was normalized in the form of Stanton numbers (referenced to the difference between tunnel stilling chamber temperature and model surface temperature).

4.3.2 Pitch-Damping Data

The resulting time-oriented displacement, moment beam, and sting-gage signals were recorded on magnetic tape by a high-speed digital converter and relayed to the computer for data reduction. The sting-gage signals were used to correct the data for sting bending effects. More detailed explanation of the data reduction is given in Ref. 46.

4.4 UNCERTAINTY OF MEASUREMENTS

4.4.1 General

This section presents an evaluation of the influence of random measurement errors to provide a partial measure of the uncertainty of the final test results given. Although evaluation of the systematic measurement error (bias) is not included, it should be noted that the instrumentation uncertainty values used in this evaluation represent a total uncertainty combination of both systematic and two-sigma random error contributions.

4.4.2 Test Conditions

Tunnel A stilling chamber pressure is measured with a 15-, 60-, 150-, or 300-psid transducer referenced to a near vacuum. Based on periodic comparisons with secondary standards, the uncertainty (a bandwidth including 95 percent of the residuals) of these transducers is estimated to be within ±0.2 percent of reading or ±0.015 psi, whichever is greater. Stilling chamber temperature is measured with a copper-constantan thermocouple with an uncertainty of ±3°F based on repeat calibrations.

Tunnel B stilling chamber pressure is measured with either a 200- or 1,000-psid transducer referenced to a near vacuum. Based on periodic comparisons with secondary standards, the uncertainty (a bandwidth including 95 percent of the residuals) of these transducers is estimated to be within ±0.25 percent of reading or ±0.3 psi, whichever is greater for the 200-psid range, and to be within ±0.1 percent of reading or ±0.5 psi, whichever is greater for the 1,000-psid range. Stilling chamber temperature measurements are made with Chromel-Alumel thermocouples that have an accuracy of ±(1.5°F + 0.375 percent of reading in °F).

The uncertainties in the tunnel stilling chamber pressure and temperature and a two-sigma deviation in Mach number determined from test section flow calibrations were used to estimate uncertainties in the other free-stream properties, using the Taylor series method of error propagation. These uncertainties are presented in Tables 9 and 10.

Measurement of tunnel model-support system attitude in pitch is precise to within ±0.05 deg, based on repeat calibrations. Model attitude corrections were made for balance and sting deflections under air load. The precision of the final model mean angle of attack was estimated to be ±0.1 deg.

4.4.3 Steady-State, Heat-Transfer Data

The sensing surface (constantan foil) of the Gardon gage was thinly coated with a black paint having a high thermal absorptivity so that the gages could be statically calibrated with a radiant heat source (in this case, a set of quartz-iodide lamps). The accuracy of the scale factors, based on repeated calibration against a secondary standard, was estimated to be ±5 percent (two-sigma deviation) (Ref. 43). A set of conventional or standard 0.25-in.-diam Gardon gages acts as a facility secondary standard by which all other thermopile Gardon gages are statically calibrated. The calculated Stanton numbers were used only to indicate the type of boundary layer present on the model. The Gardon gage uncertainty was combined with the uncertainties in the free-stream conditions using the Taylor series method of error propagation. The uncertainty of the Stanton numbers was estimated at ±6 percent.

4.4.4 Pressure Data

Based on periodic comparisons with secondary standards, the uncertainty of the Tunnel A pressure system is estimated to be ±0.15 percent of the reading or ±0.003 psia, whichever is greater. The uncertainty of the Tunnel B pressure system is ±0.2 percent of reading or ±0.01 psia, whichever is greater, for the 15-psid transducers, and ±0.2 percent of reading or ±0.0003 psia, whichever is greater, for the 1-psid transducers. After the pressure system uncertainties were combined with the uncertainties in the tunnel parameters, the Taylor series method of error propagation was used to estimate the uncertainty of the pressure parameters. These uncertainties are presented in Table 11.

4.4.5 Pitch-Damping Data

The balances were calibrated before and after the tests, and check calibrations were made during the test. The sting bending effects were included in the data reduction using the technique illustrated in Ref. 46. Uncertainties in the measurements of sting effects were included in the error analysis. Structural damping values were obtained at vacuum conditions before the test to evaluate the still-air damping contribution. The uncertainties in the balance and data system were combined with uncertainties in the tunnel parameters, in a Taylor series method of error propagation to estimate the uncertainty of the aerodynamic damping coefficients. These estimated uncertainties are presented in Table 12.

5.0 RESULTS AND DISCUSSION

5.1 STEADY-STATE, HEAT-TRANSFER DATA (SLICED-BASE, 6-DEG CONE MODEL)

Figure 19 presents typical results of the steady-state, heat-transfer tests which were used to evaluate the state of the boundary layer over the sliced region of the model at $\alpha = 0$. Figure 19a shows data for the sharp nose configuration and establishes the capability of the theory (Ref. 47) to predict the turbulent heat-transfer levels. Data typical of those used to determine trip effectiveness and the state of the model boundary layer are shown in Figs. 19b and c for the 10-percent nose bluntness model (the primary test configuration).

5.2 PRESSURE DATA (SLICED-BASE, 6-DEG CONE MODEL)

Typical pressure distributions at $\alpha = 0$ and 20 deg are presented in Fig. 20 for M = 2 to establish the axial pressure distribution of each ray. The data are for the minimum sting diameter ratio ($D_s/D = 0.19$) and for the effective sting length ratios (L_s/D) of 1.0, 2.0, and 3.9. The trends are as expected and are typical of the results at the other test Mach numbers. The fairings for Figs. 20 through 24 are straight-line, point-to-point computer fairings.

Figure 21 presents selected pressure measurements nondimensionalized by free-stream static pressure as a function of angle of attack at M = 3 for several effective sting lengths and the minimum sting diameter ($D_s/D = 0.19$). The model insert on each figure shows the location of the pressure measurement. The model boundary layer over the sliced-base region was turbulent. For $\alpha < 6$ deg, the data in Fig. 21 show that decreasing the effective sting length ratio from 2.0 to 1.0 increased the pressures in the corner region (P19, P20, P21, and P22), thus indicating support interference effects. Surface pressures on the model centerline (P11) or close to the model centerline (such as P17, which is not shown) were not affected by the decrease in sting length. The sting effects on the corner pressures were typical of the M = 2 results, but the M = 5 results showed no sting effects on any surface pressures. The base pressures for M = 3 (Figs. 21f and g) at $\alpha < 11$ deg showed sting effects for $L_s/D = 1$. The base pressures for M = 2 are presented in Fig. 22. Sting effects for $L_s/D = 1$ were present al all angles of attack. The M = 5 base pressure data were obtained only for $L_s/D = 1$ and 3.9. Sting effects were present for $L_s/D = 1$. At M = 2 and 5, the model boundary layer was turbulent. The flare used to change the effective sting length was nominally 6 in. in diameter. A 4-in.-diam flare was also tested at M = 3 with the results agreeing with the 6-in.-diam flare data.

Figure 23 shows the Mach 8 pressure data for a turbulent boundary layer over the sliced-base region. Data for effective sting length ratios (3.9, 2.0, and 1.0) and for a minimum sting diameter ratio (0.19) are presented. Decreasing the effective sting length to one model diameter produced no appreciable effect on the surface pressures. Base pressures P23 and P26 were affected, but P24 and P25 were not. The Mach 8 laminar pressure data are shown in Fig. 24 as a function of angle of attack. Both the centerline (P11) and corner (P19, P20, P21, and P22) pressure measurements were sensitive to sting length for $\alpha < 5$ deg. Sting length also affected the base pressures for angles of attack of less than 16 deg.

The data indicate that the maximum sting interference effects generally occurred at $\alpha = 0$. Pressure measurements are shown in Figs. 25 through 29 as a function of effective sting length for $\alpha = 0$. These data are for the minimum sting diameter ratio (D_s/D = 0.19) and Mach numbers 2, 3, 5, and 8. The boundary layer was turbulent for the supersonic Mach numbers. Both turbulent and laminar cases are presented for the M = 8 data. These data figures can be used for determining the critical sting length, defined as the shortest sting length that does not change the constant measurement level (base pressure, surface pressure, damping data, or static data) obtained by the longer stings.

A review of the data in Figs. 25 through 29 shows that the critical sting length was dependent on the location of the measurement, Mach number, and boundary layer. The pressure measurement locations can be divided into three categories: (1) base (P23 through P26), (2) corner (complex flow region—P18 through P22), and (3) centerline (P1 through P17). The locations of categories 2 and 3 can also be defined in terms of distance from the model base, upon which critical sting length was also dependent. Base pressures did not vary for effective sting lengths equal to or greater than two model diameters, except for the laminar boundary layer at Mach 8. For the Mach 8 laminar case, the critical sting length, based on base pressure measurements, is at least four model diameters. Corner effects on critical sting length for turbulent boundary layers were present for Mach numbers 2 and 3 but were nonexistent for Mach numbers 5 and 8. The corner effects as a function of sting length were also dependent on the distance between the pressure measurement location and the model base. This effect is evident in Figs. 25 through 28 (the turbulent boundary layers), since P18 is in the corner (complex flow) region but was unaffected by changing the effective sting length. For turbulent boundary layers and all Mach numbers, the centerline (Ray 1, Fig. 3a) and near-centerline pressure measurements (Ray 2, Fig. 3a) were not affected by decreasing the effective sting length to one model diameter. Figures 28 and 29 show a drastic difference between the pressure measurements as a function of effective sting length for the turbulent and laminar boundary layers at Mach 8. The critical sting length was much larger for the laminar boundary layer, and even four model diameters may not be free of sting length effects (Fig. 29).

Centerline pressures for the laminar boundary layer were also affected by reduced effective sting lengths. The sting effects on the pressures were propagated further forward for the laminar boundary layer, in comparison to those for the turbulent boundary layer. The dependency of critical sting length on the boundary-layer state was also substantiated in the pitch-damping tests discussed in Section 5.3.

Figure 30 summarizes Figs. 25 through 29 in the form of nondimensionalized critical sting length as a function of Mach number. For turbulent boundary layers the critical sting length as determined by the base- and centerline-pressure measurements is invariant with Mach number.

A limited investigation of sting diameter effects was conducted at Mach numbers 3, 5, and 8. Sting diameter ratios of 0.19, 0.35, and 0.50 were tested at Mach numbers 3 and 5, but $D_s/D = 0.5$ was not tested at Mach number 8. Typical data for maximum length sting ($L_s/D \approx 4$) are presented in Figs. 31, 32, and 33. In general, for a turbulent boundary layer, there was no large variation of surface or base pressure for the range of sting diameters investigated. These results were also typical of the Mach 5 data. The laminar data for Mach 8 showed more sensitivity to sting diameter (Fig. 33).

5.3 PITCH-DAMPING DATA (7-DEG CONE MODEL)

The main purpose of the pitch-damping tests was to investigate sting length effects on damping derivatives for different model boundary-layer conditions and for two frequencies of oscillation. The boundary-layer state requirement dictated an investigation to determine the proper trip size. Derivatives for pitch-damping and static stability for conical models at $\alpha = 0$ generally exhibit well-known trends (Ref. 22) with Reynolds number when the Reynolds number range covers laminar, transitional, and turbulent boundary-layer conditions over the model. The derivatives are generally independent of Reynolds number if the boundary-layer flow over the model base is either fully laminar or fully turbulent. The damping derivatives ($C_{m_q} + C_{m_{\dot{\alpha}}}$) generally increase above the laminar or turbulent level when transition is near the model base. The opposite is true for the static stability derivative (C_{m_α}). Figures 34 and 35 show typical results at $\alpha = 0$ for the various trips tested at M = 5 and 8. For both these Mach numbers, the Reynolds number range was not sufficient to produce a turbulent boundary layer near the model base. At Mach 5, number 36 grit was used to trip the boundary layer. The tripped dynamic and static stability derivative levels agreed well with the laminar data (Fig. 34), thus showing the effectiveness of the trip. At M = 8 (Fig. 35) different sphere diameters and number 36 grit trips were tested. The data in Fig. 35b show that the trips had essentially no adverse effect on the dynamic and static stability derivatives. Also, the grit produced essentially the same data as the trip spheres.

Figures 36 through 41 show the damping derivatives, static derivatives, static pitching moment, and base pressure (shown only in Figs. 36 through 39) as a function of angle of attack for the clean sting (L_s/D = 3.3) and for the interference sting (L_s/D = 1.0). Data are presented for different boundary-layer conditions, reduced frequency parameters, and Mach numbers. A detailed discussion of the α = 0 data will be presented later in the report. The sting interference effects at angles of attack are a function of model-base boundary-layer conditions, Mach number, and reduced frequency parameter. In general, the interference sting configuration produced significant effects on the damping derivatives, static stability derivatives, and base pressure. Static pitching moment was essentially affected only at M = 2 for the laminar boundary-layer condition.

The dynamic and static stability derivatives as a function of effective sting length are presented in Figs. 42 through 47 for zero angle of attack. The variables for these data were Mach number, reduced frequency parameter, and boundary-layer state. The dynamic stability derivatives ($C_{m_q} + C_{m_{\dot{\alpha}}}$) exhibited trends that depended on all the variables. At the lower Mach numbers, 2 and 3 (Figs. 42a and 43), decreasing the effective sting length did not affect the results until the value of L_s/D was less than 2. At Mach number 5 (Fig. 44) no significant effect is observed for L_s/D in the range from 3.3 to 1.0. At M = 8 (Fig. 46), the effect of sting length was observed at values of L_s/D under 2.5 for all cases tested, except for the RFP = 0.0032 laminar-flow case (Fig. 46a), for which sting effects were observed at L_s/D values under 3.3. The static stability derivative (C_{m_α}) was not generally affected by sting length except at the lowest Mach number (Figs. 42b, 45, and 47). At M = 2 (Fig. 42b) the level of C_{m_α} was reduced as the L_s/D was decreased from 2.0 to 1.0.

The behavior of the base pressure with effective sting length is shown in Figs. 48 through 50 for Mach numbers 2, 3, and 5. These results indicate significant effects for L_s/D values of less than 2.0 for Mach numbers 2, 3, and 5 with a turbulent boundary layer. At Mach number 5, effective sting lengths greater than 3.3 are required for noninterference support on a model with a laminar boundary layer.

Figure 51 summarizes the critical sting lengths determined from measurements of dynamic and static stability derivatives, base pressures, and static pitching moment for the 7-deg cone. The summary in Ref. 1 shows that different interference indicators can produce different critical sting lengths. For dynamic stability testing at supersonic speeds, the effective sting length generally should be two model diameters and is independent of the state of the boundary layer and the frequency of oscillation. At hypersonic speeds, the critical sting length for measurement of damping-in-pitch derivatives is dependent on boundary-layer state and oscillation frequency, whereas the critical sting length for the measurement of the static stability derivatives is not. The base-pressure critical sting length was a function of the boundary-layer state (which is well-documented in Ref. 2),

whereas the critical sting length that was determined from static pitching moment was insensitive to all variables, except where previously noted at M = 2 for the laminar boundary-layer condition.

The effects of the splitter plates on the damping derivatives and base pressure for the clean (L_s/D = 3.3) and interference (L_s/D = 1.0) stings are presented in Figs. 52 through 56. Because of the trend of the M = 8 damping data with L_s/D (see Fig. 46, in which the damping level at L_s/D = 1.0 is about the same as that at L_s/D = 3.3), the effectiveness of the splitter plates in reducing sting interference could not be determined. The addition of the plates to the clean sting configuration usually produced only small changes in the damping data, mainly at the higher oscillation frequencies. This encourages the incorporation of thin-rib stiffeners in the design of long slender stings. The M = 3 splitter-plate investigations are reported in Ref. 1.

6.0 CONCLUDING REMARKS

Sting interference effects as determined from measurements of surface pressures, base pressures, static pitching moment, damping-in-pitch derivatives, and static stability derivatives were investigated for Mach numbers 2 through 8. Additional variables included angle of attack, frequency of oscillation, and the state of the model boundary layer. Data were obtained for a blunt, sliced-base, 6-deg cone and for a blunt 7-deg cone. Reynolds number, based on model diameter, ranged from 0.3 x 10^6 to 4.5 x 10^6. Based on the results of this investigation the following conclusions were drawn:

General

1. Critical sting length is dependent on the parameter selected as the interference indicator.
2. Sting length effects are more likely to occur for laminar model boundary layers than for turbulent boundary layers.
3. For pressure and static force tests at supersonic and hypersonic speeds with turbulent model boundary layers, the critical sting length is generally two model diameters.
4. Critical sting length determined by the measurement of base pressures is dependent on the model boundary layer.

6-Deg Sliced-Base Cone Model

1. Sting length effects on surface pressure measurements generally disappeared for $\alpha > 6$ deg. Sting length effects on base pressure measurements generally occurred for $\alpha \leq 24$ deg.

2. Critical sting length determined by surface pressure measurements is a function of the location of the measurement (whether the measurement is in a complex flow region, such as the corner of a sliced base, or on the model centerline, located some distance from the corner).

3. In general for Mach numbers 3 and 5 for a turbulent boundary layer, there was no large variation of surface or base pressure for the range of sting diameters investigated.

7-Deg Cone Model

1. For dynamic stability testing at supersonic speeds (M = 2 to 5), the critical sting length as determined by the measurement of pitch-damping derivatives is independent of the boundary-layer state and oscillation frequency. The critical sting length is two model diameters.

2. For hypersonic Mach numbers, the critical sting length as determined by the measurement of pitch-damping derivatives is dependent on model boundary-layer state and oscillation frequency. For turbulent boundary layers at the model base, the critical sting length is 2.5 model diameters.

3. As determined by the measurement of the static stability derivative, C_{m_α}, critical sting length was dependent on Mach number but independent of the boundary-layer state and oscillation frequency. The critical sting length for C_{m_α} was generally equal to or less than that for the pitch-damping derivatives.

REFERENCES

1. Uselton, Bob L. and Cyran, Fred B. "Critical Sting Length as Determined by the Measurement of Pitch-Damping Derivatives for Laminar, Transitional, and Turbulent Boundary Layers at Mach Number 3 for Reduced Frequencies of 0.0033 and 0.0056." AEDC-TR-77-66 (AD-A042747), July 1977.

2. Whitfield, Jack D. "Critical Discussion of Experiments on Support Interference at Supersonic Speeds." AEDC-TN-58-30 (AD201108), August 1958.

3. Pick, George S. "Sting Effects in Hypersonic Base Pressure Measurements" Naval Ship Research and Development Center, Bethesda, Maryland, Report AL-85, December 1971.

4. Crocco, Luigi and Lees, Lester. "A Mixing Theory for the Interaction Between Dissipative Flows and Nearly Isentropic Streams." *Journal of the Aeronautical Sciences*, Vol. 19, No. 10, October 1952, pp. 649-676.

5. Kavanau, L. L. "Fluid Flow and Heat Transfer at Low Pressures and Temperatures, Results of Some Base Pressure Experiments at Intermediate Reynolds Numbers with M_∞ = 2.84." Institute of Engineering Research, University of California, Berkeley, Report No. HE-150-117.

6. Perkins, Edward W. "Experimental Investigation of the Effects of Support Interference on the Drag of Bodies of Revolution at a Mach Number of 1.5." NACA TN 2292, February 1951.

7. Reller, John O., Jr. and Hamaker, Frank M. "An Experimental Investigation of the Base Pressure Characteristics of Nonlifting Bodies of Revolution at Mach Numbers from 2.73 to 4.98." NACA TN 3393, March 1955.

8. Sevier, K. R. and Bogdonoff, S. M. "The Effect of Support Interference on the Base Pressure of a Body of Revolution at High Reynolds Numbers." Report No. 332, AFOSR TN 55-301, October 1955.

9. Chapman, Dan R. "An Analysis of Base Pressure at Supersonic Velocities and Comparison with Experiment." NACA TN 2137, July 1950.

10. Reichenau, David E. A. "Sting and Strut Support Interference Effects on a Cylindrical Model with an Ogive Nose at Mach Numbers from 0.7 to 1.4." AEDC-TR-72-175 (AD905771L), November 1972.

11. Reese, David E., Jr. and Wehrend, William R., Jr. "Effects of Sting-Support Interference on the Base Pressures of a Model Having a Blunt-Nosed Cylinder Body and a Conical Flare at Mach Numbers of 0.65 to 2.20." NASA TM X-161, February 1960.

12. Lee, George and Summers, James L. "Effects of Sting-Support Interference on the Drag of an Ogive-Cylinder Body with and without a Boattail at 0.6 to 1.4 Mach Numbers." NACA RM A57I09, December 1957.

13. Cassanto, John M. "Base Pressure Results at M_∞ = 4 Using Free-Flight and Sting-Supported Models." *AIAA Journal*, Vol. 6, No. 7, July 1968, pp. 1411-1414.

14. Cassanto, John M. "Radial Base-Pressure Gradients in Laminar Flow." *AIAA Journal*, Vol. 5, No. 12, December 1967, pp. 2278-2279.

15. Jaffe, P. "A Free-Flight Investigation of Transonic Sting Interference." NASA TM 33-704, January 1975.

16. Vlajinac, M., Stephens, T., Gilliam, G., and Pertsas, N. "Subsonic and Supersonic Static Aerodynamic Characteristics of a Family of Bulbous Base Cones Measured with a Magnetic Suspension and Balance System." NASA CR-1932, January 1972.

17. Adcock, J. B. "Some Experimental Relations between the Static and Dynamic Stability Characteristics of Sting-Mounted Cones with Bulbous Bases." Presented at the Third Technical Workshop on Dynamic-Stability Problems, Moffett Field, California, November 1968.

18. Fuller, Dennis E. and Langhans, Victor E. "Effect of Afterbody Geometry and Sting Diameter on the Aerodynamic Characteristics of Slender Bodies at Mach Numbers from 1.57 to 2.86." NASA TN D-2042, November 1963.

19. Tunnell, P. J. "An Investigation of Sting Support Interference on Base Pressure and Forebody Chord Force at Mach Numbers from 0.60 to 1.30." NACA-RM-A54K16a, January 1955.

20. Ericsson, Lars E. and Reding, J. Peter, "Aerodynamic Effects of Bulbous Bases." NASA CR-1339, August 1969.

21. Wehrend, William R., Jr. "An Experimental Evaluation of Aerodynamic Damping Moments of Cones with Different Centers of Rotation." NASA TN D-1768, March 1963.

22. Uselton, Bob L. "Investigation of Sting Support Interference Effects on the Dynamic and Static Stability Characteristics of a 10-deg Cone at Mach Numbers 2.5, 3.0, and 4.0." AEDC-TDR-64-226 (AD450660), November 1964.

23. Uselton, James C., Uselton, Bob L., and Helmlinger, K. R. "An Examination of the Small-Amplitude Dynamic Stability Test Technique." AEDC-TR-74-131 (AD-A008477), April 1975.

24. Uselton, Bob L. and Wallace, Arthur R. "Damping-in-Pitch and Drag Characteristics of the Viking Configuration at Mach Numbers from 1.6 through 3." AEDC-TR-72-56 (AD741826), May 1972.

25. Steinberg, Sy, Uselton, Bob L., and Siemers, Paul M. "Viking Pitch Damping Derivatives as Influenced by Support Interference and Test Techniques." *Journal of Spacecraft and Rockets*, Vol. 10, No. 7, July 1973, pp. 443-449.

26. Sallet, Dirse W. "A Splitter Plate for the Prevention of Vortex Shedding behind Finite Circular Cylinders in Uniform Cross Flow." NOL TR 69-31, July 1967.

27. Roshko, Anatol. "On the Drag and Shedding Frequency of Two-Dimensional Bluff Bodies." NACA TN 3169, July 1954.

28. Roshko, Anatol. "On the Development of Turbulent Wakes from Vortex Streets." NACA R 1191, 1954.

29. Baughman, L. Eugene and Jack, John R. "Experimental Investigation of the Effects of Support Interference on the Pressure Distribution of a Body of Revolution at a Mach Number of 3.12 and Reynolds Numbers from 2 x 10^6 to 14 x 10^6." NACA RM E53E28, August 1953.

30. Clay, J. T. and Walchner, O. "Nose Bluntness Effects on the Stability Derivatives of Cones in Hypersonic Flow." In *Transactions of the Second Technical Workshop on Dynamic Stability Testing*, Arnold Engineering Development Center, Arnold Air Force Station, Tennessee, April 20–22, 1965, Vol. 1, Paper 8.

31. Love, Eugene S. "A Summary of Information on Support Interference at Transonic and Supersonic Speeds." NACA-RM-L53K12, January 1954.

32. Sieling, W. R. "The Effect of Sting Diameter and Length on Base Pressure at M = 3.88." *The Aeronautical Quarterly*, Vol. 19, November 1968, pp. 368-374.

33. Peckham, D. H. "Exploratory Tests on Sting Interference at a Mach Number of 6–8." RAE TN AERO 2721, October 1960.

34. Trescot, Charles D., Jr., Brown, Clarence A., Jr., and Howell, Dorothy T. "Effects of Reynolds Number and Model Support on the Supersonic Aerodynamic Characteristics of a 140°-Included-Angle Cone." NASA TM X-3019, July 1974.

35. Hart, Roger C. "Effects of Stabilizing Fins and a Rear-Support Sting on the Base Pressures of a Body of Revolution in Free Flight at Mach Numbers from 0.7 to 1.3." NACA-RM-L52E06, September 1952.

36. Ericsson, Lars E. and Reding, J. Peter. "Viscous Interactions or Support Interference–The Dynamicist's Dilemma." *AIAA Journal*, Vol. 16, No. 4, April 1978, pp. 363-368.

37. Reding, J. Peter and Ericsson, Lars E. "Dynamic Support Interference." *Journal of Spacecraft and Rockets*, Vol. 10, No. 7, July 1972.

38. Blaha, Bernard J. "Wind Tunnel Blockage and Support Interference Effects on Winged-Body Models at Mach Numbers from 0.6 to 1.0." NASA TM X-3011, March 1974.

39. Dix, R. E. "Influences of Sting Support on Aerodynamic Loads Acting on Captive Store Models." AEDC-TR-76-1 (AD-A022257), March 1976.

40. German, R. C. "Strut Support Interference on a Cylindrical Model with Boattail at Mach Numbers from 0.6 to 1.4." AEDC-TR-76-40 (AD-A024473), May 1976.

41. Nelson, R. C. and Mouch, T. N. "Cylinder/Splitter-Plate Data Illustrating High α Support Interference." *Journal of Spacecraft and Rockets*, Vol. 16, No. 2, March–April 1979.

42. *Test Facilities Handbook*. Eleventh Edition. "Von Kármán Gas Dynamics Facility, Vol. 3." Arnold Engineering Development Center, June 1979.

43. Trimmer, L. L., Matthews, R. K., and Buchanan, T. D. "Measurements of Aerodynamic Heating Rates at the AEDC von Kármán Facility." ICIASF, 1973. Institute of Electrical and Electronics Engineers, Inc., New York, 1973.

44. Burt, G. E. "A Description of a Pitch/Yaw Dynamic Stability, Forced-Oscillation Test Mechanism for Testing Lifting Configurations." AEDC-TR-73-60 (AD762286), June 1973.

45. Schueler, C. J., Ward, L. K., and Hodapp, A. E., Jr. "Techniques for Measurements of Dynamic-Stability Derivatives in Ground Test Facilities." AGARDograph 121 (AD669227), October 1967.

46. Burt, G. E. and Uselton, J. C. "Effect of Sting Oscillations on the Measurements of Dynamic Stability Derivatives." *Journal of Aircraft*, Vol. 13, No. 3, March 1976, pp. 210-216.

47. Mayne, Arloe W., Jr. and Dyer, D. F. "Comparisons of Theory and Experiment for Turbulent Boundary Layers on Simple Shapes at Hypersonic Conditions." In *Proceedings*, Heat Transfer and Fluid Mechanics Institute Meeting, 22nd, U.S. Naval Postgraduate School, Monterey, California, June 10–12, 1970. Stanford University Press, Stanford, California, 1970, pp. 168-188.

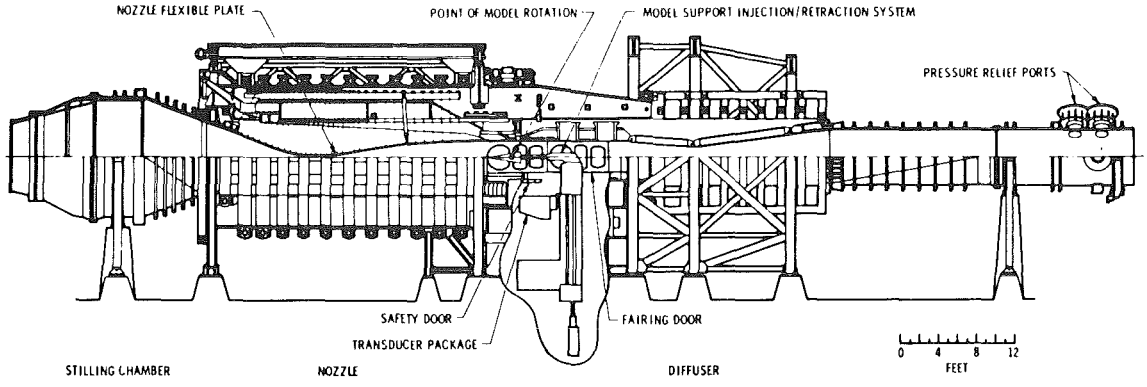

a. VKF Tunnel A

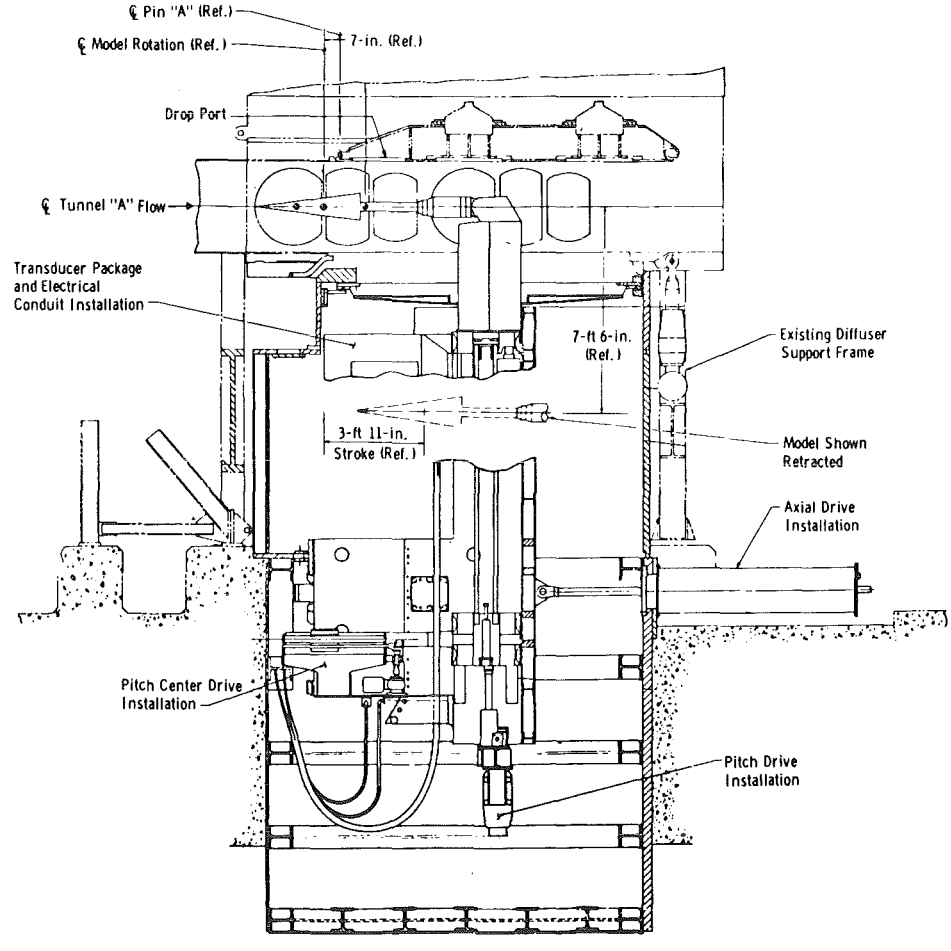

b. Tunnel A model injection system

Figure 1. Wind tunnels and model injection systems.

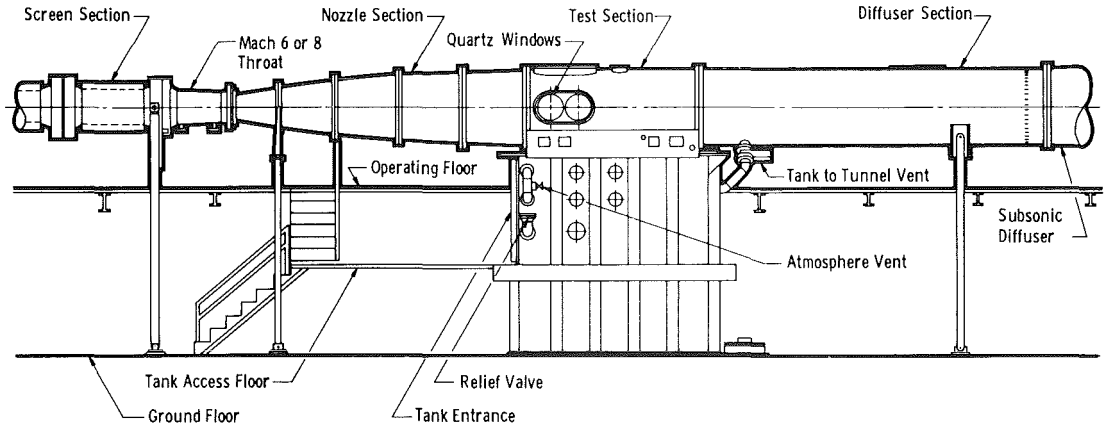

c. VKF Tunnel B

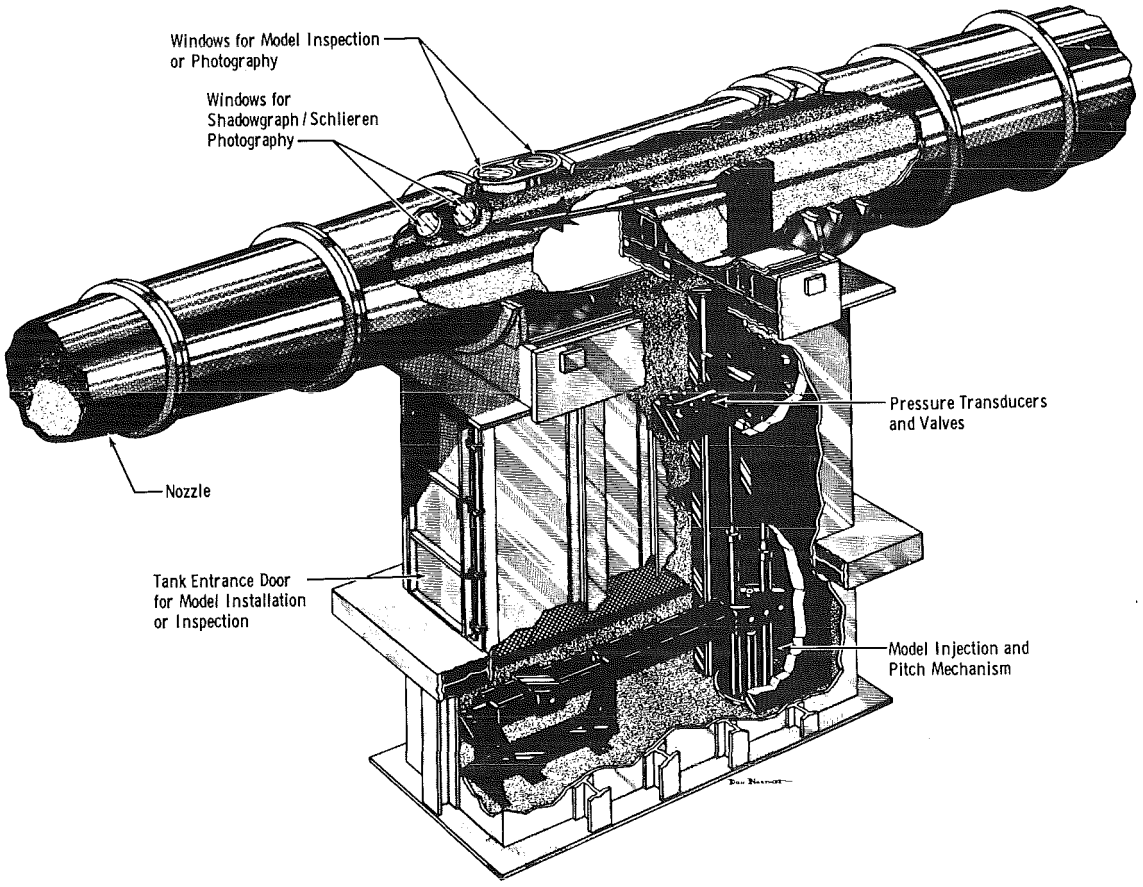

d. Tunnel B model injection system

Figure 1. Concluded.

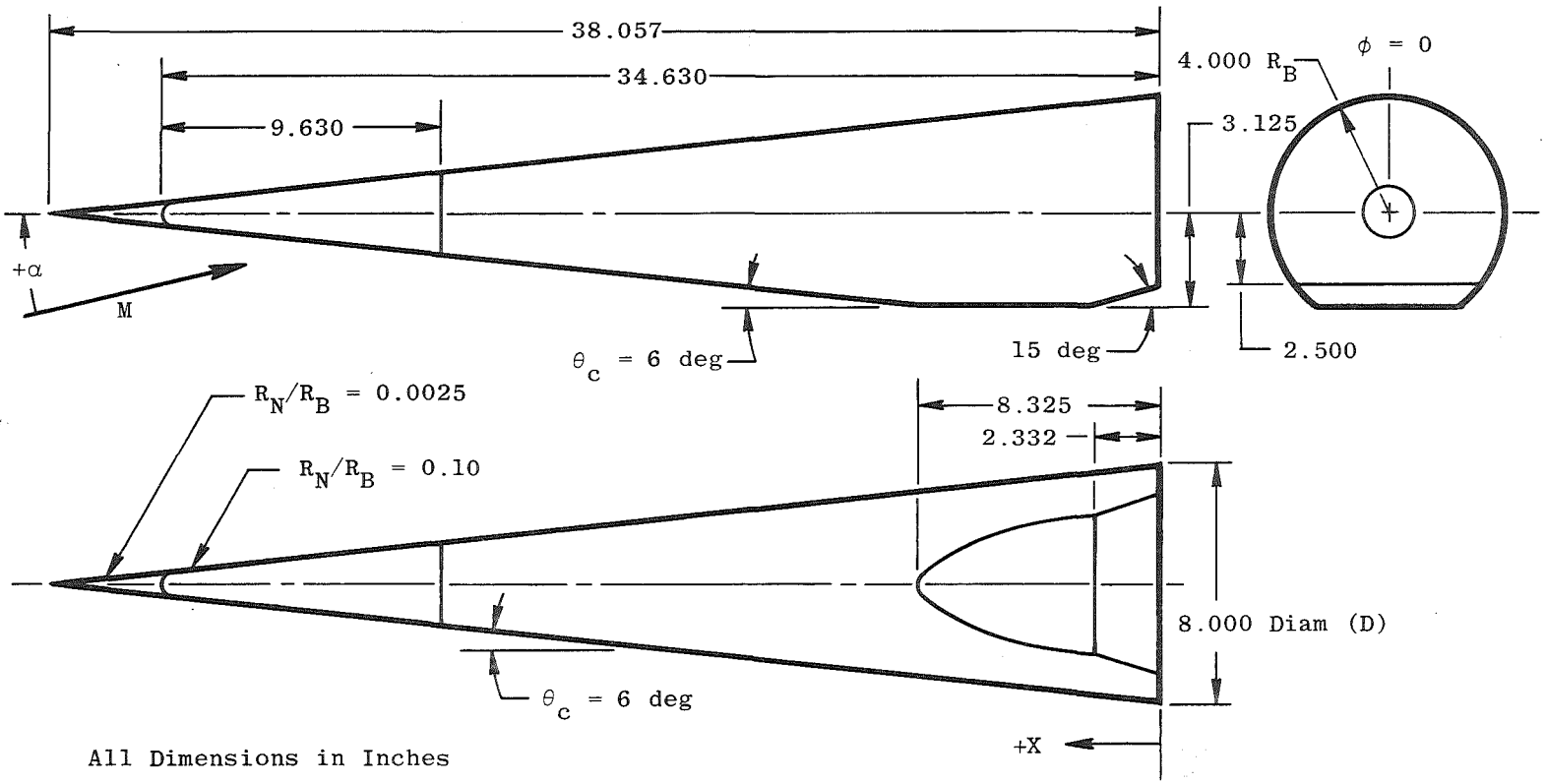

Figure 2. Details of pressure model.

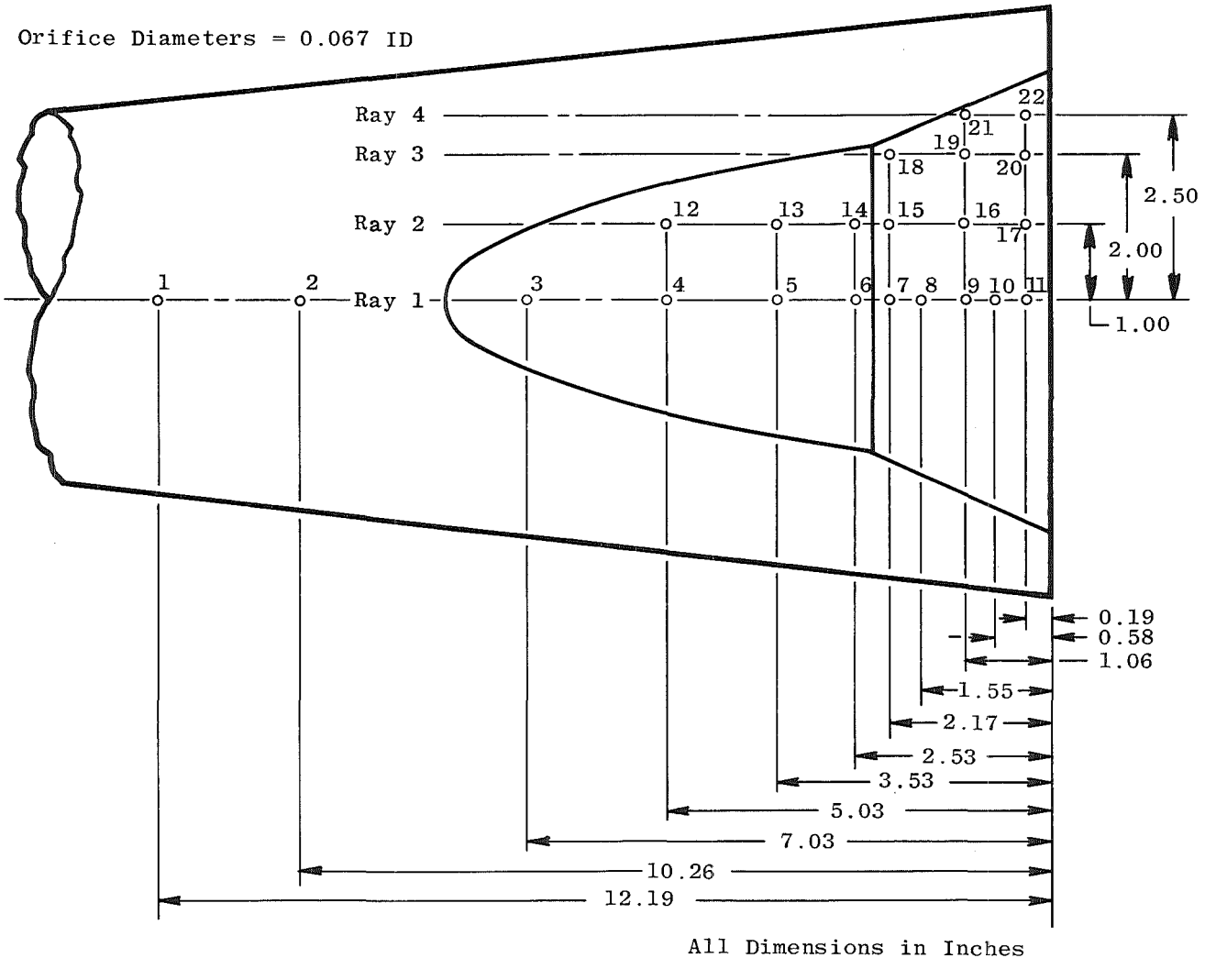

a. Surface pressure taps

Figure 3. Pressure model instrumentation locations.

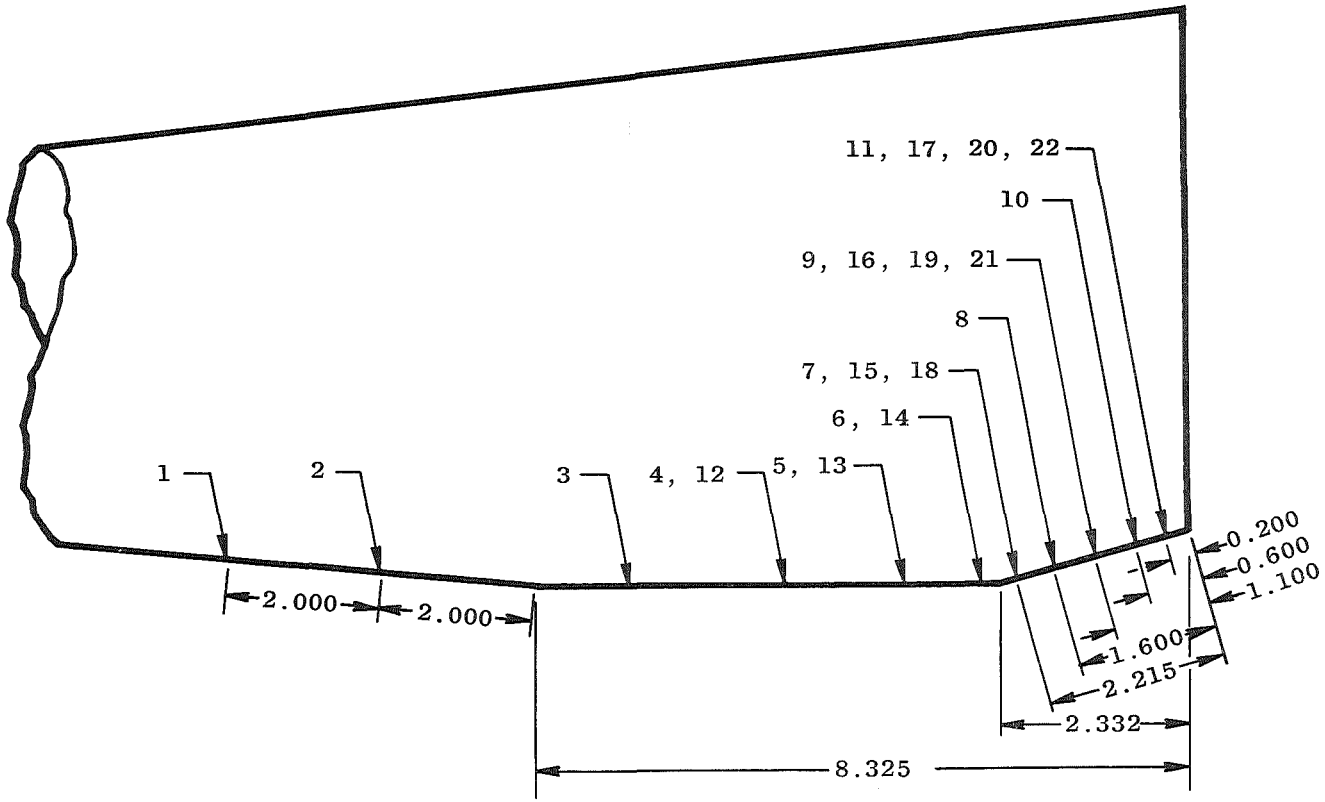

All Dimensions in Inches

a. Continued

Figure 3. Continued.

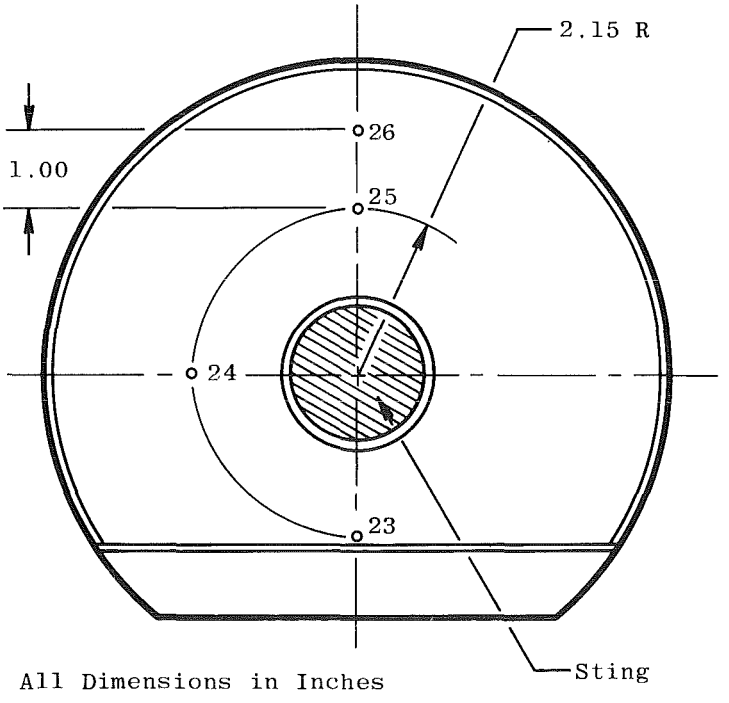

b. Base pressure taps
Figure 3. Continued.

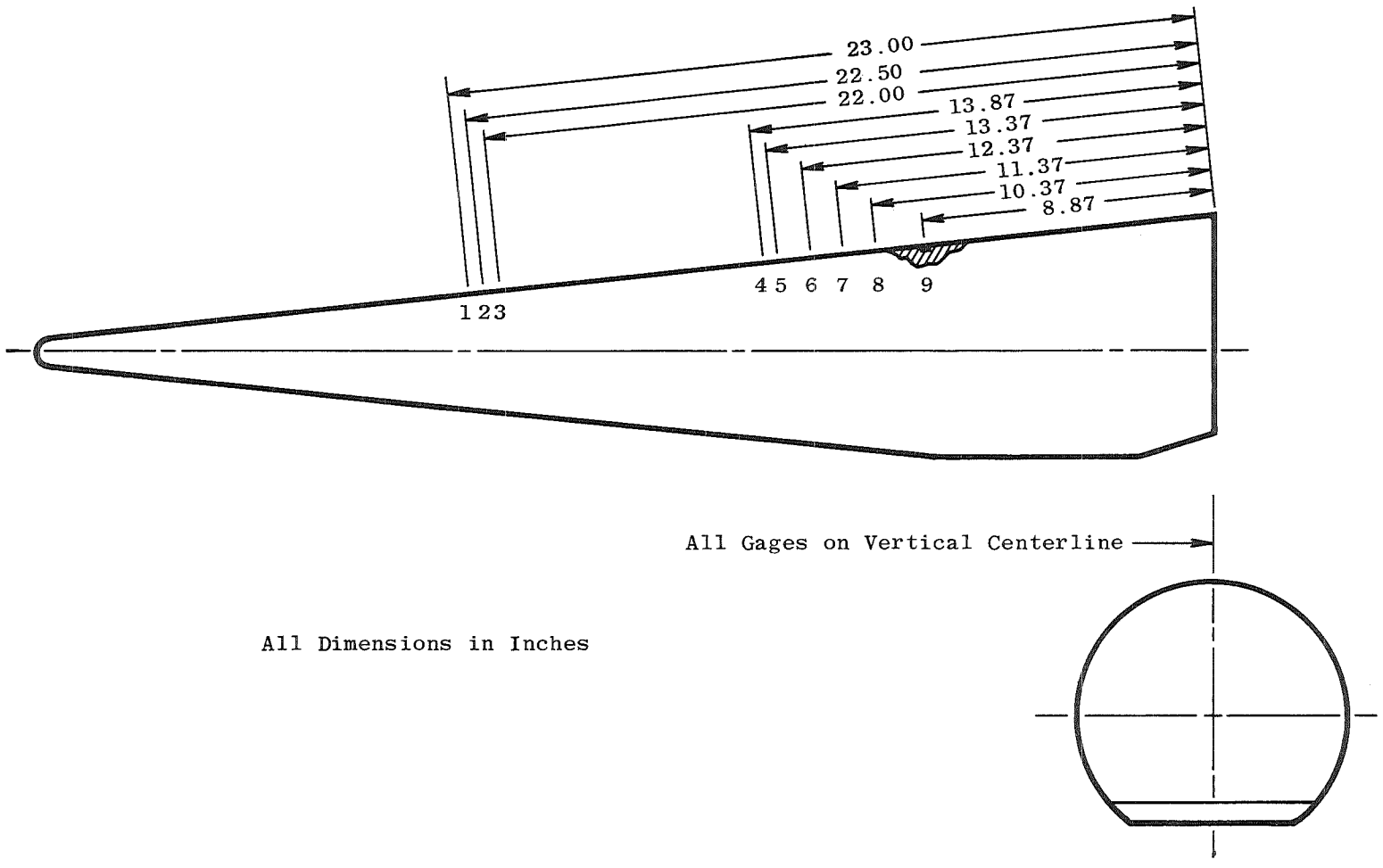

c. Gardon gage locations

Figure 3. Concluded.

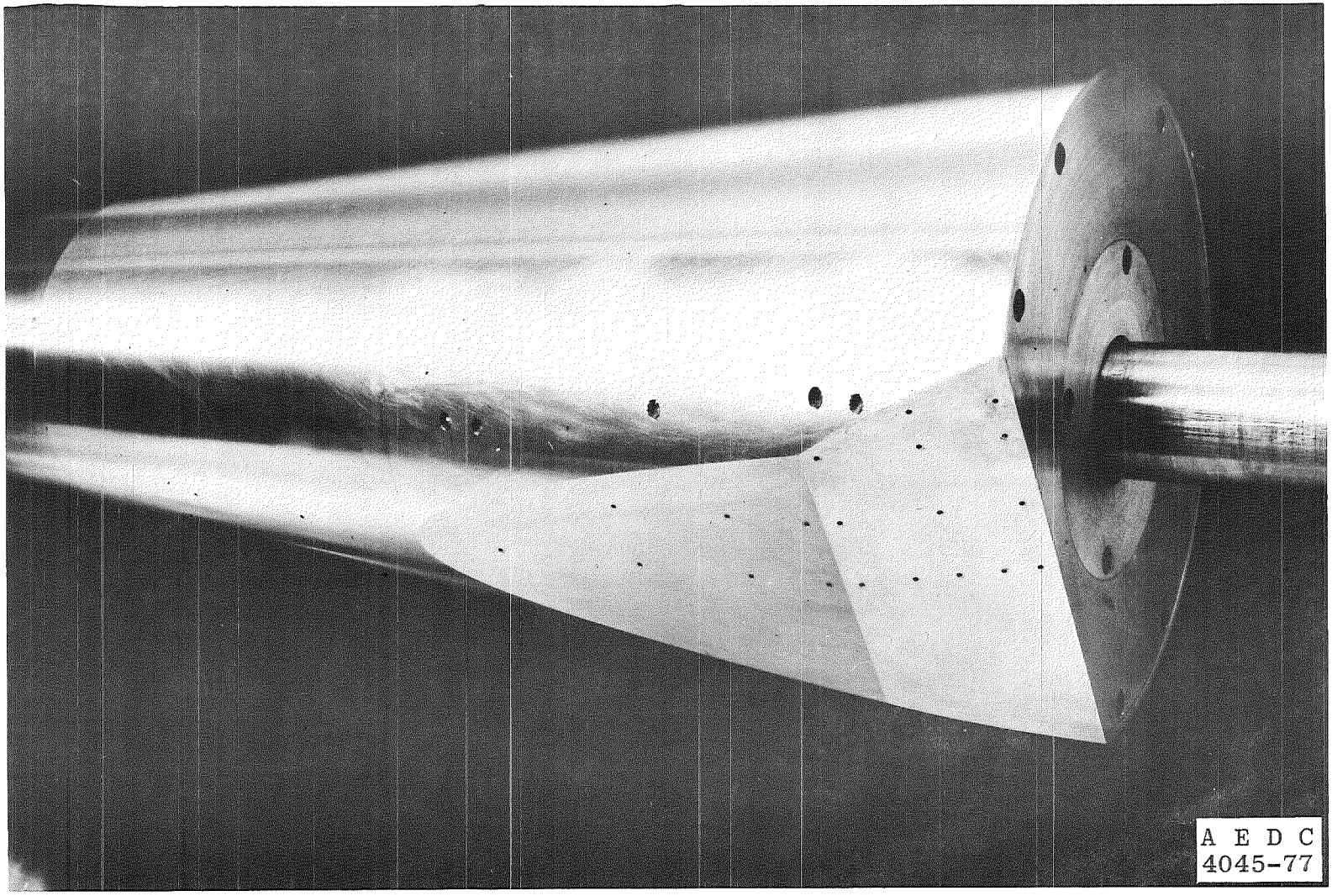

a. Surface pressure tap locations, P1 to P22

Figure 4. Pressure tap and Gardon gage locations.

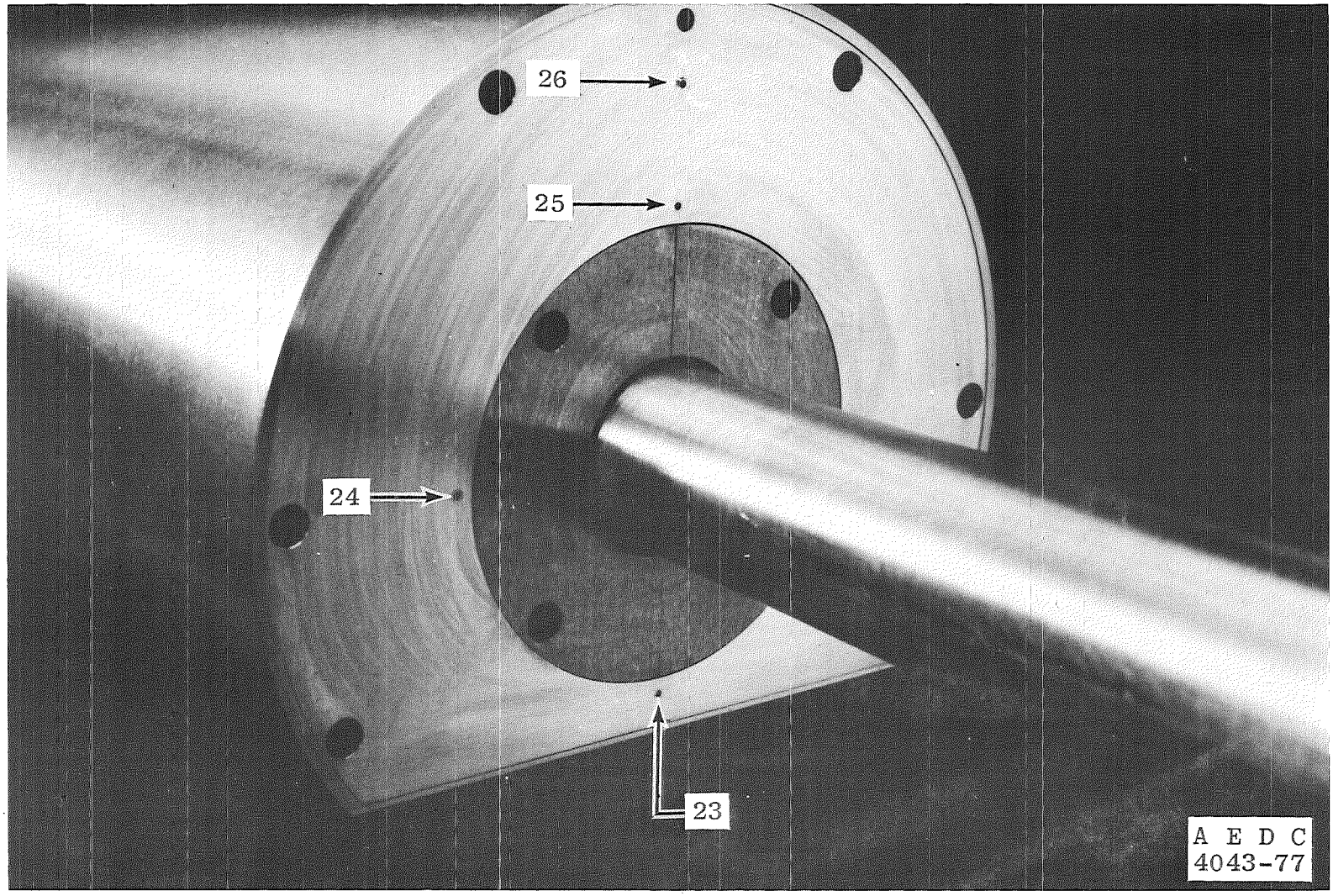

b. Base pressure tap locations, P23 to P26
Figure 4. Continued.

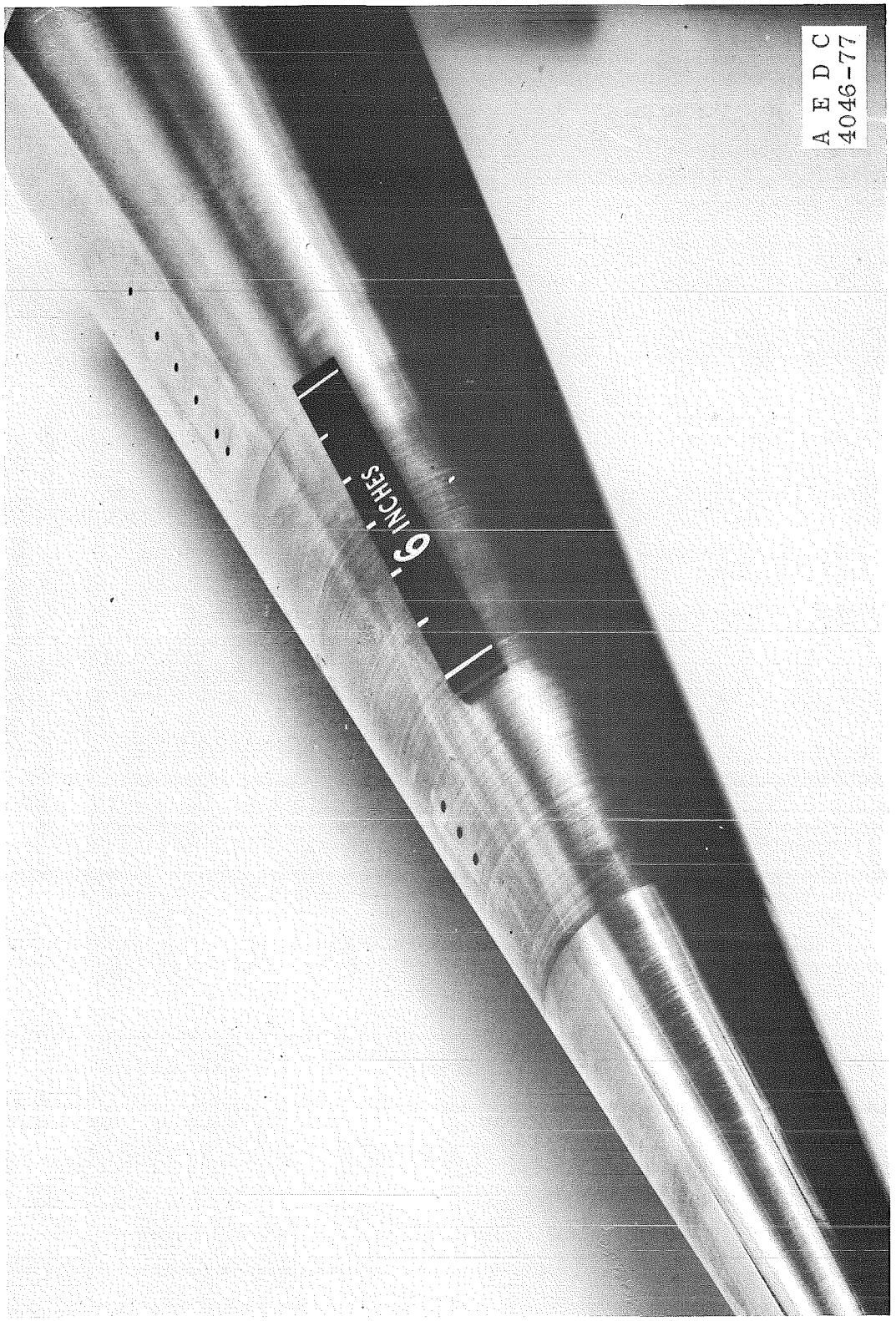

c. Gardon gage locations
Figure 4. Concluded.

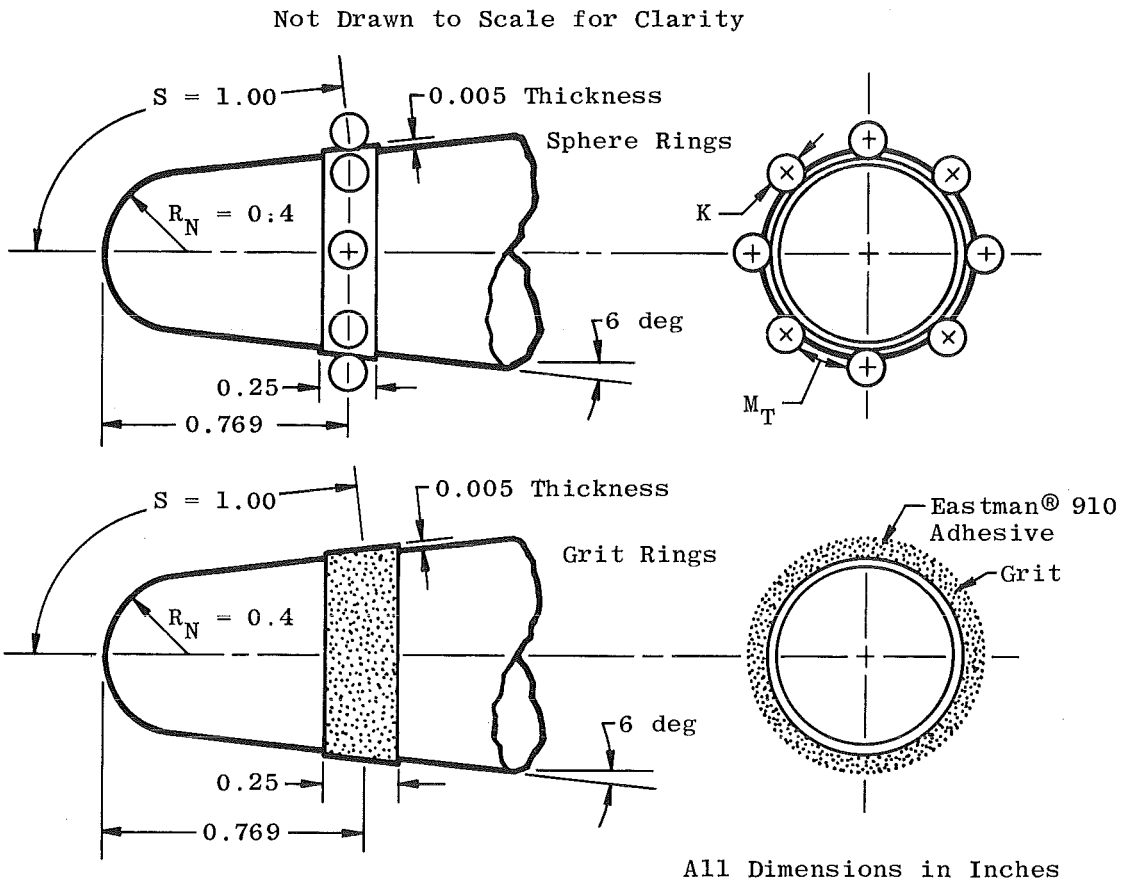

Trip Type		Number of Spheres	K*	M_T	S/R_N	Test	
						Pressure	H.T.**
Spheres		14	0.063	0.214	2.5	√	√
		11	0.078	0.277	2.5		√
		9	0.094	0.344	2.5		√
Grit	Number 60	--	0.012	--	2.5	√	√
	Number 36	--	0.020	--	2.5	√	√
	Number 20	--	0.038	--	2.5	√	√

Notes:

*K is the sphere diameter or the average height of Carborundum® grit.

**H.T. = Heat Transfer

Figure 5. Boundary-layer trip details for pressure-heat transfer tests.

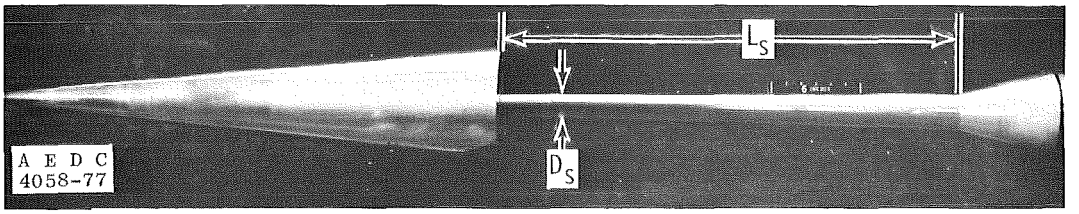

a. $L_s/D = 3.9$

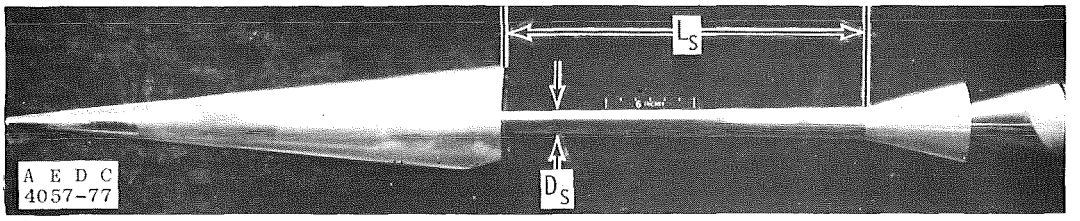

b. $L_s/D = 3.0$, 6-in. flare

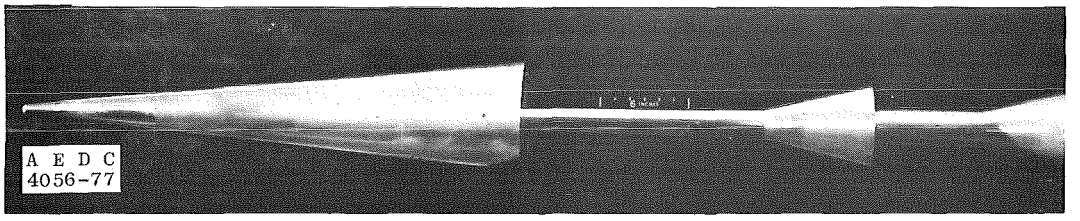

c. $L_s/D = 2.0$, 6-in. flare

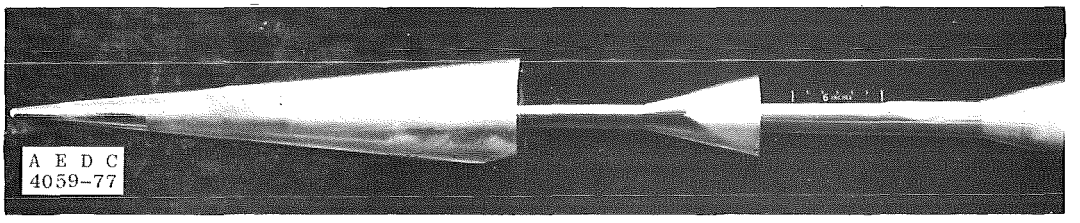

d. $L_s/D = 1.0$, 6-in. flare

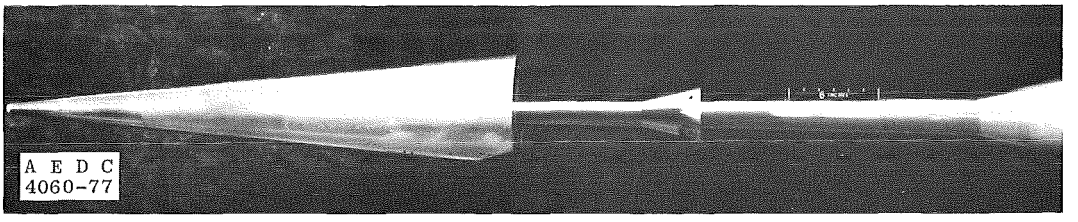

e. $L_s/D = 1.0$, 4-in. flare

Figure 6. Sting configurations for pressure model, $D_s = 0.19$.

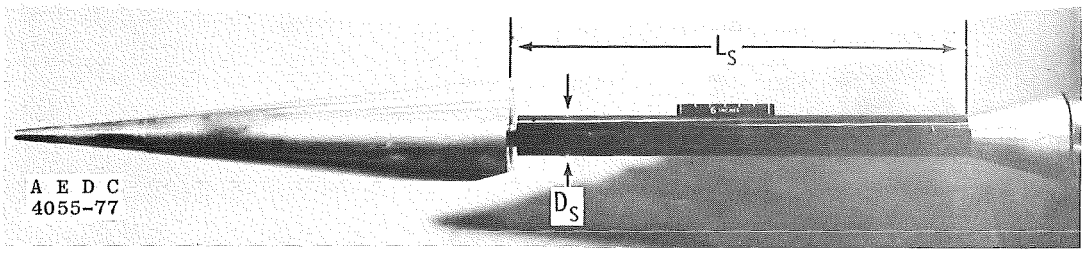

a. L_s/D = 3.9

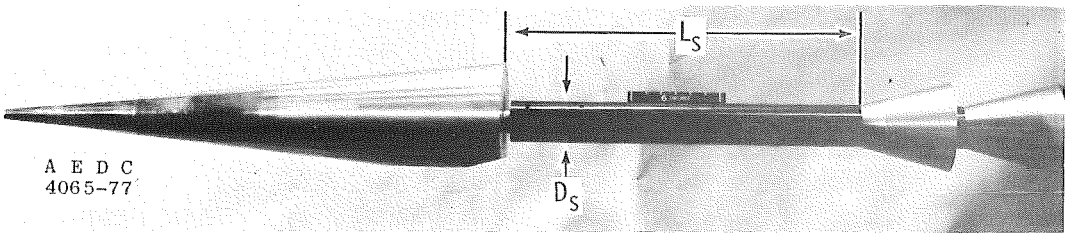

b. L_s/D = 3.0, 6-in. flare

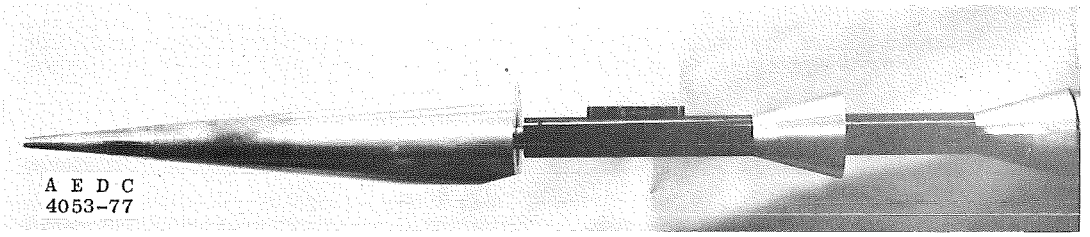

c. L_s/D = 2.0, 6-in. flare

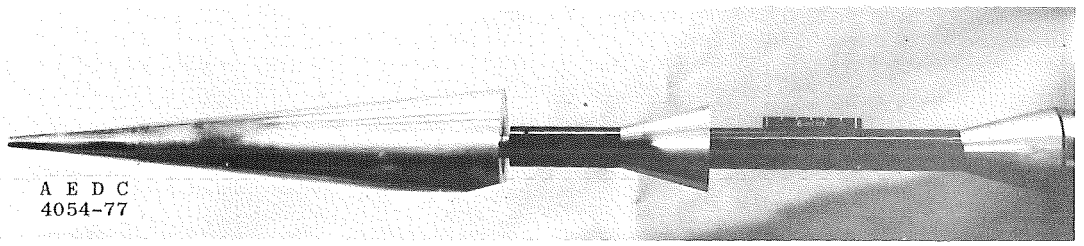

d. L_s/D = 1.0, 6-in. flare

Figure 7. Sting configurations for pressure model, D_s/D = 0.35.

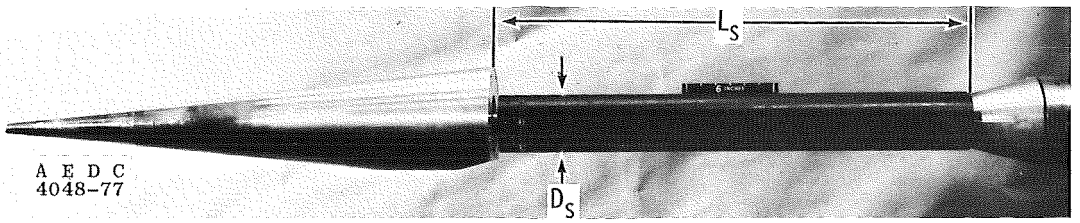

a. $L_s/D = 4.2$

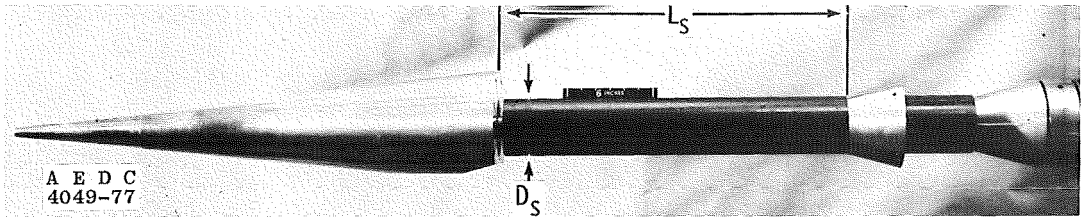

b. $L_s/D = 3.0$, 6-in. flare

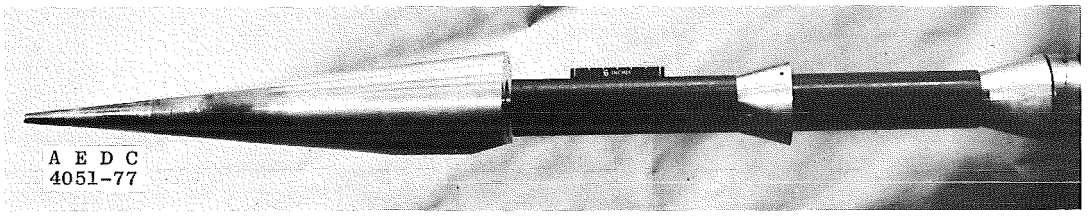

c. $L_s/D = 2.0$, 6-in. flare

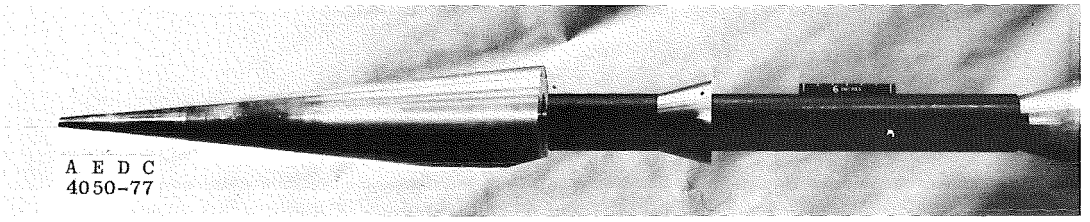

d. $L_s/D = 1.0$, 6-in. flare

Figure 8. Sting configurations for pressure model, $D_s/D = 0.50$.

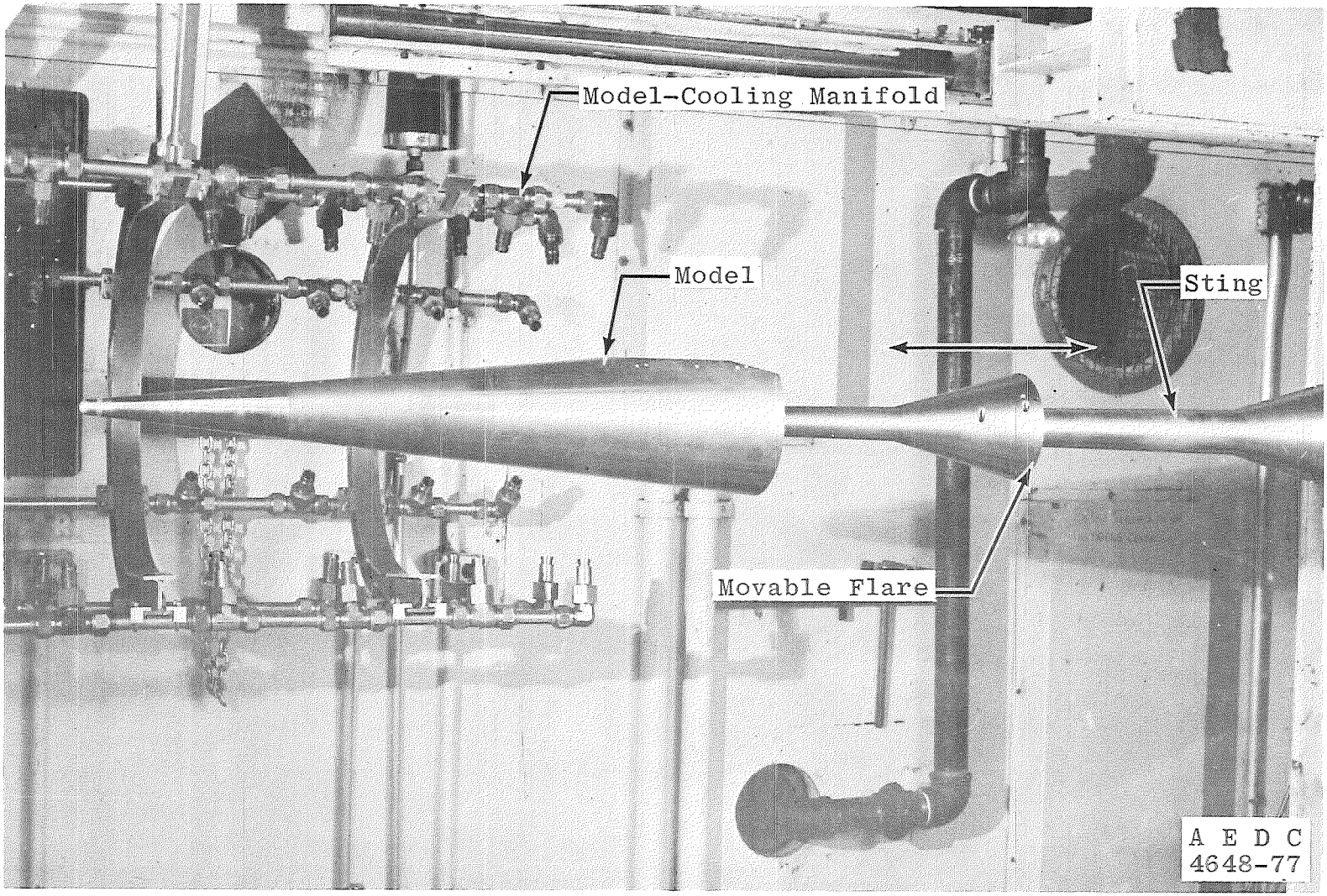

Figure 9. Pressure model installation in Tunnel A test section tank, L_s/D = 1.0, D_s/D = 0.19, 6-in. flare.

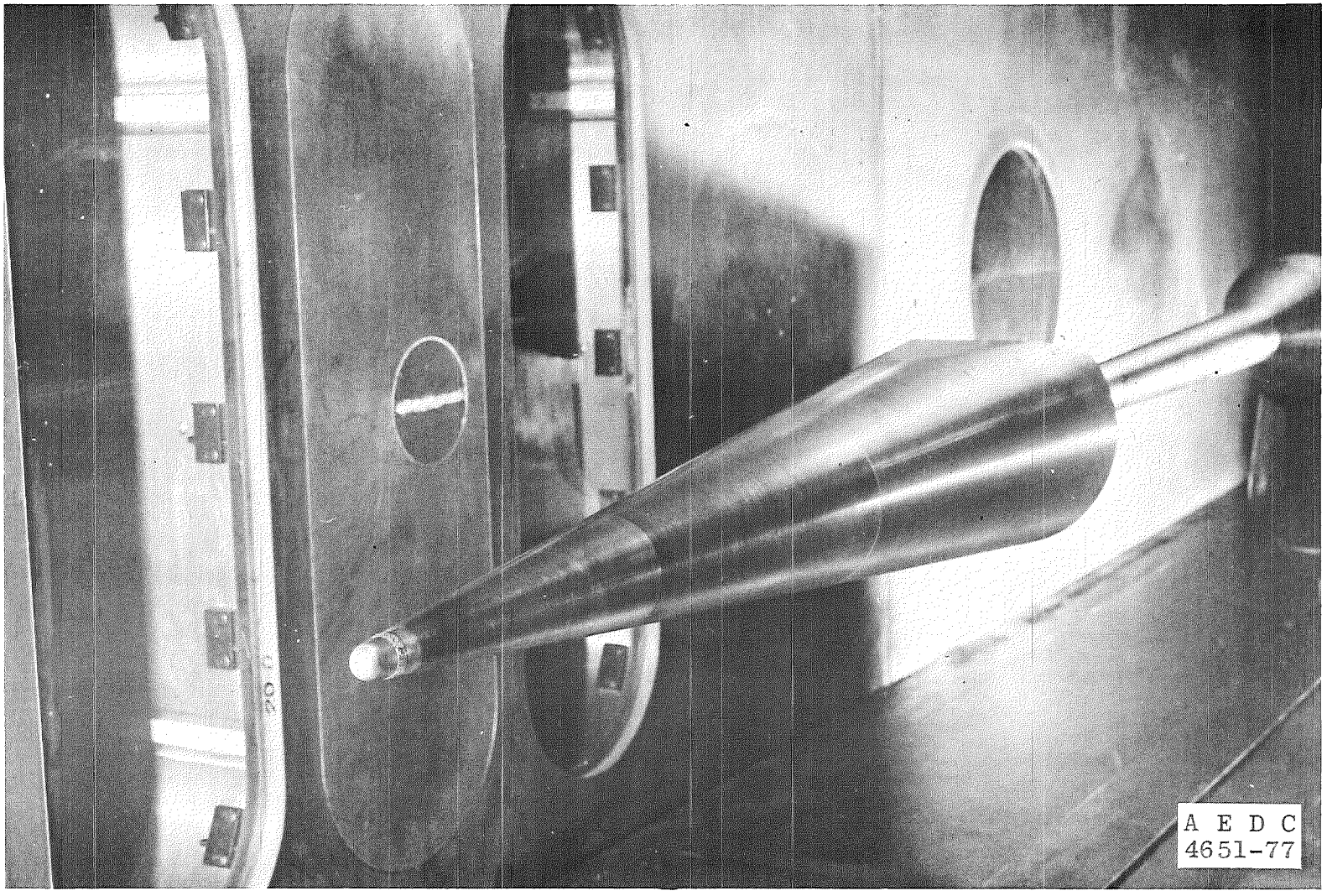

Figure 10. Pressure model installation in Tunnel A test section, $L_s/D = 3.9$, $D_s/D = 0.19$.

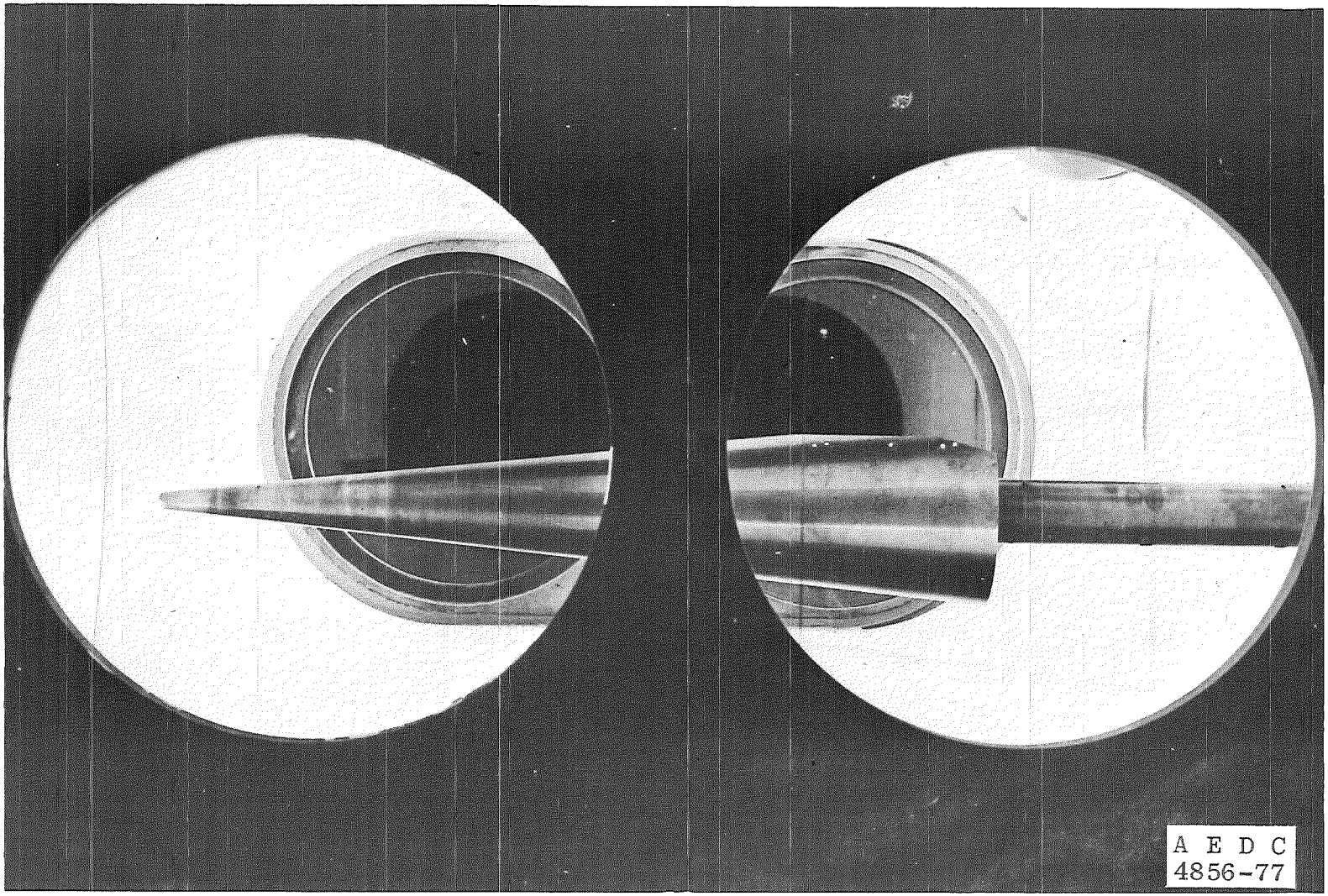

Figure 11. Pressure model installation in Tunnel B test section, $L_s/D = 3.9$, $D_s/D = 0.35$.

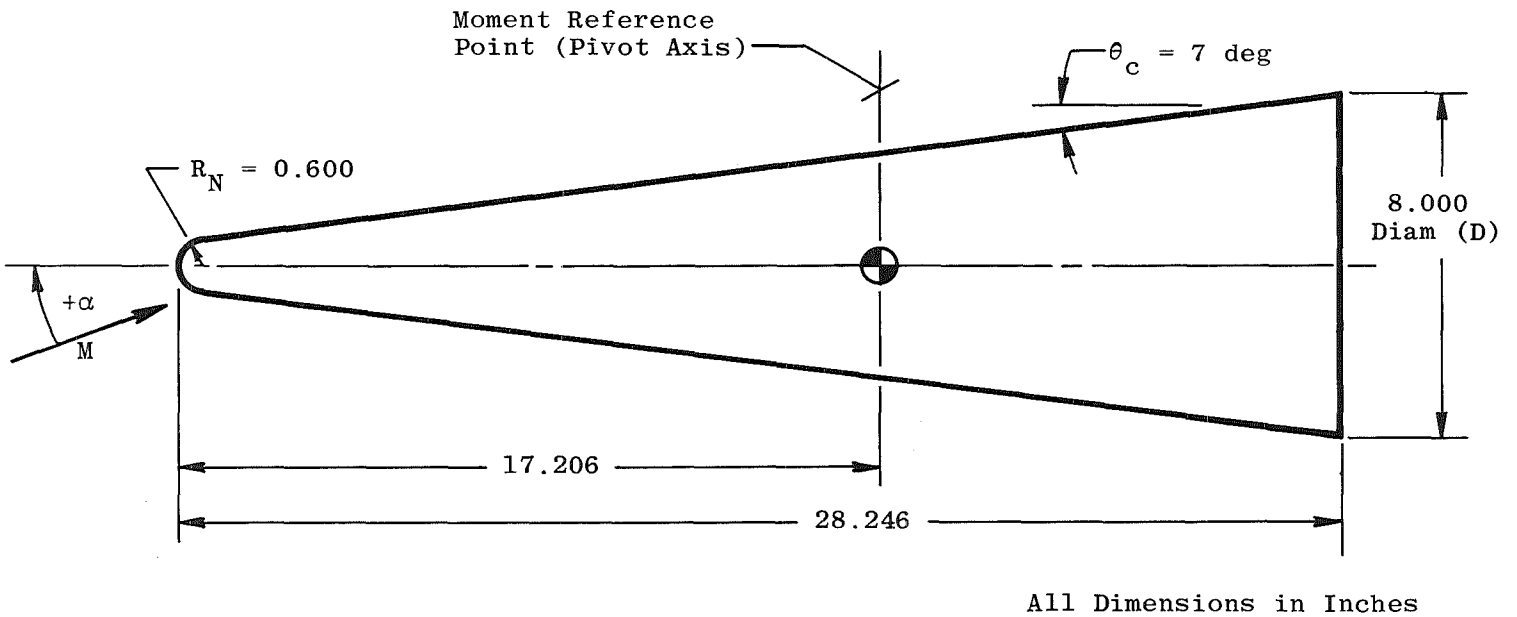

Figure 12. Details of pitch-damping model.

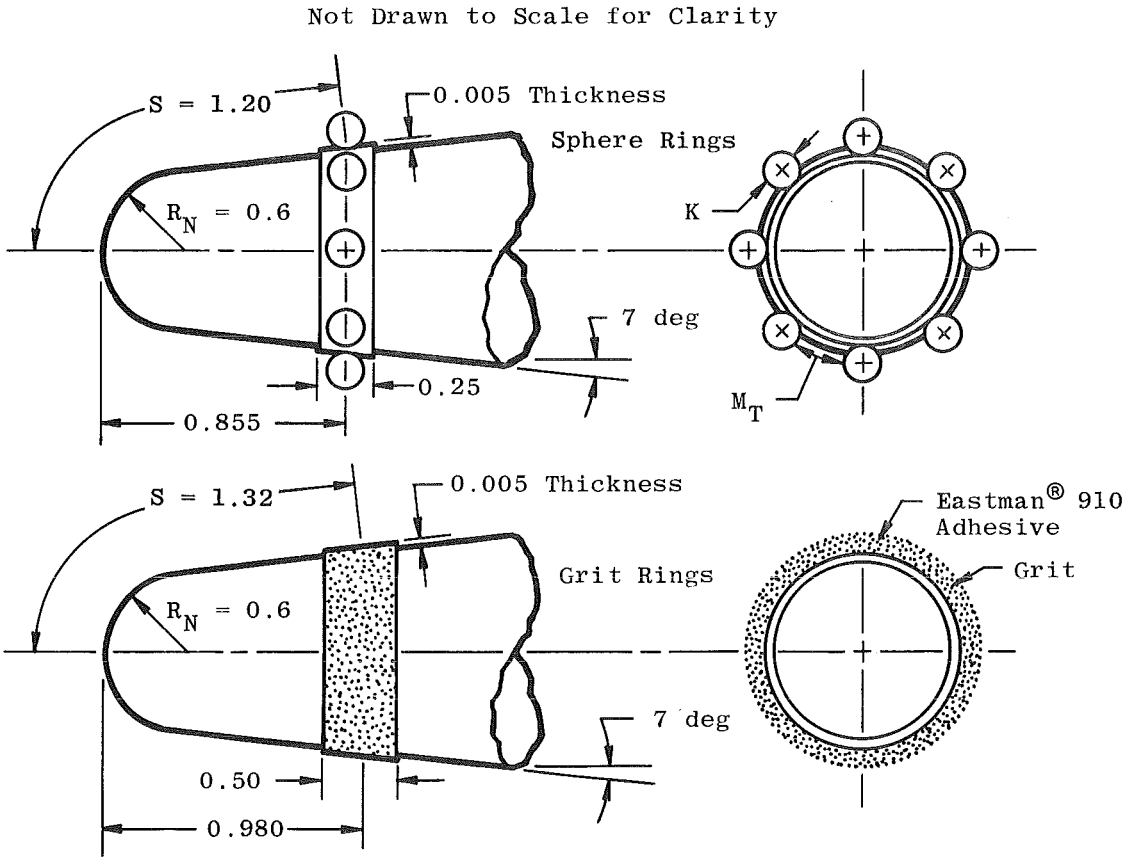

Trip Type		Number of Spheres	K*	M_T	S/R_N
Spheres		19	0.063	0.159	2.0
		25	0.047	0.120	2.0
		30	0.039	0.099	2.0
		38	0.031	0.077	2.0
Grit	Number 36	--	0.020	--	2.2
	Number 20	--	0.038	--	2.2

Note:

*K is the sphere diameter or the average height of Carborundum® grit.

Figure 13. Boundary-layer trip details for pitch-damping test.

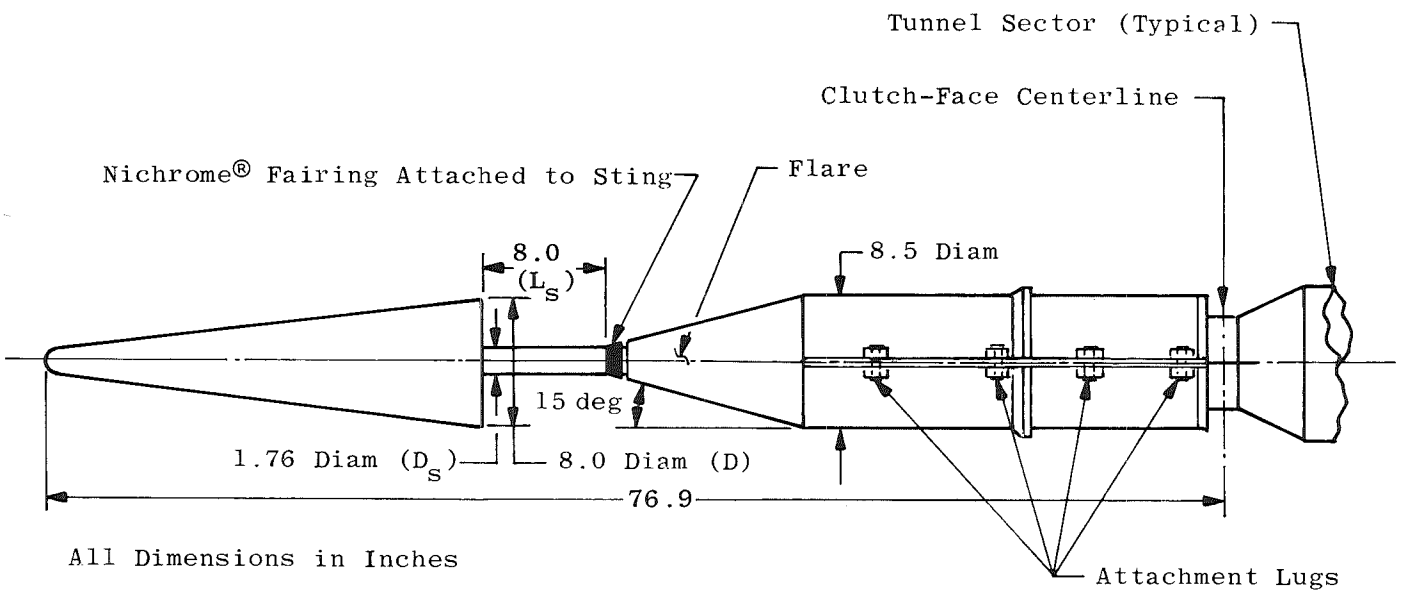

a. Interference sting, $L_s/D = 1.0$

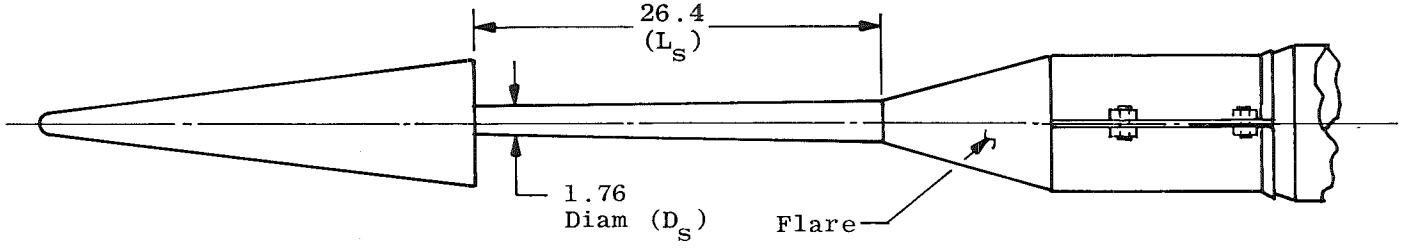

b. Clean sting, $L_s/D = 3.3$

Figure 14. Details of pitch-damping model support configurations.

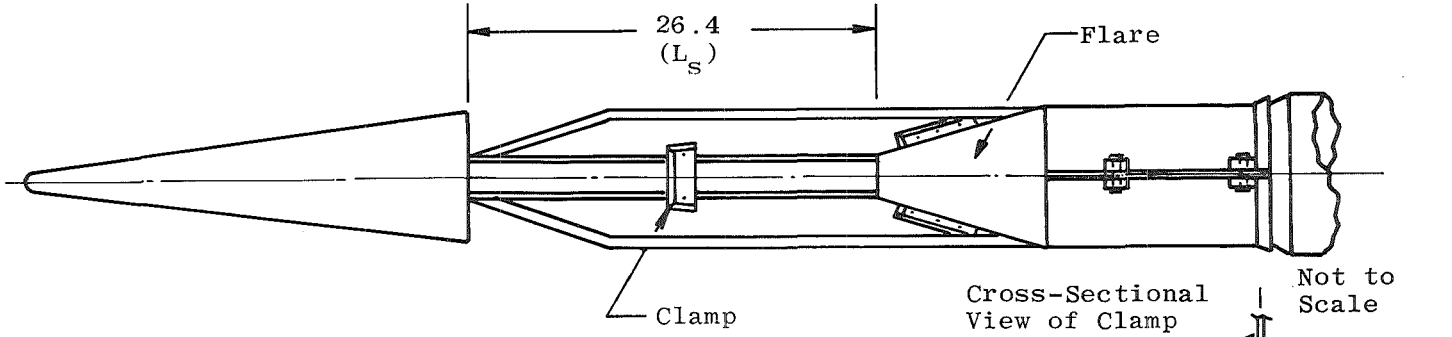

c. Plate 4 installed, $L_s/D = 3.3$

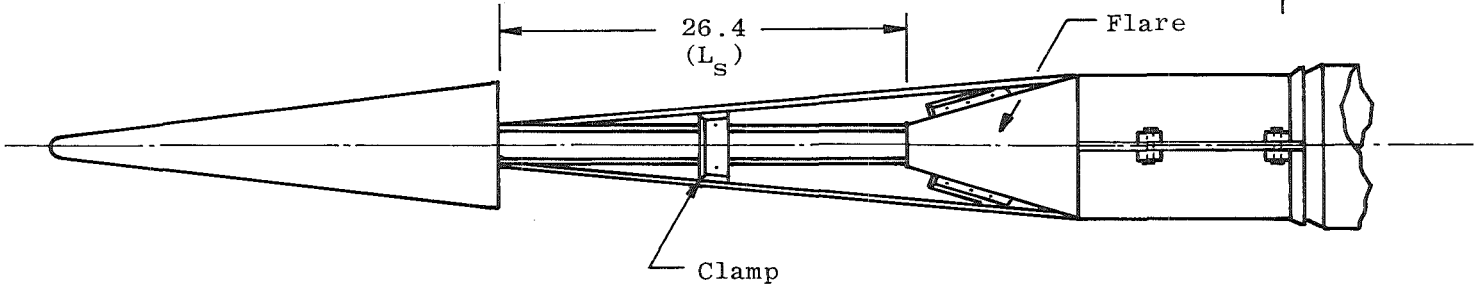

d. Plate 8 installed, $L_s/D = 3.3$

Figure 14. Continued.

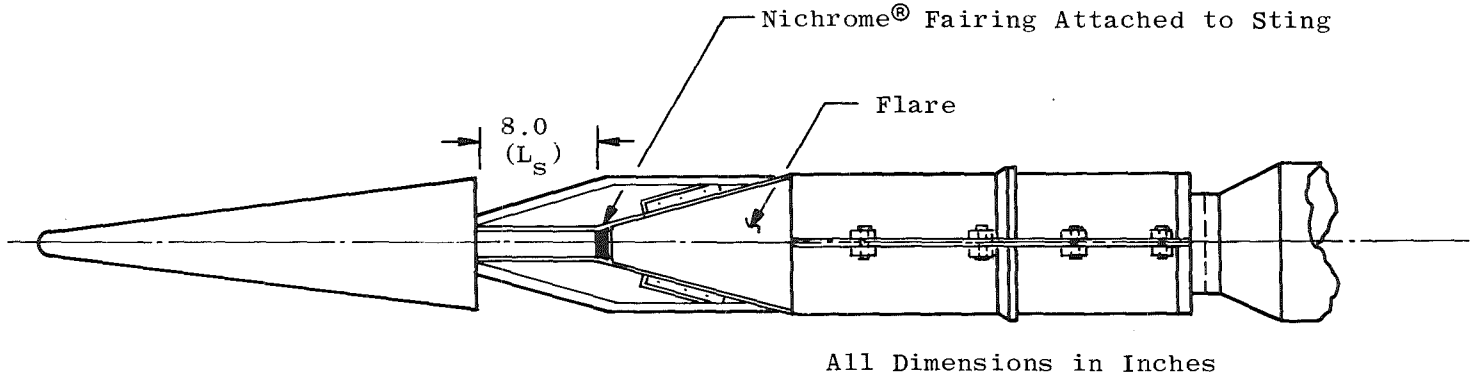

e. Plate 1 installed, L_s/D = 1.0

Figure 14. Concluded.

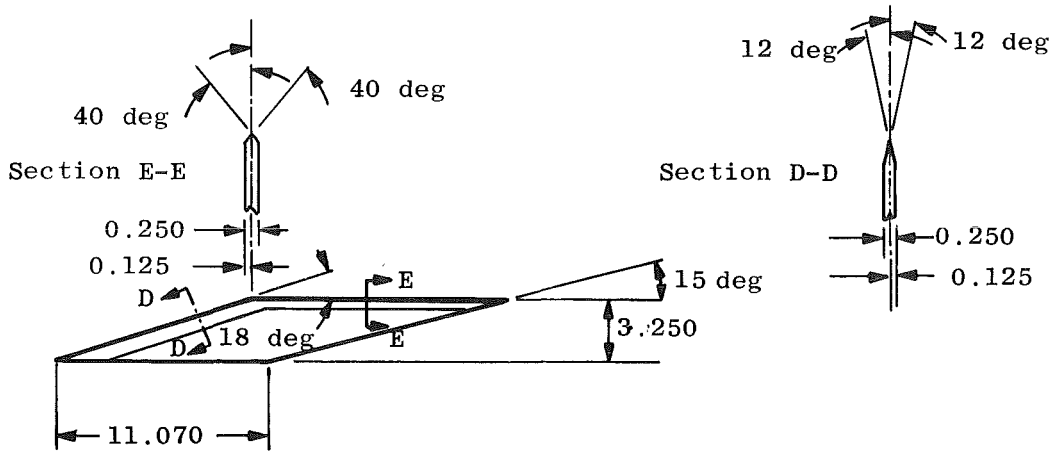

Plate 1

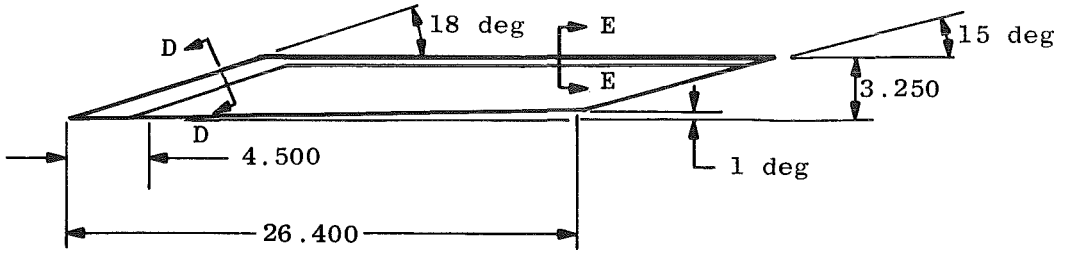

Plate 4

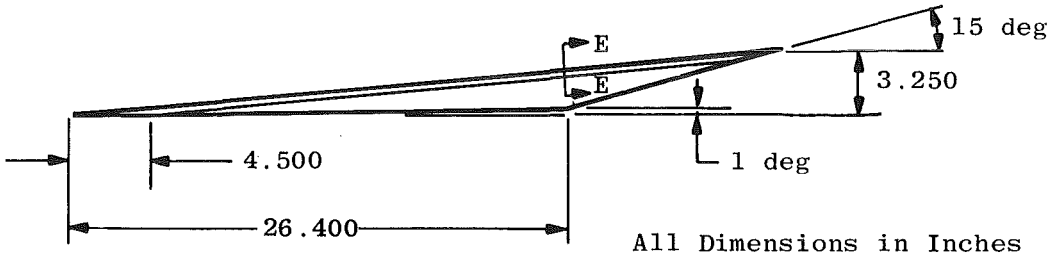

All Dimensions in Inches

Plate 8

Figure 15. Plate details.

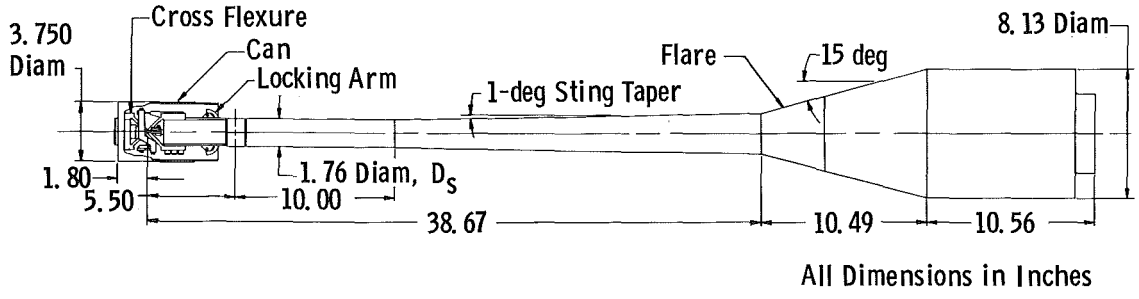

Figure 16. 1-DOF test mechanism (VKF-1.C) details.

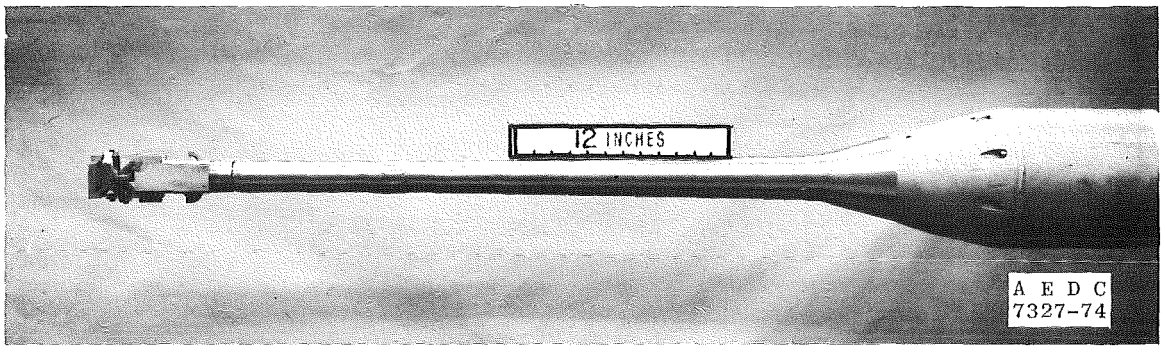

a. Forced-oscillation test mechanism

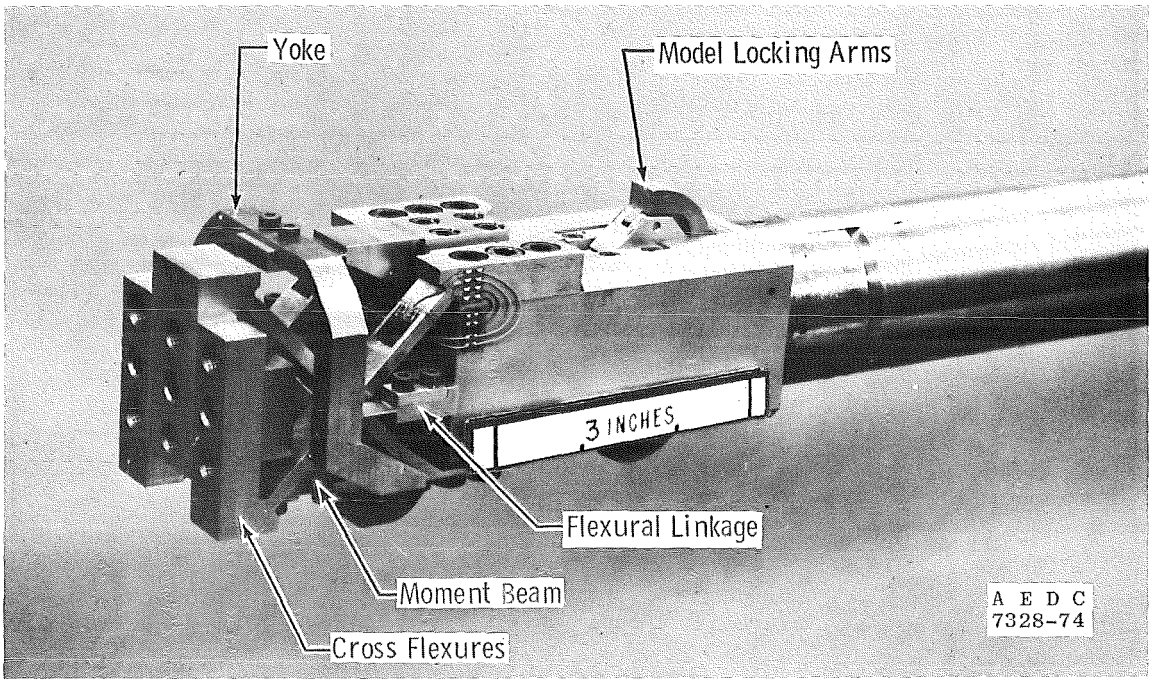

b. Cross-flexure balance

Figure 17. 1-DOF test mechanism (VKF-1.C).

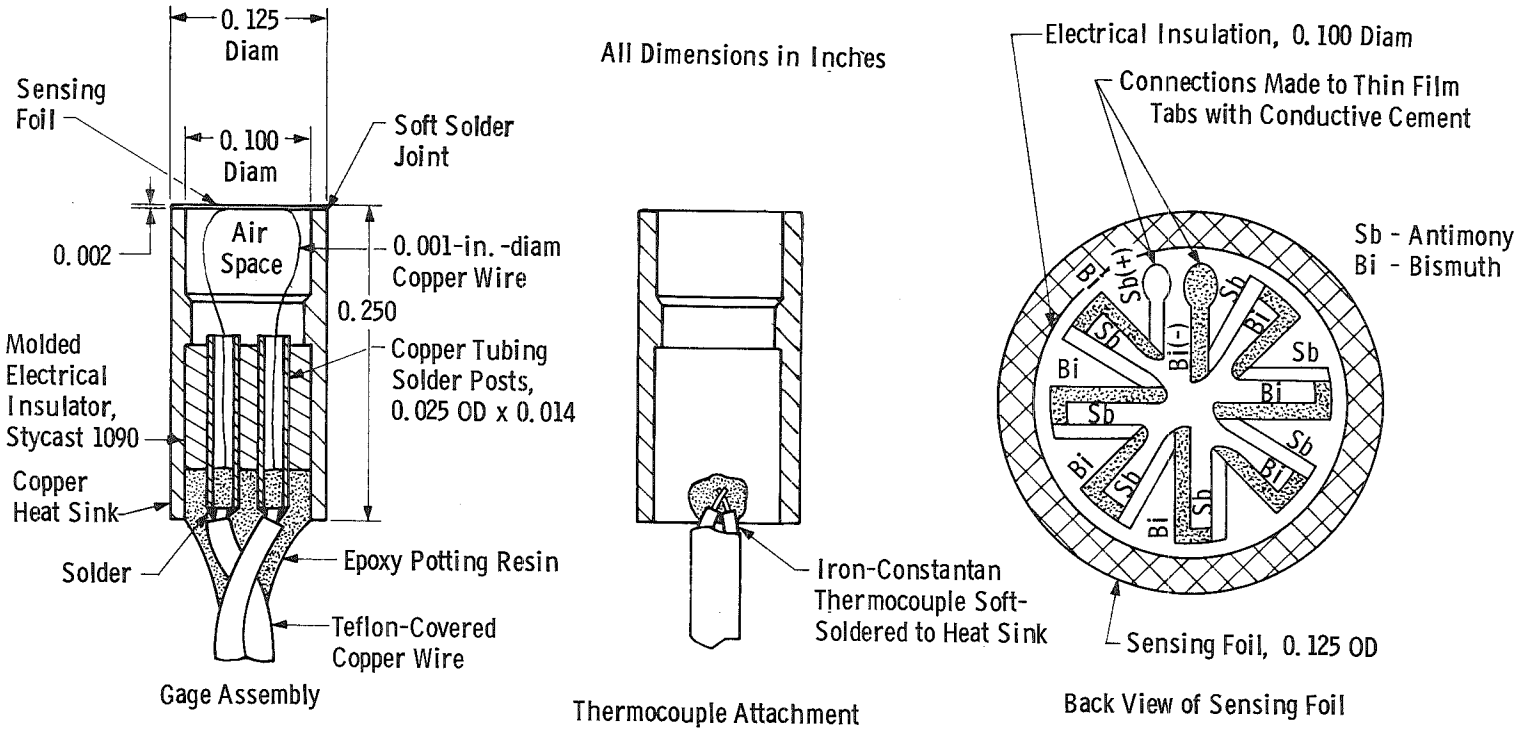

Figure 18. Details of thermopile Gardon gage.

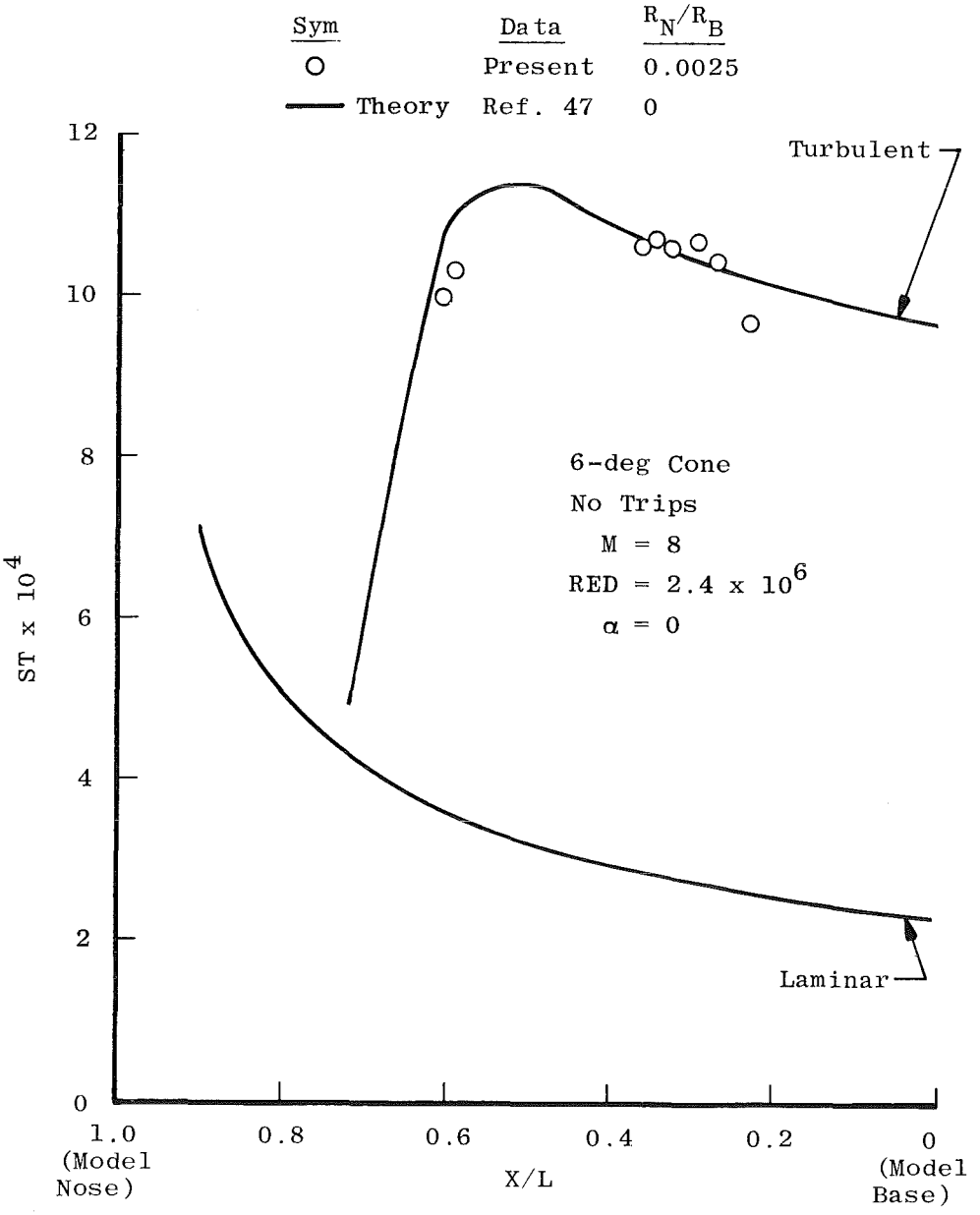

a. M = 8, R_N/R_B = 0.0025

Figure 19. Presentation of steady-state heat-transfer results.

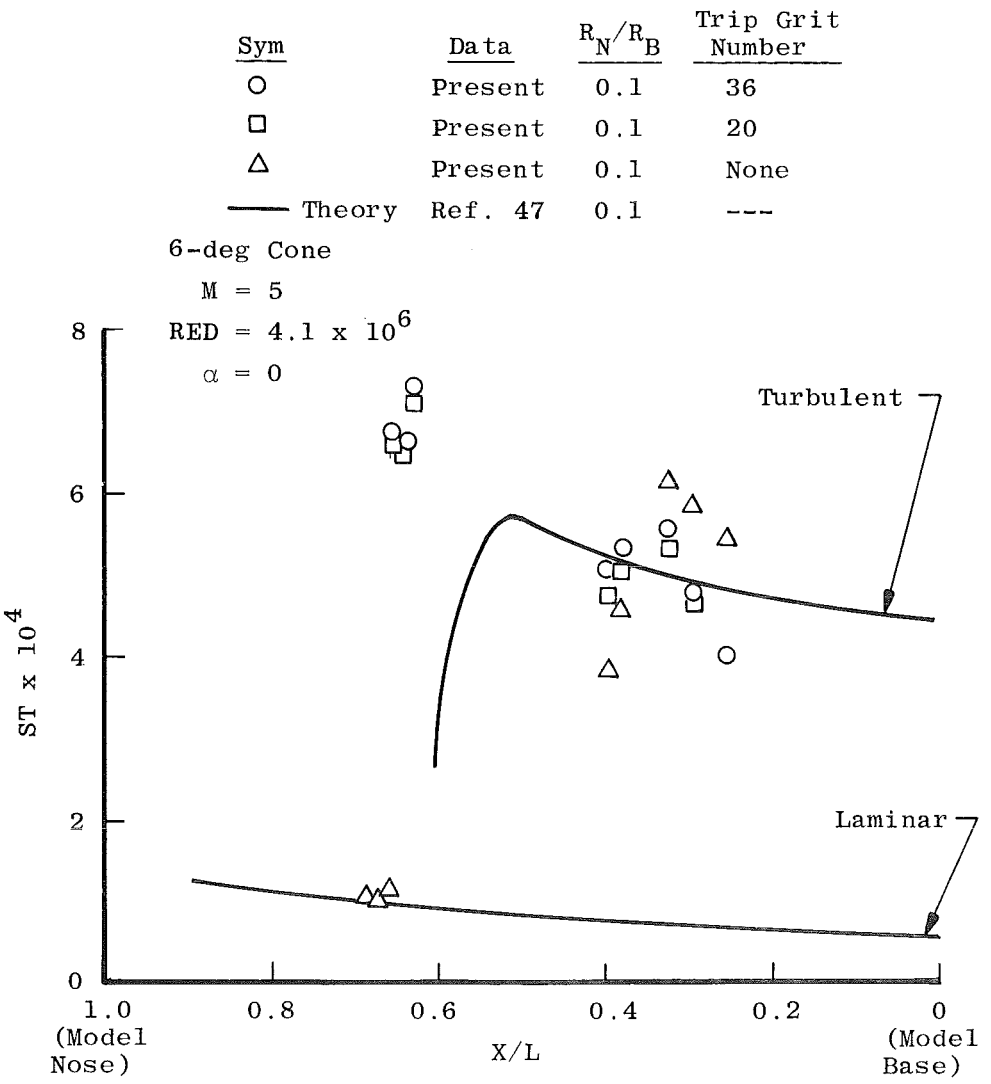

b. M = 5, R_N/R_B = 0.1

Figure 19. Continued.

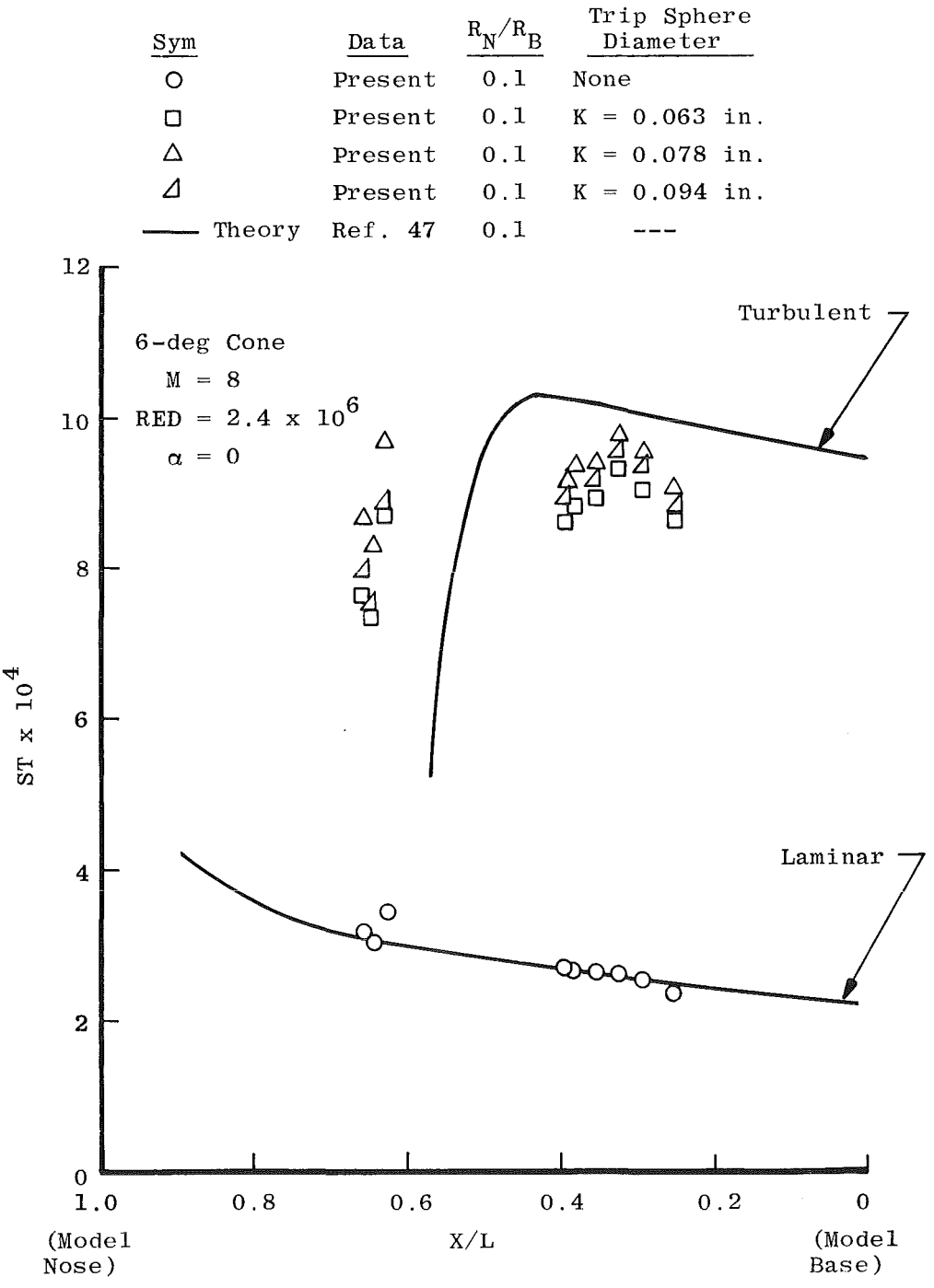

c. M = 8, R_N/R_B = 0.1

Figure 19. Concluded.

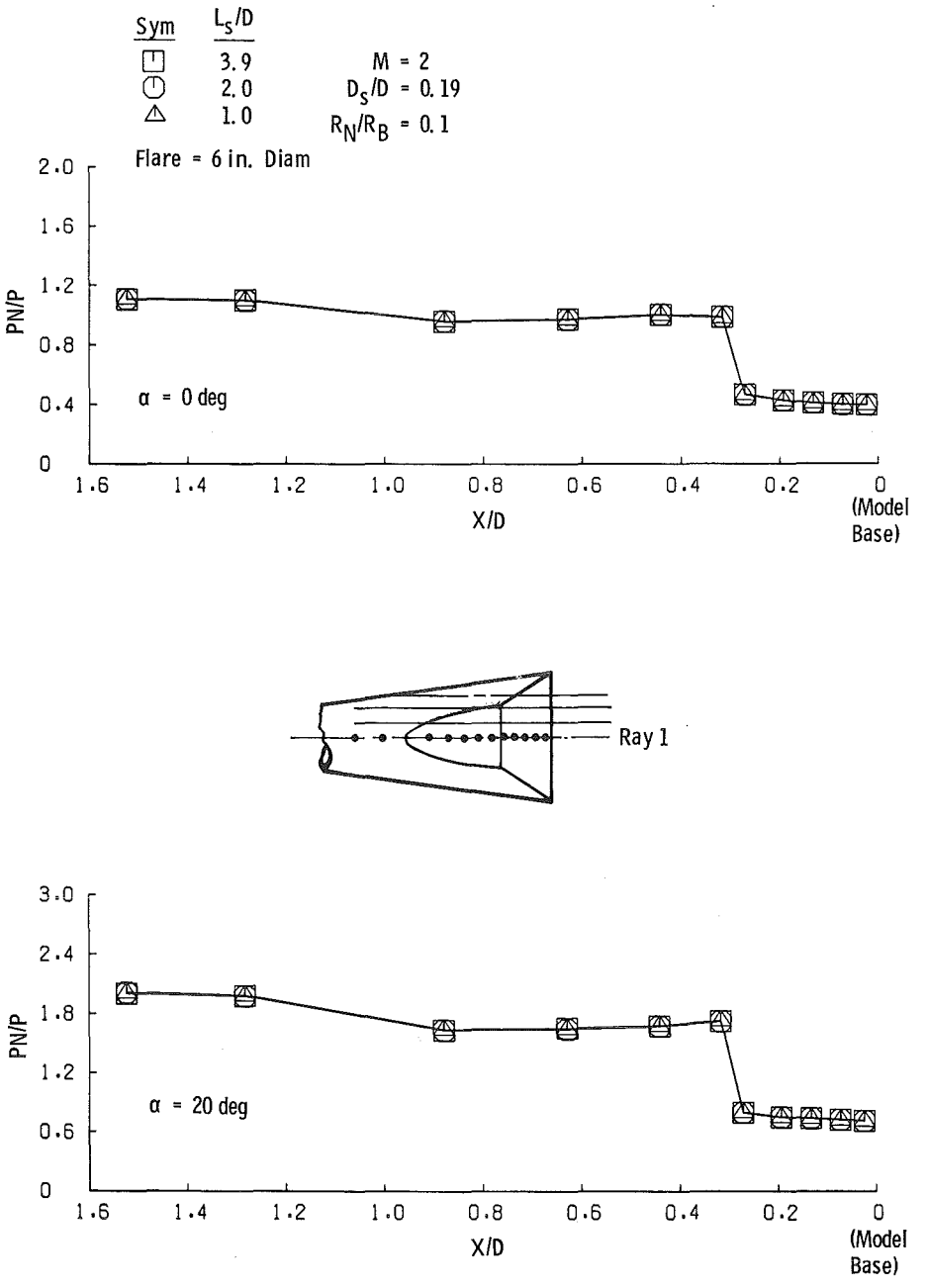

a. Ray 1

Figure 20. Typical pressure distributions.

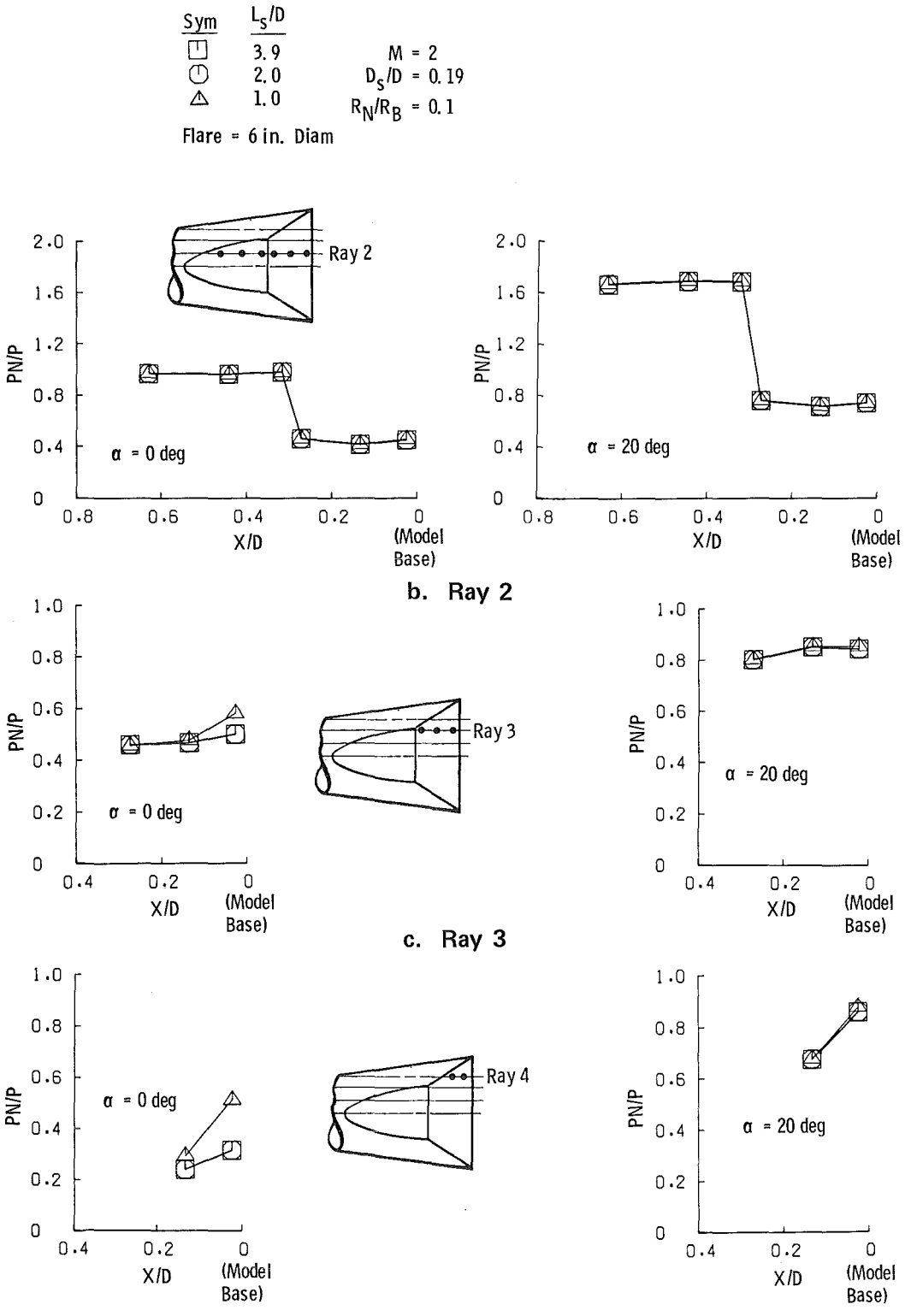

b. Ray 2

c. Ray 3

d. Ray 4

Figure 20. Concluded.

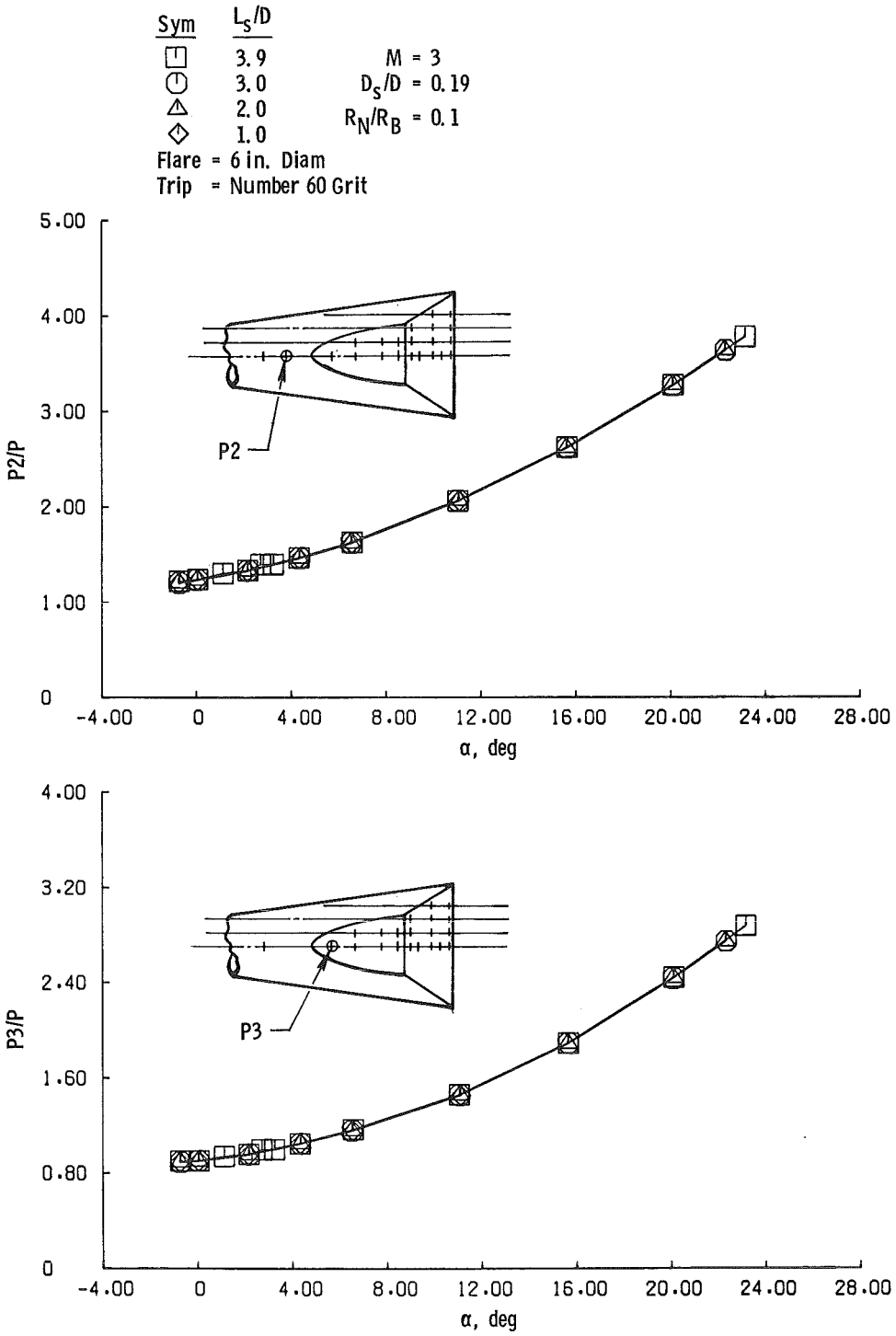

a. P2 and P3

Figure 21. Sting effects as a function of angle of attack, M = 3, turbulent boundary layer.

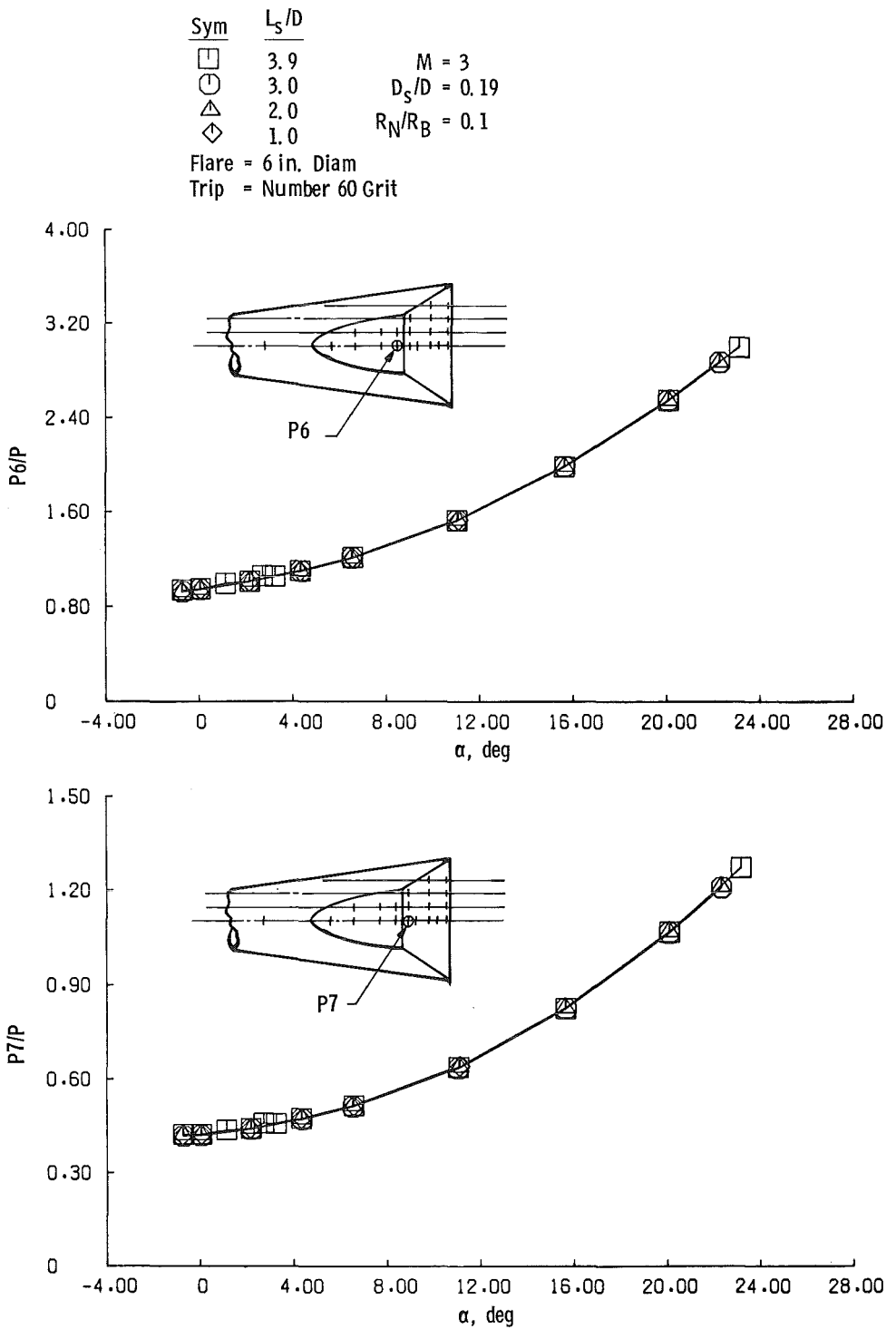

b. P6 and P7

Figure 21. Continued.

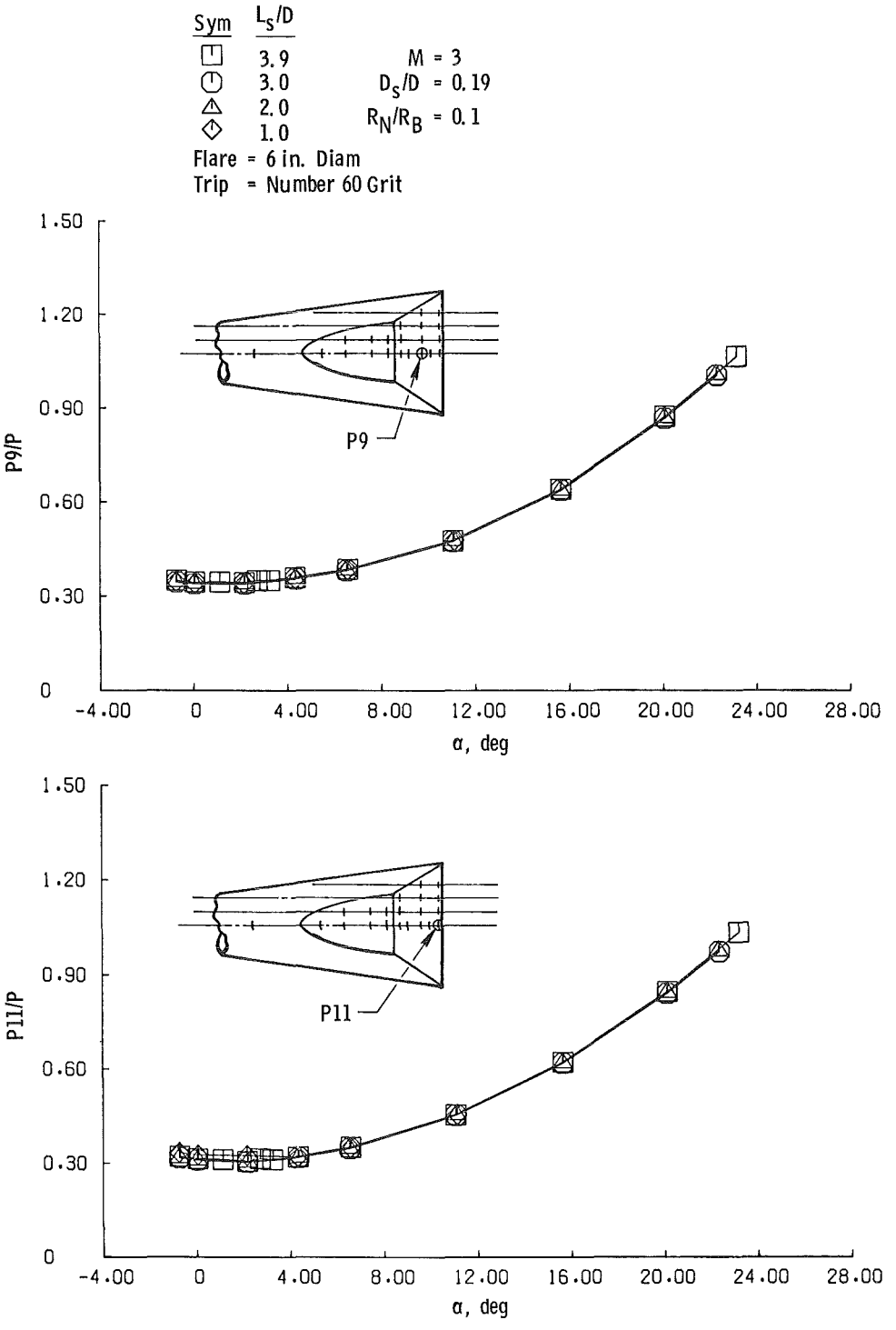

c. P9 and P11
Figure 21. Continued.

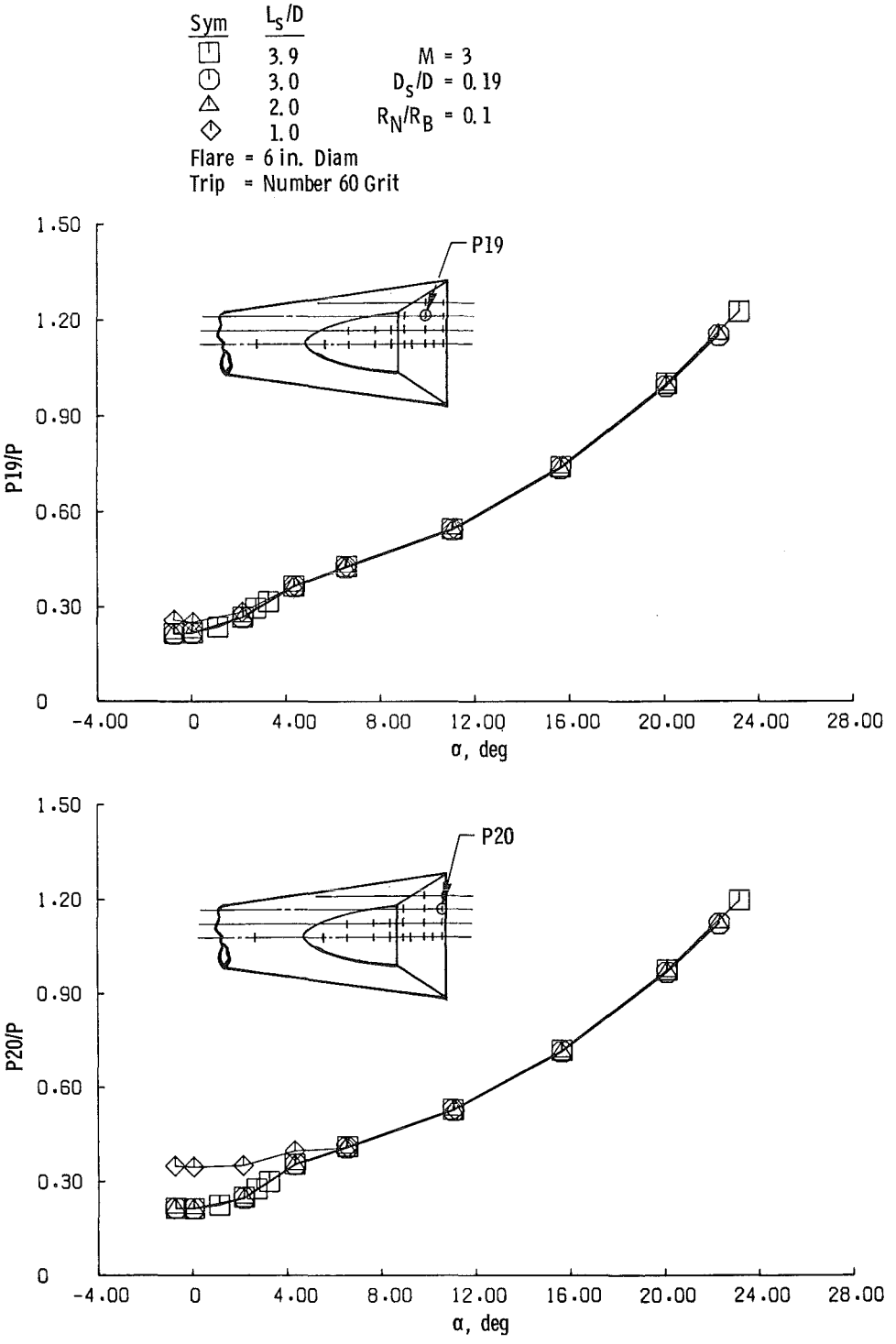

d. P19 and P20

Figure 21. Continued.

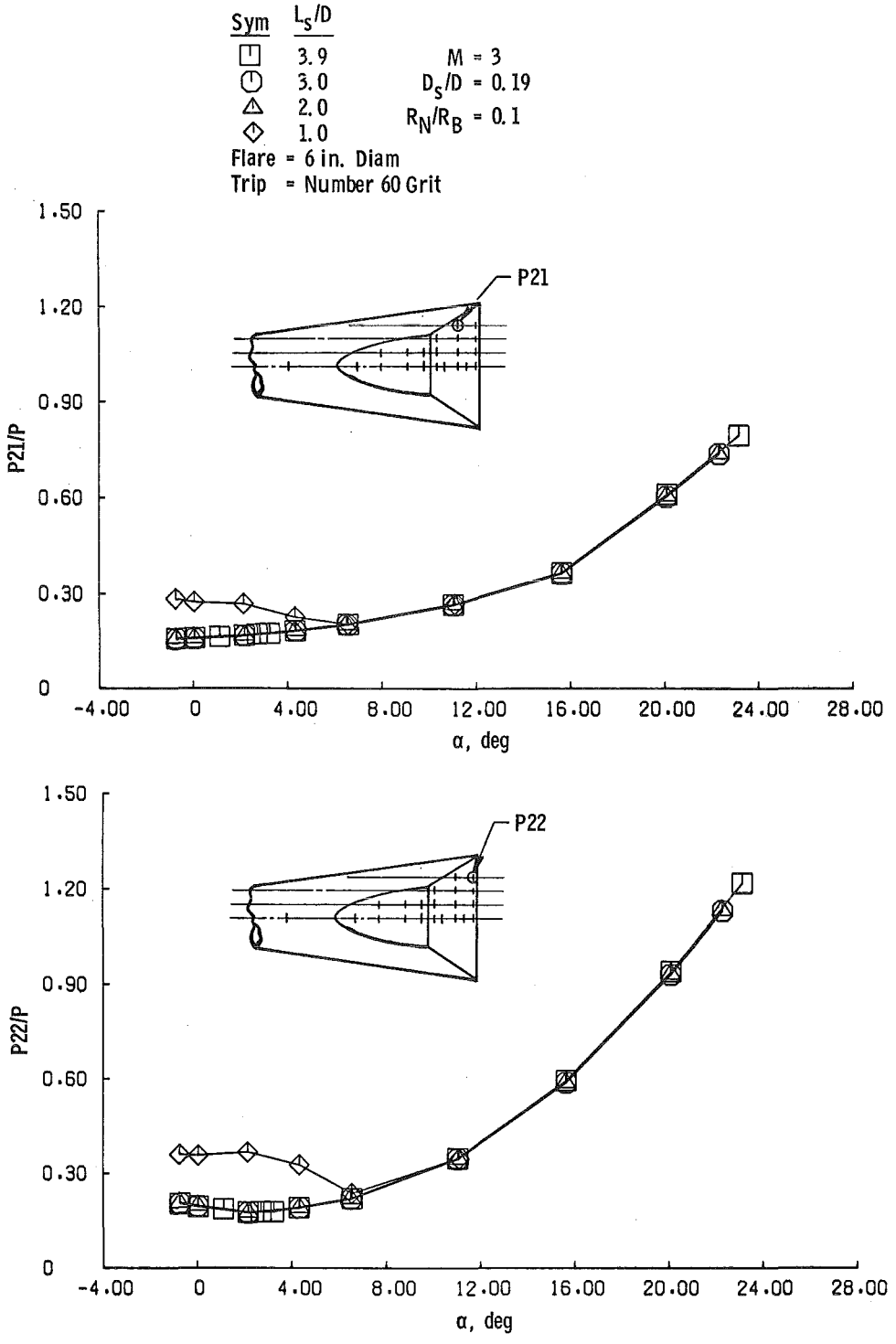

e. P21 and P22
Figure 21. Continued.

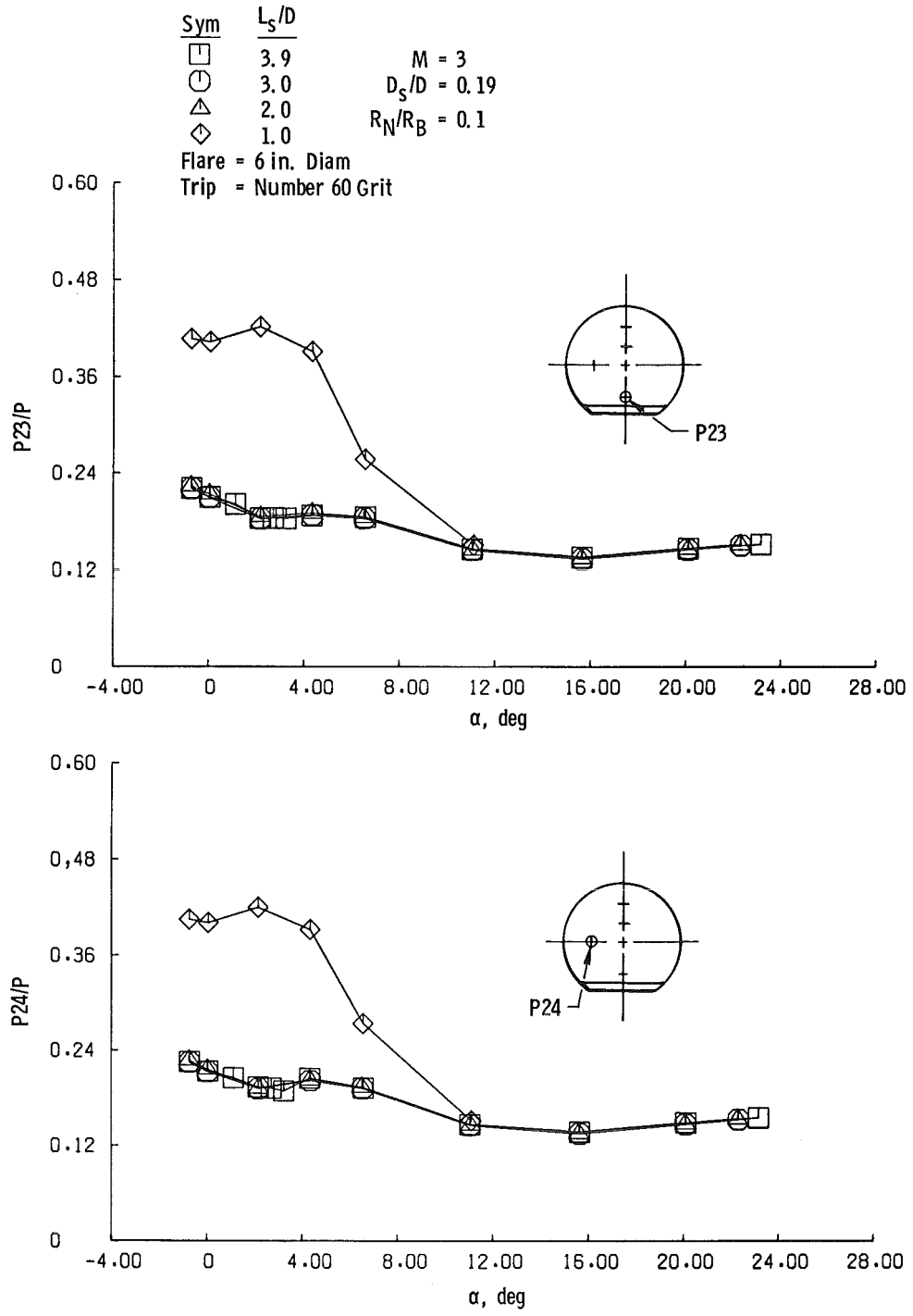

f. P23 and P24

Figure 21. Continued.

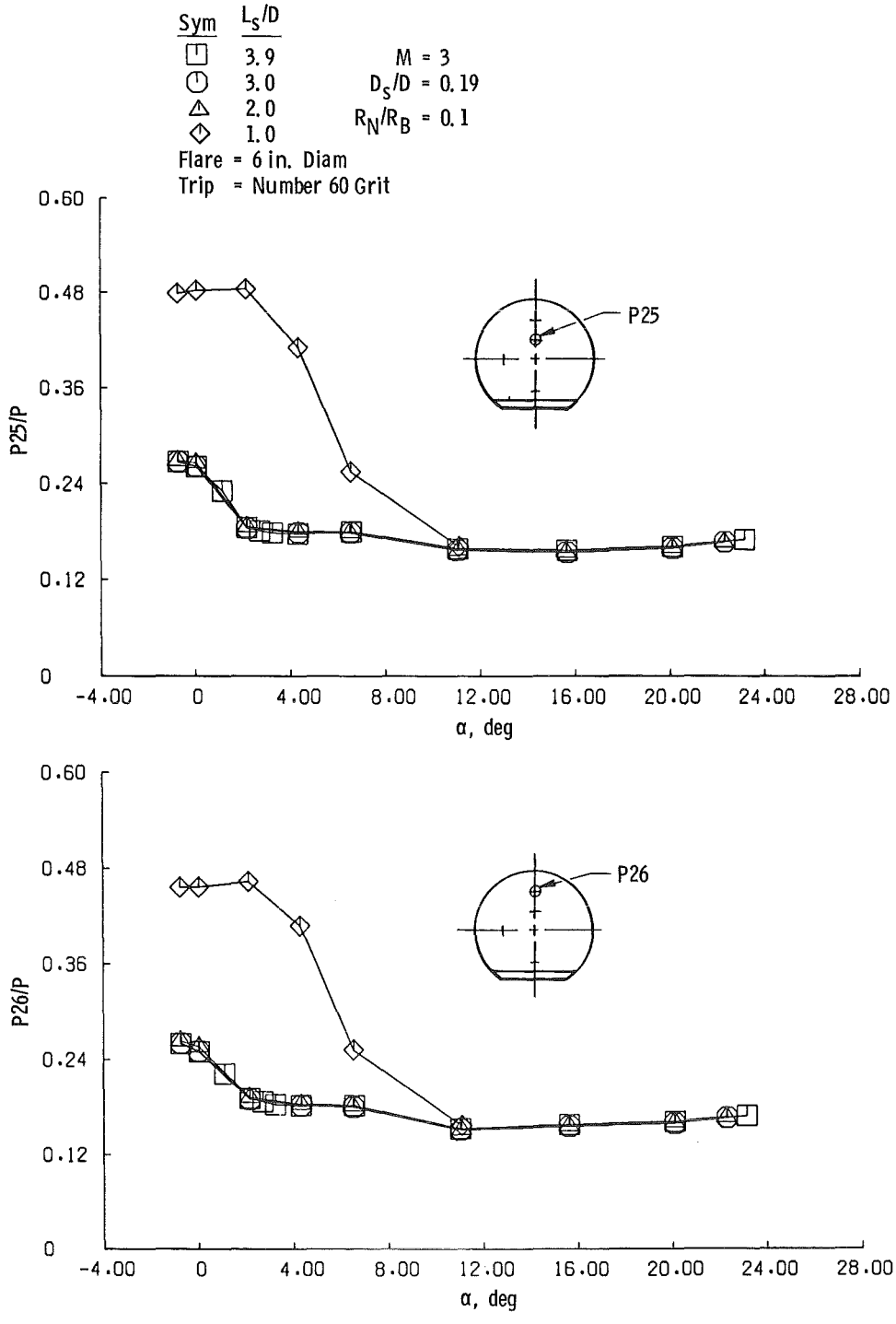

g. P25 and P26

Figure 21. Concluded.

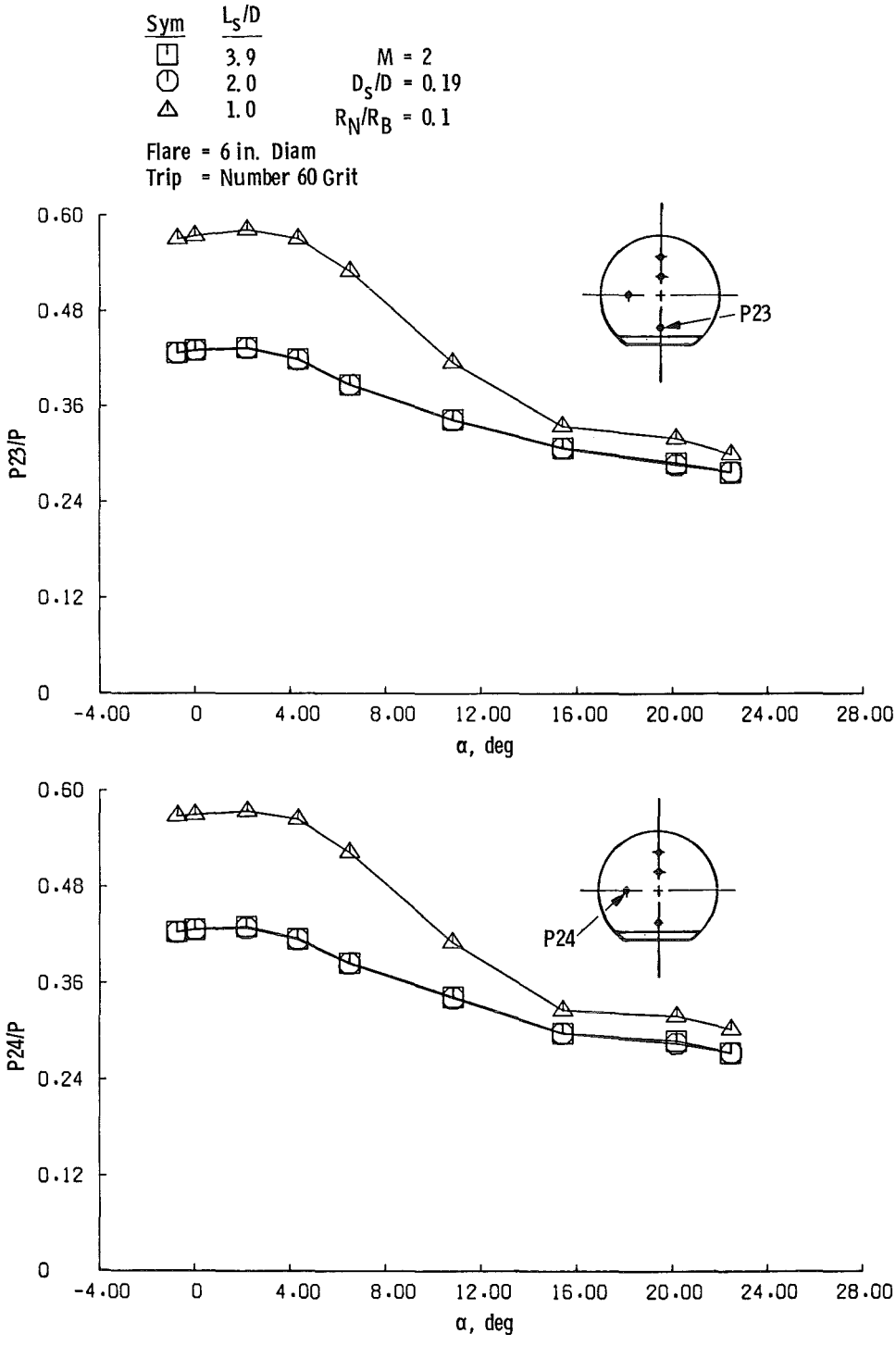

a. P23 and P24

Figure 22. Sting effects on base pressure, M = 2.

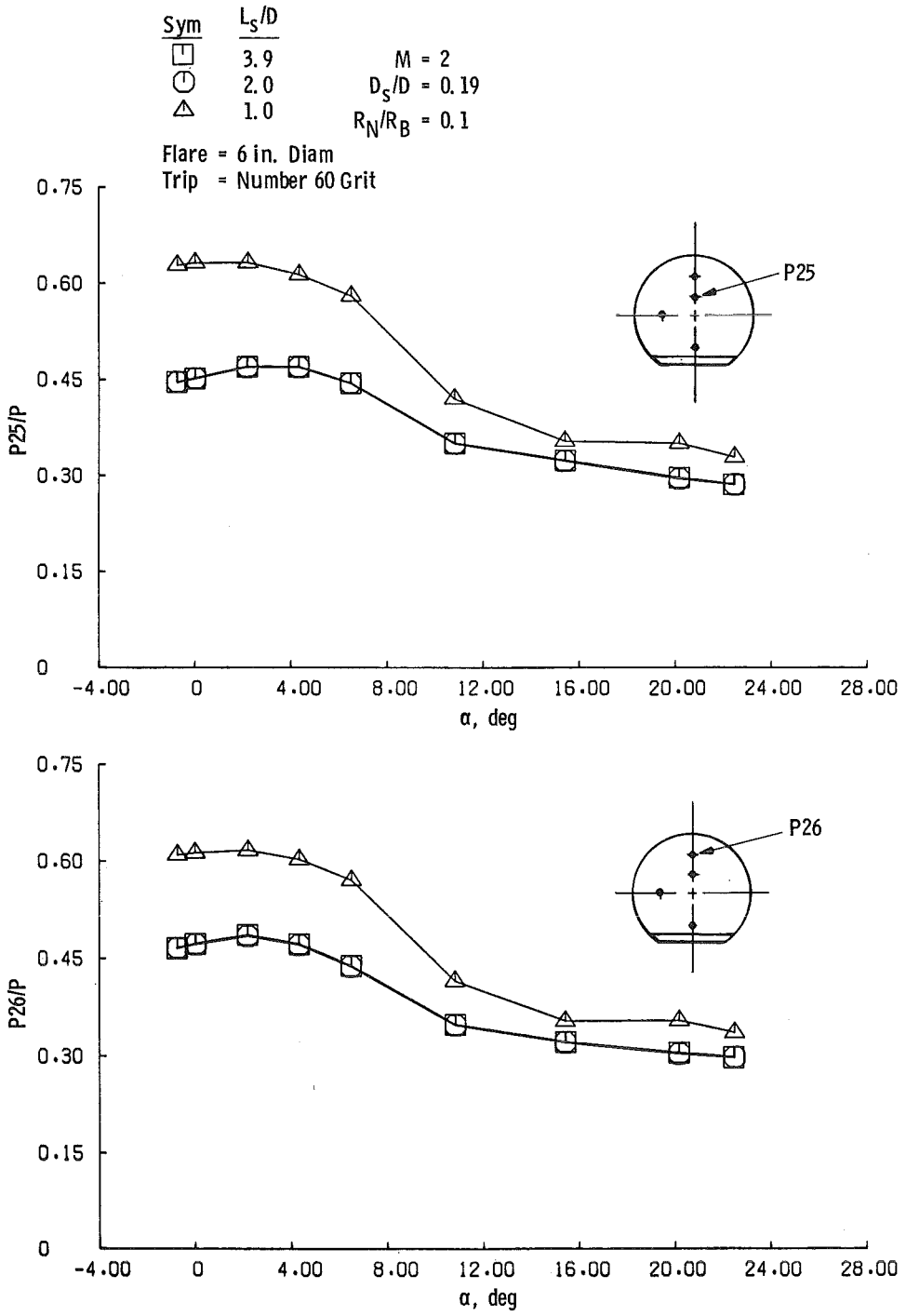

b. P25 and P26

Figure 22. Concluded.

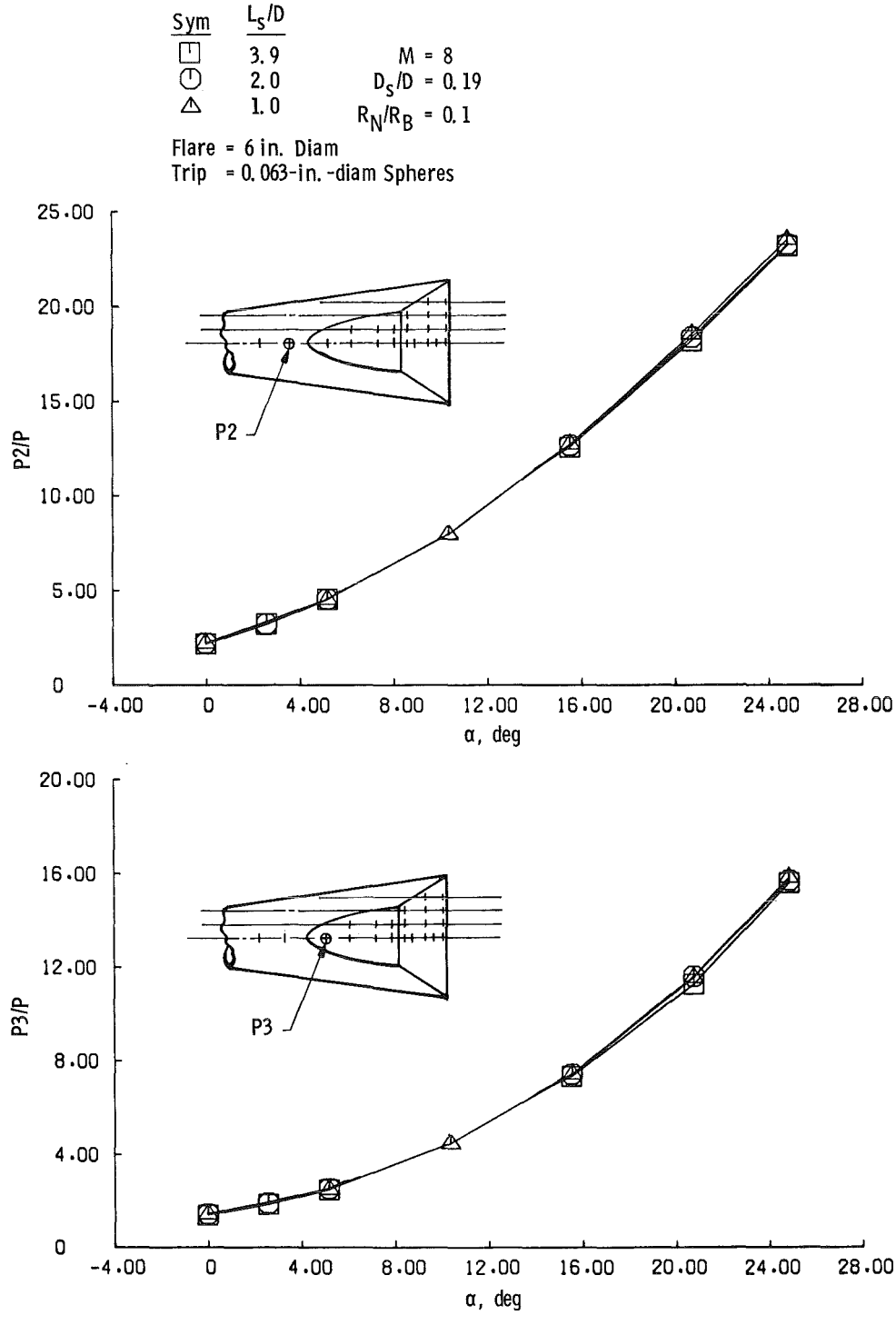

a. P2 and P3

Figure 23. Sting effects as a function of angle of attack, M = 8, turbulent boundary layer.

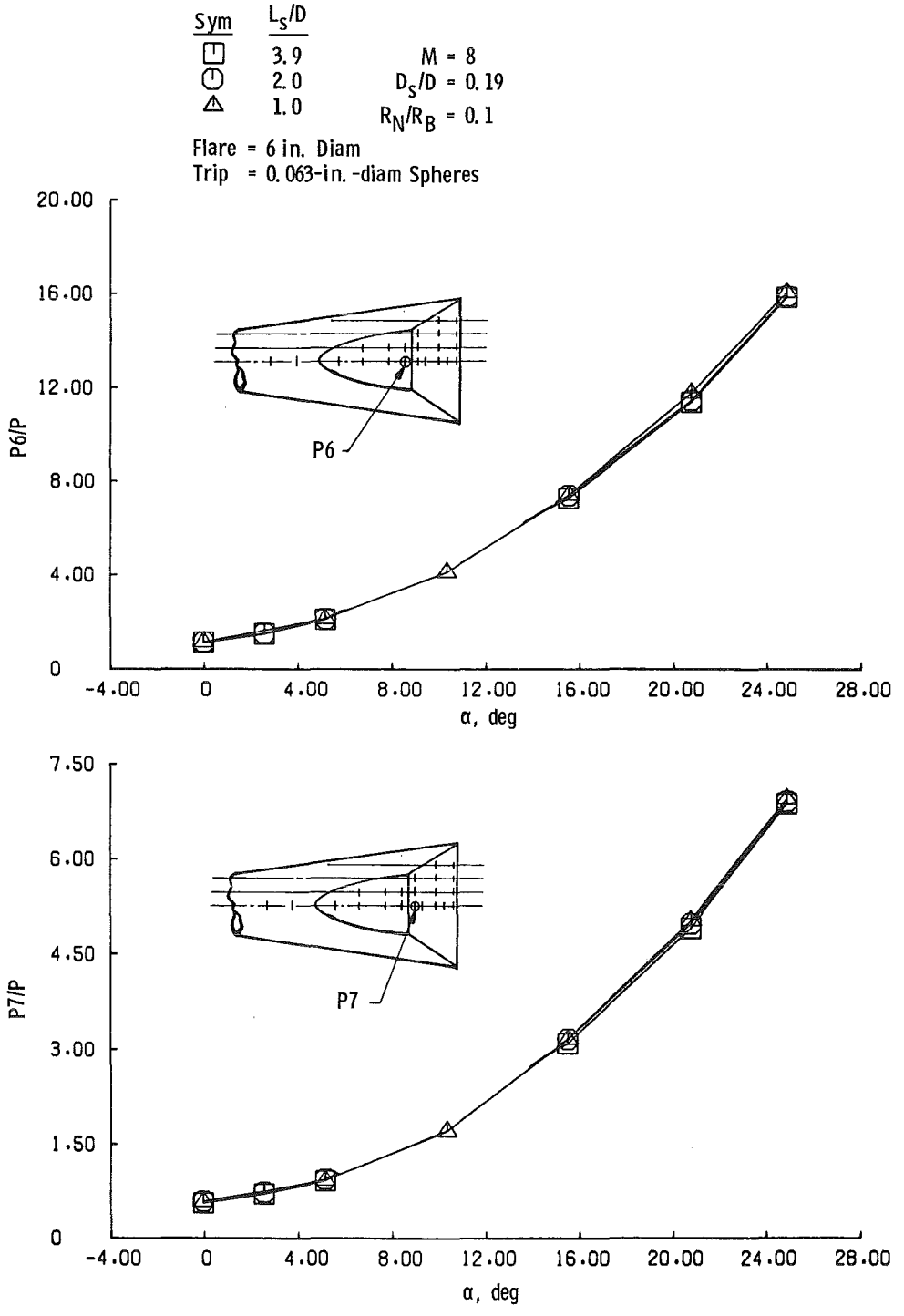

b. P6 and P7

Figure 23. Continued.

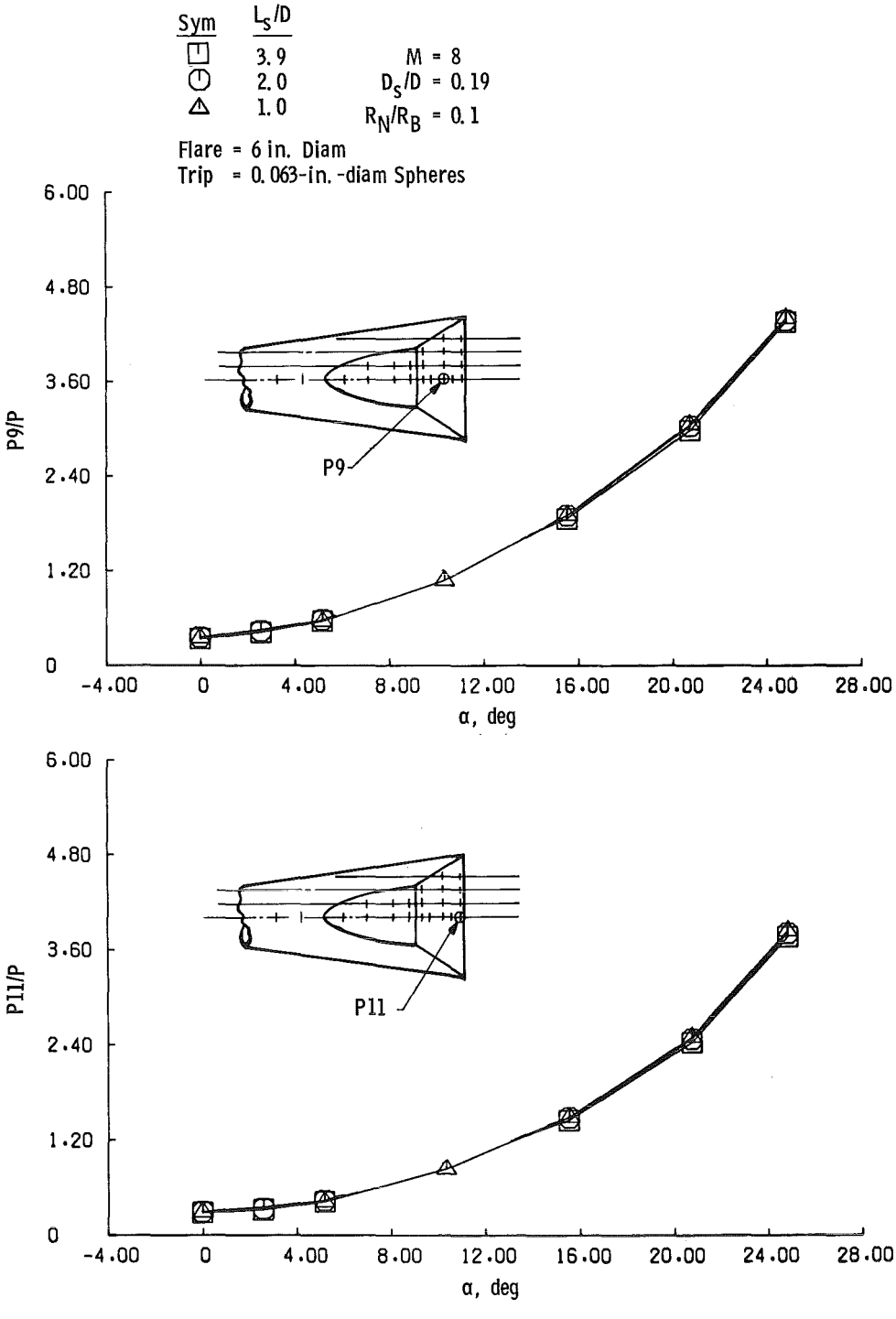

c. P9 and P11

Figure 23. Continued.

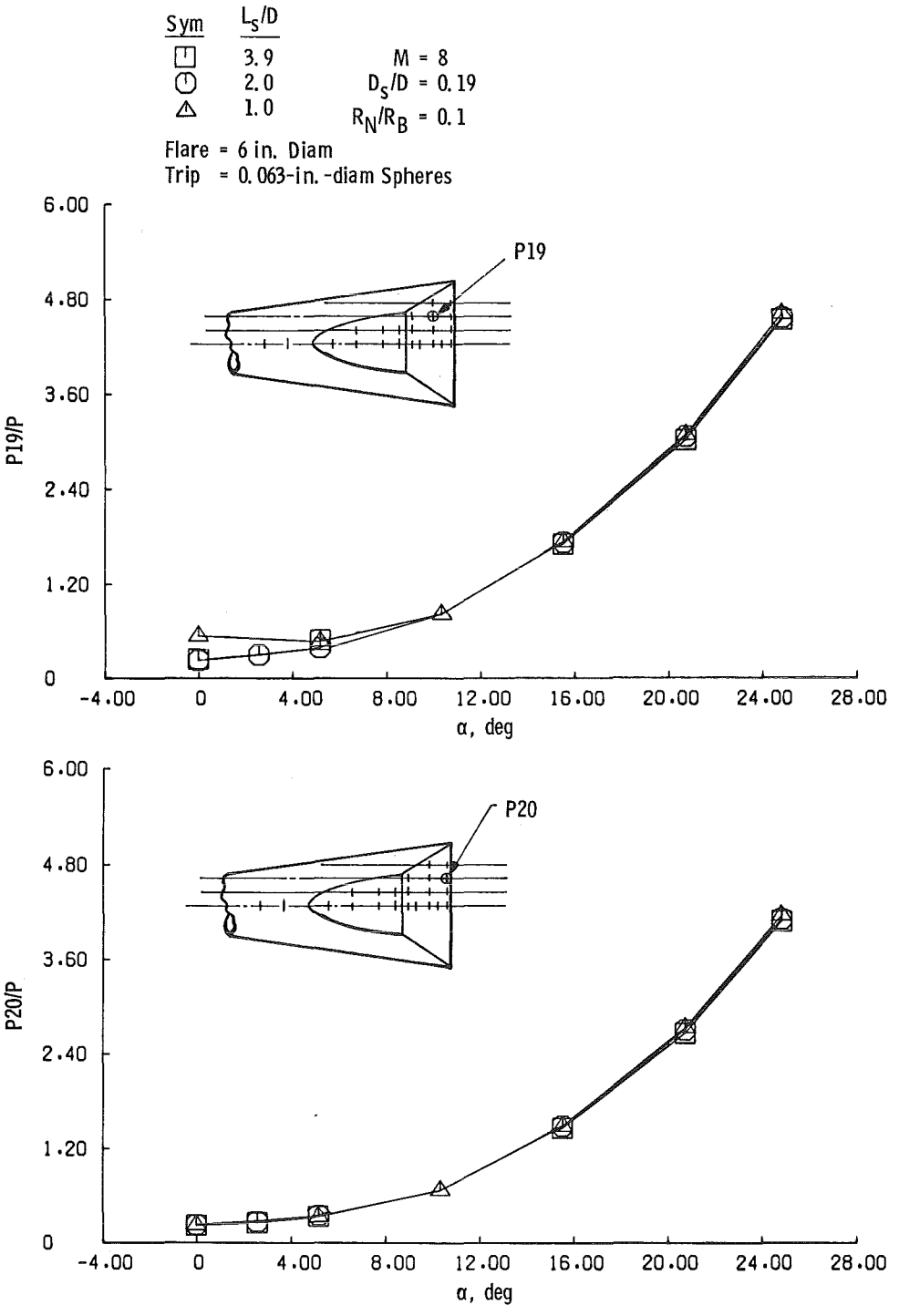

d. P19 and P20

Figure 23. Continued.

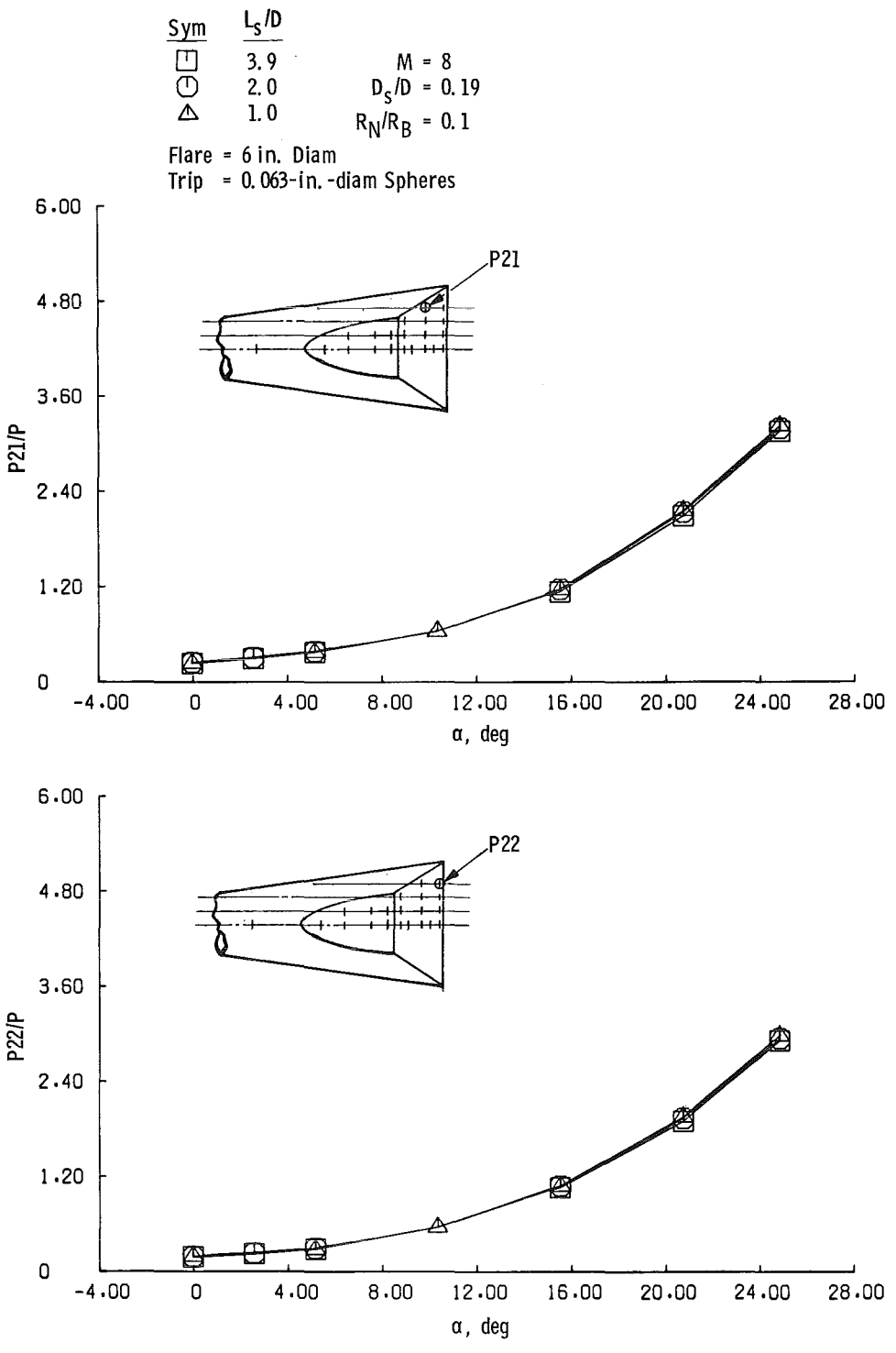

e. P21 and P22

Figure 23. Continued.

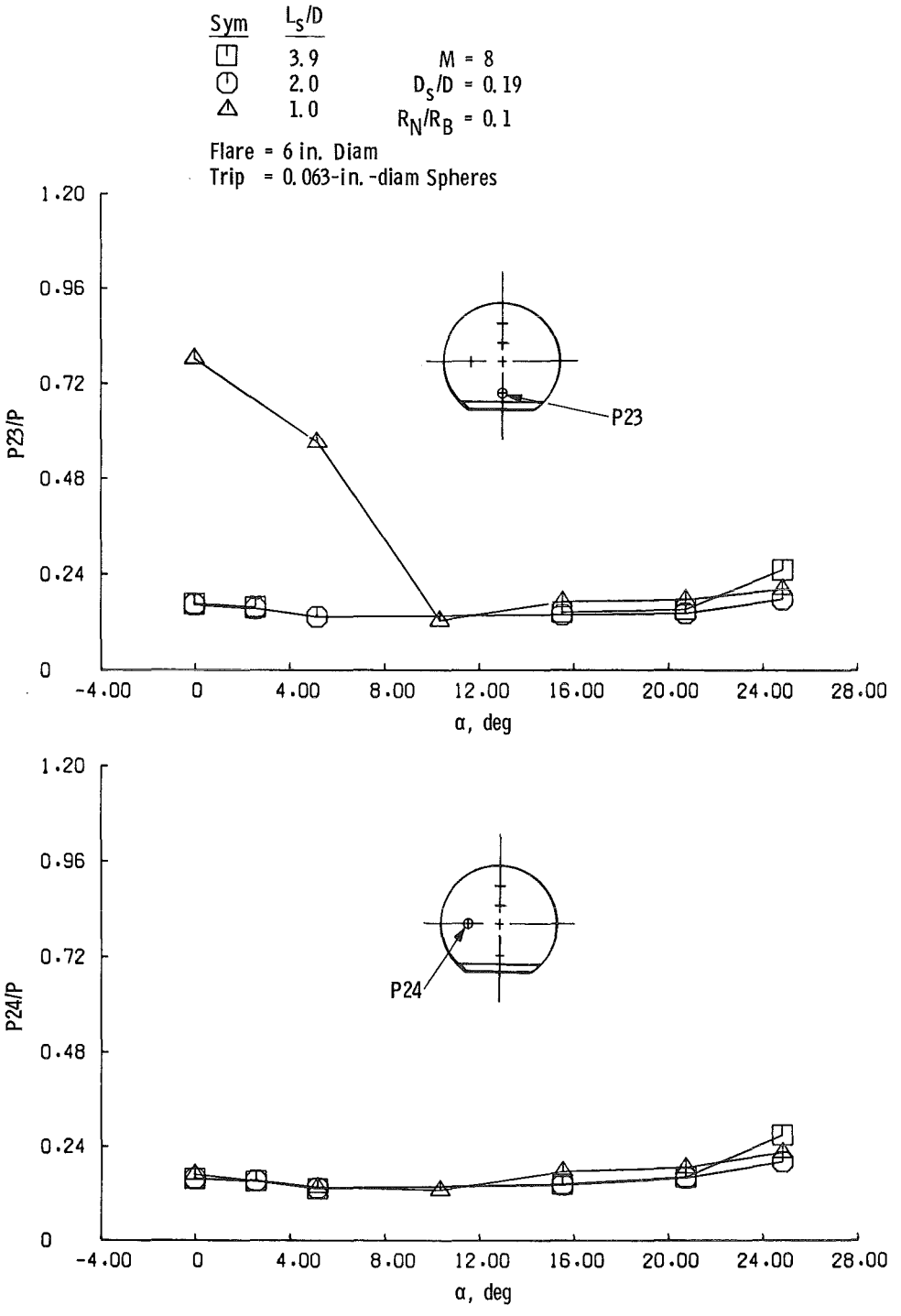

f. P23 and P24

Figure 23. Continued.

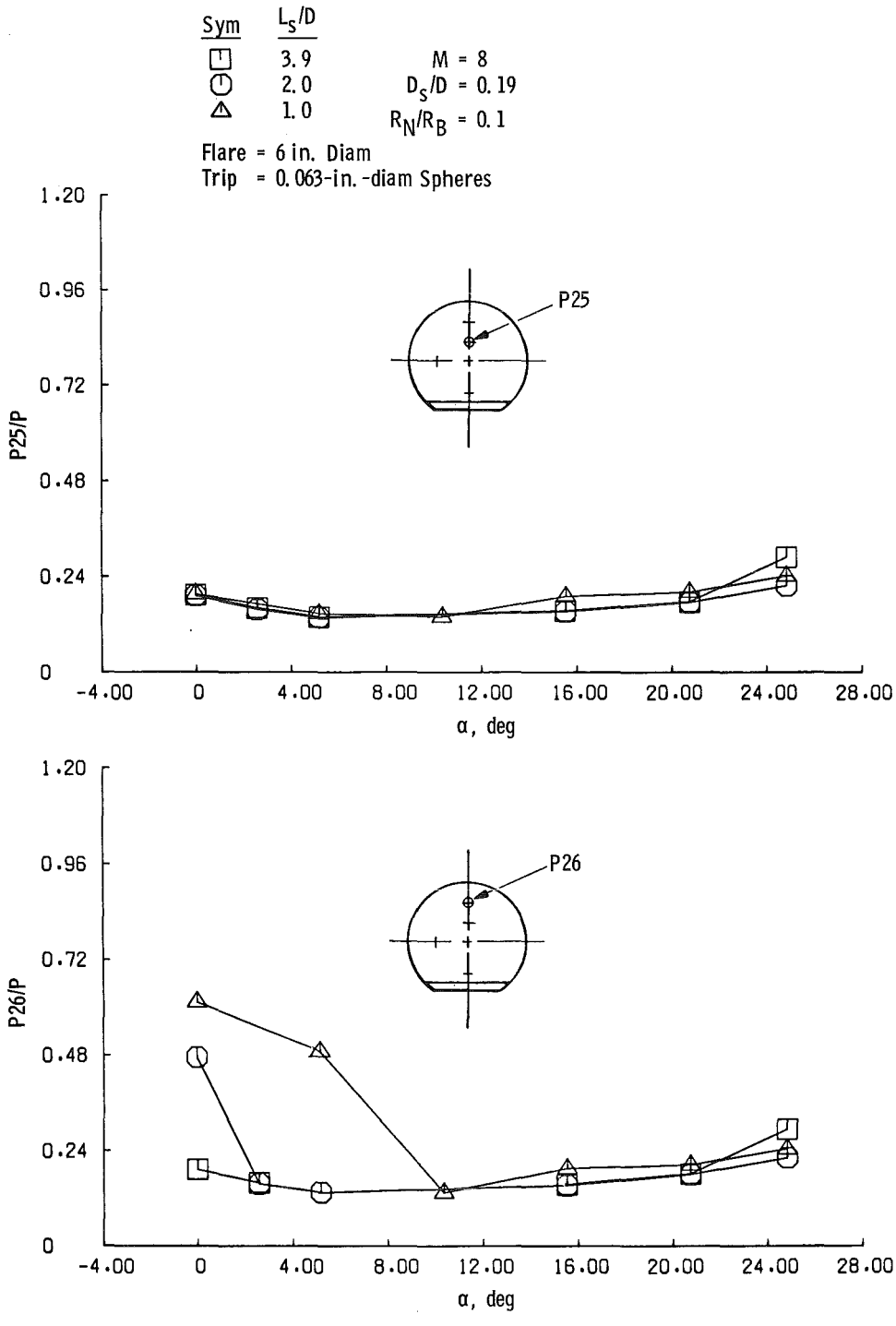

g. P25 and P26

Figure 23. Concluded.

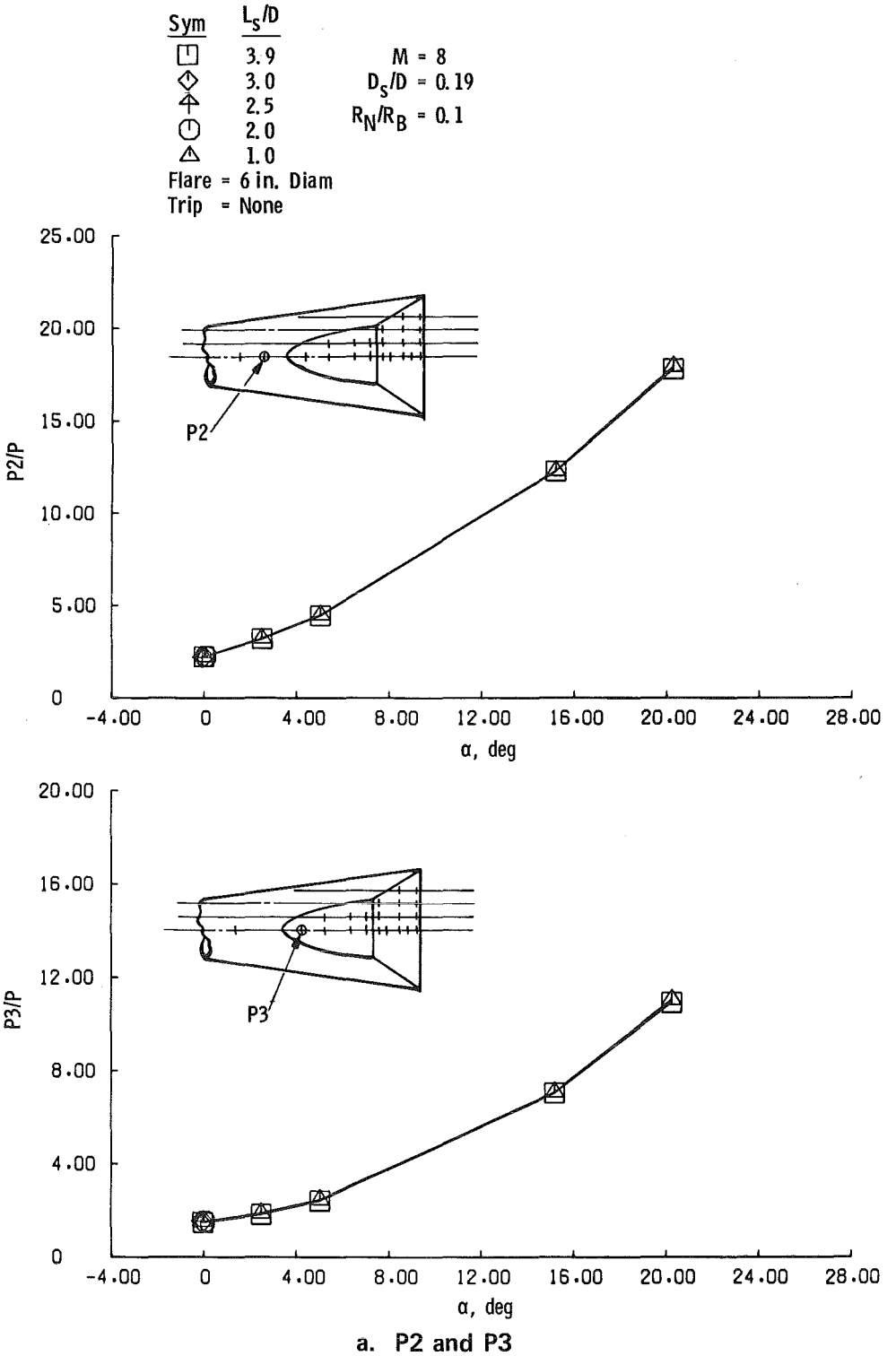

a. P2 and P3

Figure 24. Sting effects as a function of angle of attack, M = 8, laminar boundary layer.

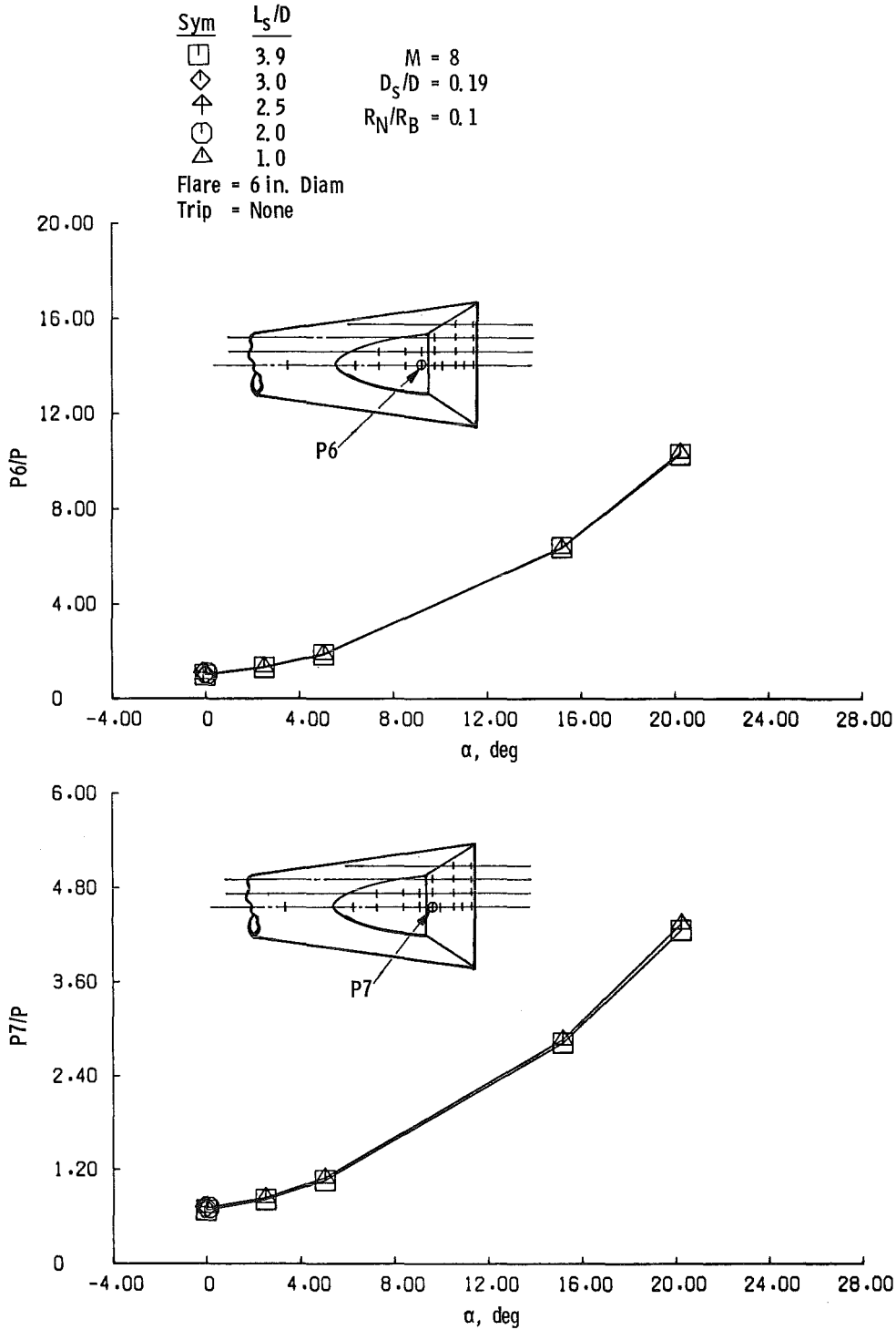

b. P6 and P7

Figure 24. Continued.

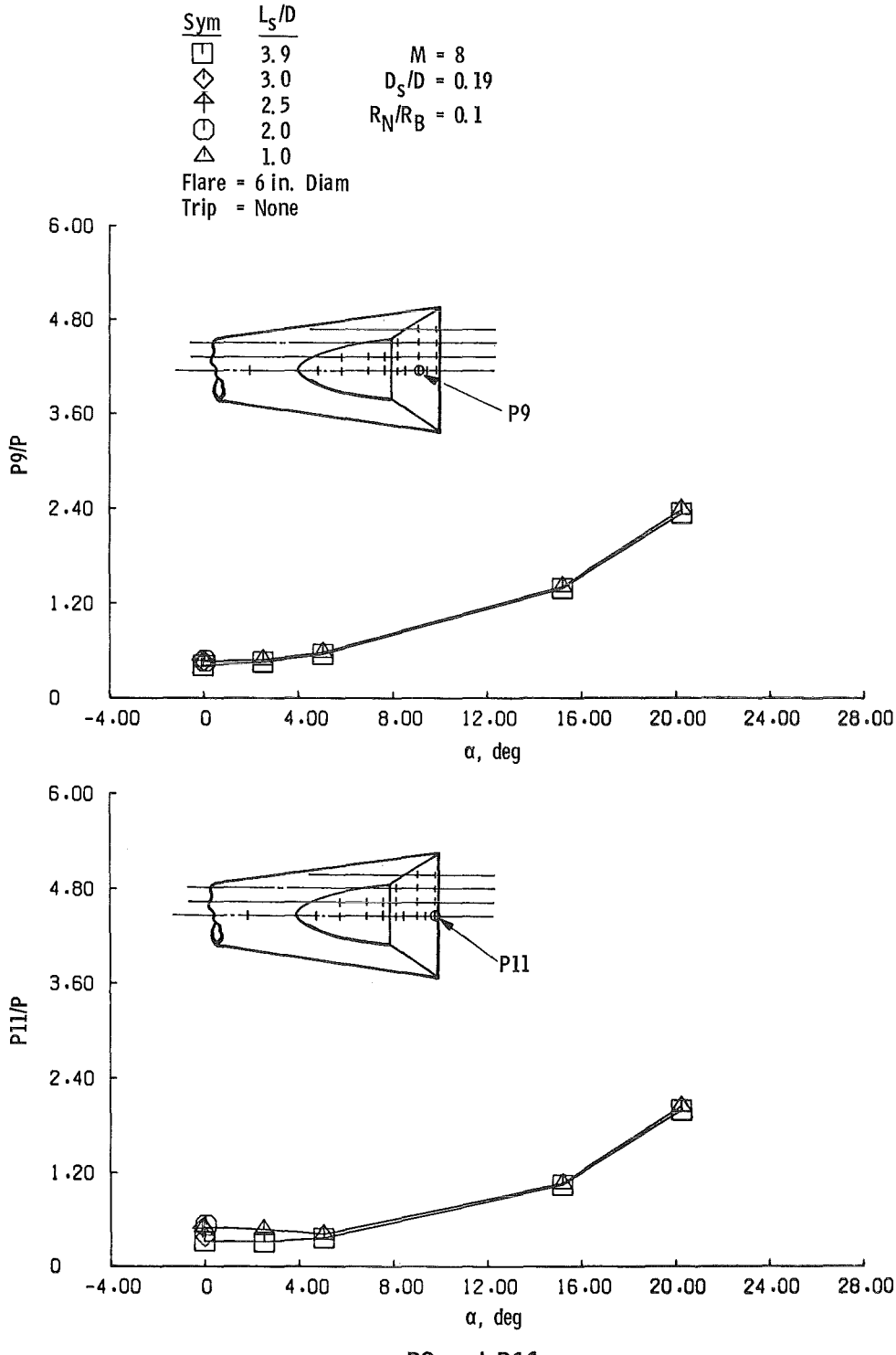

c. P9 and P11

Figure 24. Continued.

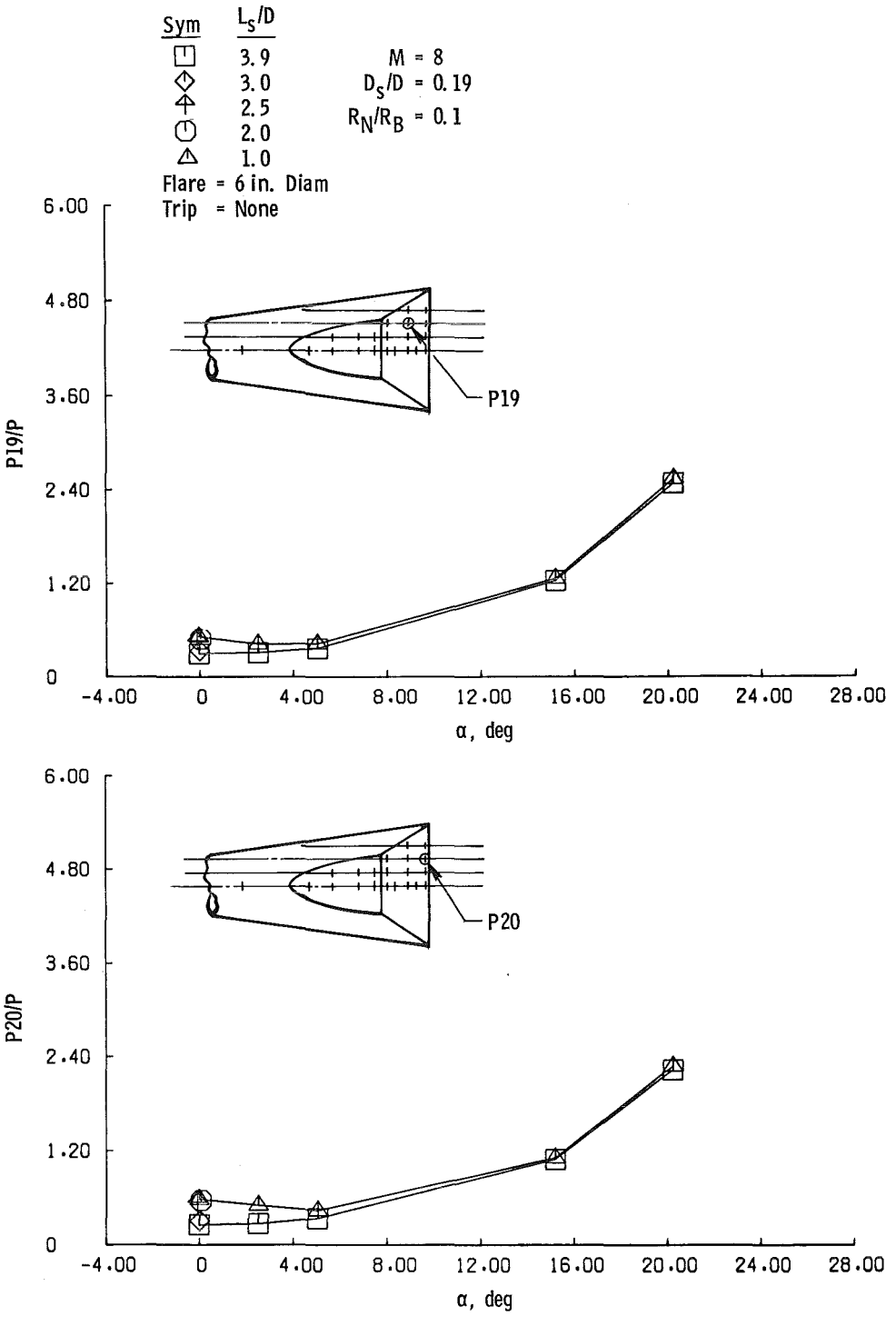

d. P19 and P20

Figure 24. Continued.

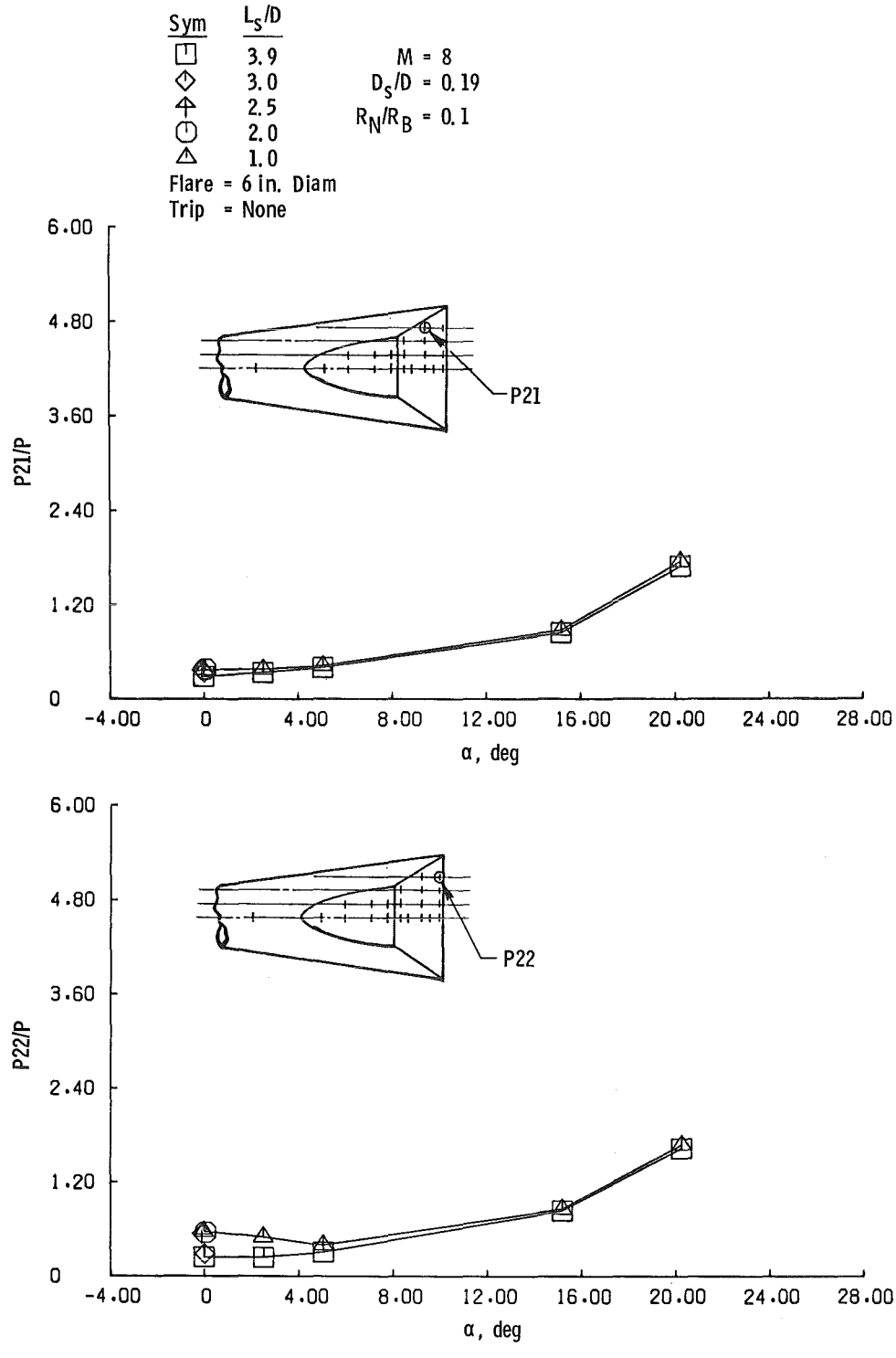

e. P21 and P22

Figure 24. Continued.

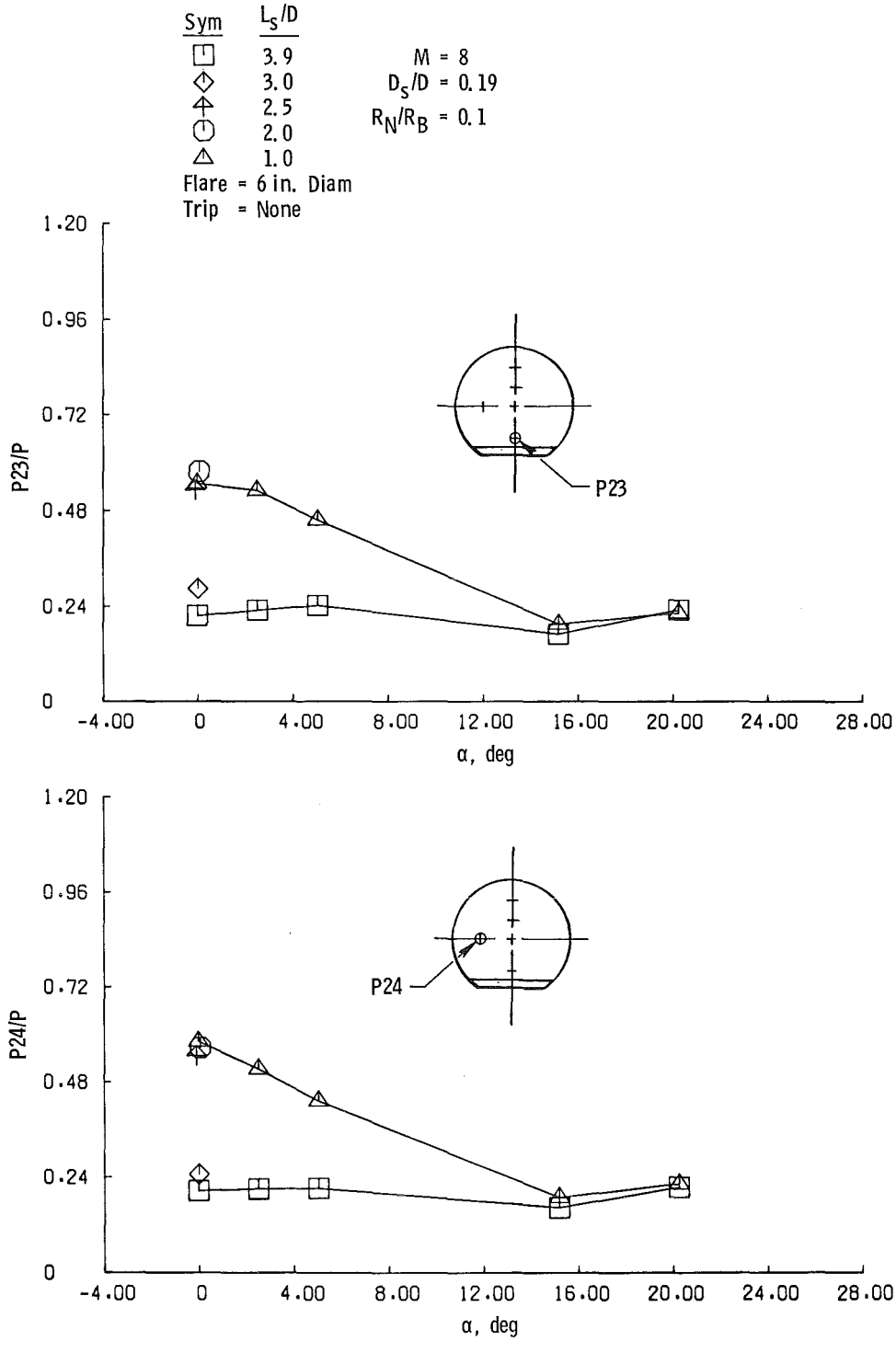

f. P23 and P24

Figure 24. Continued.

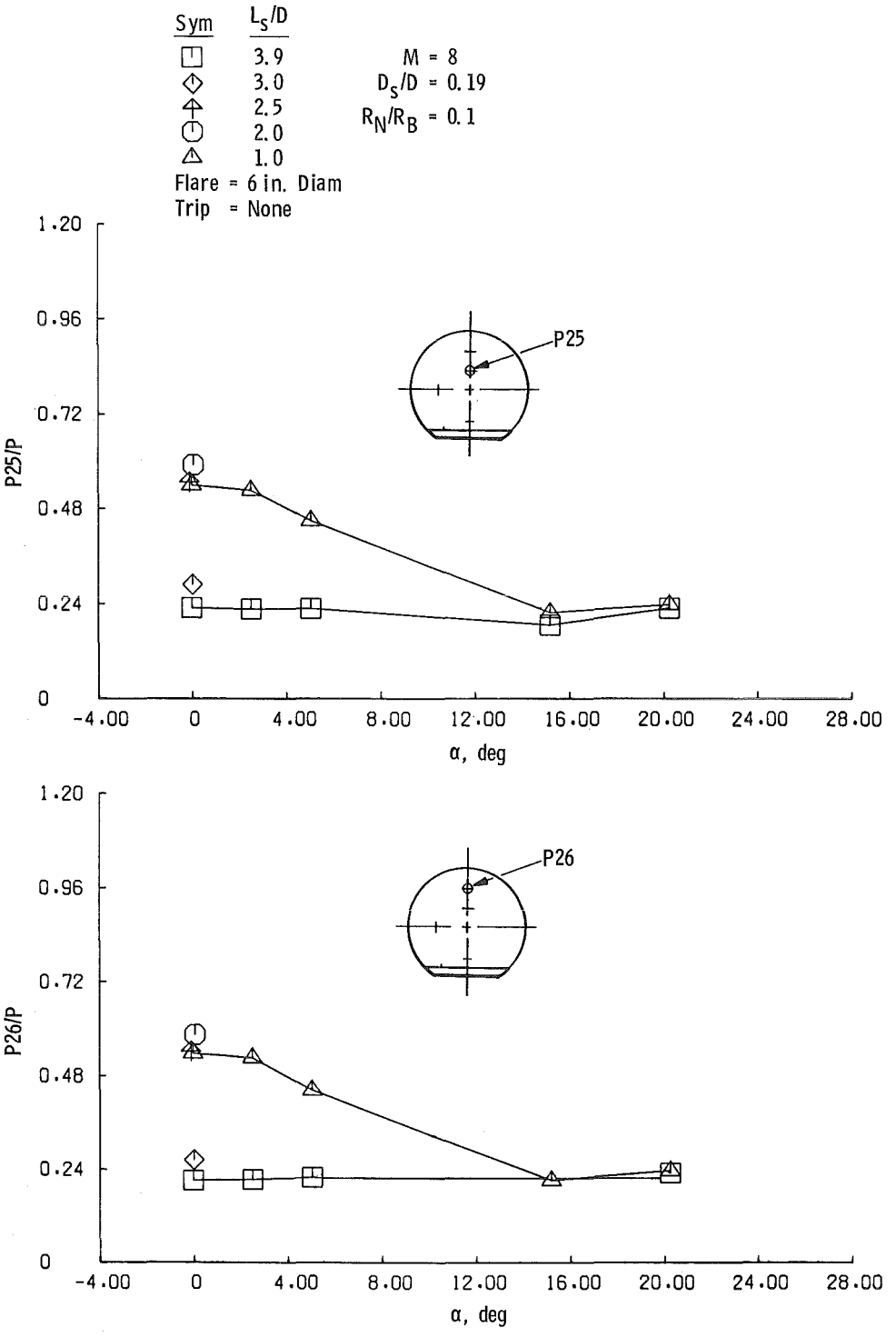

g. P25 and P26

Figure 24. Concluded.

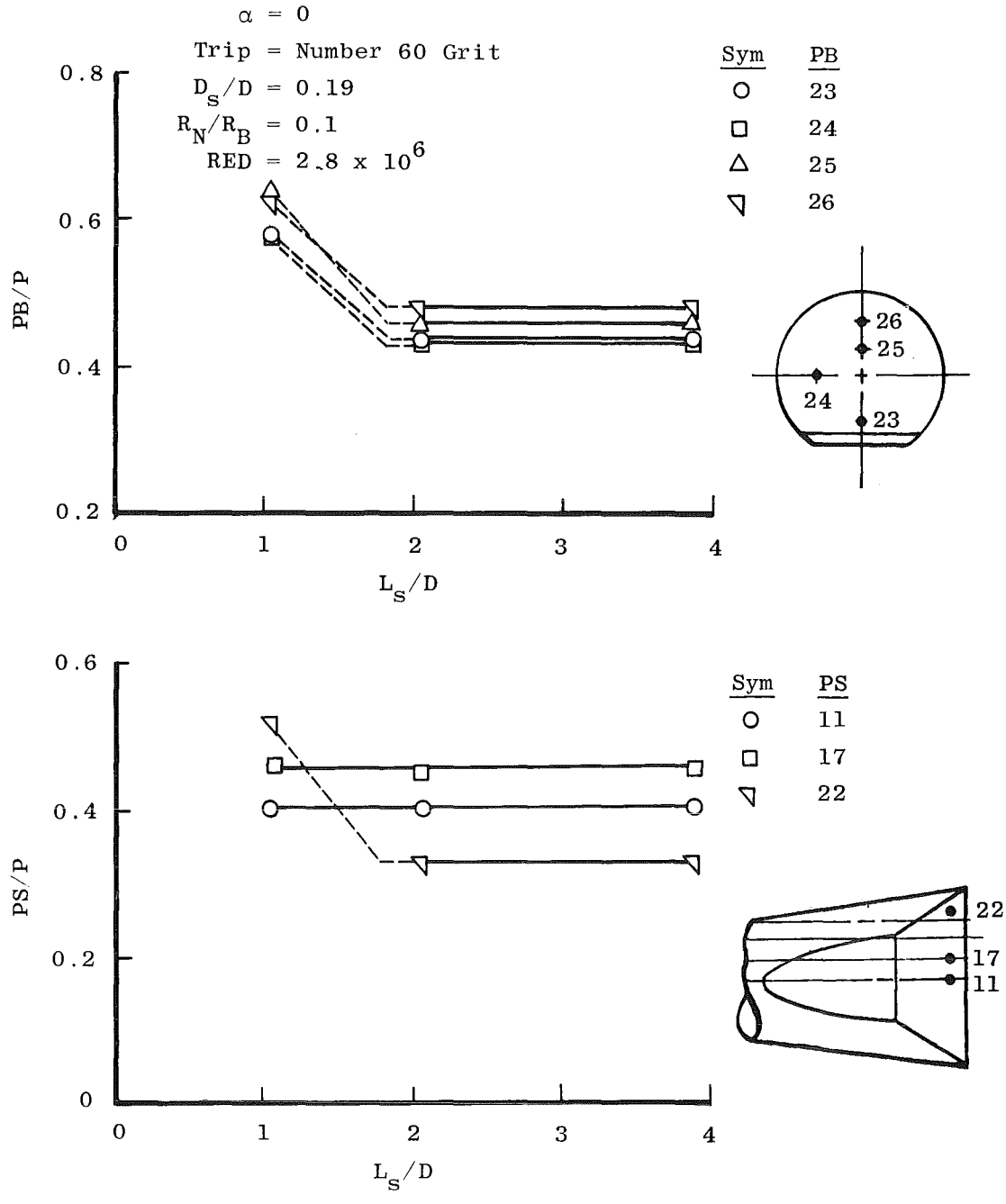

Figure 25. Base and surface pressure as a function of effective sting length, turbulent boundary layer, M = 2.

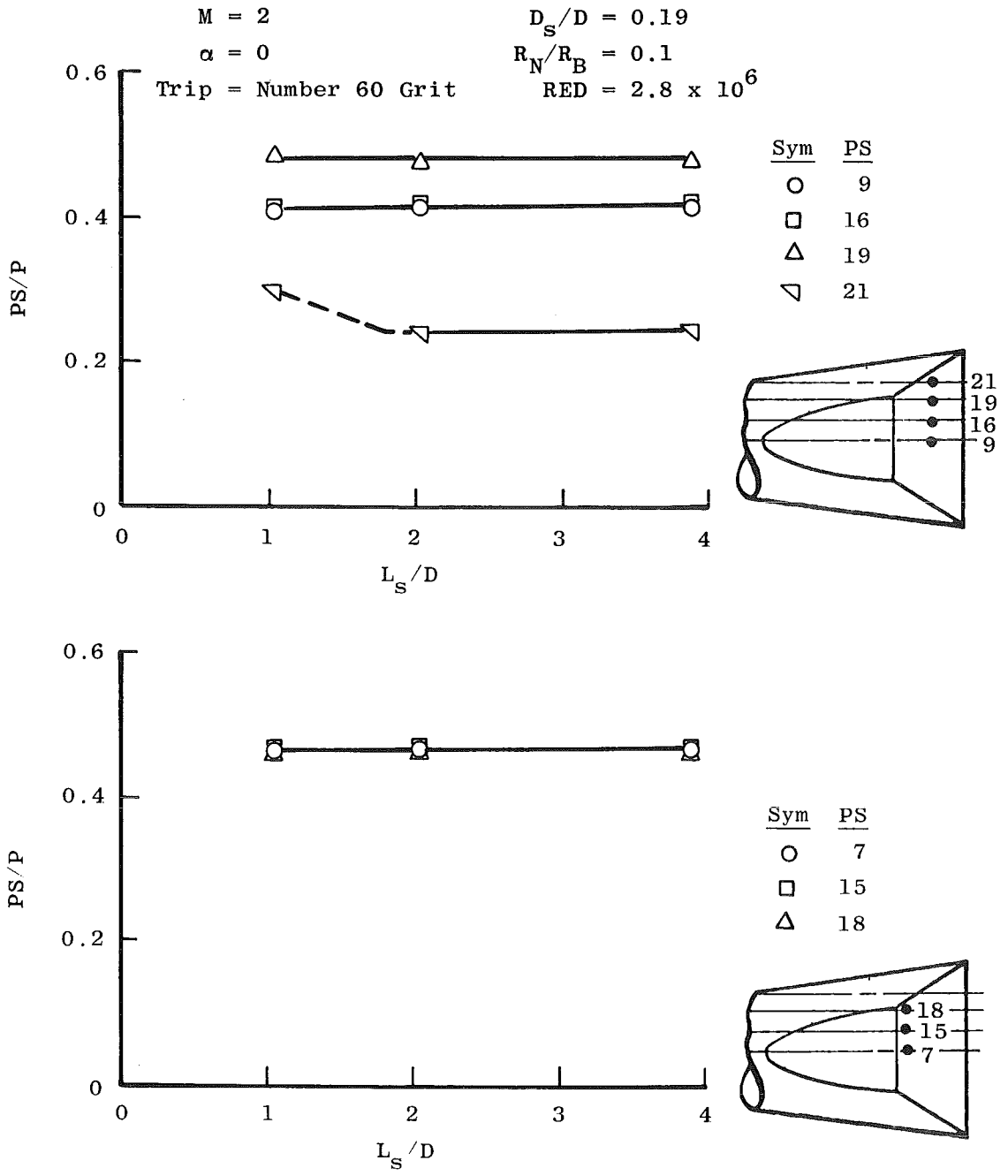

Figure 25. Concluded.

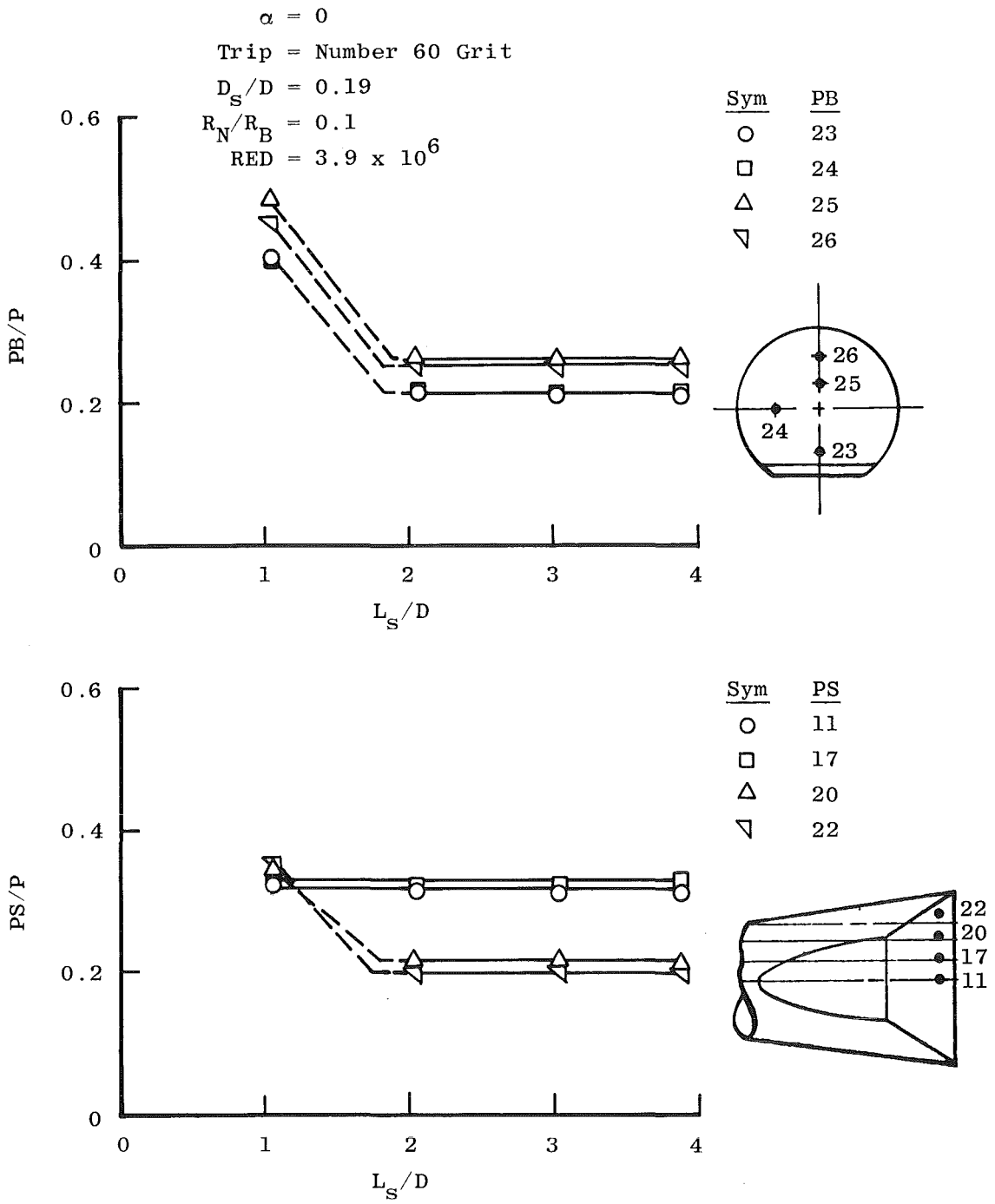

Figure 26. Base and surface pressure as a function of effective sting length, turbulent boundary layer, M = 3.

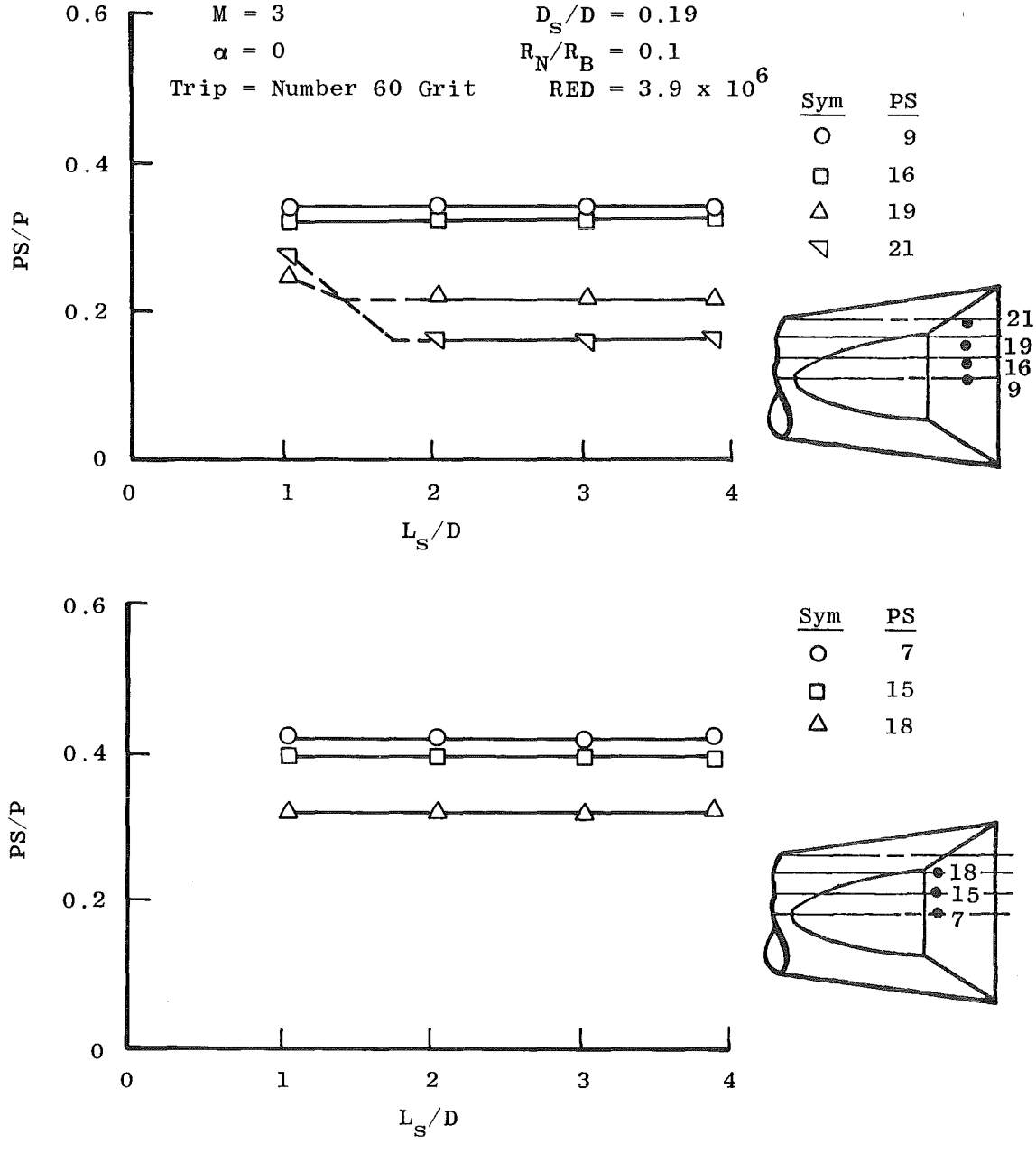

Figure 26. Concluded.

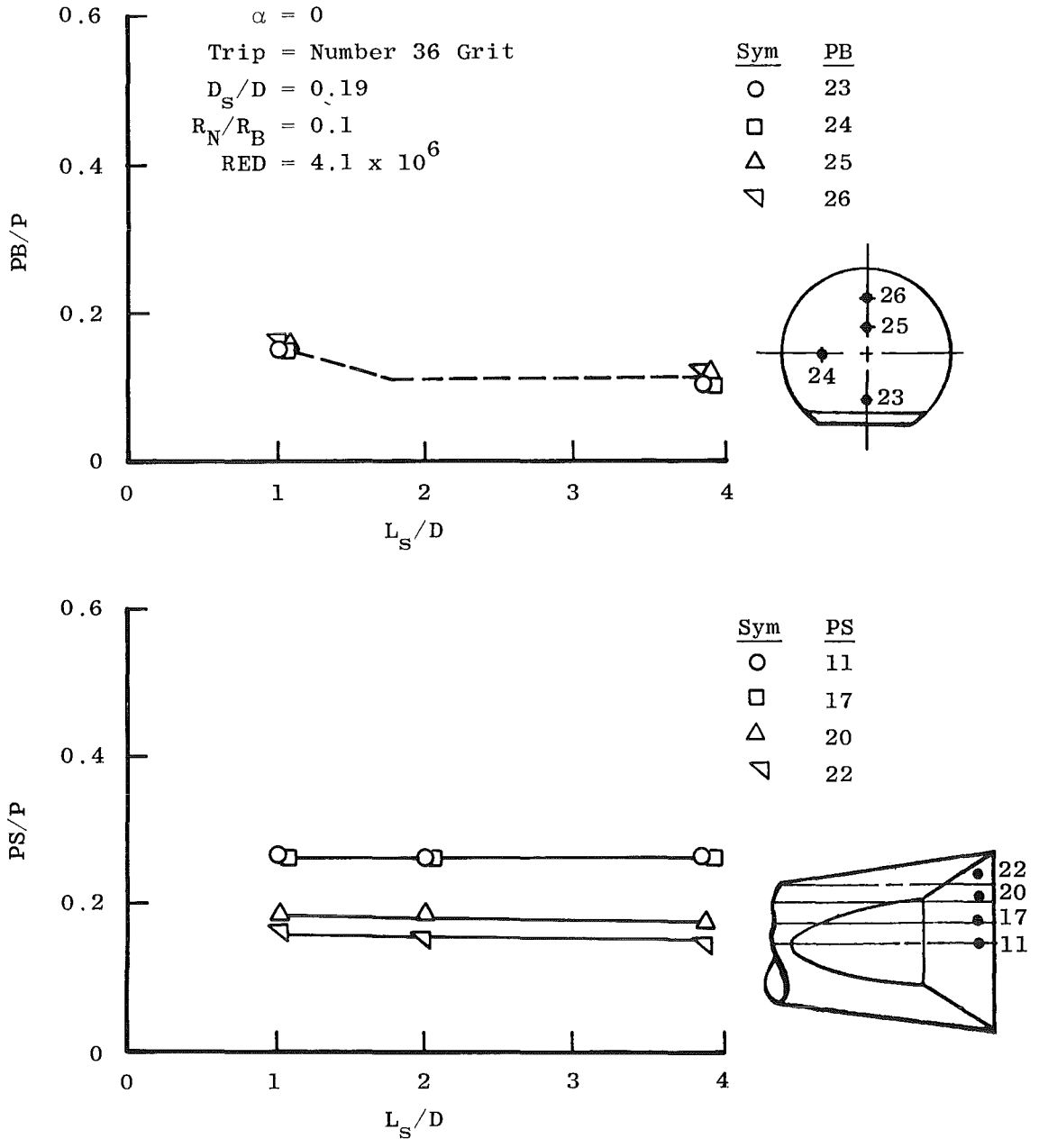

Figure 27. Base and surface pressure as a function of effective sting length, turbulent boundary layer, M = 5.

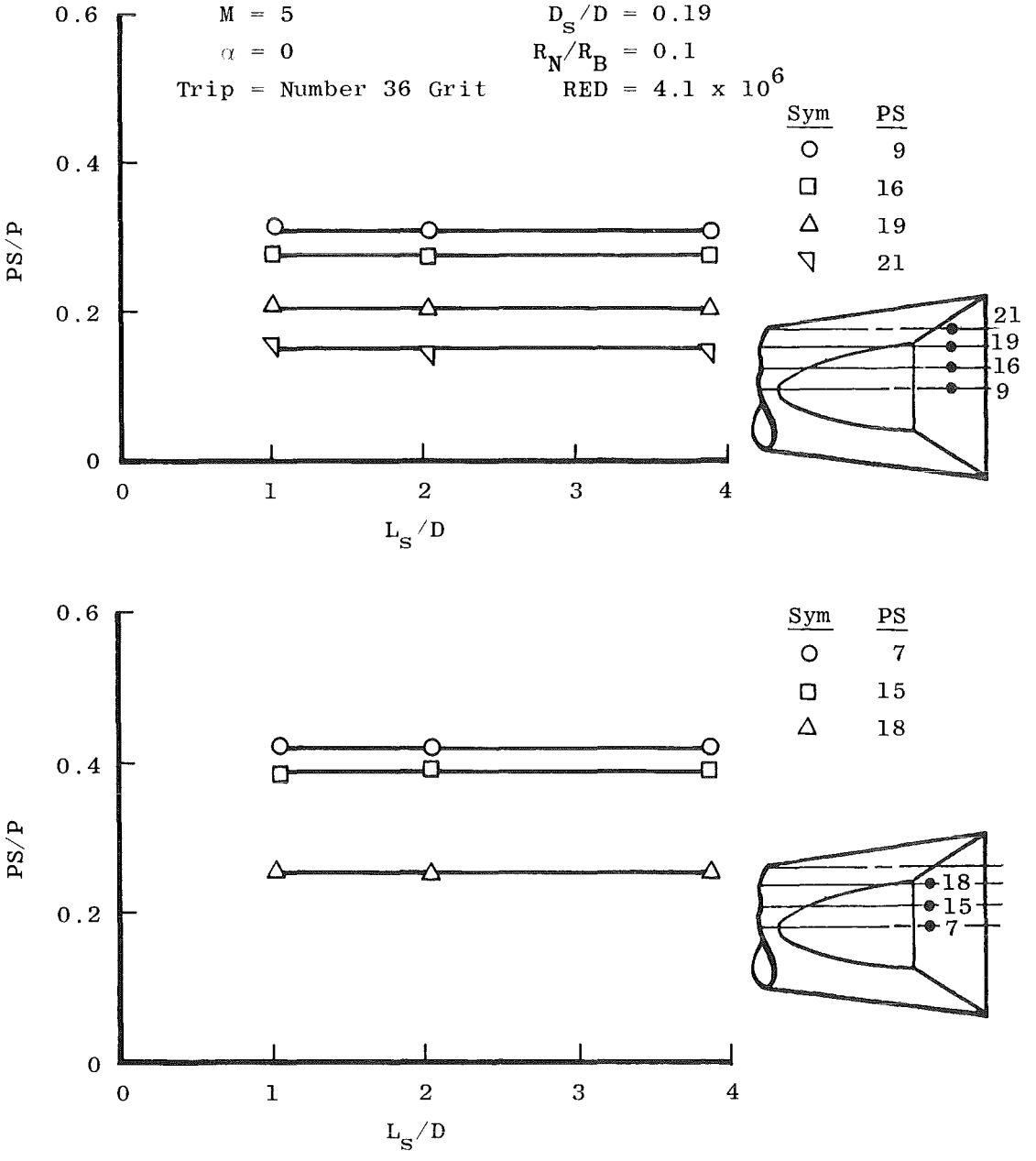

Figure 27. Concluded.

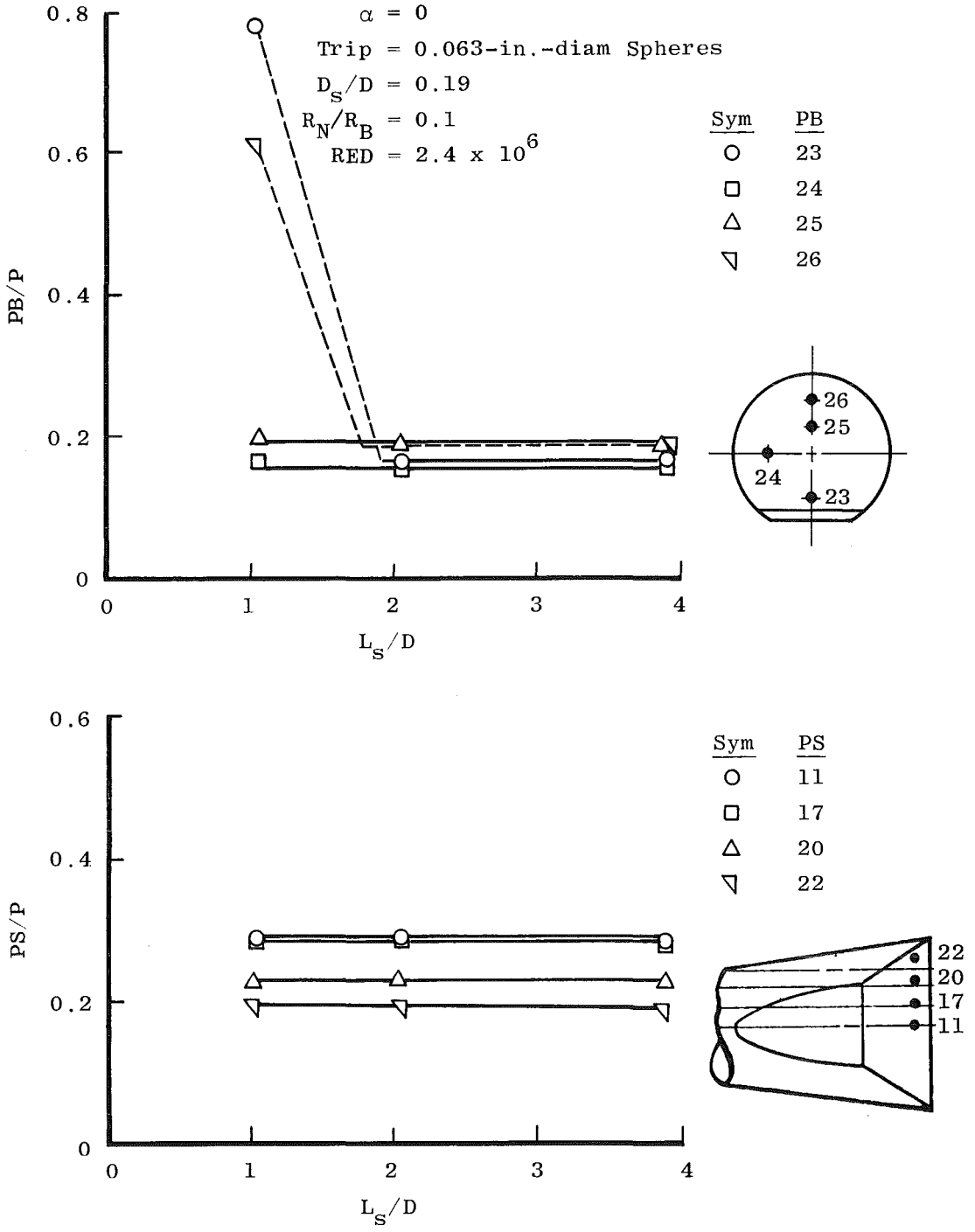

Figure 28. Base and surface pressure as a function of effective sting length, turbulent boundary layer, M = 8.

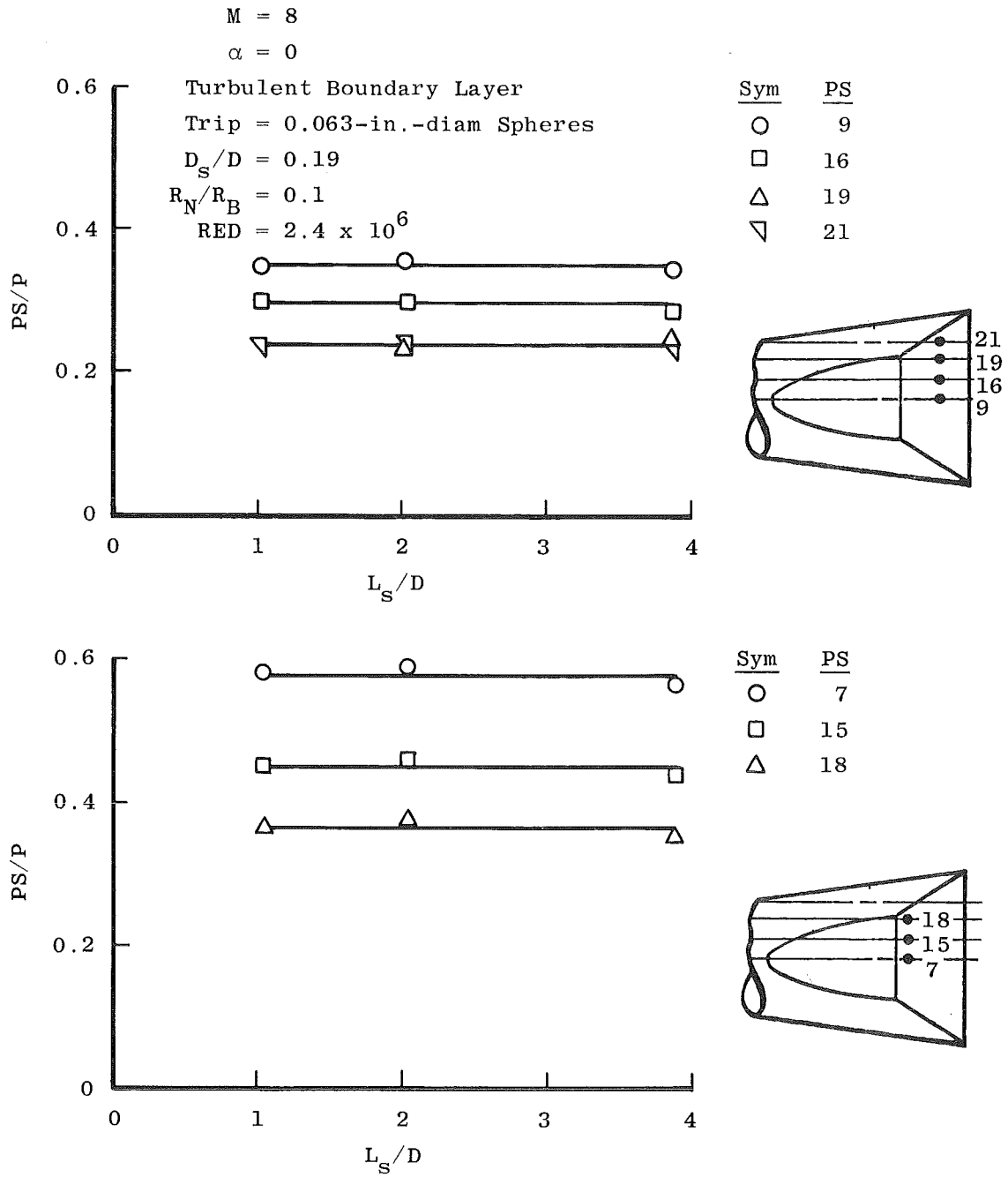

Figure 28. Concluded.

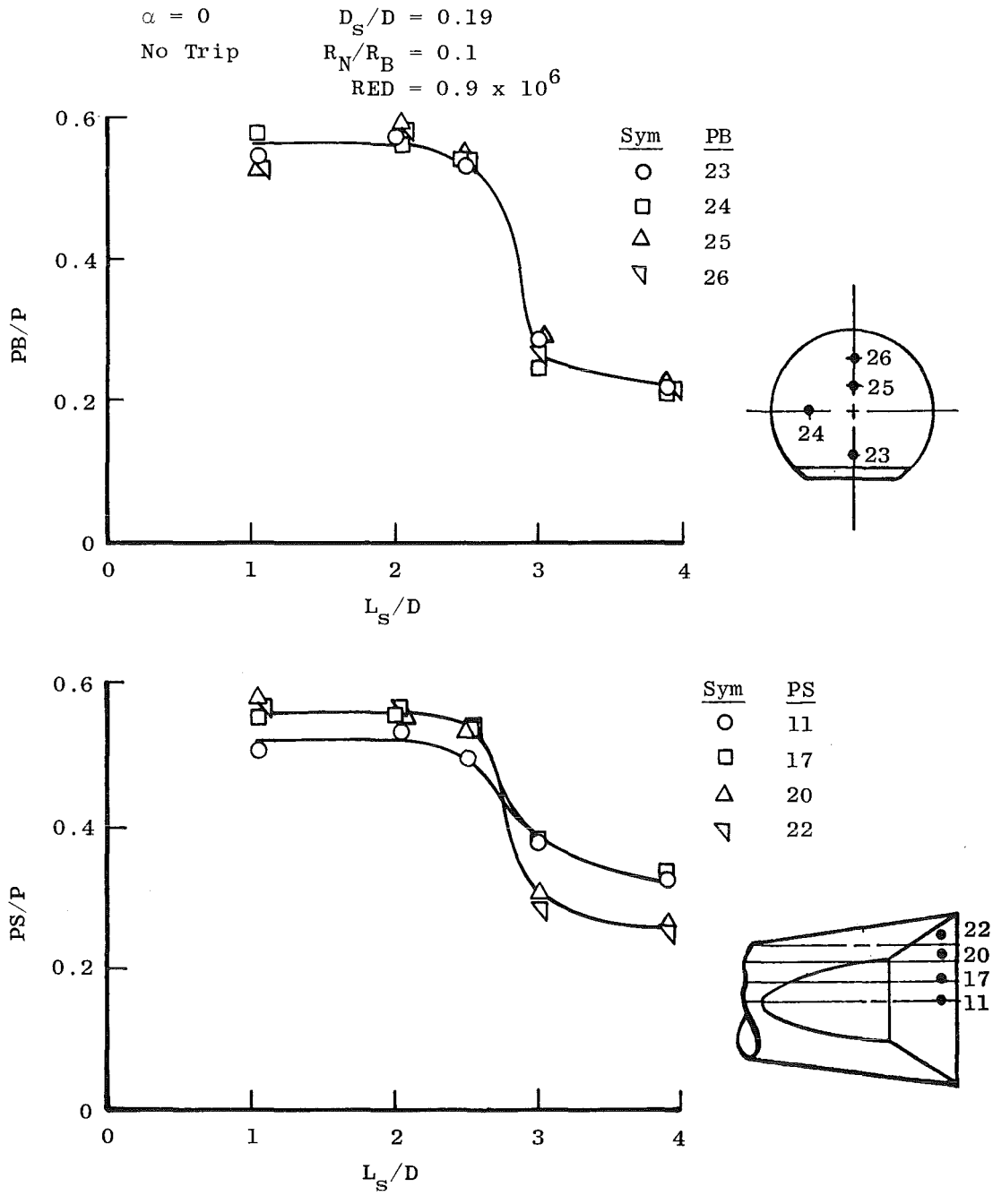

Figure 29. Base and surface pressure as a function of effective sting length, laminar boundary layer, M = 8.

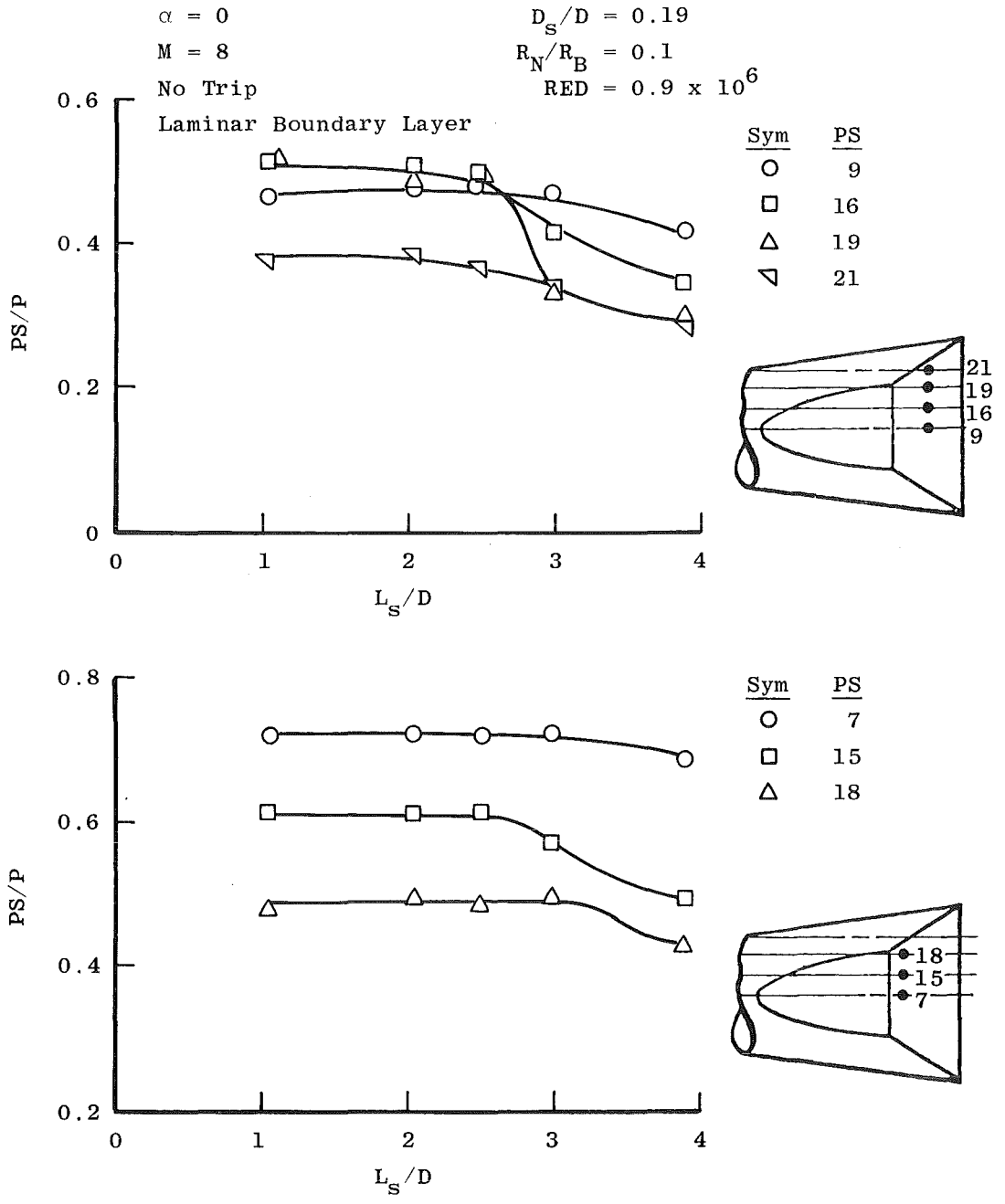

Figure 29. Concluded.

Sym	Boundary Layer at Model Base	
○	Laminar	$\alpha = 0$
□	Transitional	
△	Turbulent	

Unflagged Symbols: 6-deg Cone with Sliced Base, $D_s/D = 0.19$, $R_N/R_B = 0.1$ (Present Pressure Test)

Flagged Symbols: 7-deg Cone, $D_s/D = 0.22$, $R_N/R_B = 0.15$ (Present Pitch-Damping Test and Ref. 1 Test)

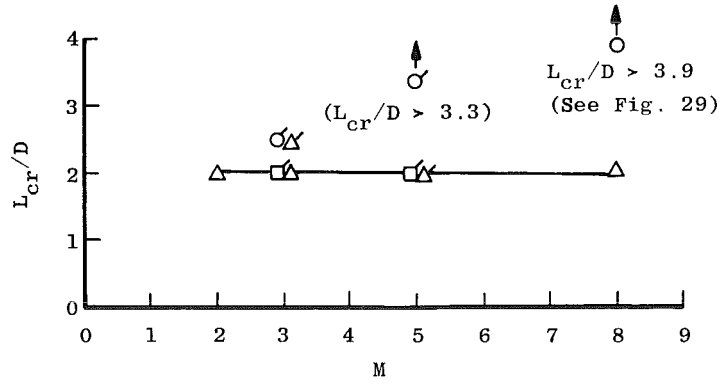

a. Determined by base pressure measurements

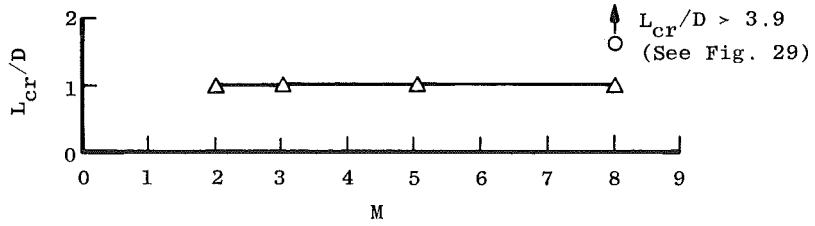

b. Determined by centerline pressure measurements

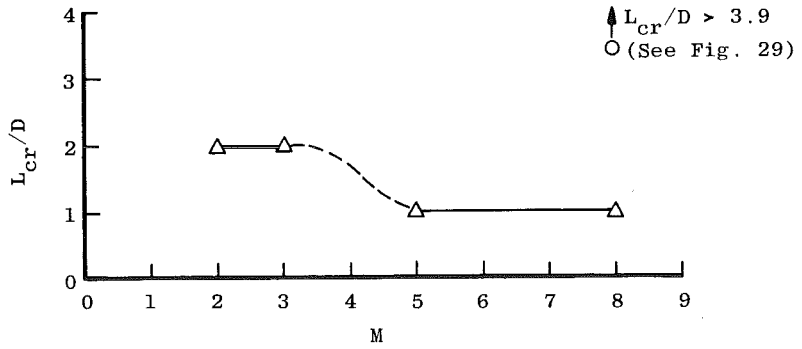

c. Determined by corner pressure measurements

Figure 30. Critical sting length defined by base and surface pressure measurements.

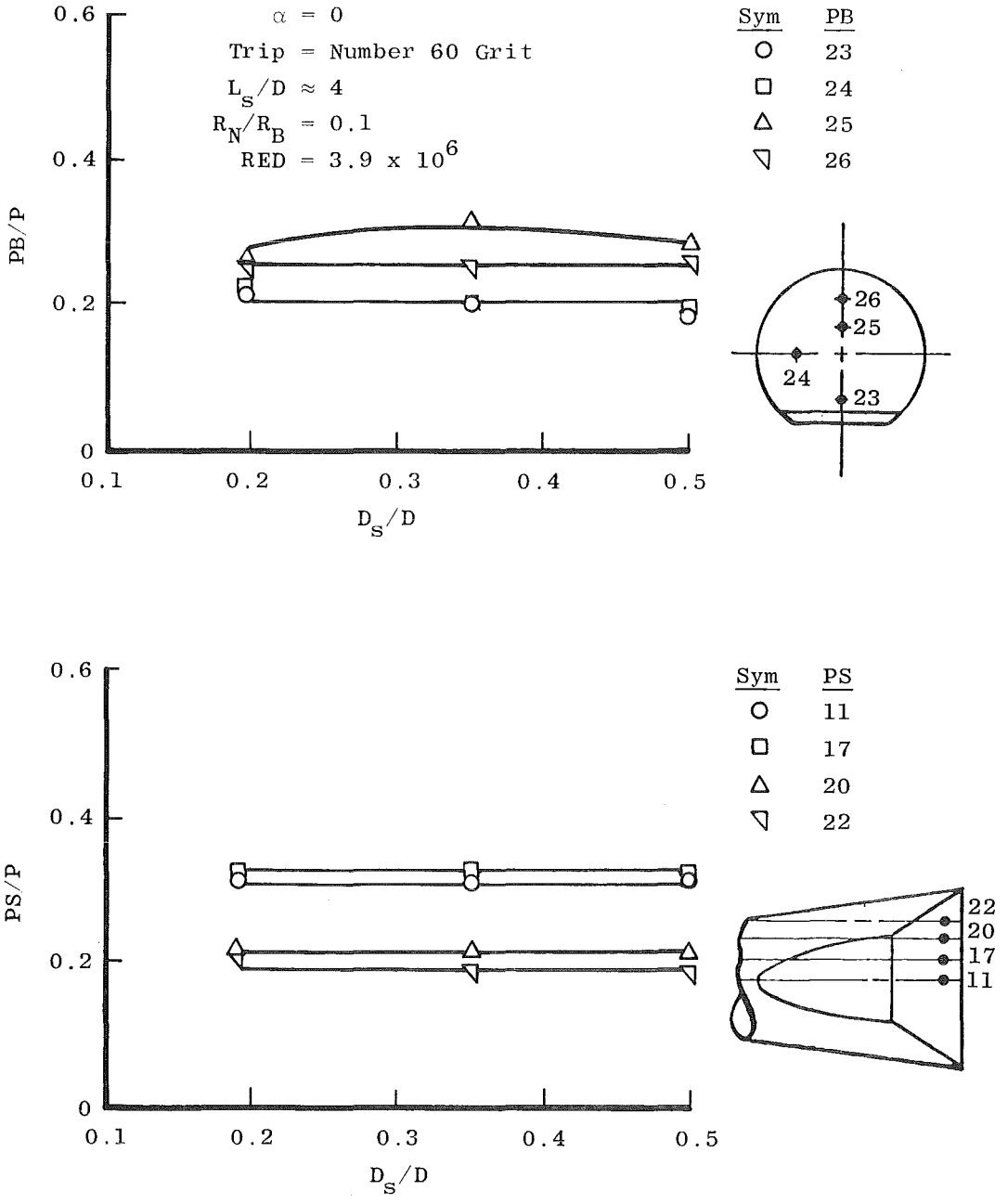

Figure 31. Base and surface pressure as a function of sting diameter, turbulent boundary layer, M = 3.

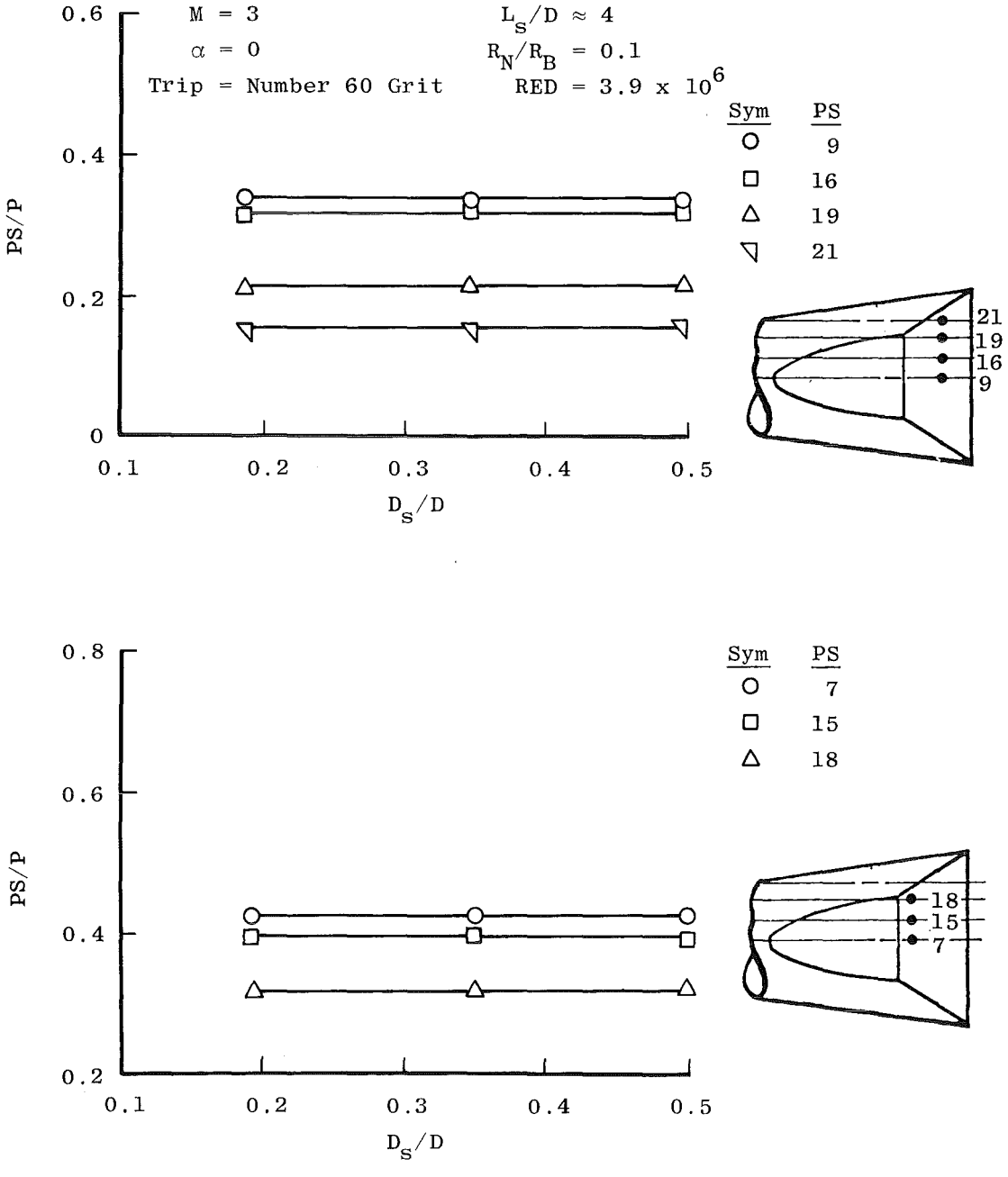

Figure 31. Concluded.

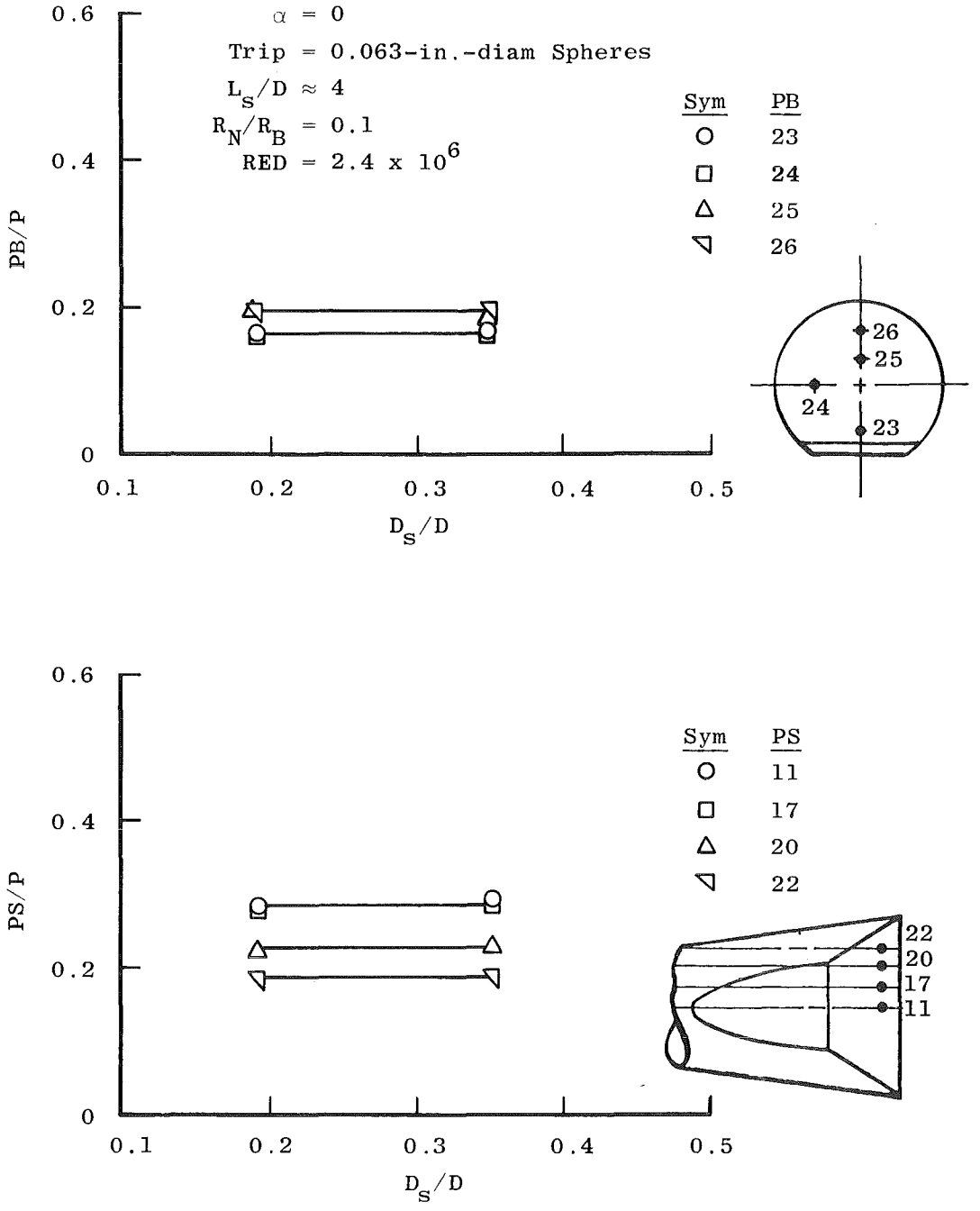

Figure 32. Base and surface pressure as a function of sting diameter, turbulent boundary layer, M = 8.

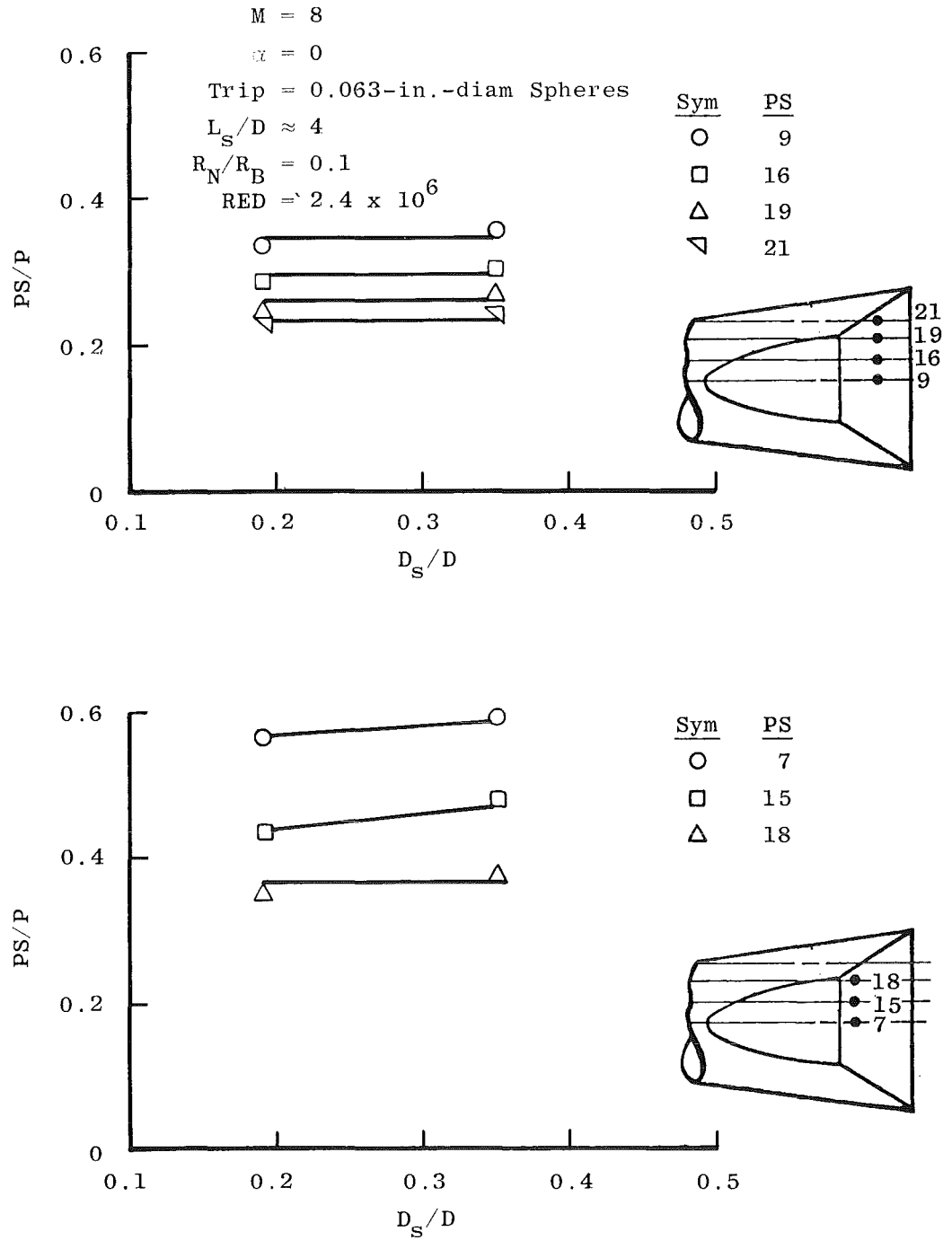

Figure 32. Concluded.

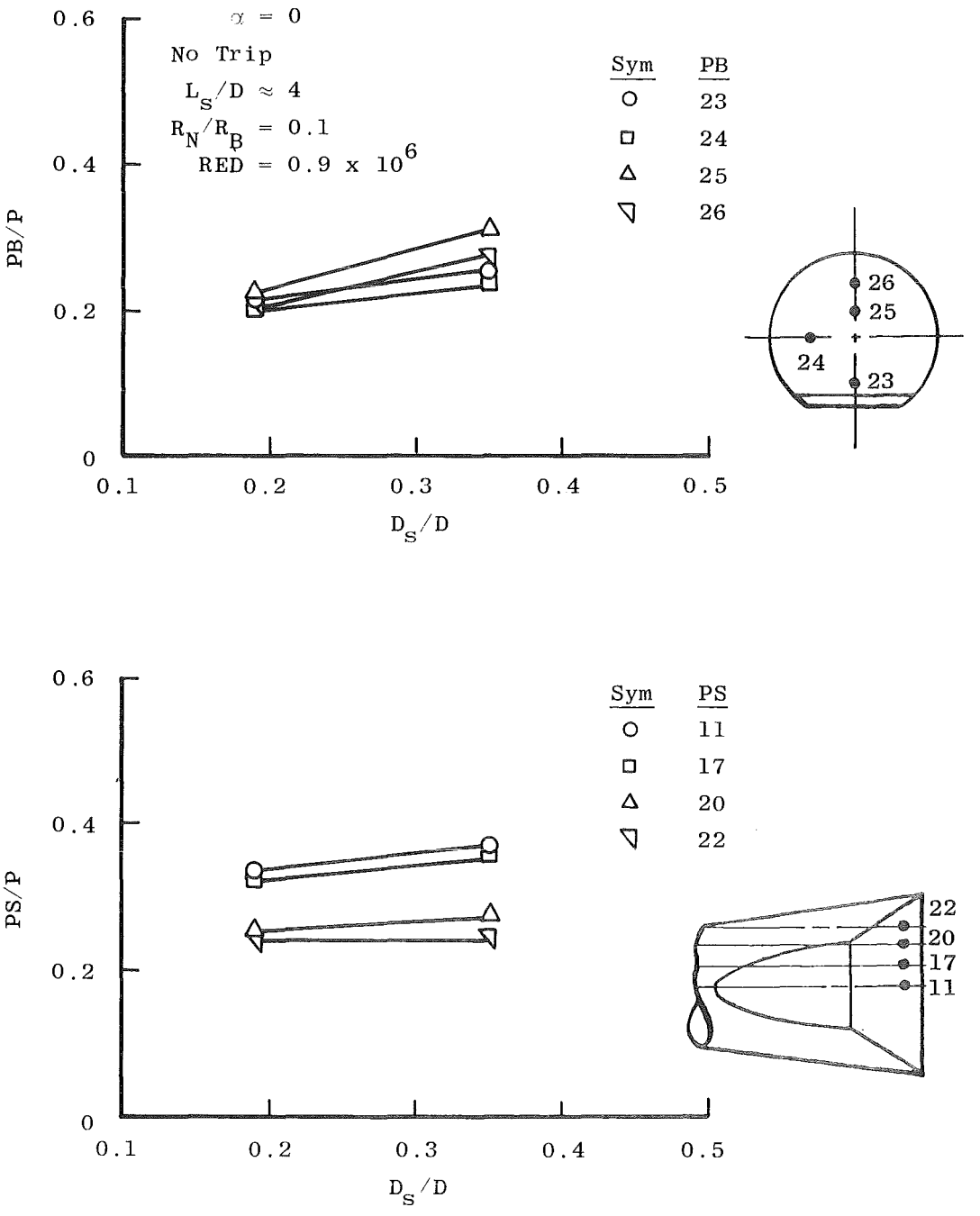

Figure 33. Base and surface pressure as a function of sting diameter, laminar boundary layer, M = 8.

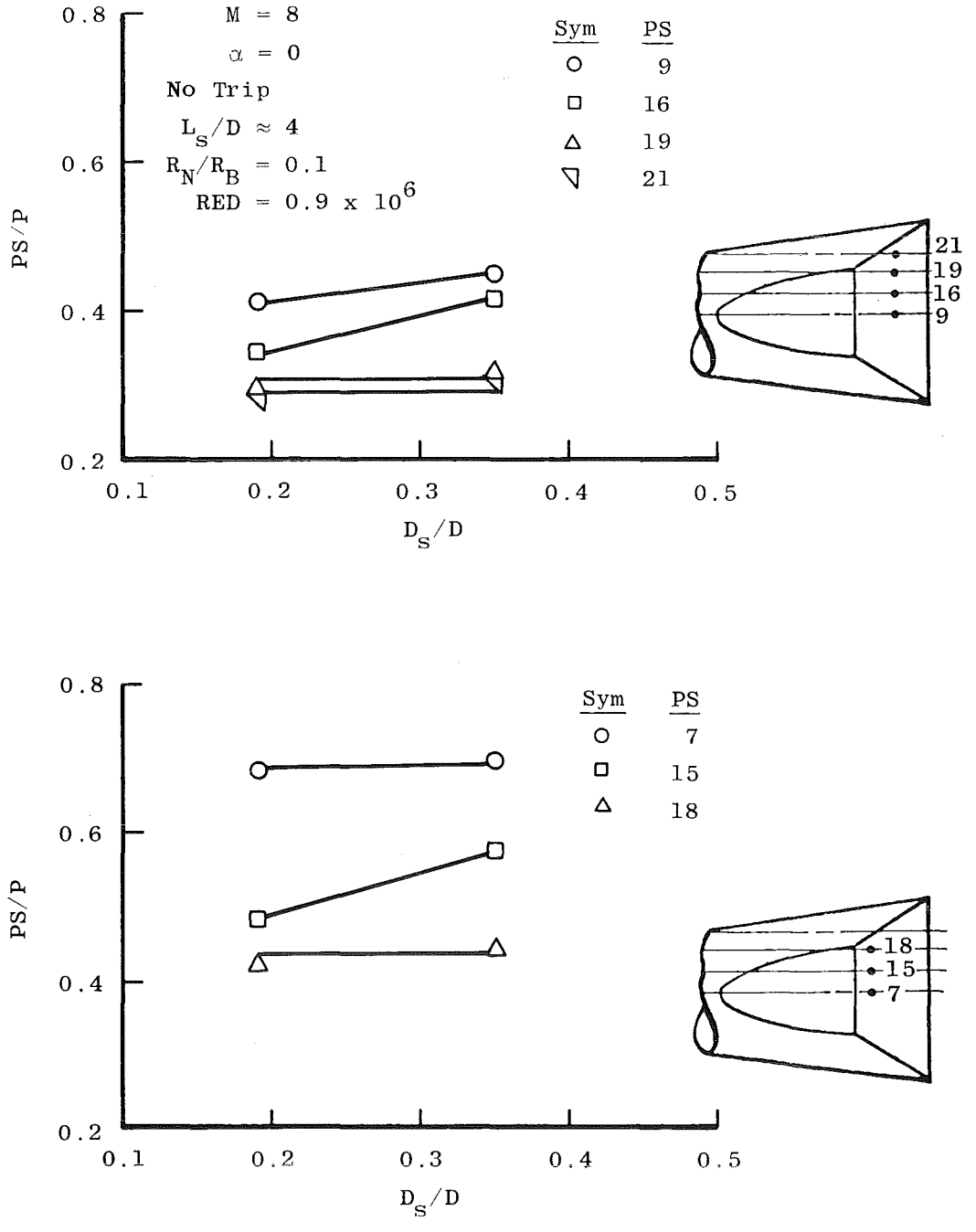

Figure 33. Concluded.

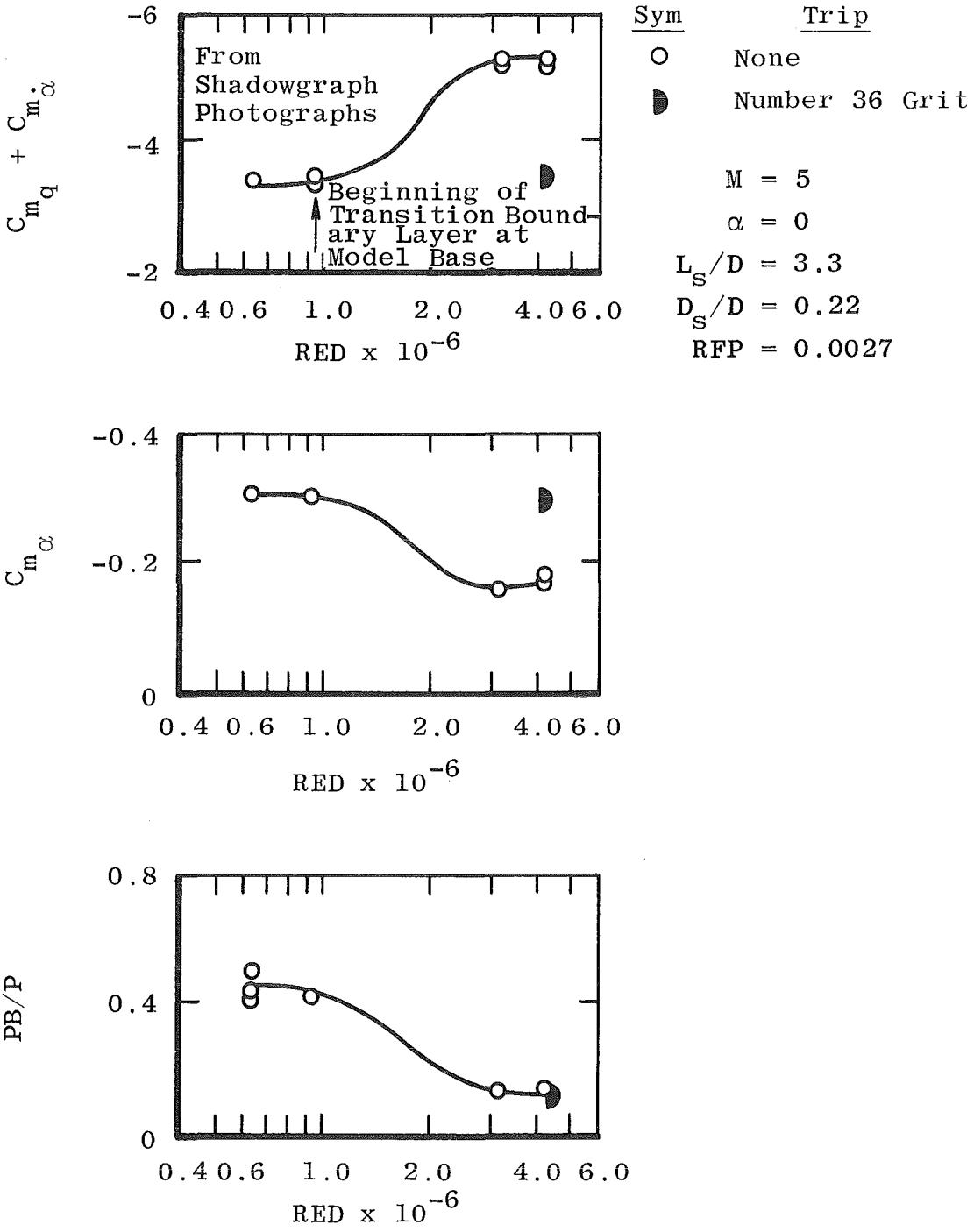

Figure 34. Boundary-layer trip effects at M = 5.

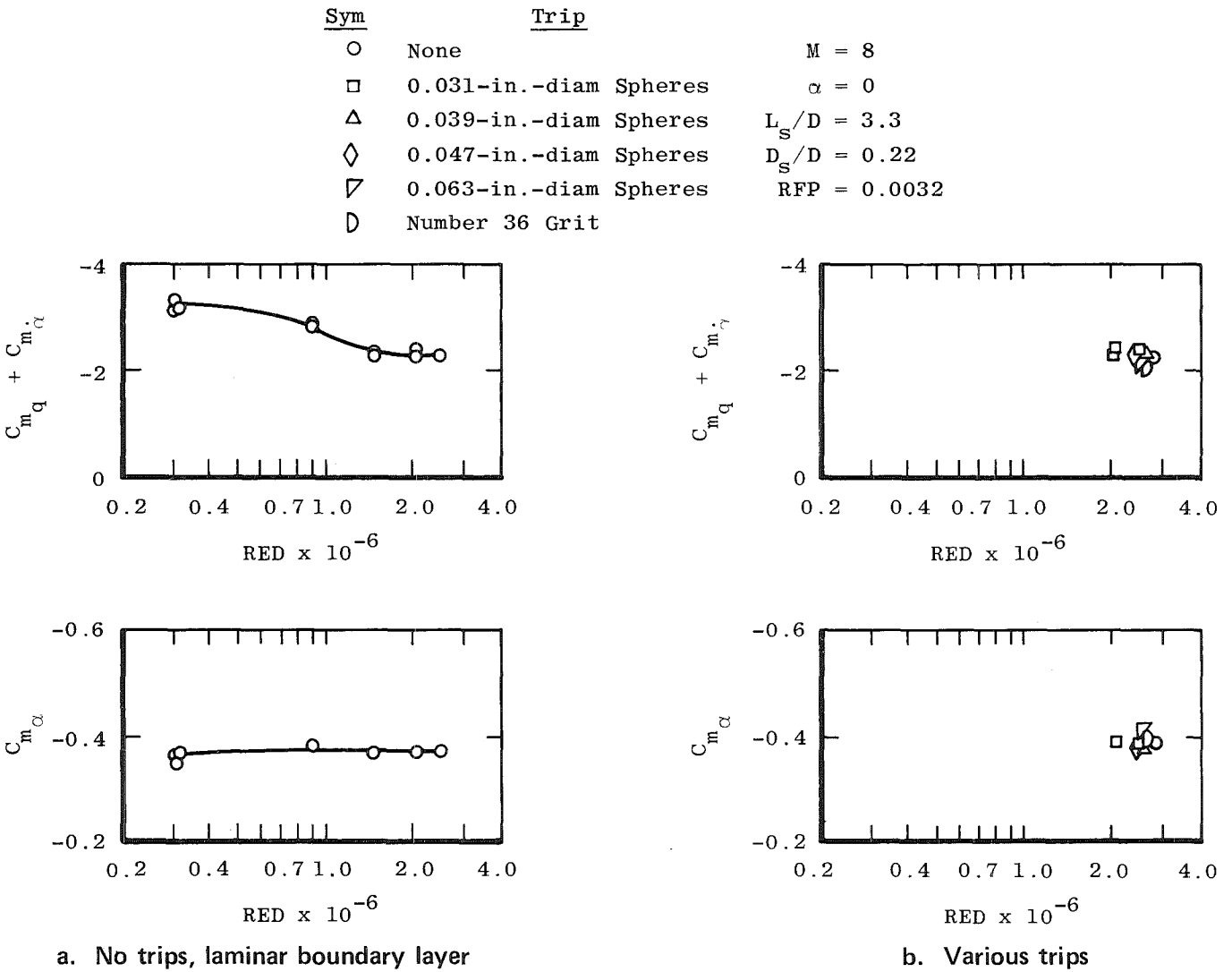

a. No trips, laminar boundary layer

b. Various trips

Figure 35. Boundary-layer trip effects at M = 8.

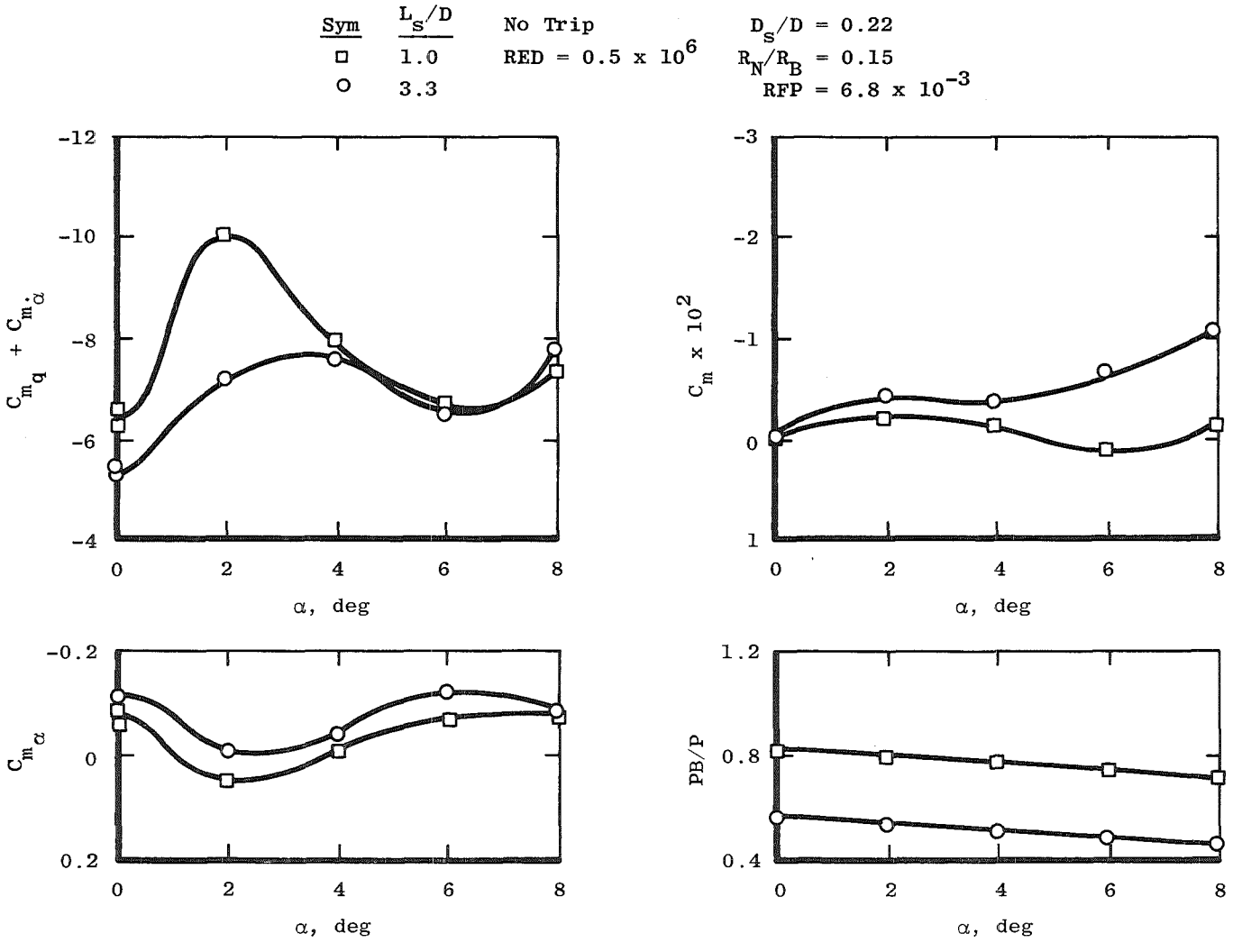

a. Laminar boundary layer

Figure 36. Sting effects as a function of angle of attack, M = 2.

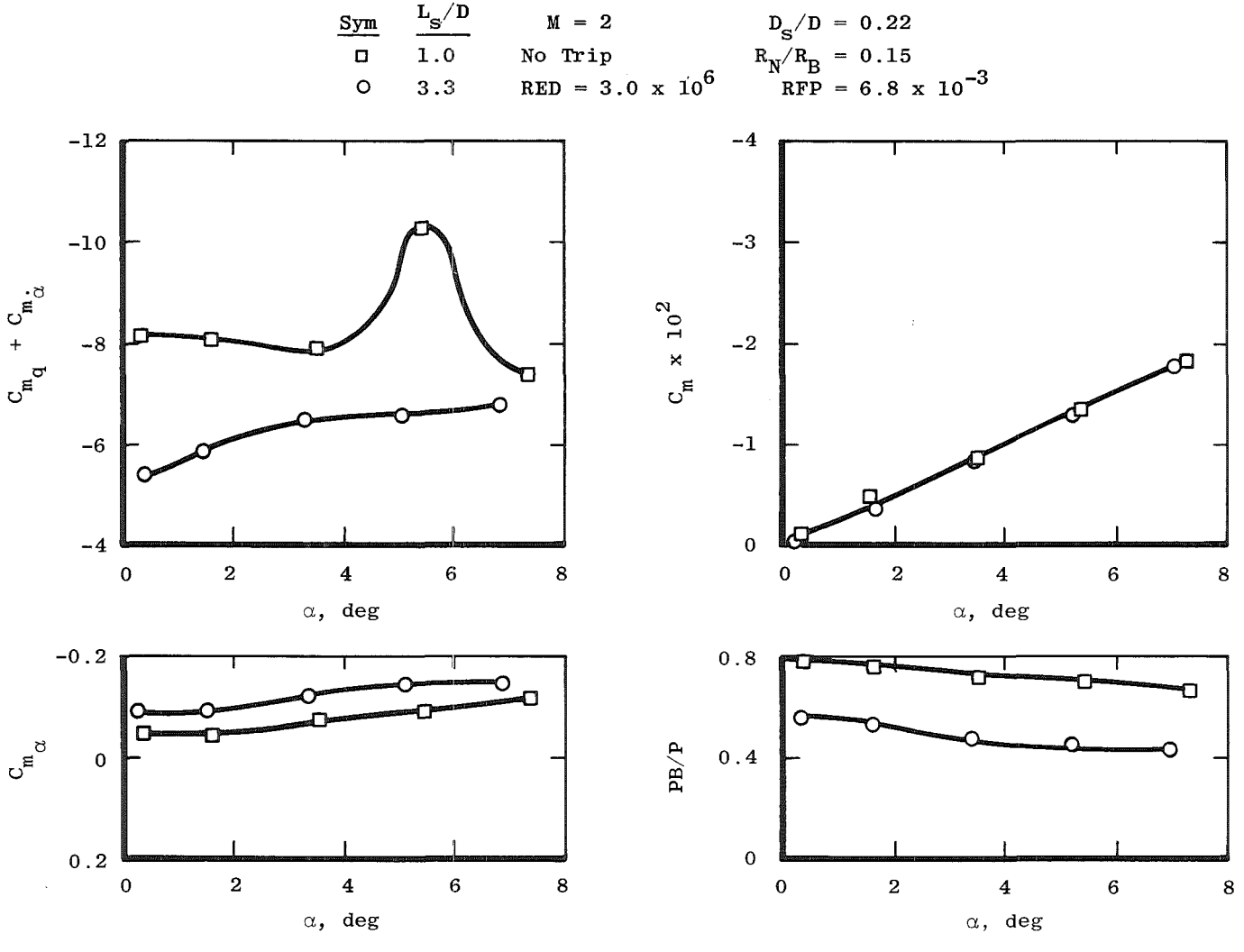

b. Turbulent boundary layer

Figure 36. Concluded.

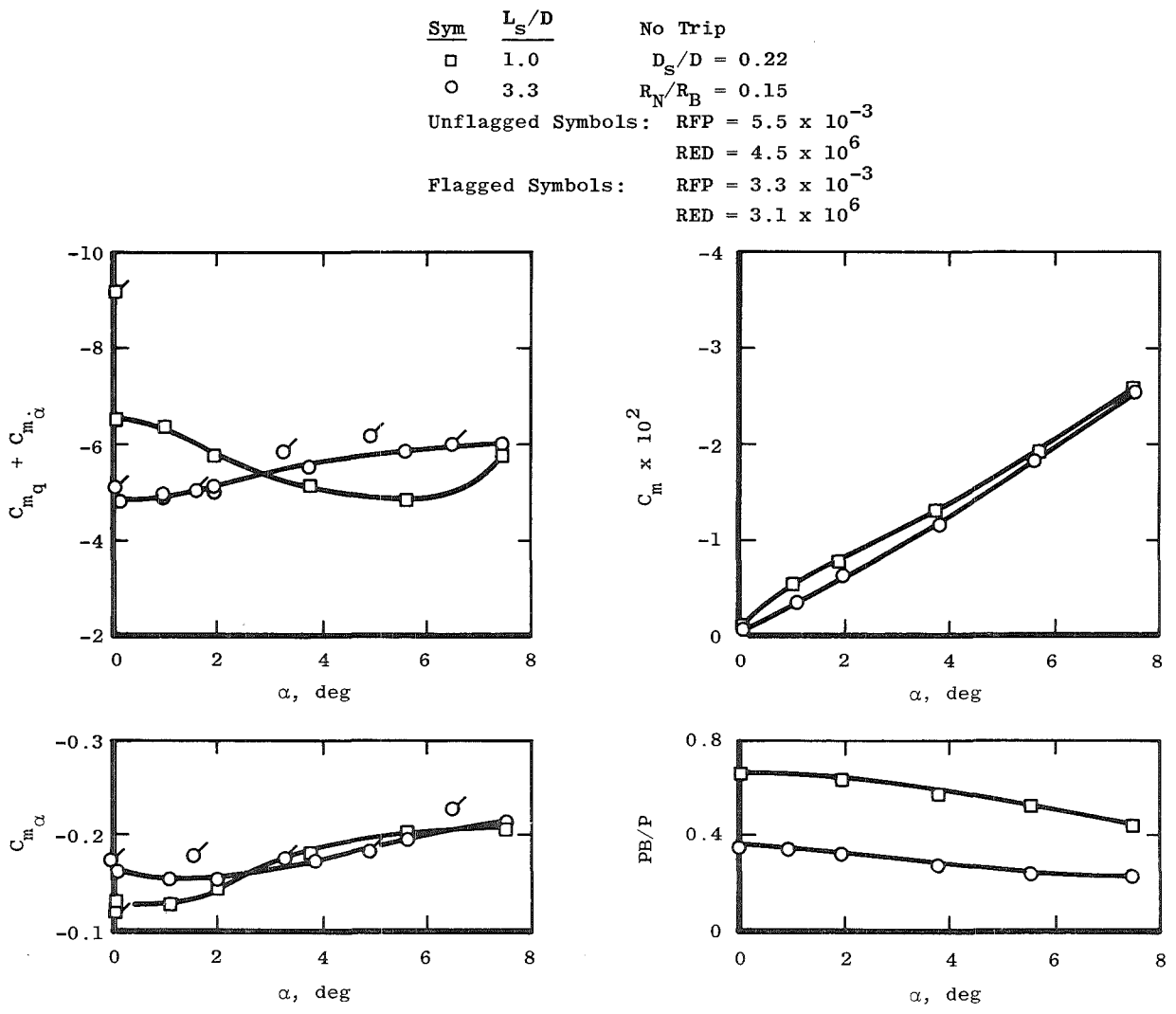

Figure 37. Sting effects as a function of angle of attack, M = 3, turbulent boundary layer.

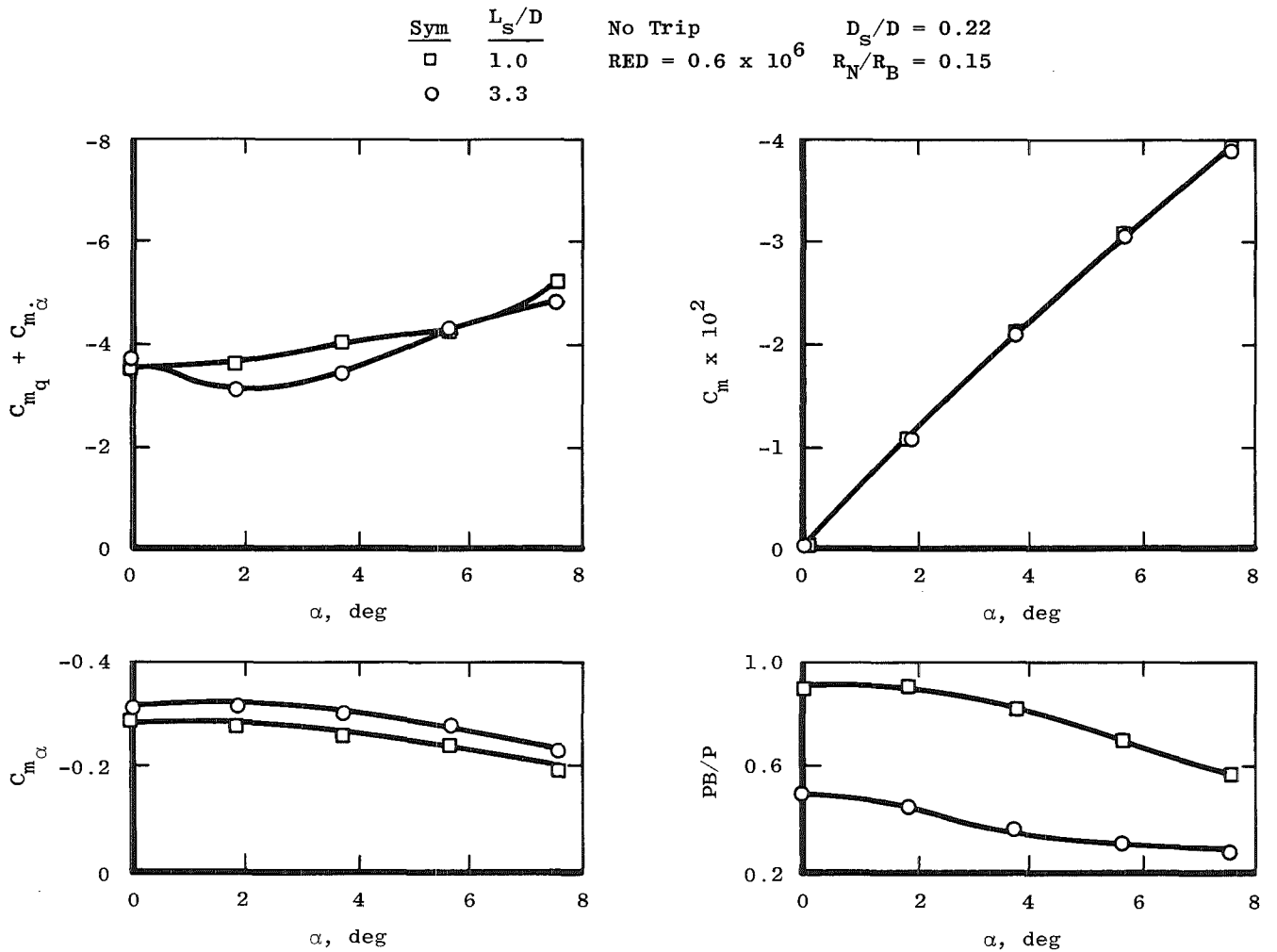

a. Laminar boundary layer

Figure 38. Sting effects as a function of angle of attack, M = 5, RFP = 0.0027.

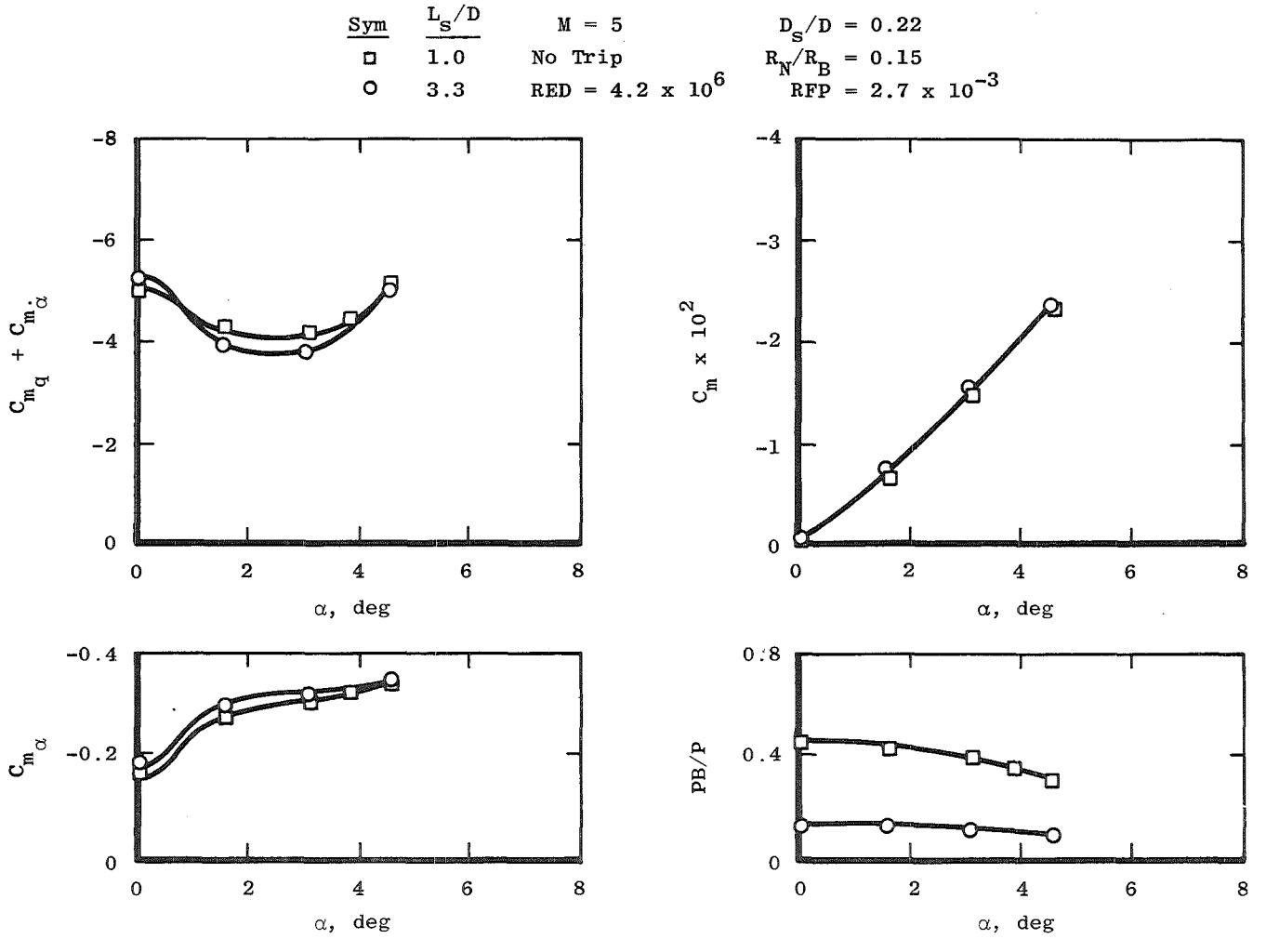

b. Transitional boundary layer
Figure 38. Continued.

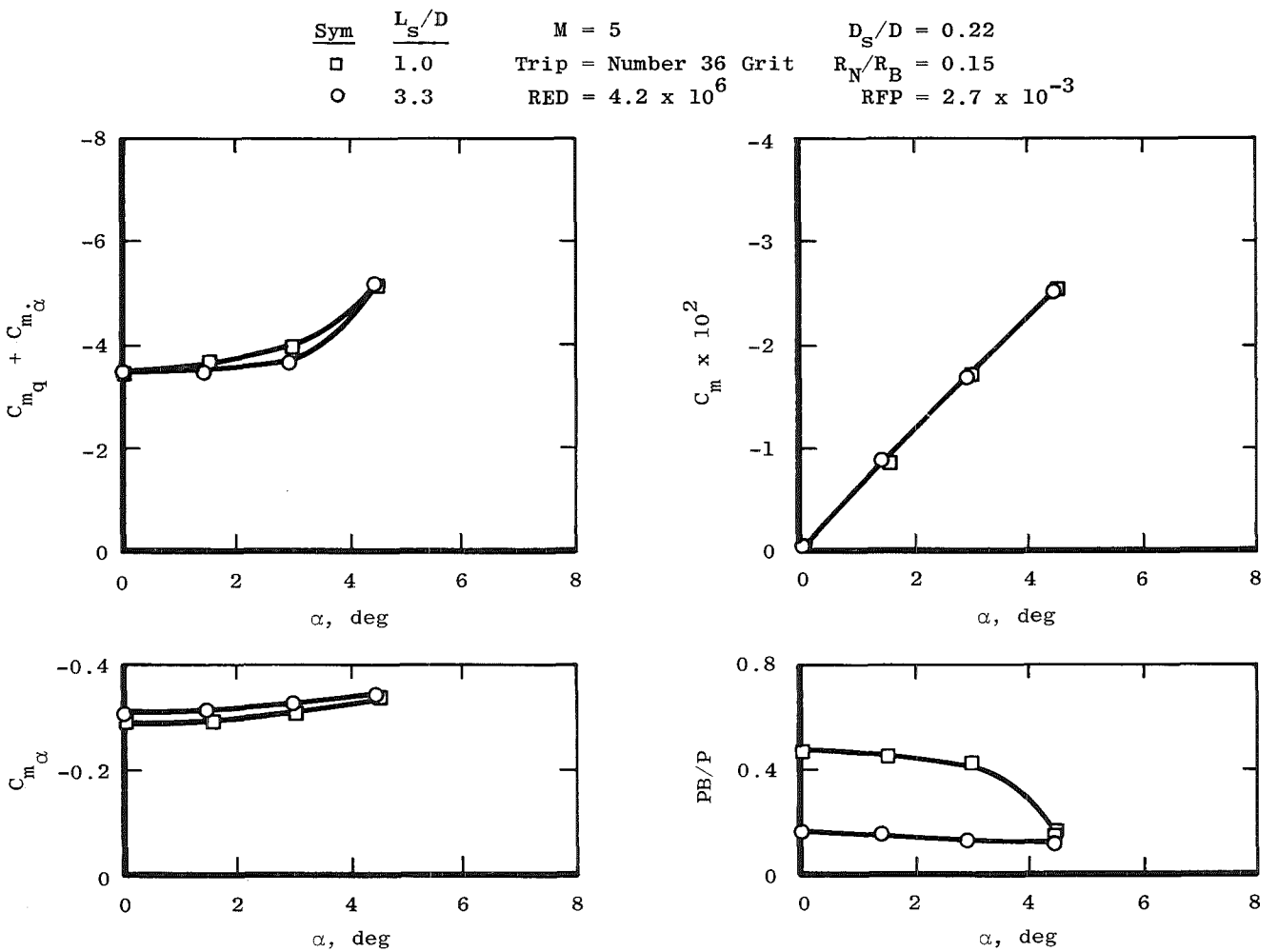

c. Turbulent boundary layer
Figure 38. Concluded.

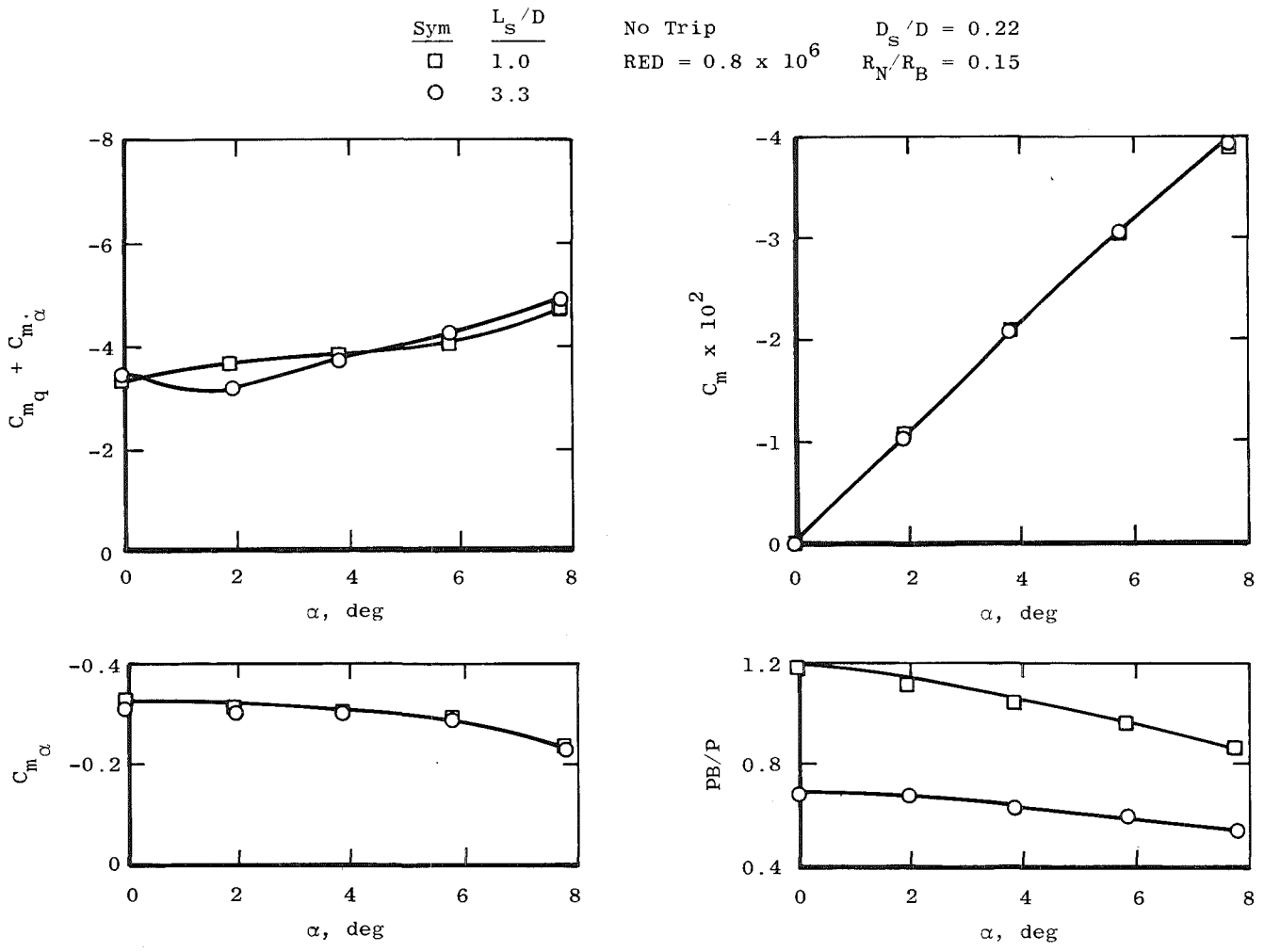

a. Laminar boundary layer

Figure 39. Sting effects as a function of angle of attack, M = 5, RFP = 0.0047.

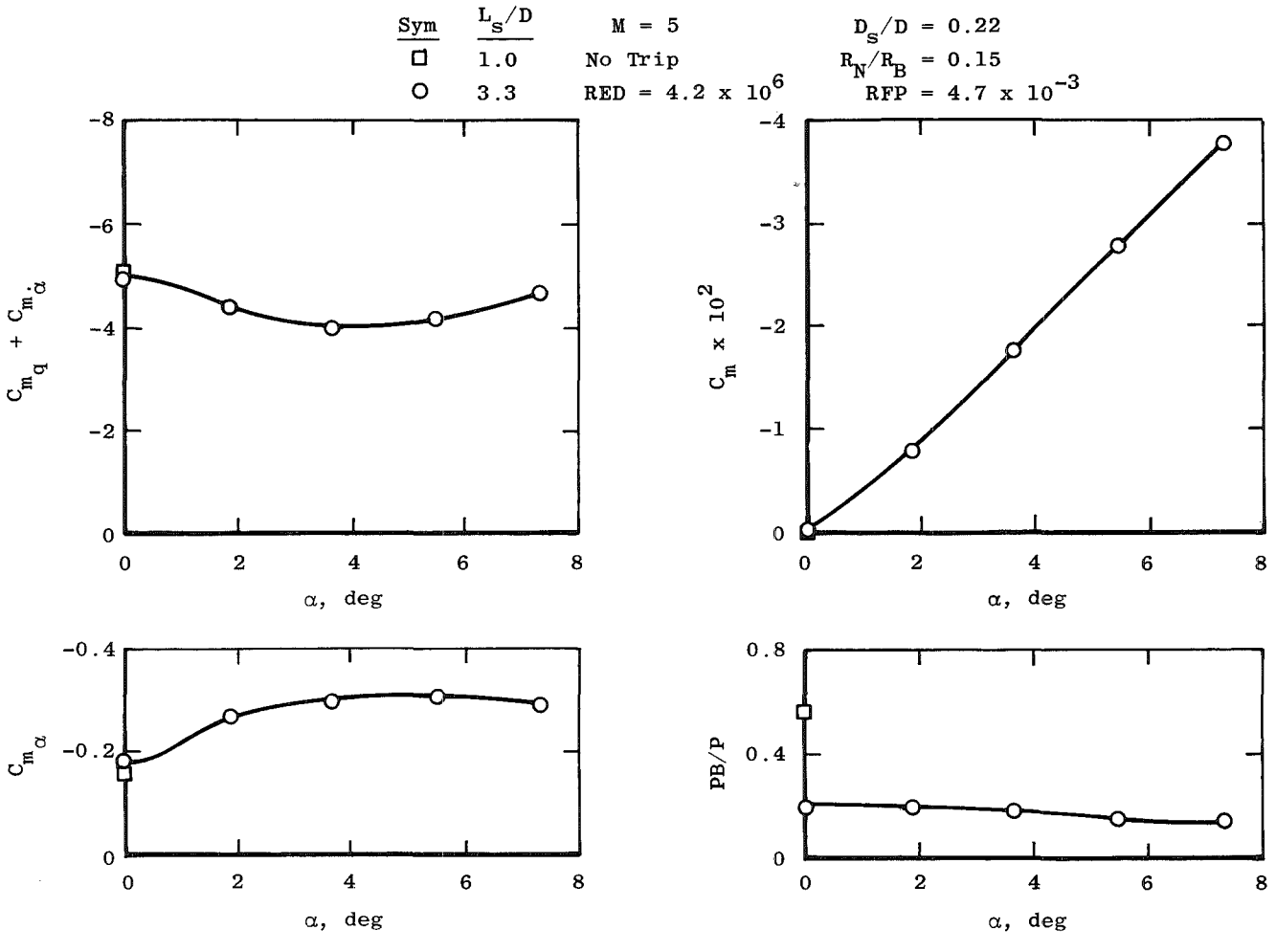

b. Transitional boundary layer
Figure 39. Continued.

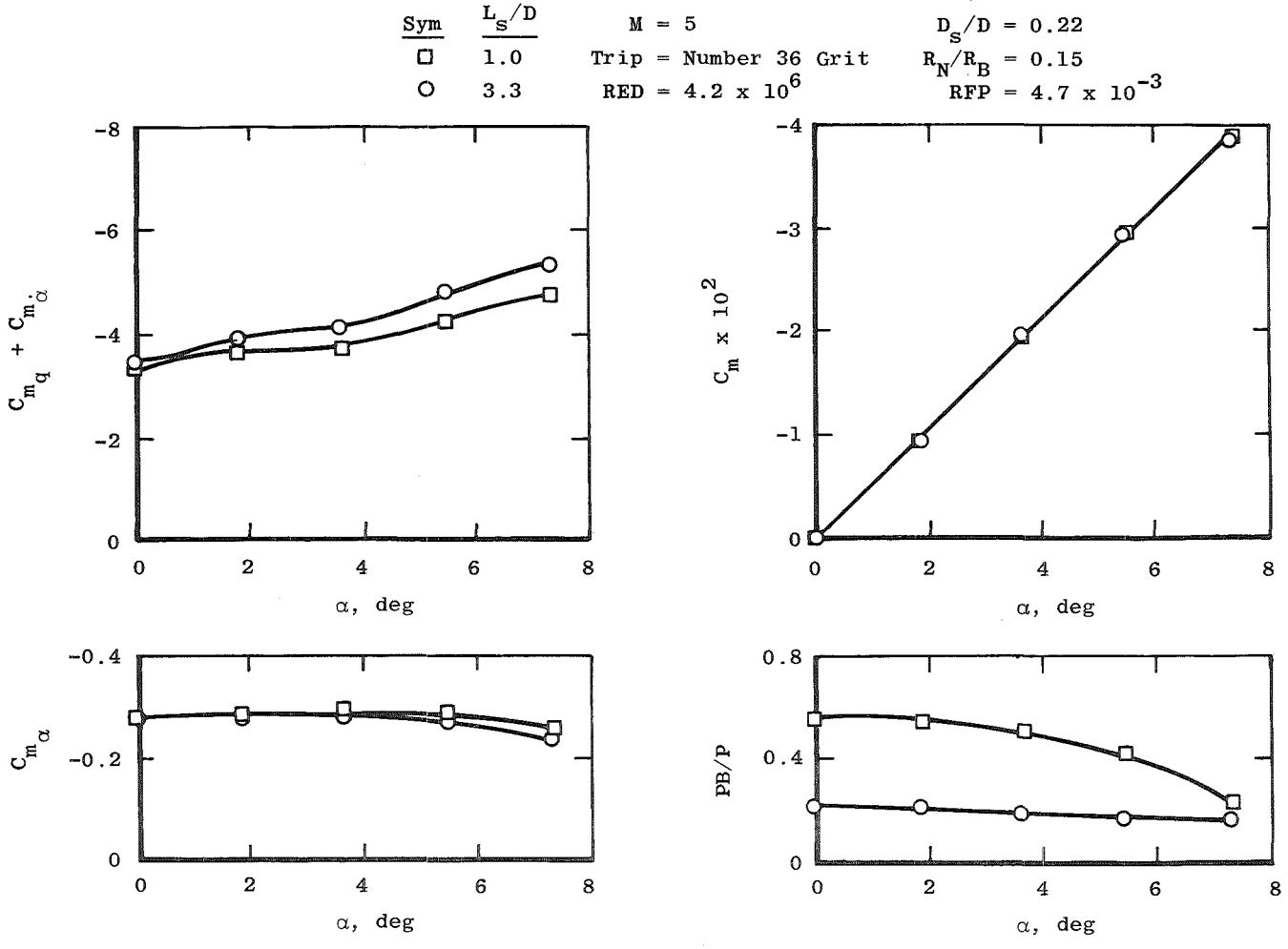

c. Turbulent boundary layer
Figure 39. Concluded.

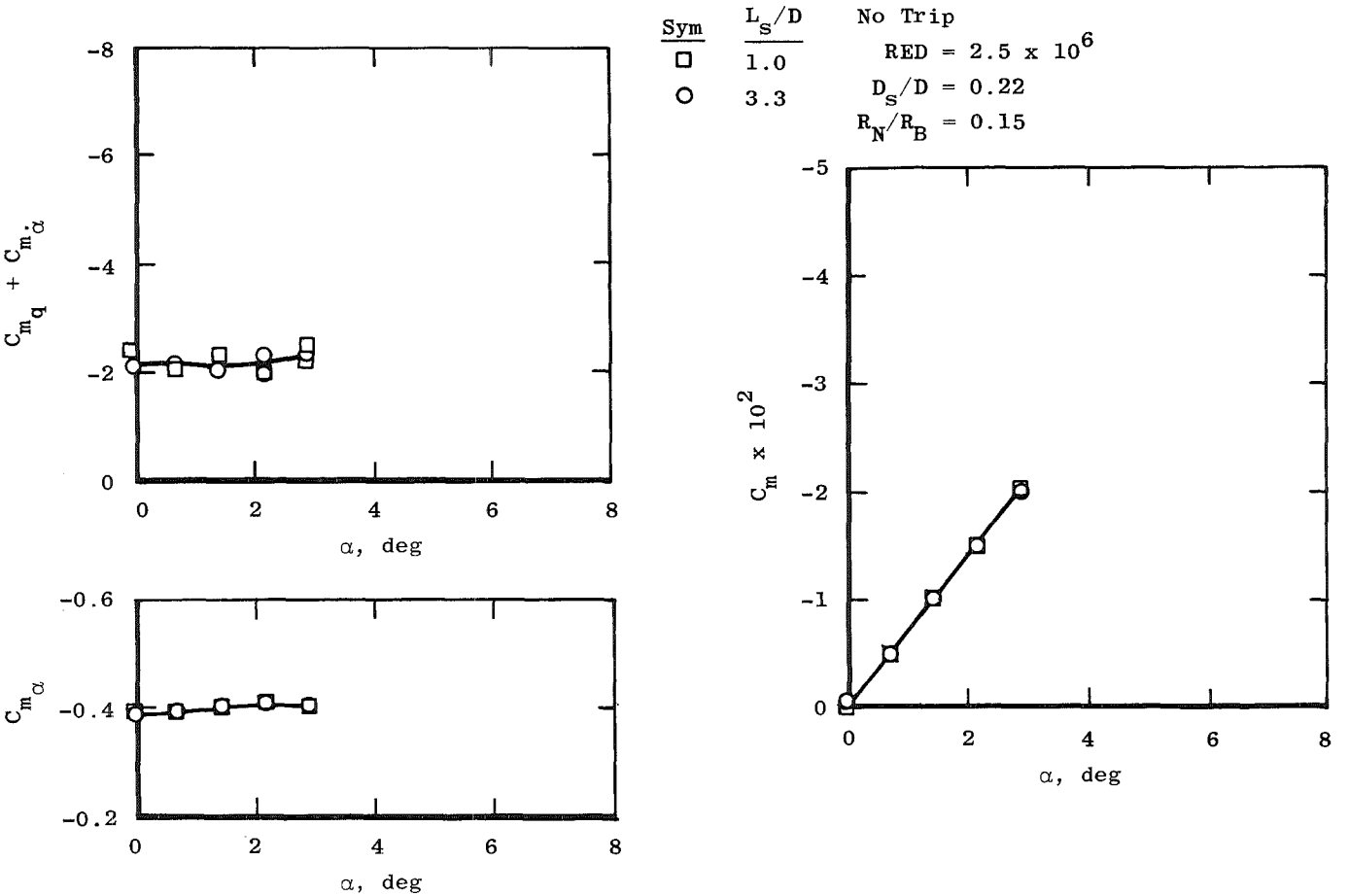

a. Laminar boundary layer

Figure 40. Sting effects as a function of angle of attack, M = 8, RFP = 0.0019.

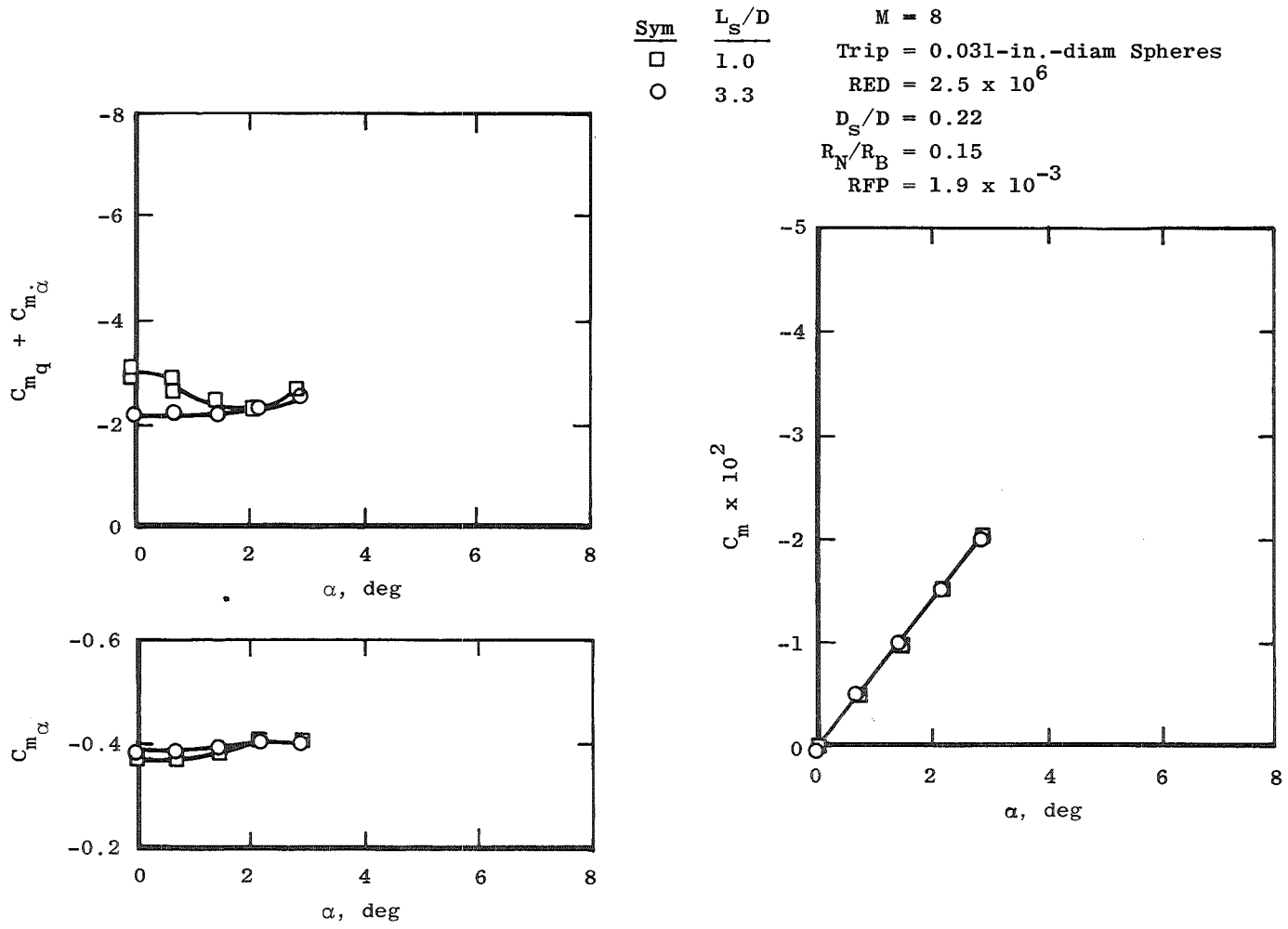

b. Trubulent boundary layer

Figure 40. Concluded.

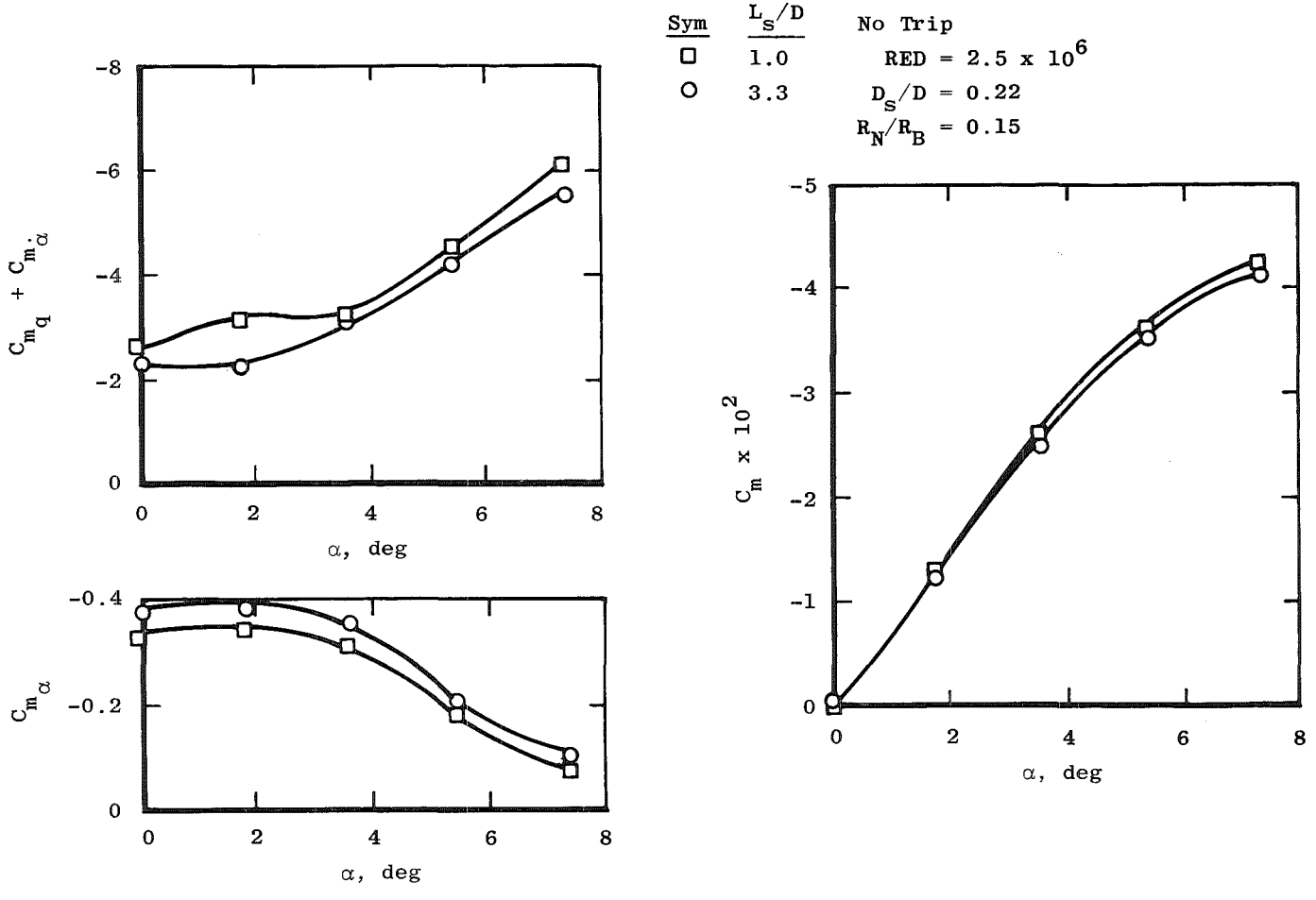

a. Laminar boundary layer

Figure 41. Sting effects as a function of angle of attack, M = 8, RFP = 0.0032.

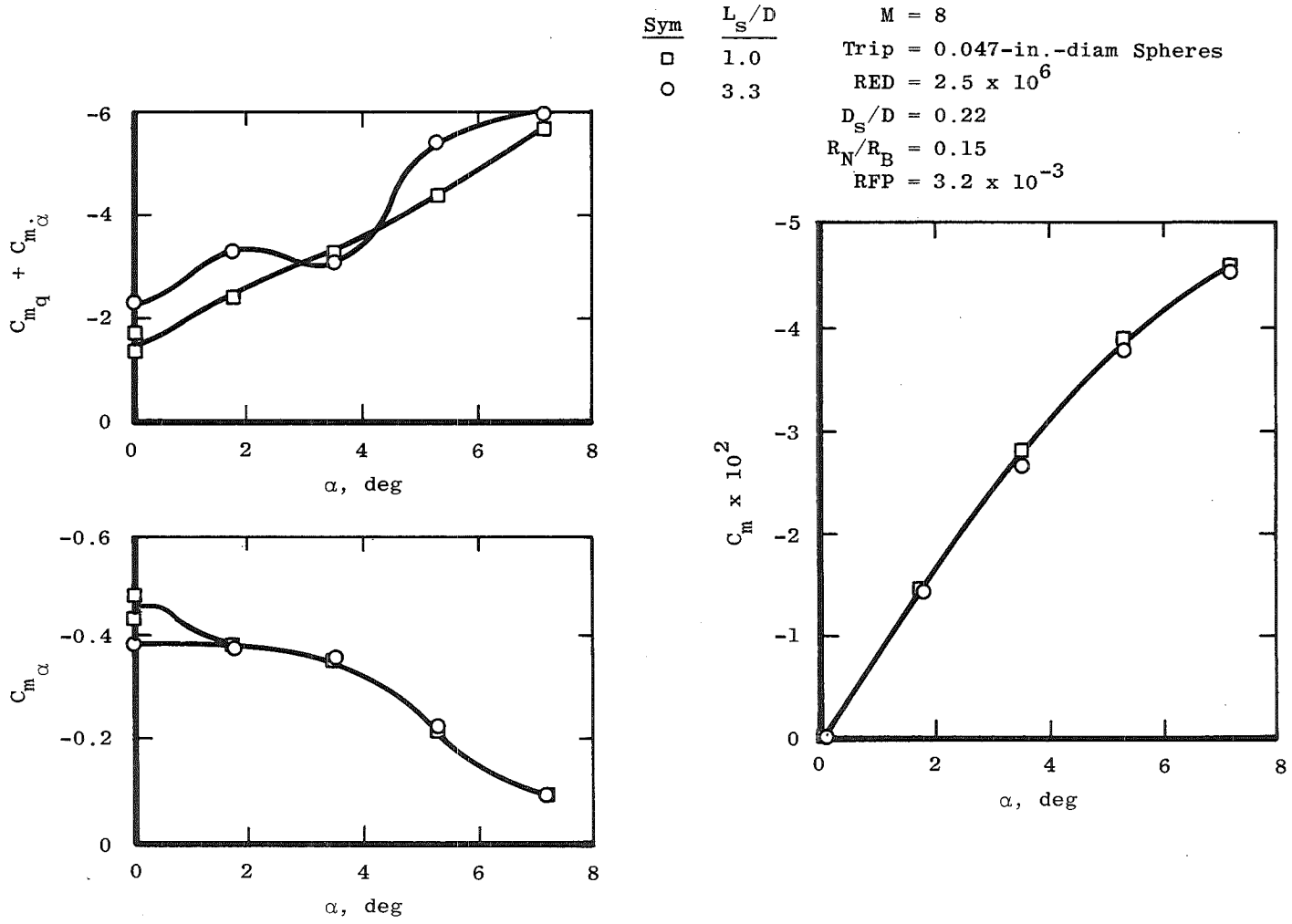

b. Turbulent boundary layer
Figure 41. Concluded.

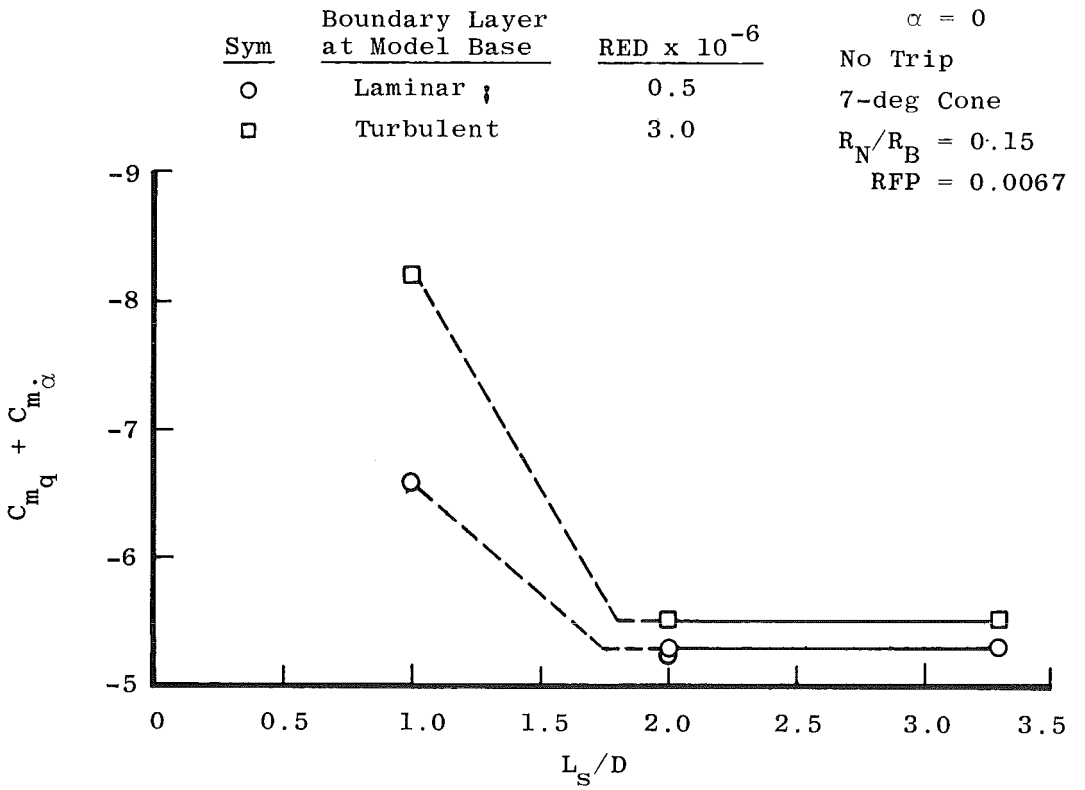

a. Damping derivatives

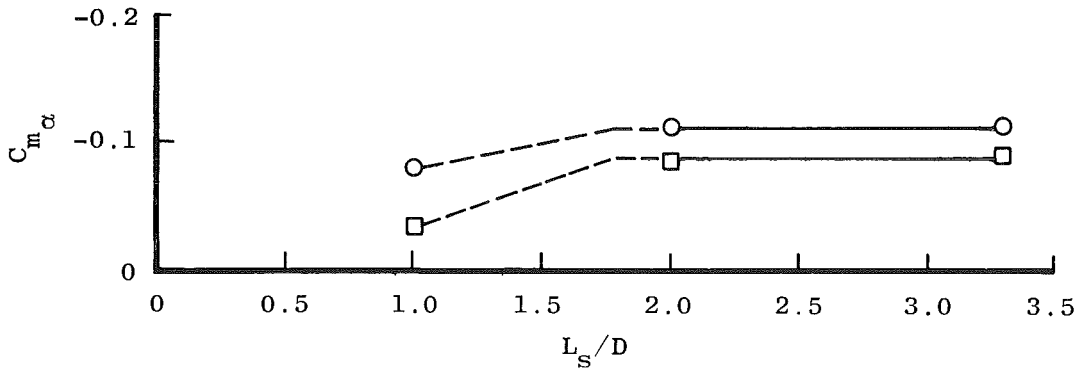

b. Static stability derivatives

Figure 42. Damping and static stability derivatives as a function of effective sting length, M = 2.

Sym	Boundary Layer at Model Base	RED x 10^{-6}	Test	M
○	Laminar	≈0.4	Ref. 1	2.9
□	Transitional	≈1.7	Ref. 1	3.0
△	Turbulent	≈4.5	Ref. 1	3.0
⊿	Turbulent	≈3.1	Ref. 23	3.0

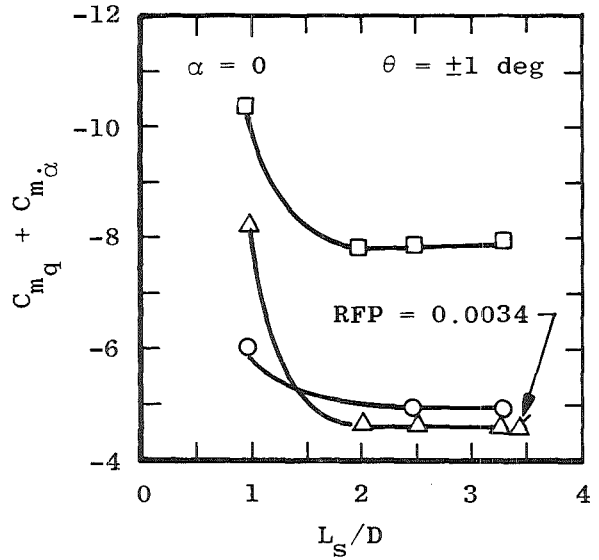

a. RFP = 0.0033

Sym	Boundary Layer at Model Base	RED x 10^{-6}	Test	M
○	Laminar	≈0.3	Ref. 1	2.7
□	Transitional	≈1.7	Ref. 1	2.9
△	Turbulent	≈4.6	Ref. 1	3.0
⊿	Turbulent	≈3.1	Ref. 23	3.0

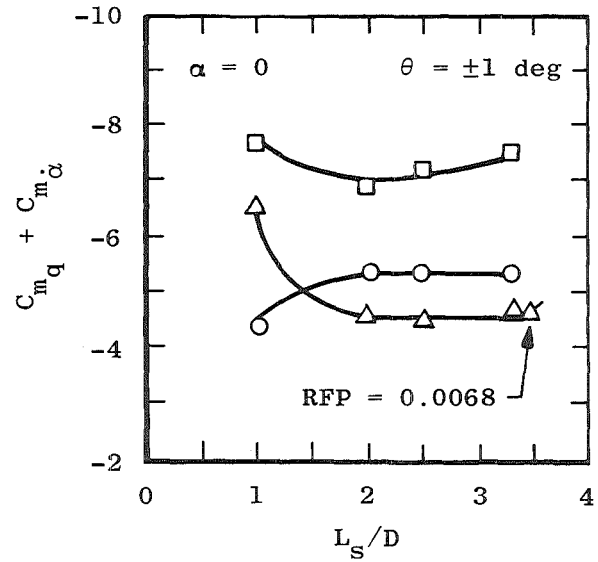

b. RFP = 0.0056

Figure 43. Damping derivatives as a function of effective sting length, D_s/D = 0.22, M ≈ 3 (reproduced from Ref. 1).

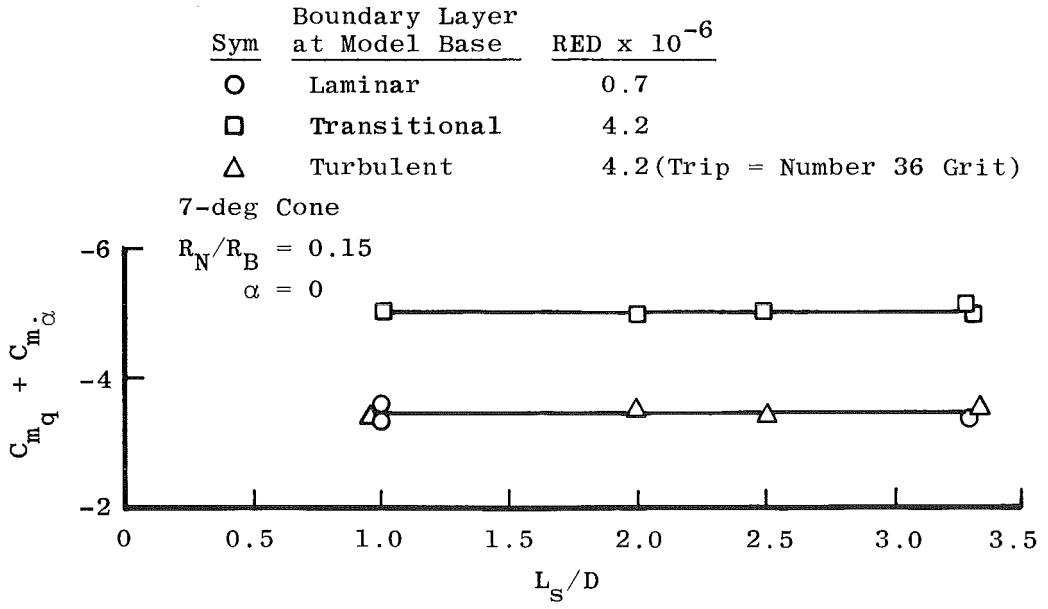

a. RFP = 0.0047

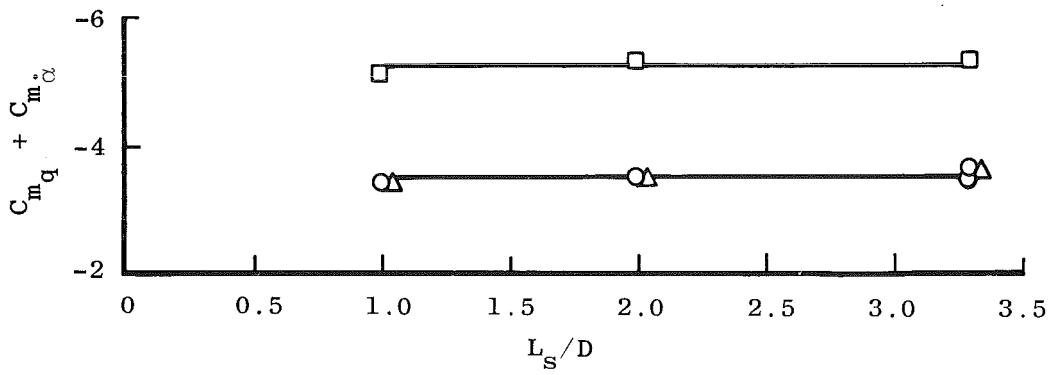

b. RFP = 0.0027

Figure 44. Damping derivatives as a function of effective sting length for two reduced frequencies, M = 5.

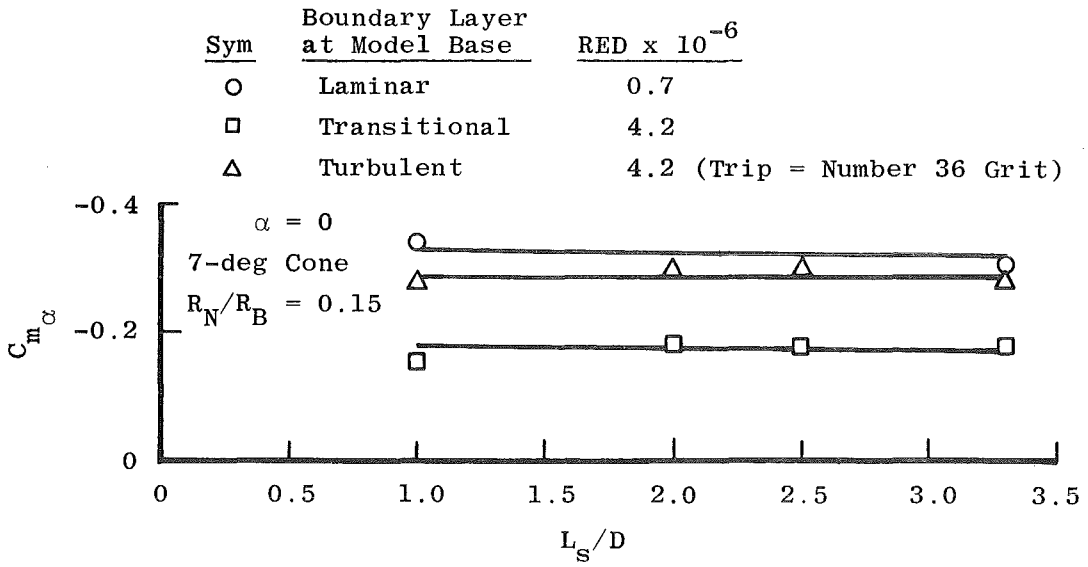

a. RFP = 0.0047

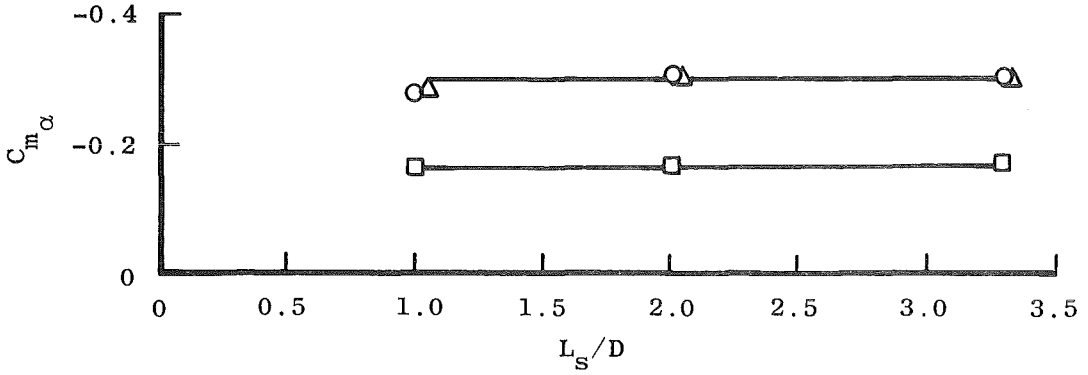

b. RFP = 0.0027

Figure 45. Static stability derivatives as a function effective sting length for two reduced frequencies, M = 5.

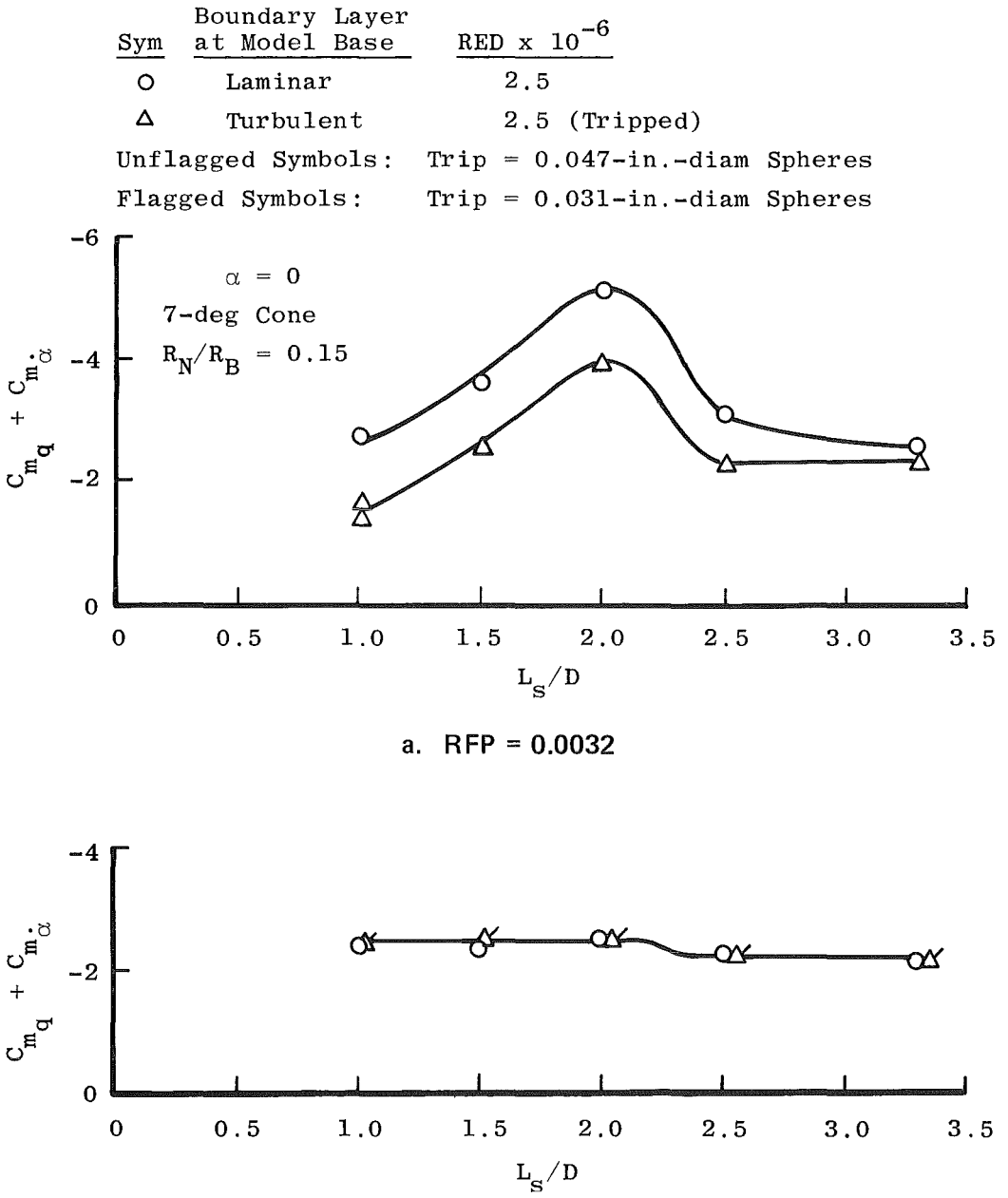

Figure 46. Damping derivatives as a function of effective sting length for two reduced frequencies, M = 8.

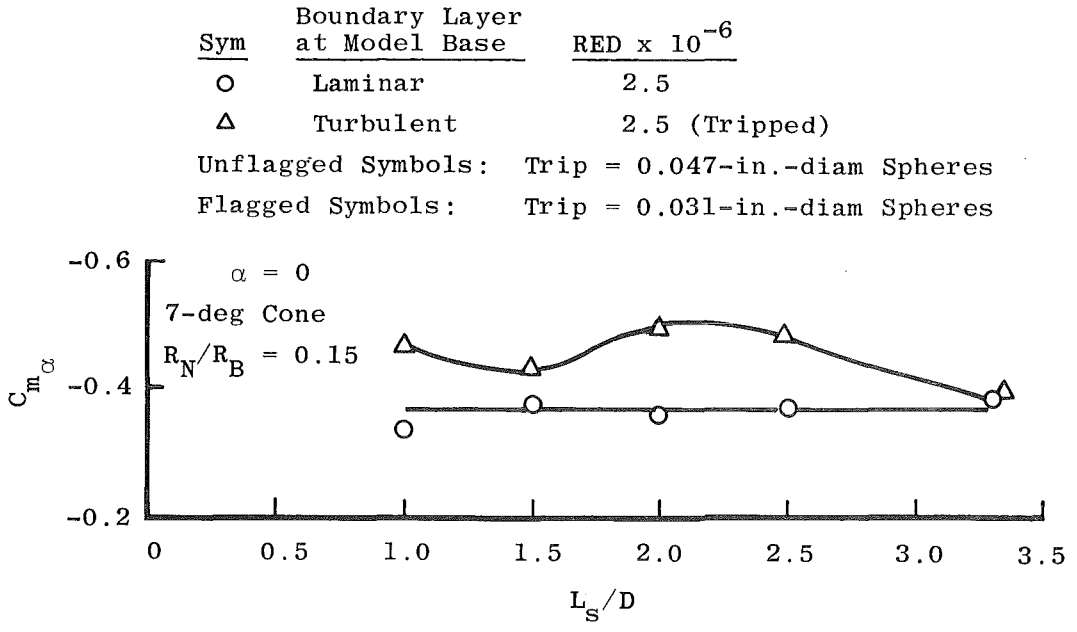

a. RFP = 0.0032

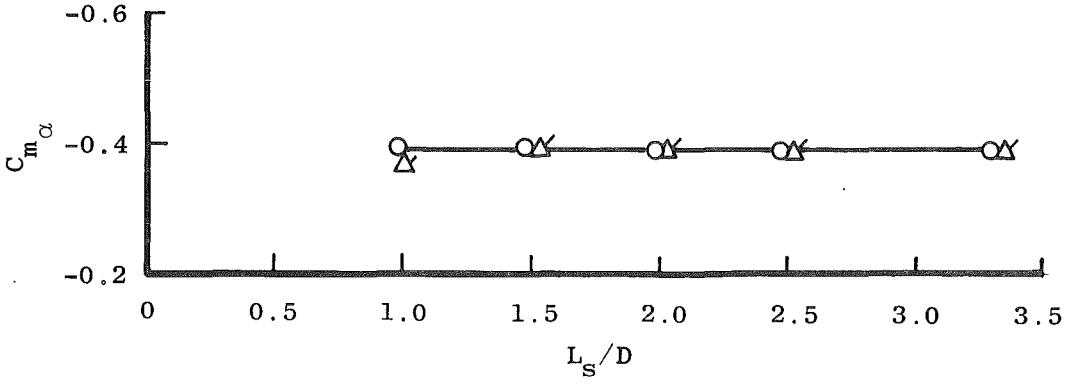

b. RFP = 0.0019

Figure 47. Static stability derivatives as a function of effective sting length for two reduced frequencies, M = 8.

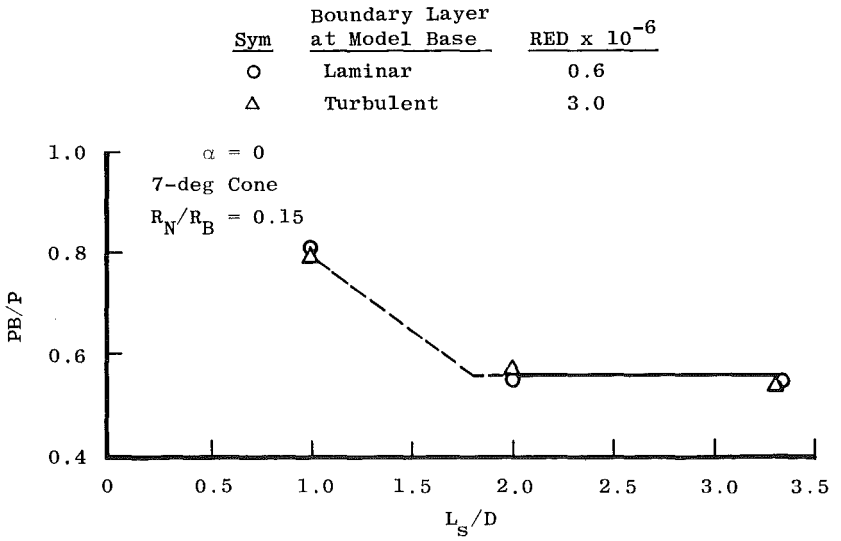

Figure 48. Base pressure as a function of effective sting length, M = 2.

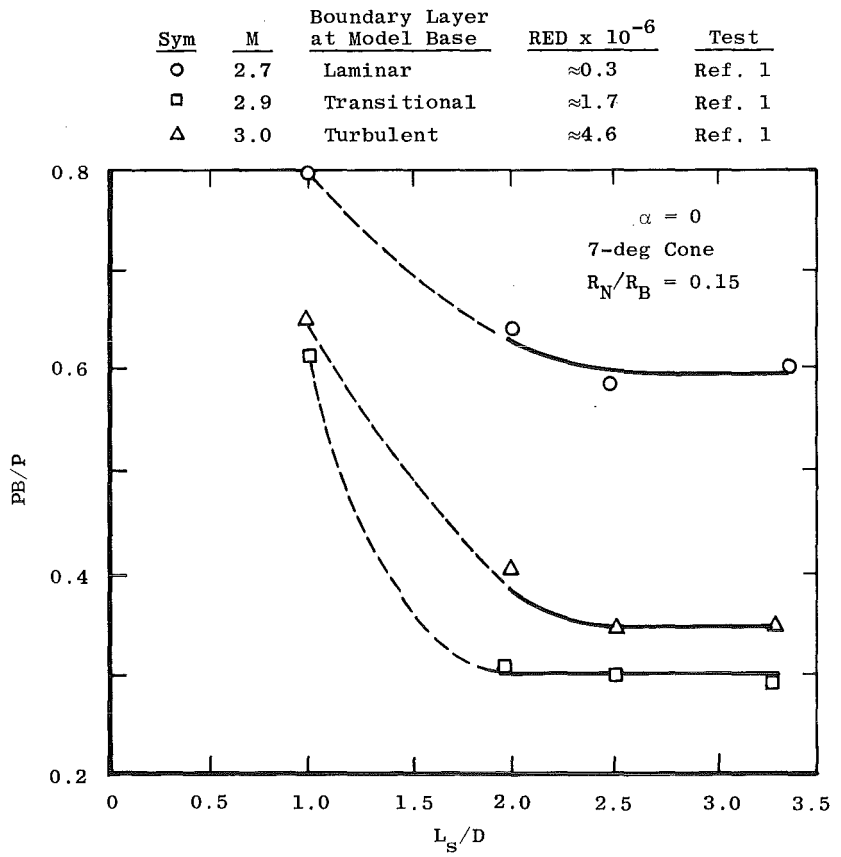

Figure 49. Base pressure as a function of effective sting length, M ≈ 3 (reproduced from Ref. 1).

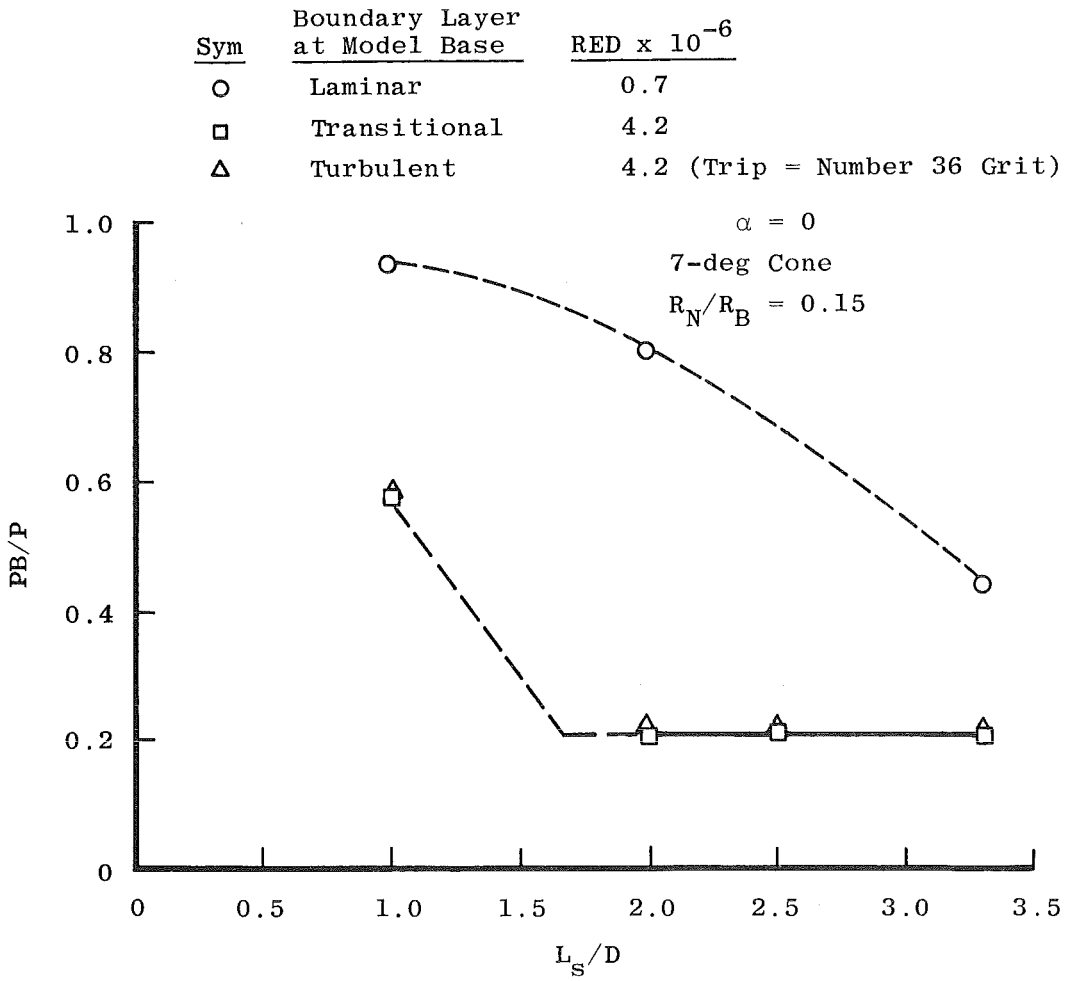

Figure 50. Base pressure as a function of effective sting length, M = 5.

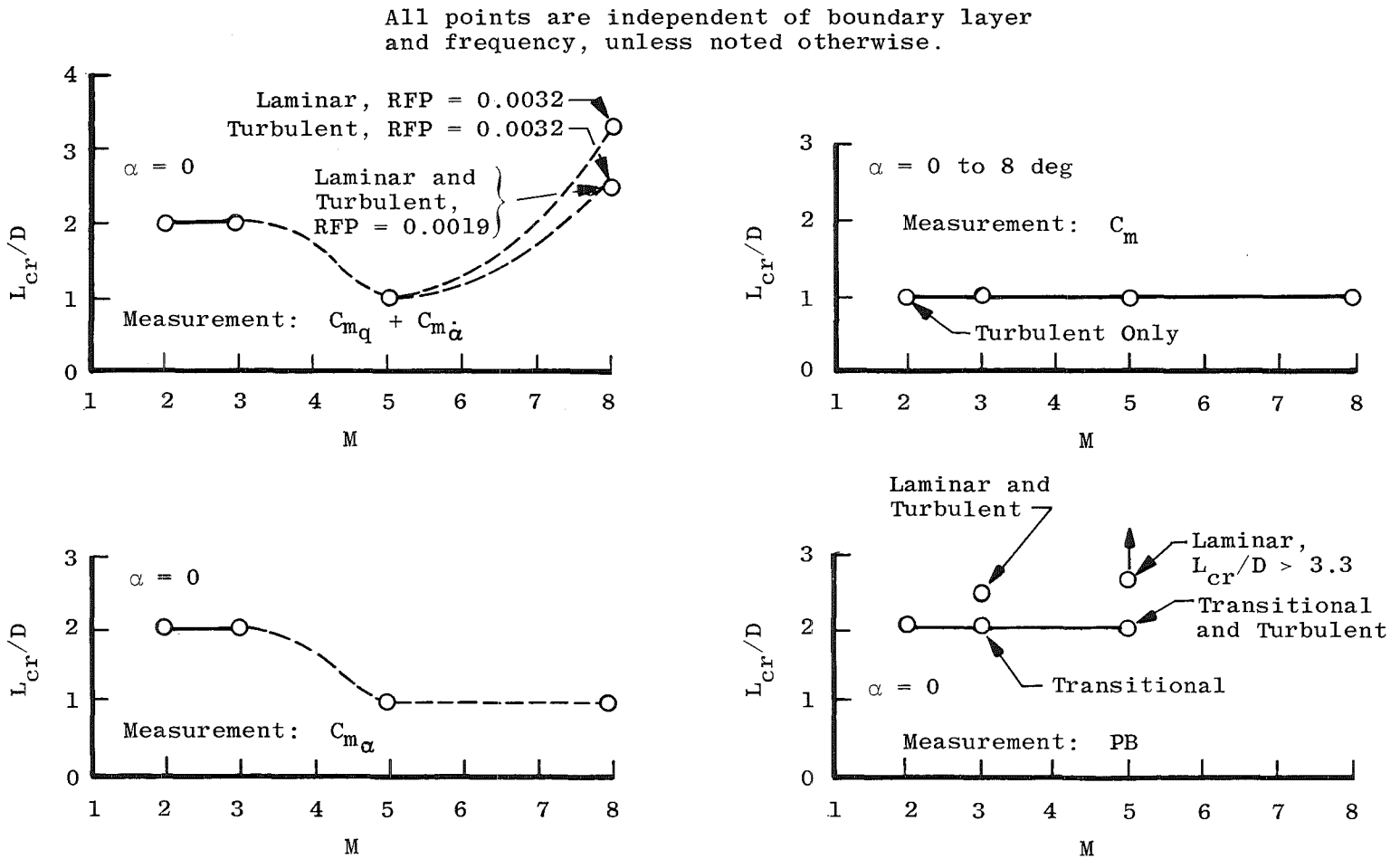

Figure 51. Critical sting length defined by static and dynamic measurements, 7-deg cone.

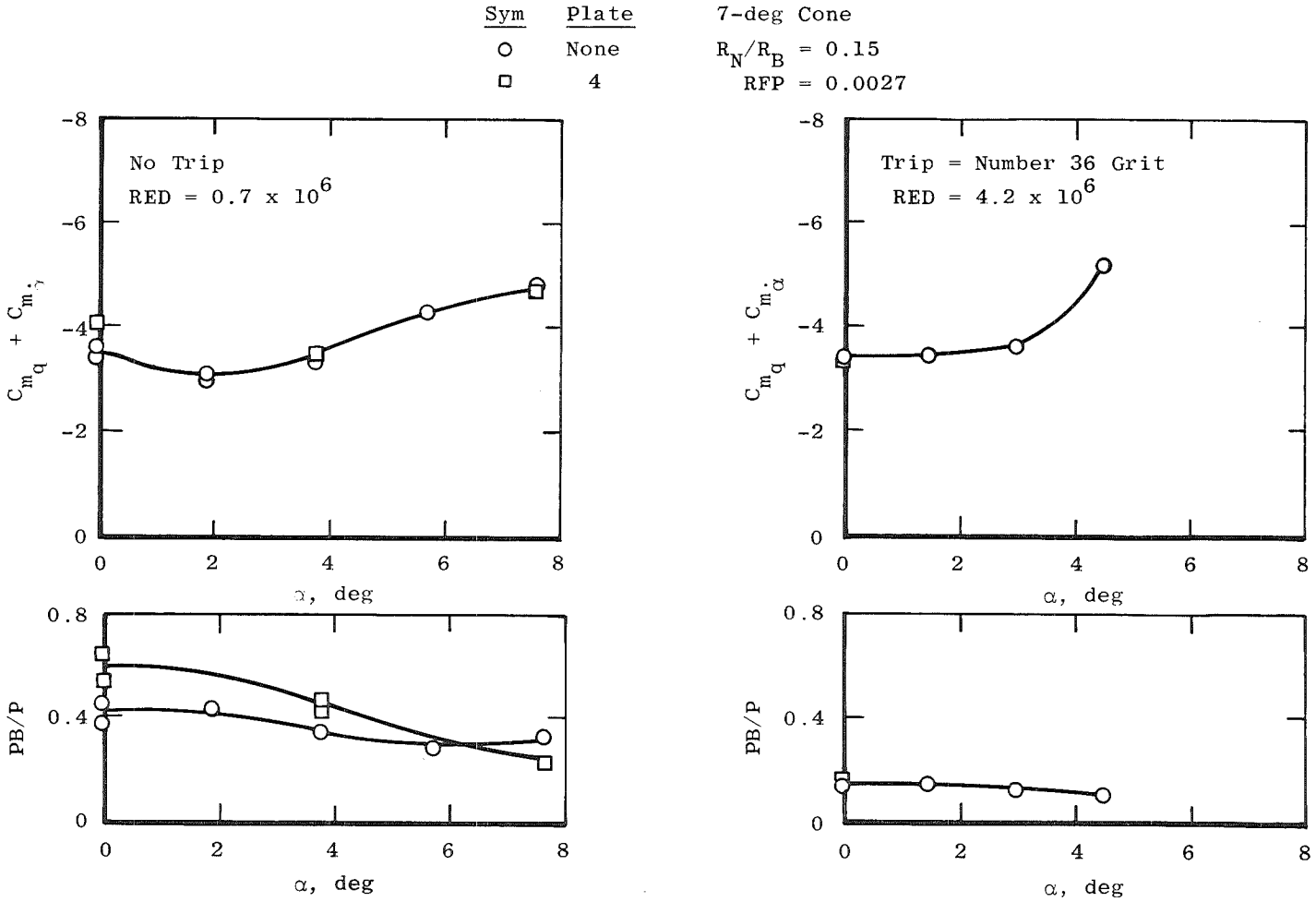

a. Laminar boundary layer

b. Turbulent boundary layer

Figure 52. Splitter-plate effects on damping derivatives and base pressure ratio, M = 5, L_s/D = 3.3.

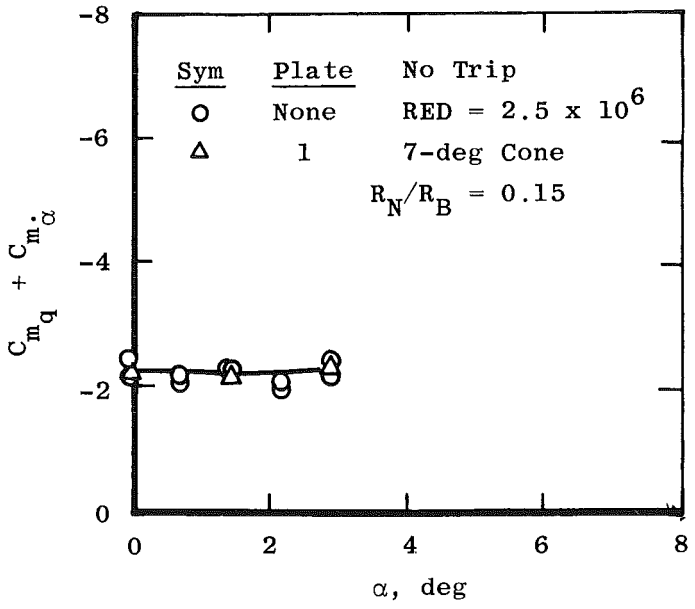

a. RFP = 0.0019

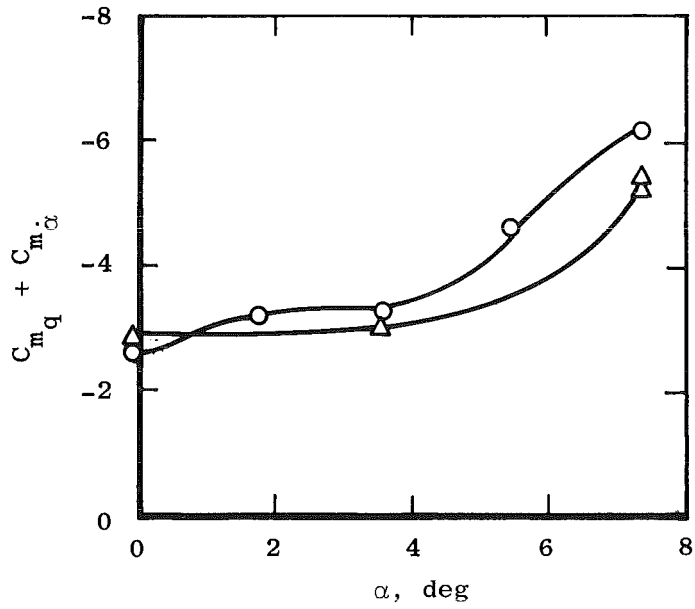

b. RFP = 0.0032

Figure 53. Splitter-plate effects on damping derivatives for two reduced frequencies, laminar boundary layer, M = 8, L_s/D = 1.0.

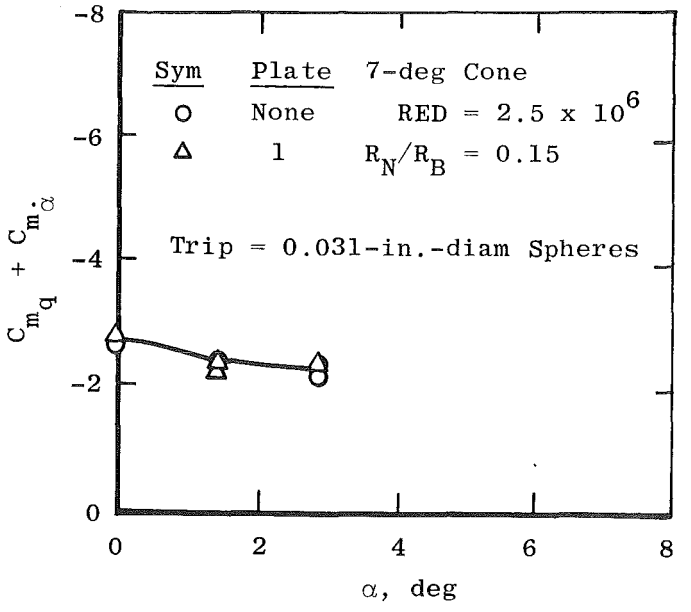

a. RFP = 0.0019

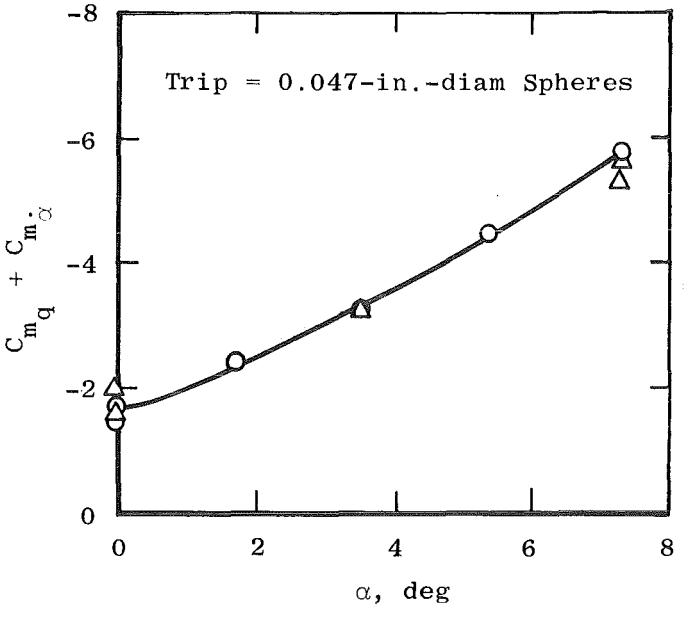

b. RFP = 0.0032

Figure 54. Splitter-plate effects on damping derivatives for two reduced frequencies, turbulent boundary layer, M = 8, L_s/D = 1.0.

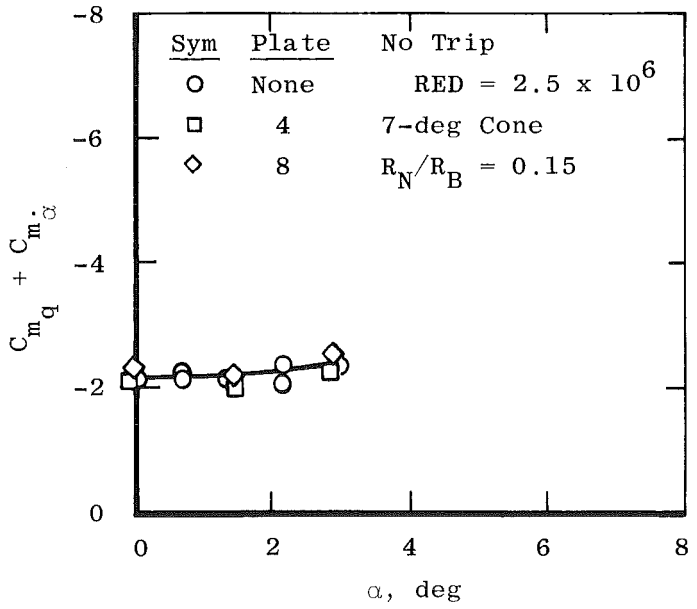

a. RFP = 0.0019

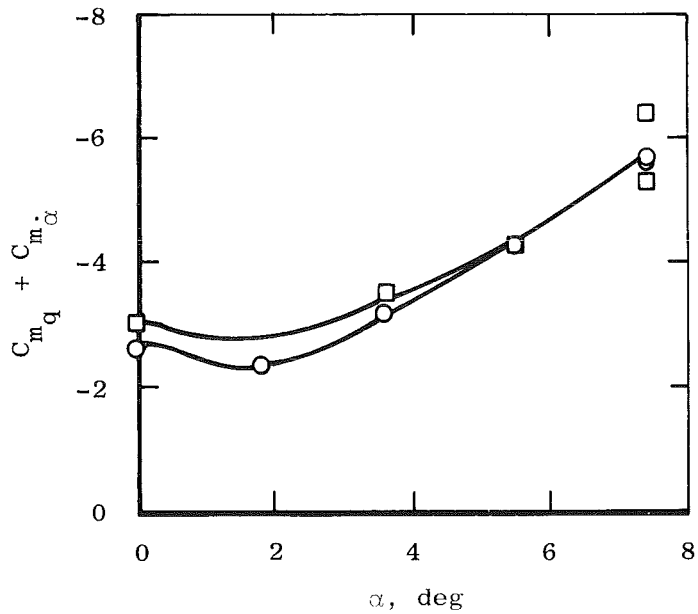

b. RFP = 0.0032

Figure 55. Splitter-plate effects on damping derivatives for two reduced frequencies, laminar boundary layer, M = 8, L_s/D = 3.3.

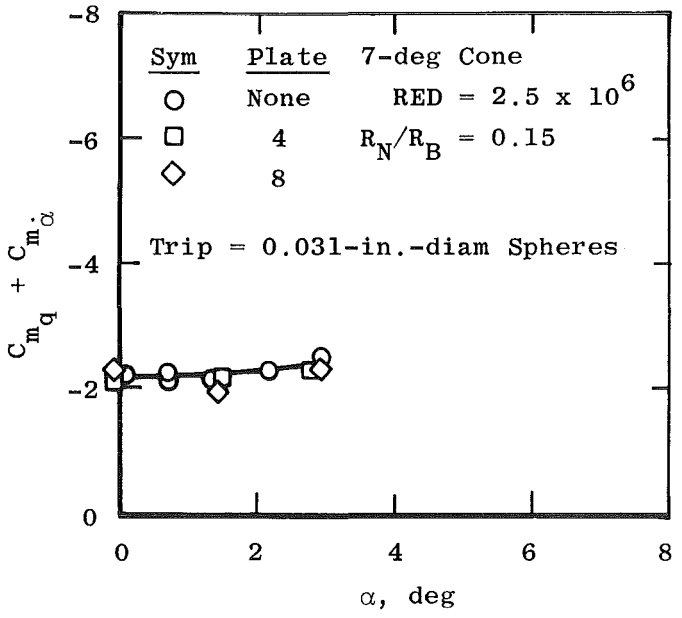

a. RFP = 0.0019

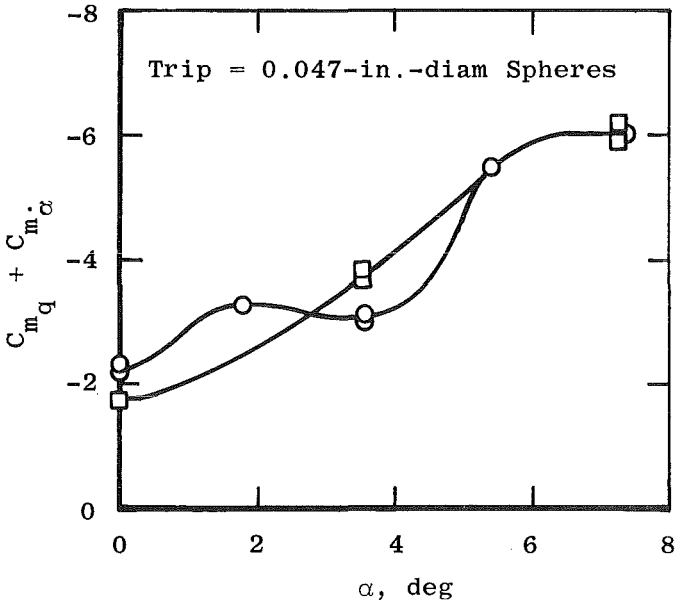

b. RFP = 0.0032

Figure 56. Splitter-plate effects on damping derivatives for two reduced frequencies, turbulent boundary layer, M = 8, L_s/D = 3.3.

Table 1. Test Conditions (Pressure Tests)

M	PT, psia	TT, °R	V, ft/sec	P, psi	Q, psi	T, °R	RE/ft x 10^{-6}	RED x 10^{-6}
2.00	21	650	1,862	2.68	7.51	361	4.17	2.78
3.01	51	660	2,260	1.37	8.67	235	5.86	3.91
5.06	150	660	2,575	0.26	4.74	108	6.10	4.07
7.96	300	1,260	3,744	0.03	1.41	92	1.46	0.97
7.96	300	1,370	3,904	0.03	1.41	100	1.29	0.86
8.00	850	1,350	3,877	0.09	3.90	98	3.68	2.45

Table 2. Test Conditions (Pitch-Damping Tests)

M	PT, psia	TT, °R	V, ft/sec	P, psi	Q, psi	T, °R	RE/ft x 10^{-6}	RED x 10^{-6}
1.88	3.4	579	1,697	0.523	1.30	339	0.83	0.56
1.92	5.4	573	1,709	0.781	2.02	330	1.32	0.88
1.97	19.8	580	1,745	2.65	7.20	327	4.66	3.11
2.99	50.1	591	2,134	1.39	8.66	212	6.85	4.57
5.02	20.2	607	2,467	0.037	0.66	101	0.95	0.63
5.02	28.0	582	2,416	0.052	0.91	96	1.40	0.93
5.09	114.6	650	2,559	0.195	3.54	105	4.71	3.14
5.09	154.3	651	2,561	0.263	4.77	105	6.32	4.22
7.90	104.3	1,356	3,884	0.012	0.51	101	0.46	0.31
7.96	301.8	1,338	3,860	0.032	1.42	98	1.34	0.89
7.98	502.4	1,359	3,891	0.052	2.33	99	2.17	1.45
8.00	704.8	1,358	3,890	0.072	3.23	98	3.02	2.02
8.00	858.1	1,355	3,886	0.088	3.94	98	3.70	2.46

Table 3. Pressure Test Summary (Tunnel A)

M	DTI*	Flare	L_S/D	D_S/D	PT, psia	RED $\times 10^{-6}$	α, deg	R_N/R_B	Trip Grit Number
5.06	1	None	3.88	0.19	150	4.1	0	0.1	None
5.06	2	None	3.88	0.19	150	4.1	-0.7 to 22.0	0.1	None
5.06	1	None	3.88	0.19	150	4.1	0	0.1	36
5.06	2	None	3.88	0.19	150	4.1	-0.7 to 22.0	0.1	36
5.06	1	None	3.88	0.19	150	4.1	0	0.1	20
5.06	2	None	3.88	0.19	150	4.1	-0.7 to 22.0	0.1	20
5.06	2	None	3.88	0.19	150	4.1	-0.7 to 22.0	0	None
5.06	2	6	1.04	0.19	150	4.1	-0.7 to 22.0	0.1	36
5.06	2	6	2.03	0.19	150	4.1	-0.7 to 22.0	0.1	↓
5.06	2	None	3.90	0.35	150	4.1	-0.8 to 22.0	0.1	↓
5.06	2	6	1.00	0.35	150	4.1	-0.8 to 22.0	0.1	↓
5.06	2	None	4.16	0.50	150	4.1	-0.8 to 22.0	0.1	↓
5.06	2	6	1.00	0.50	150	4.1	-0.7 to 22.0	0.1	↓
3.01	1	None	3.88	0.19	51	3.9	0	0.1	60
3.01	2	None	3.88	0.19	51	3.9	-0.7 to 23.2	0.1	60
3.01	1	None	3.88	0.19	51	3.9	0	0	None
3.01	2	None	3.88	0.19	51	3.9	-0.7 to 23.2	0	None
3.01	2	6	3.03	0.19	51	3.9	-0.7 to 22.3	0.1	60
3.01	2	6	2.03	0.19	51	3.9	-0.7 to 22.3	0.1	↓
3.01	2	6	1.04	0.19	51	3.9	-0.7 to 6.6	0.1	↓
3.01	2	4	1.05	0.19	51	3.9	-0.7 to 22.3	0.1	↓
3.01	2	None	3.90	0.35	51	3.9	-0.7 to 22.3	0.1	↓
3.01	2	6	2.00	0.35	51	3.9	-0.7 to 22.3	0.1	↓
3.01	2	6	1.00	0.35	51	3.9	-0.7 to 22.3	0.1	↓
3.01	2	None	4.16	0.50	51	3.9	-0.7 to 22.3	0.1	↓
3.01	2	6	2.00	0.50	51	3.9	-0.7 to 22.3	0.1	↓
3.01	2	6	1.00	0.50	51	3.9	-0.7 to 22.3	0.1	↓
2.00	2	None	3.88	0.19	21	2.8	-0.7 to 22.4	0.1	↓
2.00	2	6	2.03	0.19	21	2.8	-0.7 to 22.5	0.1	↓
2.00	2	6	1.04	0.19	21	2.8	-0.7 to 22.5	0.1	↓
5.00	2	None	3.88	0.19	150	4.3	-0.7 to 21.2	0.1	36
5.00	2	6	1.04	0.19	150	4.3	+0.1 to 21.2	0.1	36

*1 indicates heat-transfer data; 2 indicates pressure data.

Table 4. Pressure Test Summary (Tunnel B)

M	DTI*	Flare	L_S/D	D_S/D	PT, psia	RED × 10-6	α, deg	R_N/R_B	Trip Sphere Diameter
7.96	1	None	3.88	0.19	300	1.0	0.1	0.1	None
8.00	1	None	3.88	0.19	850	2.4	0	0.1	None
8.00	1	None	3.88	0.19	850	2.4	0	0.1	0.063
8.00	1	None	3.88	0.19	850	2.4	-0.1	0	None
8.00	1	None	3.88	0.19	850	2.4	-0.1	0.1	0.078
8.00	1	None	3.88	0.19	850	2.4	-0.1	0.1	0.094
8.00	1	None	3.88	0.19	850	2.4	-0.1	0.1	0.063
8.00	2	None	3.88	0.19	850	2.4	-1.1 to 24.8	0	None
8.00	2	None	3.88	0.19	850	2.4	0 to 24.8	0.1	0.063
8.00	2	6	2.03	0.19	850	2.4	0 to 24.8	0.1	0.063
8.00	2	6	2.03	0.19	850	2.4	0	0	None
8.00	2	6	1.04	0.19	850	2.4	0	0	None
8.00	2	6	1.04	0.19	850	2.4	0 to 24.8	0.1	0.063
8.00	2	None	3.90	0.35	850	2.4	0 to 20.7	0.1	0.063
8.00	2	6	2.00	0.35	850	2.4	0 to 20.7	0.1	0.063
8.00	2	6	1.00	0.35	850	2.4	0 to 20.7	0.1	0.063
7.96	2	6	1.00	0.35	300	0.9	-0.1	0.1	None
7.96	2	6	2.00	0.35	300	0.9	-0.1	0.1	None
7.96	2	None	3.90	0.35	300	0.9	-0.1	0.1	None
7.96	2	6	3.00	0.35	300	0.9	0	0.1	None
7.96	2	None	3.90	0.19	300	0.9	0 to 20.2	0.1	None
7.96	2	6	2.03	0.19	300	0.9	0	0.1	None
7.96	2	6	1.04	0.19	300	0.9	0 to 20.2	0.1	None
7.96	2	6	3.03	0.19	300	0.9	0	0.1	None
7.96	2	6	2.50	0.19	300	0.9	-0.1	0.1	None

*1 indicates heat-transfer data; 2 indicates pressure data.

Table 5. Tunnel A Pitch-Damping Test Summary (RFP ≈ 0.003)

M	Plate Number	Trip Grit Number	L_S/D	PT, psia	RED $\times 10^{-6}$	α, deg
2.99	None	None	3.3	50.1	4.5	-0.26 to 2.73
1.97	None	None	3.3	19.9	3.1	-4.98 to 1.16
1.92	None	None	3.3	5.4	0.8	-0.24 to 7.67
1.87	None	None	3.3	3.4	0.5	-0.13
5.02	None	None	3.3	28.0	0.9	-0.08
5.02	None	None	3.3	20.2	0.6	-0.08
5.02	None	None	3.3	20.2	0.6	-0.05 to 7.62
5.09	None	None	3.3	154.3	4.2	-0.01 to 4.57
5.09	None	36	3.3	154.5	4.2	-0.04 to 4.48
5.09	None	None	3.3	116.4	3.1	-0.02
5.05	None	None	2.0	150.1	4.2	0.02
5.05	None	36	2.0	150.0	4.1	0.01
5.02	None	None	2.0	19.3	0.5	-0.07 to 7.60
5.07	None	None	1.0	152.2	4.2	0 to 3.88
5.07	None	36	1.0	152.4	4.2	-0.17 to 4.51
5.02	None	None	1.0	19.7	0.5	-0.09 to 7.61
5.02	4	None	3.3	19.9	0.6	-0.08 to 7.61
5.06	4	36	3.3	149.9	4.1	-0.05
1.99*	4	None	3.3	19.0	2.9	-0.18
1.99*	4	None	3.3	19.0	2.9	-0.18
1.99*	4	None	3.3	19.0	2.9	-0.17

* Base-pressure data only.

Table 6. Tunnel A Pitch-Damping Test Summary (RFP ≈ 0.006)

M	Plate Number	Trip Grit Number	L_S/D	PT, psia	RED $\times 10^{-6}$	α, deg
5.10	None	None	3.3	156.7	4.2	-0.05 to 7.35
5.10	None	36	3.3	156.7	4.2	-0.05 to 7.34
5.10	None	36	2.0	156.8	4.2	-0.05
5.07	None	36	2.5	151.8	4.2	-0.04
5.07	None	None	2.5	151.8	4.2	-0.04
5.07	None	None	2.0	151.8	4.2	-0.04
5.07	None	None	1.0	151.7	4.2	-0.05
5.07	None	36	1.0	151.7	4.2	-0.07 to 7.34
4.99	None	36	1.0	29.1	0.8	-0.11
4.99	None	None	1.0	29.0	0.8	-0.08 to 7.81
4.99	None	None	3.3	29.0	0.8	-0.12 to 7.81
1.98	None	None	3.3	19.6	3.1	-0.34
1.98	None	None	3.3	19.4	3.0	-0.35
1.98	None	None	3.3	19.2	3.0	-7.95 to 7.38
1.98	None	None	2.0	19.3	3.0	-0.34
1.98	None	None	1.0	19.3	3.0	-0.33 to 7.38
1.88	None	None	1.0	3.5	0.6	-0.05 to 8.0
1.88	None	None	3.3	3.3	0.5	-0.05 to 7.97
1.88	None	None	2.0	3.5	0.6	-0.05 to 7.97

Table 7. Tunnel B Pitch-Damping Test Summary (RFP ≈ 0.002)

M = 8.00 TT = 1,350°R.

Plate Number	Trip Sphere Diameter	L_S/D	PT, psia	RED $\times 10^{-6}$	α, deg
None	None	3.3	859	2.5	-0.07 to 2.92
None	0.031	3.3	859	2.5	-0.07 to 2.91
None	0.031	2.0	858	2.5	-0.08
None	None	2.0	859	2.5	-0.10
None	None	2.5	859	2.5	-0.09
None	0.031	2.5	859	2.5	-0.09
None	0.031	1.5	851	2.4	-0.09
None	None	1.5	852	2.4	-0.10
None	None	1.0	851	2.4	-0.10 to 2.90
None	0.031	1.0	851	2.4	-0.08 to 2.88
None	0.031	1.0	851	2.4	-0.08 to 2.89
1	0.031	1.0	851	2.4	-0.10 to 2.88
1	None	1.0	851	2.4	-0.08 to 2.88
4	None	3.3	850	2.4	-0.07 to 2.89
4	0.031	3.3	851	2.4	-0.07 to 2.87
8	0.031	3.3	850	2.4	-0.07 to 2.88
8	None	3.3	852	2.4	-0.08 to 2.88
None	None	3.3	501	1.5	-0.07
None	None	3.3	501	1.5	-0.08 to 4.96
None	0.031	3.3	500	1.5	-0.07 to 4.95
None	0.031	2.5	499	1.5	-0.08
None	None	2.5	500	1.5	-0.08
None	None	2.0	500	1.5	-0.08
None	None	2.0	500	1.5	3.22
None	0.031	2.0	501	1.5	-0.10
None	0.031	2.0	502	1.5	-0.10
None	None	1.0	501	1.5	-0.10 to 4.96
None	None	3.5	501	1.5	-0.07

Table 8. Tunnel B Pitch-Damping Test Summary (RFP ≈ 0.003)

M = 8.00 TT = 1,350°R

Plate Number	Trip Sphere Diameter	L_S/D	PT, psia	RED $\times 10^{-6}$	α, deg
None	None	3.3	100	0.3	-0.07
None	None	3.3	300	0.9	-0.12
None	None	3.3	502	1.4	-0.12
None	None	3.3	704	2.0	-0.10
None	None	3.3	858	2.5	-0.10
None	*	3.3	856	2.4	-0.10
None	0.040	3.3	855	2.4	-0.11
None	0.030	3.3	856	2.5	-0.11
None	0.063	3.3	857	2.5	-0.08
None	0.030	3.3	706	2.0	-0.01
None	None	3.3	857	2.5	-0.05 to 7.42
None	0.047	3.3	857	2.5	-0.04 to 7.34
None	0.047	2.0	857	2.5	-0.05
None	None	2.0	856	2.5	-0.06
None	None	2.5	860	2.5	-0.06
None	0.047	2.5	858	2.5	-0.06
None	0.047	1.0	857	2.5	-0.06 to 7.31
None	None	1.0	857	2.5	-0.08 to 7.38
None	None	1.5	857	2.5	-0.08
None	0.047	1.5	858	2.5	-0.07
1	0.047	1.0	856	2.5	-0.07 to 7.30
1	None	1.0	858	2.5	-0.09 to 7.34
4	None	3.3	855	2.4	-0.08 to 7.39
4	0.047	3.3	856	2.5	-0.07 to 7.29
4	0.047	3.3	859	2.5	-7.44, 0, 7.26

* Trip = Number 36 Grit

Table 9. Test Condition Uncertainties (Pressure Tests)

M	RED × 10^{-6}	Uncertainty, ±Percent of Actual Value							
		M	PT	P	TT	T	V	Q	RED
2.00	2.78	0.8	0.2	2.5	0.5	0.9	0.5	0.9	1.0
3.01	3.91	0.6	0.2	2.6	0.5	0.9	0.3	1.4	1.2
5.06	4.07	0.5	0.2	3.0	0.5	1.0	0.3	2.0	1.4
7.96	0.86	0.4	0.1	2.4	0.4	0.8	0.2	1.7	1.2
7.96	0.97	0.4	0.1	2.4	0.4	0.8	0.2	1.7	1.2
8.00	2.45	0.3	0.1	1.6	0.4	0.6	0.2	1.1	0.9

Table 10. Test Condition Uncertainties (Pitch-Damping Tests)

M	RED × 10^{-6}	Uncertainty, ±Percent of Actual Value							
		M	PT	P	TT	T	V	Q	RED
1.88	0.56	0.8	0.4	2.5	0.5	0.9	0.6	0.8	0.9
1.97	3.11	0.8	0.2	2.5	0.5	0.9	0.5	0.9	1.0
5.02	0.63	0.5	0.2	3.0	0.5	1.0	0.6	2.0	1.4
5.09	4.22	0.5	0.2	3.0	0.5	1.0	0.3	2.0	1.4
7.98	1.45	0.3	0.1	1.6	0.4	0.6	0.2	1.1	0.9
8.00	2.46	0.3	0.1	1.6	0.4	0.6	0.2	1.1	0.9

Table 11. Uncertainties of Pressure Measurements

M	α, deg	PN/P	Uncertainty, ±Percent PN/P
2	0	0.24	2.5
	22.5	2.10	2.5
3	0	0.20	2.8
	23.1	4.10	2.6
5	0	0.10	10.4
	21.2	7.7	3.0
7.96	0	0.21	5.2
	20.2	17.6	2.4
8.00	0	0.16	2.7
	24.8	24.30	1.7

Table 12. Uncertainties of Pitch-Damping Measurements

M	RED × 10^{-6}	α,deg	RFP × 10^{3}	Δ(RFP) × 10^{3}	$C_{m_q} + C_{m_{\dot{\alpha}}}$	$\Delta(C_{m_q} + C_{m_{\dot{\alpha}}})$	C_{m_α}	$\Delta(C_{m_\alpha})$	C_m	$\Delta(C_m)$
1.88	0.55	0	6.92	±0.041	-5.3	±0.11	-0.11	±0.009	-	-
		8.0			-7.8	±0.15	-0.08	±0.009	-0.003	±0.00006
1.98	2.98	-0.3	6.90	±0.035	-5.4	±0.10	-0.09	±0.003	-	-
		7.4			-6.7	±0.13	-0.14	±0.004	-0.027	±0.0006
4.99	0.83	-0.1	4.62	±0.014	-3.4	±0.12	-0.31	±0.013	-	-
		7.8			-4.8	±0.15	-0.22	±0.013	-0.038	±0.0011
5.02	0.63	0	2.70	±0.008	-3.6	±0.12	-0.31	±0.008	-	-
		7.6			-4.9	±0.15	-0.22	±0.007	-0.039	±0.0012
5.09	4.21	0	2.70	±0.008	-5.3	±0.13	-0.17	±0.004	-	-
		4.6			-4.9	±0.12	-0.35	±0.007	-0.022	±0.0006
5.10	4.26	0	4.76	±0.014	-4.9	±0.13	-0.18	±0.005	-	-
		7.4			-4.6	±0.12	-0.30	±0.007	-0.038	±0.0011
7.98	1.46	-0.1	1.80	±0.004	-2.3	±0.06	-0.38	±0.005	-	-
		5.0			-3.9	±0.09	-0.30	±0.004	-0.033	±0.0008
8.00	2.47	0	3.18	±0.006	-2.4	±0.06	-0.39	±0.005	-	-
		7.3			-6.0	±0.12	-0.09	±0.003	-0.041	±0.0012
8.00	2.47	-0.1	1.95	±0.004	-2.2	±0.05	-0.39	±0.005	-	-
		2.9			-2.6	±0.05	-0.40	±0.005	-0.020	±0.0006

Appendix A
Summary of Available References

References	M	Reynolds Number	Boundary Layer	Model	Model Support	L_s/D	D_s/D	Measurements	Findings
Whitfield, Ref. 2	3.4	REL = 0.4 x 10^6 to 10 x 10^6	Laminar, Transitional, Turbulent	Ogive Cylinders with without Boattails	Sting	1 to 5.75	0.3, 0.5	PB Drag	1. PB and L_{cr} dependent on transition location and length Reynolds number. 2. L_{cr}/D = 1 to 5. 3. L_{cr} determined by the measurements of fore drag and base drag were approximately equal.
Pick Ref. 3	6.3, 9.9	REL = 0.5 x 10^6	—	9- and 10-deg Cones	Sting and free flight	11.0	0.33	PB	1. Severe differences between free-flight and sting-supported base pressures.
Crocco, Ref. 4	—	—	—	—	—	—	—	—	1. Theoretical prediction of base pressure.
Kavanau, Ref. 5	2.84	REL = 0.05 x 10^6 to 0.4 x 10^6	Laminar	Cone Cylinder	Sting	0.5 to 10.5	0.18, 0.23	PB	1. L_{cr}/D = 3 to 10.5 depending on REL. 2. No effect of base pressure orifice location.
Perkins, Ref. 6	1.5	REL = 0.6 x 10^6 to 5 x 10^6	Laminar, Turbulent	Ogive Cylinders with and without Boattails	Sting, Strut	0.7 to 7.2	-0.25 to 1.0	PB Drag	1. L_{cr}/D = 5.2 for zero boattail configuration with laminar or turbulent flow. 2. L_{cr}/D = 1.7 for boattail configurations with laminar or turbulent boundary layer. 3. For zero boattail configuration C_A was not affected by the presence of a rear support. 4. For a boattail configuration with laminar boundary layer, C_A was affected by the presence of a rear support.
Reller, Ref. 7	2.7 to 5	REL = 0.6 x 10^6 to 8.8 x 10^6	Laminar, Turbulent	Ogive Cylinders	Sting	2 to 8	0.25 to 0.75	PB	1. L_{cr}/D = 2 for M = 2.7, 3.5 and 4 for laminar and turbulent boundary layer. 2. At M = 5, L_{cr}/D = 6 and 4 for laminar and turbulent boundary layers, respectively. 3. Essentially no effect of base pressure orifice location.
Sevier, Ref. 8	2.97	REL = 10 x 10^6 to 40 x 10^6	Turbulent	Ogive Cylinders	Strut and Dummy Stings	2.5 to 6	0.06 to 0.6	PB	1. PB decreased with increasing D_s/D and was REL dependent. 2. For D_s/D = 0.375, PB was insensitive to REL. 3. Decreasing L_s/D from 6 to 2.5 had no effect on PB.

Appendix A
Continued

References	M	Reynolds Number	Boundary Layer	Model	Model Support	L_s/D	D_s/D	Measurements	Findings
Chapman, Ref. 9	2, 2.9	REL = 4 x 10^6 to 7.5 x 10^6	Laminar, Turbulent	Cone Cylinders and Ogive Cylinders	Sting	1.2 to 4.4	0 to 1	PB	1. L_{cr}/D = 3 at M = 2 for laminar and turbulent boundary layer. 2. L_{cr}/D = 3 at M = 2.9 for turbulent boundary layer. 3. PB generally decreased with increasing D_s/D.
Reichenau, Ref. 10	0.7 to 1.4	REL = 2.7 x 10^6 to 3.3 x 10^6	—	Ogive Cylinder	Strut, Sting	2.4 to 8.4	0.5	PB, PS	1. Strut configurations had little effect on PB at subsonic M but induced significant base interference at low supersonic M.
Reese, Ref. 11	0.65 to 2.2	RED = 0.5 x 10^6 to 1.1 x 10^6	—	Blunt-Cylinder-Flare	Sting	2.5 to 4.8	0.23 to 0.59	PB	1. $L_{cr}/D > 4.8$ for subsonic M. 2. $L_{cr}/D < 2.5$ for supersonic M.
Lee, Ref. 12	0.6 to 1.4	REL = 8 x 10^6	—	Ogive Cylinder with and without Boattail	Strut, Sting	0 to 8.5	0.25 to 0.75	PB, Drag	1. Cylindrical model: L_{cr}/D = 4.5 at M = 0.6, L_{cr}/D = 5.5 at M = 0.95, L_{cr}/D = 2.6 at M = 1.4 all for D_s/D = 0.5 and based on PB. 2. Boattail model: L_{cr}/D = 5.1 at M = 0.6, L_{cr}/D = 6.1 at M = 0.95, L_{cr}/D = 4.3 at M = 1.4 all for D_s/D = 0.43 and based on PB. 3. Critical sting lengths for the boattail model determined by measurements of base drag were approximately 1 model diameter greater than those determined by fore drag.
Cassanto, Ref. 13	4	REL = 0.4 x 10^6 to 10 x 10^6	Laminar, Transitional, Turbulent	10-deg Cone	Free Flight, Sting	—	0.25	PB	1. For laminar boundary layer, (PB) free = 0.75 (PB) sting. 2. For turbulent boundary layer, (PB) free = (PB) sting. 3. Found no radial gradients in sting base pressure data.
Cassanto, Ref. 14	≈ 20	REL = 0.5 x 10^6 to 7 x 10^6	Laminar	10-deg Cone	Flight Data	—	—	PB	1. Flight base pressures showed radial gradients which decreased monotonically from the centerline value.

Appendix A
Continued

Jaffe, Ref. 15	0.7 to 1.2	RE/ft = 1.5 x 10^6 to 3.5 x 10^6	Turbulent	10-deg Cone, Sphere, 60-deg Cone, Blunt Cylindrical Configuration	Free Flight, Sting	7 to 11.6	0.37 to 1.0	PB, Drag	1. 60-deg cone and sphere were insensitive to the presence of the sting. 2. For 10-deg cone, sting effect was appreciable for D_S/D = 0.67 and negligible for D_S/D = 0.37. Comparison of free-flight data with D_S/D = 0.37 data was good. 3. The fore drag for the 10-deg cone and blunt cylindrical configuration was influenced by the presence of the sting. 4. The free-flight drag data for the blunt configuration was 15 percent higher than the sting data.
Vlajinac, Ref. 16	0.28	RED = 0.12 x 10^6	Turbulent	6-deg Cone with Bulbous Base	Magnetic Suspension with Dummy Sting	4.7	0.25	Lift, Drag	1. The presence of the sting (D_S/D = 0.25, L_S/D = 4.7) produced considerable effects on lift and drag. 2. The sting increased model stability at and near α = 0.
Adcock, Ref. 17	0.26 and 0.9	RED = 1.2 x 10^6	Turbulent	6-deg Cone with Bulbous Base	Sting	—	—	Static Cofficients, Surface Pressure	1. Offset stings relative to the model base produced significant effects on the static data and the model surface pressures in the base region.
Fuller, Ref. 18	1.5 to 2.86	RED = 0.75 x 10^6	Turbulent	Ogive Cylinders with and without Boattails	Strut with Dummy Stings	3.3	0.25, 0.5, 0.75	Static Coefficients	1. Variation of D_S/D from 0 to 0.75 had little effect on the static data.
Tunnell, Ref. 19	0.6 to 1.3	—	Turbulent	Winged Vehicle	Sting	0.5 to 4.6	0.85, 0.93	PB, Drag	1. Theoretical prediction of base pressure resulting from conical flare on sting. 2. Sting length effects were a maximum in the subsonic-transonic region.
van der Zwaan	0.5	—	—	Winged Vehicle	Strut, Sting	—	—	Lift, C_m	1. Theoretical predictions of support interference on lift and pitching moment agreed well with experimental data.
Ericsson, Ref. 20	—	—	—	Blunt and Slender Cones with Rounded Bases	—	—	—	—	1. Proposed an analytical means for evaluating sting interference effects in dynamic stability measurements on bulbous base configurations. 2. Discussed effects of separated flow about bulbous base configurations.

Appendix A
Continued

References	M	Reynolds Number	Boundary Layer	Model	Model Support	L_S/D	D_S/D	Measurements	Findings
Wehrend, Ref. 21	0.65, 1.0, 1.6	RED = 0.68 x 10^6 to 1.54 x 10^6	—	12.5 deg Blunt Cone with and without Rounded Base	Sting	0, 1.85, 3.7	0.31 to 0.47	$C_{m_q} + C_{m_{\dot{\alpha}}}$	1. Variation of L_S/D = 0 to 3.7 and D_S/D = 0.31 to 0.47 affected $C_{m_q} + C_{m_{\dot{\alpha}}}$ only at M = 0.65 for the rounded-base configuration. 2. Results should be used with caution since interference hardware was attached to the sting. 3. The addition of a plate to the sting (L_S/D = 3.7) decreased model instability at M = 0.65 (rounded base), but had essentially no effect at M = 1 and 1.6
Uselton, Ref. 22	2.5, 3.4	RED = 0.45 x 10^6 to 10.2 x 10^6	Laminar, Transitional, Turbulent	10-deg Cone	Sting	0.75 to 3	0.2 to 0.8	PB, $C_{m_q} + C_{m_{\dot{\alpha}}}$, C_{m_α}	1. L_{cr}/D as determined by PB for D_S/D = 0.4 was between 1.5 and 2.25 for M = 2.5 and 3. At M = 4, L_{cr}/D was between 0.75 and 1.5 for turbulent boundary layer. 2. Interference damping results should be used with caution since interference hardware was attached to sting.
Uselton, Ref. 23	3	RED = 3.2 x 10^6	Turbulent	7-deg Cone	Sting	1 to 5	0.22	$C_{m_q} + C_{m_{\dot{\alpha}}}$ C_m	1. Magnitude of the sting interference effect was frequency dependent. 2. Decreasing L_S/D from 3.5 to 1 produced no effects on C_m.
Uselton, Ref. 24 Steinberg, Ref. 25	1.6 to 3	RED = 0.25 x 10^6 to 1.49 x 10^6	—	70-deg Cone	Sting, Free Flight	1.5 to 3.5	0.18 to 0.53	$C_{m_q} + C_{m_{\dot{\alpha}}}$ Wake Geometry	1. Wake geometries of sting-supported models showed significant differences as compared to free-flight wake geometries. 2. Interference damping results should be used with caution since interference hardware was attached to sting.
Sallet, Ref. 26 Roshko, Refs. 27 and 28	—	—	—	—	—	—	—	—	1. Discussion of effects of splitter or wedge plates behind circular cylinders.
Baughman, Ref. 29	3.1	REL = 2 x 10^6 to 14 x 10^6	—	Cone Cylinder	Sting	4	0.5	PS, PB	1. Splitter-plate effects on body and base pressures were generally small.

Appendix A
Continued

Clay, Ref. 30	14	REL = 0.6 x 10^6	—	Blunt 5.6-deg Cone	Sting	1.2, 4.2	—	PB	1. The addition of a splitter plate to the support strut behind the sting smoothed and reduced PB significantly.
Love, Ref. 31	Transonic, Supersonic	—	—	—	—	—	—	—	1. Summary of support interference problems at transonic and supersonic speeds.
Sieling, Ref. 32	3.88	RED = 3.9 x 10^6	Turbulent	Nose-Cylinder	Sting	0 to 4	0 to 0.5	PB	1. $D_S/D > 0.15$ influenced base pressure by more than 4 percent. 2. The base pressure was unaffected by sting length for $L_S/D > 1.3$.
Peckham, Ref. 33	6.8	—	Laminar, Transitional	Delta Wing, Cone	Sting	3.1 to 6.3	0.3 to 0.6	Schlieren Photographs	1. Results showed that short sting lengths have less support interference if transition occurs upstream of the model base.
Trescot, Ref. 34	1.5 to 4	RED = 0.16 x 10^6 to 0.41 x 10^6	—	70-deg Cone	Sting	5.8	0.12 to 0.5	Static Coefficients, PB	1. At M = 1.5 and 2 an increase in D_S decreased PB and increased the axial-force coefficient. No appreciable effect was found at M = 3 and 4.
Hart, Ref. 35	0.7 to 1.3	REL = 15 x 10^6 to 45 x 10^6	—	Ogive Cylinder with and without Fins	Flight Tests with Dummy Stings	2.4	0.6	PB	1. The sting reduced base suction by about 40 percent at subsonic-transonic speeds but had no measurable effect for M > 1.15.
Ericsson, Ref. 36	0.9 to 20.2	REL = 0.14 x 10^6 to 1.2 x 10^6	Laminar	Sharp and Blunt Cones	Sting with and without Splitter Plates, Free Flight	1.2, 4.2	—	PB $C_{m_q} + C_{m_{\dot{\alpha}}}$, C_{m_α}	1. A review of theoretical and experimental information about the effects of viscous interactions and support interference. 2. Comparison between ballistic range and wind tunnel data.
Reding, Ref. 37	0.28 to 10	RE/ft = 0.3 x 10^6 to 2.1 x 10^6	Laminar, Transitional, Turbulent	Sharp and Blunt Cones with and without Bulbous Bases	Sting, with and without Splitter Plates, Free Flight, Transverse Rod	0 to 3.6	0.314 to 0.471	PB, C_{m_α}, $C_{m_q} + C_{m_{\dot{\alpha}}}$	1. Transverse rod interference occurs at all speeds for certain trim angles or pitch amplitudes. 2. An analytical method of corrective wind tunnel dynamic support interference effects. 3. Any attempt to simulate ablation increases the probability of dynamic support interference.

Appendix A
Concluded

References	M	Reynolds Number	Boundary Layer	Model	Model Support	L_S/D	D_S/D	Measurements	Findings
Blaha, Ref. 38	0.6 to 1.0	RE/ft = 3.73 x 10^6 to 4.57 x 10^6	—	Winged Bodies of Revolution	Sting, Strut	—	—	PB	1. The effect of a lower-fuselage, forward-swept strut is generally small near the strut-model intersection and negligible over the the rest of the model.
Dix, Ref. 39	0.6 to 1.2	RE/ft = 3.5 x 10^6	—	Symmetric Bombs	Sting	5.1 to 12.3	0.31 to 0.92	Static Coefficients	1. The effect of the presence of a sting generally decreases with increasing Mach number. 2. Rolling moment is practically insensitive to the presence of a sting.
German, Ref. 40	0.6 to 1.4	RE/ft = 3.9 x 10^6 to 5.1 x 10^6	—	Ogive Cylinder with and without Boattails	Strut, Sting	2 to 5	—	PB	1. The 45-deg swept strut gives the greatest decrease in base pressure interference for M > 0.99. 2. L_S/D = 3 for 10-deg boattail, L_S/D = 5 for no boattail.
Nelson Ref. 41	Low Subsonic	—	—	Cylinder	Wall Mounted	—	—	Pressure Distribution Drag	1. Flow visualization of a cylinder in two-dimensional flow with a trail splitter plate and its application to strut-supported model interference at high angles of attack.

Appendix B
Suggested Sting Criteria[a]

Models	Mach Regime	Mach Number	Measurements	Boundary Layer[b]	Critical Sting Length, L_{cr}/D
Nose-Cylinder without Boattail	Subsonic	0.6 to 0.9	PB, C_A	Unknown	6
		---	C_N, C_m	---	No Data
		---	$C_{m_q} + C_{m_{\dot{\alpha}}}$	---	No Data
		0.6 to 1.4	PS	Unknown	3
	Transonic	0.95 to 1.2	PB, C_A	Unknown	6
		---	C_N, C_m	---	No Data
		---	$C_{m_q} + C_{m_{\dot{\alpha}}}$	---	No Data
	Supersonic	1.5 to 5	PB, C_A	Laminar	3 to 10[c]
		1.5 to 4	PB, C_A	Turbulent	2 to 3
		5	PB, C_A	Turbulent	4
		---	C_N, C_m	Laminar	No Data
		1.5 to 3	C_N, C_m	Turbulent	$L_{cr}/D \leq 3.3$[d]
		---	$C_{m_q} + C_{m_{\dot{\alpha}}}$	---	No Data
	Hypersonic	---	PB, C_A	---	No Data
		---	C_N, C_m	---	No Data
		---	$C_{m_q} + C_{m_{\dot{\alpha}}}$	---	No Data
Nose-Cylinder with Boattail	Subsonic	0.6 to 0.9	PB, C_A	Unknown	6
		---	C_N, C_m	---	No Data
		---	$C_{m_q} + C_{m_{\dot{\alpha}}}$	---	No Data
		0.6 to 1.4	PS	Unknown	3
	Transonic	0.95 to 1.2	PB, C_A	Unknown	6
		---	C_N, C_m	---	No Data
		---	$C_{m_q} + C_{m_{\dot{\alpha}}}$	---	No Data
	Supersonic	1.5 to 5	PB, C_A	Laminar	5 to 10[c]
		1.5 to 4	PB, C_A	Turbulent	$L_{cr}/D \leq 3$[d]
		---	C_N, C_m	Laminar	No Data
		1.5 to 3	C_N, C_m	Turbulent	$L_{cr}/D \leq 3.3$[d]
		---	$C_{m_q} + C_{m_{\dot{\alpha}}}$	---	No Data
	Hypersonic	---	PB, C_A	---	No Data
		---	C_N, C_m	---	No Data
		---	$C_{m_q} + C_{m_{\dot{\alpha}}}$	---	No Data
Slender Flat-Base Cones	Subsonic[e]	---	PB, C_A	---	No Data
		---	C_N, C_m	---	No Data
		---	$C_{m_q} + C_{m_{\dot{\alpha}}}$	---	No Data

Definitions for notes a through g are given on p. 144.

Appendix B
Continued

Models	Mach Regime	Mach Number	Measurements	Boundary Layer[b]	Critical Sting Length, L_{cr}/D
Slender Flat-Base Cones	Transonic[e]	---	PB, C_A	---	No Data
		---	C_N, C_m	---	No Data
		---	$C_{m_q} + C_{m_{\dot{\alpha}}}$	---	No Data
	Supersonic	2	PB, C_A	Laminar	2
		2	PB, C_A	Turbulent	2
		3	PB, C_A	Laminar	2.5
		3	PB, C_A	Transitional	2
		3	PB, C_A	Turbulent	2.5
		4	PB, C_A	Laminar	$L_{cr}/D > 3$[f]
		4	PB, C_A	Turbulent	1.5
		2 to 4	C_N, C_m	Laminar	1
		3	C_N, C_m	Transitional	1
		2 to 4	C_N, C_m	Turbulent	1
		2 to 3	$C_{m_q} + C_{m_{\dot{\alpha}}}$	Laminar	2
		3	$C_{m_q} + C_{m_{\dot{\alpha}}}$	Transitional	2
		2 to 3	$C_{m_q} + C_{m_{\dot{\alpha}}}$	Turbulent	2
	Hypersonic	5	PB, C_A	Laminar	$L_{cr}/D > 3.3$[f]
		5	PB, C_A	Transitional	2
		5	PB, C_A	Turbulent	2
		14	PB, C_A	Unknown	$L_{cr}/D > 4.2$[f]
		5	C_N, C_m	Laminar	1
		5	C_N, C_m	Transitional	1
		5	C_N, C_m	Turbulent	1
		8	C_N, C_m	Laminar	1
		8	C_N, C_m	Turbulent	1
		5	$C_{m_q} + C_{m_{\dot{\alpha}}}$	Laminar	1
		5	$C_{m_q} + C_{m_{\dot{\alpha}}}$	Transitional	1
		5	$C_{m_q} + C_{m_{\dot{\alpha}}}$	Turbulent	1
		8	$C_{m_q} + C_{m_{\dot{\alpha}}}$	Laminar	3.3[g]
		8	$C_{m_q} + C_{m_{\dot{\alpha}}}$	Turbulent	2.5
Slender Cones with Bulbous Bases	Subsonic	---	PB, C_A, C_N, C_m, $C_{m_q} + C_{m_{\dot{\alpha}}}$	---	No Data
	Transonic	---	PB, C_A, C_N, C_m, $C_{m_q} + C_{m_{\dot{\alpha}}}$	---	No Data
	Supersonic	---	PB, C_A, C_N, C_m, $C_{m_q} + C_{m_{\dot{\alpha}}}$	---	No Data
	Hypersonic	---	PB, C_A, C_N, C_m, $C_{m_q} + C_{m_{\dot{\alpha}}}$	---	No Data

Definitions for notes a through g are given on p. 144.

Appendix B
Continued

Models	Mach Regime	Mach Number	Measurements	Boundary Layer[b]	Critical Sting Length, L_{cr}/D
High-Drag Cones	Subsonic	---	PB, C_A	---	No Data
		---	C_N, C_m	---	No Data
		---	$C_{m_q} + C_{m_{\dot{\alpha}}}$	---	No Data
	Transonic	---	PB, C_A	---	No Data
		---	C_N, C_m	---	No Data
		---	$C_{m_q} + C_{m_{\dot{\alpha}}}$	---	No Data
	Supersonic	1.6 to 3	PB, C_A	Unknown	4
		---	C_N, C_m	---	No Data
		---	$C_{m_q} + C_{m_{\dot{\alpha}}}$	---	No Data
	Hypersonic	---	PB, C_A	---	No Data
		---	C_N, C_m	---	No Data
		---	$C_{m_q} + C_{m_{\dot{\alpha}}}$	---	No Data
Wing Configurations	Subsonic	0.6 to 0.9	PB, C_A	Turbulent	$L_{cr}/D \geq 5$[f]
		---	C_N, C_m	---	No Data
		---	$C_{m_q} + C_{m_{\dot{\alpha}}}$	---	No Data
	Transonic	0.95 to 1.05	PB, C_A	Turbulent	$L_{cr}/D \geq 5$[f]
		1.1 to 1.3	PB, C_A	Turbulent	2
		---	C_N, C_m	---	No Data
		---	$C_{m_q} + C_{m_{\dot{\alpha}}}$	---	No Data
	Supersonic	---	PB, C_A	---	No Data
		---	C_N, C_m	---	No Data
		---	$C_{m_q} + C_{m_{\dot{\alpha}}}$	---	No Data
	Hypersonic	---	PB, C_A	---	No Data
		---	C_N, C_m	---	No Data
		---	$C_{m_q} + C_{m_{\dot{\alpha}}}$	---	No Data
Sliced-Base Configuration	Subsonic	---	PB, C_A	---	No Data
		---	C_N, C_m	---	No Data
		---	$C_{m_q} + C_{m_{\dot{\alpha}}}$	---	No Data
	Transonic	---	PB, C_A	---	No Data
		---	C_N, C_m	---	No Data
		---	$C_{m_q} + C_{m_{\dot{\alpha}}}$	---	No Data
	Supersonic	2	PB, PS	Turbulent	2
		3	PB, PS	Turbulent	2
		---	C_N, C_m	---	No Data
		---	$C_{m_q} + C_{m_{\dot{\alpha}}}$	---	No Data

Definitions for notes a through g are given on p. 144.

Appendix B
Concluded

Models	Mach Regime	Mach Number	Measurements	Boundary Layer	Critical Sting Length L_{cr}/D
Sliced-Base Configuration	Hypersonic	5	PB	Turbulent	$L_{cr}/D > 3.9$[d]
		5	PS	Turbulent	1
		8	PB, PS	Laminar	$L_{cr}/D < 3.9$[d]
		8	PB	Turbulent	$L_{cr}/D < 3.9$[d]
		8	PS	Turbulent	1
		---	C_N, C_m	---	No Data
		---	$C_{m_q} + C_{m_{\dot{\alpha}}}$	---	No Data

NOTES:

[a] Criteria for $\alpha = 0$ for PB, $C_{m_q} + C_{m_{\dot{\alpha}}}$; C_A.

[b] Boundary-layer condition generally at model base.

[c] L_{cr}/D strongly dependent on REL.

[d] Available data are insufficient to indicate specific critical sting lengths. Stings with effective sting lengths greater than the value shown are interference-free of length effects.

[e] Test similar to those reported herein; tentatively scheduled for 1979 at M = 0.6 to 1.3.

[f] Available data are insufficient to indicate specific critical sting lengths. Stings with effective sting lengths less then the value shown will have interference effects.

[g] Frequency effects present: $L_{cr}/D = 3.3$ for RFP = 0.0032 and $L_{cr}/D - 2.5$ for RFP = 0.0019.

NOMENCLATURE

A	Reference area (based on model base diameter, D), 0.349 ft^2
C_A	Forebody axial-force coefficient, forebody axial force/Q · A
C_N	Normal-force coefficient, normal force/Q · A
C_m	Pitching-moment coefficient, pitching moment/Q · A · D
C_{m_q}	Pitching-moment coefficient due to pitch velocity, $\partial(C_m)/\partial(qD/2V)$, $radian^{-1}$
C_{m_α}	Pitching-moment coefficient due to angle of attack, $\partial C_m/\partial\alpha$, $radian^{-1}$
$C_{m_{\dot{\alpha}}}$	Pitching-moment coefficient due to rate of change of angle of attack, $\partial(C_m)/\partial(\dot{\alpha}D/2V)$, $radian^{-1}$
D	Reference length (model base diameter), 0.667 ft (all models)
D_s	Effective sting diameter, in. (at model base, see Figs. 6, 7, 8, 14, and 16)
DTI	Data Type Indicator: 1 = heat transfer, 2 = pressure
ITT	Enthalpy based on tunnel stilling chamber total temperature, Btu/lb_m
ITW	Enthalpy based on model wall temperature, Btu/lb_m
K	Boundary-layer trip sphere diameter or the average height of Carborundum grit, in.
L	Model length, in.
L_{cr}	Critical sting length, in. (for $L_s < L_{cr}$, model data are affected)
L_s	Effective sting length, in. (from model base to sting flare, see Figs. 6, 7, 8, 14, and 16)
M or M_∞	Free-stream Mach number
M_T	Boundary-layer trip sphere spacing, in.
OC	Oscillatory components
P	Free-stream static pressure, psi

PB	Model base pressure, psia
PN	Nth model pressure (surface or base pressure), psia
PS	Model surface pressure, psia
PT	Tunnel stilling chamber pressure, psia
P1 to P22	Pressure model surface pressures, psia
P23 to P26	Pressure model base pressures, psia
Q	Free-stream dynamic pressure, psi or psf
q	Pitching velocity, radian/sec
QDOT	Heat-transfer rate, Btu/ft^2-sec
RAY	Reference line on pressure model (see Figs. 3a and 20)
RE/ft	Free-stream Reynolds number per ft
RED	Free-stream Reynolds number based on reference length (D), RED = RE/ft · D
REL	Free-stream Reynolds number based on model length (L), REL = RE/ft · L
RFP	Reduced frequency parameter, $\omega D/2V$, radian
RHO	Free-stream density, lbm/ft^3
R_B	Model base radius, in.
R_N	Model nose radius, in.
S	Model surface distance (wetted distance) from nose to trip, in.
SC	Static components
ST	Stanton number based on tunnel stilling chamber temperature, TT; ST = QDOT/[RHO · V · (ITT - ITW)]
T	Free-stream static temperature, °R

TT	Tunnel stilling chamber temperature, °R
V	Free-stream velocity, ft/sec
X	Distance from model base (positive toward nose), in.
a	Angle of attack, deg or radians
$\dot{a}$	Time rate of change of angle of attack, radian/sec
$\Delta( )$	Uncertainty of parameter designated within parenthesis
θ	Oscillation amplitude, deg
θ_c	Cone half-angle, deg
ϕ	Model roll angle, deg
ω	Oscillation frequency, radian/sec